2023

Thermal Performance and Fluid Flow Studies of Twisted Tape Inserts Using Scaled Surrogate Fluids for Molten Salt Energy Applications

Arturo Cabral
Virginia Commonwealth University

Thermal Performance and Fluid Flow Studies of Twisted Tape Inserts Using Scaled Surrogate Fluids for Molten Salt Energy Applications

Thesis by
Arturo Cabral

In Partial Fulfillment of the Requirements for the
Degree of
Mechanical and Nuclear Engineering

VIRGINIA COMMONWEALTH UNIVERSITY
Richmond, Virginia

2023
Defended August 2^{nd}

Arturo Cabral
ORCID: 0000-0002-8297-9544

Arturo Cabral

Candidate

Mechanical and Nuclear Engineering

Department

This dissertation is approved, and it is acceptable in quality and form for publication:

Approved by the Dissertation Committee:

Lane B. Carasik, Ph.D. – Chair

Supathorn Phongikaroon, Ph.D. – Member

Worth P. Longest, Ph.D. – Member

Darius D. Lisowski, Ph.D. – Member

Cody S. Wiggins, Ph.D. – Member

Joshua D. Fishler, Ph.D. – Member

To my entire family, despite living in different cities, states, and countries, always felt connected and close. And to my late grandfather, Ismael Seanez Porras.

ACKNOWLEDGEMENTS

This work was done with the help of a lot of people. I am not a self-made man, and I will never be, but I got to where I am due to the people that surrounded and supported me.

To begin with, I would like to thank my parents, Maria del Carmen (Vicky) and Gerardo Arturo Cabral, thank you for always believing in me and supporting me throughout the different stages of my life. Your willingness to support my crazy ideas of where to take my life will always be appreciated. To my sister, Marcela, our young sibling rivalry turned into a friendship I could not live without. Thank you for exploring the world with me. To my entire family, too long to list, thank you for your support and your hospitality whenever I visited.

I would like to thank my advisor, Dr. Lane Carasik, for his constant guidance and ideas in this work. Your valuable feedback and early stage discussions of where to take the research group were always appreciated. The spontaneous ideas of what to research provided small projects that kept me engaged and helped me explore other sides of thermal hydraulic research. To the members of my thesis committee, thank you for taking the time in reading this paper and providing valuable feedback, as well as the comments through the proposal to better guide the work that is presented herein. To Dr. Supathorn Phongikaroon, thank you for opening your lab space to me when I was the only graduate student working for Dr. Carasik. I will always be amazed by your knowledge and expertise across multiple disciplines. To Dr. Darius Lisowski, thank you for mentoring me the summer I worked at Argonne National Laboratory with you. Under your guidance, I was able to win the Young Professional Thermal Hydraulics Research Competition. To Dr. Joshua Fishler, your guidance in my first journal paper provided valuable comments on what, without them, would have led to far more rejections before it was accepted for publication. To Dr. Worth Longest, thank you for agreeing to be part of this committee and for your valuable feedback. I learned of your research and your work through your graduate students, through their comments, I knew you had to be part of my committee. Finally, but definitely not least, to Dr. Cody Wiggins. Our first two years working together and developing, designing, building, and testing MSETF-1 provided a great place for a friendship to start. My time as a fellow PEPTer was short, but I hope I made you proud through my efforts and work. PEPT was far more complicated and complex than I ever imagined, thank you for all your efforts in this work. I will always cherish our talks on research, fluid dynamics, life, and sports.

My start as a thermal hydraulics researcher started at Texas A&M University, under the guidance of a lot of fellow colleagues and mentors. I would like to thank Dr. Saya Lee for being my first teacher in this field. His constant curiosity, optimism, and work ethic were always appreciated, especially when I did not know the answer or how to solve a problem. To Dr. Se Ro Yang, thank you for your patience in teaching a dumb undergraduate student the complexity of fluid dynamics and your love for research. To Dr. Giacomo Busco, thank you for the opportunity to work for you at Kairos Power. You helped me develop better CFD skills, a deeper appreciation of hard work, and that the best solutions were often the simplest ones. To Dr. Dimitris Killinger, our constant discussions about research and ideas were always valuable. You provided valuable guidance on what to expect as a graduate student, I took your most important lesson to heart, to learn to say NO.

To my coworkers and everyone at the FAST Research Group. Thank you for working with me. Teaching you all and learning from you has been an honor. Seeing the development of talented young researchers has been a great pleasure and I can not wait to see where your curiosity takes you. Special thanks go to Connor F. Donlan, Ryan P. McGuire, and Adam Mafi. I learned as much from you all as you did from me. I hope I was a good mentor, and sorry if I neglected my role as a teacher when I was dealing with my own fires.

To everyone working at VCU that provided help through their different services, such as Operations Management, package delivery, custodial, and I.T., thank you. The love for your job created a nice environment for research and work. It also made working at East Engineering Building and Sanger Building more manageable.

In addition, the daily coffee walks with different co-workers and graduate students provided excellent stress relief through the uncertainties of graduate school and a friendly catch-up. A special thank you to everyone working at Blanchard's Coffee, who kept me heavily caffeinated for the majority of my time at VCU.

Finally, this work was funded by the Nuclear Regulatory Commission under award 31310018M0031. The statements, findings, conclusions, and recommendations are those of the author and do not necessarily reflect the view of the U.S. Nuclear Regulatory Commission. This work was also supported by the Jeffress Trust Award in Interdisciplinary Research Program funded by the Thomas F. and Kate Miller Jeffress Memorial Trust, Bank of America, Trustee.

ABSTRACT

Global energy consumption is expected to increase with population growth and innovative clean sources of energy are sought out that can help meet the needs of a continuously power-hungry world. Some of these innovative sources of energy use molten salts as their operating and cooling fluid, such as fission reactors, fusion reactors, and solar power with energy storage. Molten salts are considered due to their efficient heat transfer properties, thermal energy storage capabilities, and high operating temperatures. To expedite their deployment, a further understanding of the heat transfer systems is required to accurately design and develop the heat transfer components and increase their efficiency. This is typically done through experimental campaigns and computational tools, though the computational tools require further validation and verification usually done through experiments. Experimental molten salt heat transfer campaigns can be inherently costly for a university laboratory setting.

This work investigated the viability of water as a surrogate fluid for five different molten salts for heat transfer experiments. A methodology was explored to understand the inherent differences, or distortions, that arise when utilizing a surrogate fluid for heat transfer experiments, and it demonstrated water to be a viable surrogate for these five molten salts. The distortions calculated can be better accounted for and improved with improved uncertainty in the thermophysical properties of the molten salts. Thermal performance studies were conducted using water as a surrogate fluid for a passive heat transfer enhancement technique, i.e. twisted tape inserts, that is considered for high heat flux applications. Friction factor, Nusselt number, and thermal performance factor data were obtained for a variety of twisted tape insert geometries and operating conditions. A clear dependence on the width of the twisted tape insert was observed that is not fully accounted for in the leading correlations found in the literature. Friction factor and Nusselt number correlation adjustments were made to better match the current experimental data. Additionally, higher thermal performance was observed at lower Reynolds numbers when using twisted tape inserts.

Fluid flow studies were done on three different twisted tape inserts for three Reynolds numbers of 17,700, 8,000, and 4,000. Flow structures such as high-velocity islands, inflow regions, secondary flow regions, and vortices were observed similar to those found in the literature. Additionally, the flow crossing between the gap of the twisted tape and the circular pipe for smaller widths dominated the transaxial flow. This resulted in vortices near the gaps that further propagated throughout the semi-circular geometry which can lead to further flow separation, lower heat transfer, and higher wall temperatures for loose-fitting twisted tape inserts. It is thus recommended to use twisted tape inserts that have a width-to-diameter ratio (w/D) as close to one as possible.

TABLE OF CONTENTS

LIST OF ILLUSTRATIONS

LIST OF TABLES

Chapter 1

INTRODUCTION

The work presented in this dissertation is divided into five main chapters. This first chapter consists of a quick introduction to the topic at hand. Since each chapter of this work has a detailed introduction, this one serves as a brief outline of the research work done. Specifically, this chapter details the underlying motivation of the work and summarizes the main ideas of the chapters that follow.

1.1 Motivation

Global energy consumption is expected to increase due to population growth. In order to meet the energy demands of a power-hungry world, innovative and carbon-free power plants are necessary to be designed and built in a timely manner. In addition, improving heat transfer has further contributed to the reduction of CO_2 emissions [1, 2], which has been an ongoing task in various energy and engineering disciplines [3]. Molten salts are currently considered innovative coolants for advanced energy systems due to their heat transfer, thermophysical properties, and high operating temperatures. Such advanced energy systems consist of fission reactors [4], fusion reactors [5], and solar power plants with concentrated energy storage [6]. In order to expedite their deployment, operating and fluid flow studies of their proposed heat transfer system components are required. This is usually done via experimental efforts or computational simulations, but computational simulations require further validation usually done by further experimentations. Heat transfer and fluid flow experiments using molten salts can be challenging due to their corrosive nature and high operating temperatures leading to significant expenses in materials, instrumentation, and maintenance. The significant financial burden associated with molten salt experiments can pose challenges for a laboratory setting in its early stages. Therefore, experimental efforts usually consist of scaling down the heat transfer components while preserving physical phenomena of interest [7].

1.2 Hypothesis - Objective

Twisted tape inserts have been studied as a heat transfer enhancement method in various engineering fields and energy applications. For this work, experimental efforts were conducted on this passive heat transfer enhancement technique currently studied for molten salt applications, i.e. twisted tape inserts, using a surrogate fluid that mimics heat transfer characteristics of molten salts [8]. These twisted tape inserts have been studied across literature for various engineering applications, with a recent resurgence of interest due to their application in high heat flux environments. Given the diverse range of manufacturing possibilities resulting from multiple geometric parameters, twisted tape inserts have been extensively studied in various thermal hydraulic investigations. Unfortunately, the majority of the work found in the literature is only applicable to specific applications and operating conditions. One parameter that has not been widely studied and understood is the width of the twisted tape insert. The aim of this work consisted of studying the thermal hydraulic and fluid flow effects caused by the width of the twisted tape insert for molten salt energy applications. In order to accomplish this, the specific tasks of this work consisted of:

- Develop a methodology to assess the applicability of surrogate fluids for heat transfer experiments for molten salt applications
- Develop a methodology to quantify the expected differences, or distortions, that arise when a surrogate fluid is used instead of the molten salt
- Further propagate the distortions that arise to heat transfer experimental data using a surrogate fluid
- Study the thermal performance of twisted tape inserts using the surrogate fluid. This consists of:
  - Studying the friction factor and how it changes with varying widths
  - Studying the heat transfer of the twisted tape insert and the effects of the twisted tape width.
- Further understand the secondary flow phenomena that have been reported in the literature and how it is affected by different twisted tape geometries.

The overall thermal hydraulic assessment of twisted tape inserts were studied for this work and its applications with molten salt heat transfer systems, which consist of friction factor, heat transfer, and fluid flow. After the investigation, suggestions on the geometric characteristics of the twisted tape inserts are provided.

1.3 Approaches

The work done consisted of a study using water as a surrogate fluid for five different molten salts, LiF - NaF - KF (FLiNaK), $NaNO_3$ - KNO_3, $NaNO_3$ - $NaNO_2$ - KNO_3, LiCl - KCl, and NaF - $NaBF_4$. These molten salts are of great interest due to their current investigation as innovative coolants in the energy industry. Water was initially matched with the molten salts across different temperature ranges to better match the Prandtl number of each individual surrogate fluid. A theoretical study based on a simple geometry was conducted to study the effects of the pumping power, heating power, friction factor, and Nusselt number difference, and predictions based on the surrogate fluid for molten salt scaled experiments. A method to quantify the differences in heat transfer results when using a surrogate fluid, distortion, was developed and conducted. Additionally, the distortions were then propagated to actual experimental heat transfer data to observe the Nusselt number predictions based on the experimental data of the surrogate fluid.

The friction factor of a twisted tape geometry was obtained for eight different twisted tape inserts. The eight twisted tape inserts consisted of a pitch of $y = 1.9$ and 3.81 for widths of $w/D = 0.95$, 0.85, and 0.75, and a twisted tape pitch of $y = 2.86$ for widths of $w/D = 1.0$ and 0.95. The Reynolds numbers explored for the friction factor consisted of ≈ 3,000 to 40,000. A friction factor correction was added to account for the different twisted tape widths for the most widely used correlation of twisted tape inserts. Nusselt number data were obtained for three twisted tape inserts of width $w/D = 0.95$ and pitches of $y = 1.91$, 2.86, and 3.81, at Reynolds numbers of ≈ 3,000 to 24,000. A channel flow transformation of the twisted tape insert was studied with good results for loose-fitting twisted tape inserts. This can lead to the potential for lessons learned in channel flow, such as fouling and roughness, to be better applicable in these geometries. There is a lack of understanding of these concepts for twisted tape inserts, due to the lack of work found in literature. An adjustment to the channel flow Nusselt number was created for a better prediction at low Reynolds numbers. Thermal performance data were also collected for these three twisted tape insert geometries, showing an improvement in thermal performance at lower Reynolds numbers and a dependence on the type of fluid used.

Finally, a flow visualization technique that detects particles based on the detection of 511 keV gamma rays was used to measure flow velocity across the complex geometries of the twisted tape inserts. The gamma rays penetrate through the opaque geometry allowing it to interrogate the flow without the need for clear optical access, making this visualization technique ideal to study fluid flow inside twisted tape inserts. Three geometries, twisted tapes of pitch $y \approx 2.8$ for widths of $w/D = 1.0$, 0.95, and 0.85 at Reynolds numbers of 17,700, 8,000, and 4,000, were explored.

This dissertation is divided into three major chapters, one exploring the applicability of water as a surrogate fluid for molten salt applications (Chapter 2), then one studying the thermal hydraulic performance of various twisted tape inserts (Chapter 3), and one investigating the fluid flow of twisted tape inserts (Chapter 4). Finally, the major conclusions of each chapter are summarized and a path for future work is outlined.

Chapter 2

SURROGATE FLUIDS

Molten salts are sought out in various engineering disciplines due to their high melting temperatures and thermophysical characteristics. Molten salts were initially studied at Oak Ridge National Laboratory (ORNL) for the Aircraft Reactor Experiment [9, 10]. Afterward, ORNL explored the applications of molten salts in breeder reactors with the Molten Salt Reactor Experiment, concluding in the 1970s [11]. In 1976, the Department of Energy urged for innovative technologies for solar, wind, and thermal power, which led Sandia National Laboratory to build the National Solar Thermal Test Facility (NSTTF) [12]. The NSTTF investigated components and systems that used molten salts for solar power applications. Solar One was born after NSTTF, consisting of a 10-megawatt solar plant in California with water as a working fluid. Solar One operated successfully with some minor difficulties consisting of operation under cloudy days and its energy storage system. Solar Two was designed with this in mind and improvements from Solar One, the major one consisting of molten salt as the heat transfer fluid and method of energy storage [13].

Recently, interest in molten salts has risen, and they are currently being explored for different engineering disciplines. Different countries and companies are investigating the design of molten salt fission reactors [14–16] and fusion energy [17, 18]. This renewed interest in molten salt energy applications necessitates studies of the behavior of molten salt in novel heat transfer systems. In addition, there is a search for methods to improve heat transfer, as more efficient energy plants have helped in the reduction of CO_2 emissions [1, 2]. Heat transfer experiments are typically conducted to study heat transfer behavior and improve thermal performance. However, performing such experiments using molten salts can be expensive and complicated in experimental settings [8]. Therefore, surrogate fluids are sought that can mimic heat transfer characteristics of molten salts at lower temperatures for experimental purposes. The chemical effects of the molten salts are not discussed nor considered in this work. The surrogate fluids are sought out that can mimic only the heat transfer characteristics of the molten salts and further work should be done to study the chemical effects of the molten salts.

This chapter identifies five different molten salts that can be scaled down for heat transfer experiments using water as a surrogate fluid. The five molten salts consist of LiF - NaF - KF (FLiNaK), $NaNO_3$ - KNO_3, $NaNO_3$ - $NaNO_2$ - KNO_3, LiCl - KCl, and NaF - $NaBF_4$. These molten salts were chosen because they match the Prandtl number of water as surrogate fluid at different temperature ranges. This section further quantifies the applicability of water as a surrogate fluid for the five molten salts by studying the temperature ranges in which water matches the Prandtl number of each molten salt. A theoretical study of a simple geometry is conducted to examine the effects of important thermal hydraulic parameters of interest that would be studied when using surrogate fluids for molten salt applications, such as friction factor, pressure drop, pumping power, heating power, and forced convection heat transfer. In addition, the usage of surrogate fluids for molten salt heat transfer experiments is expected to introduce distortions between the results obtained in the surrogate fluid experiments and their application to molten salt components. A methodology to quantify these distortions is presented, and forced convection experimental heat transfer data is used to further investigate these distortions.

2.1 Molten Salt Heat Transfer Experiments

Molten salt heat transfer experiments encompassing a variety of molten salts have been documented in the literature, particularly focused on forced convection. A summary of the relevant literature can be found in Table 2.1. Grele and Gedeon [19] investigated forced convection heat transfer with LiF - NaF - KF on Inconel X circular tubes. Their experimental results indicated lower heat transfer values compared to those predicted using correlations derived from other fluids. Grele and Gedeon observed a time dependence in their heat transfer results, in which the heat transfer coefficient changed dependent on time. They stated two possible reasons for the low heat transfer values. The first consisted of errors in the thermophysical properties, but the difference was too large to come from the uncertainty in the thermophysical properties alone. The second consisted of a theoretical thermal resistance layer caused by the molten salt and the Inconel X.

Hoffman and Lones [20] conducted a study on the heat transfer of the molten salt LiF - NaF - KF through circular tubes. Hoffman and Lones matched forced convection correlations with the molten salt by characterizing the thickness and thermal conductivity of the interfacial layer created between the molten salt and the Inconel. Hoffman and Lones concluded that forced convection correlations derived from other fluids, at similar Prandtl numbers, aligned with their experimental results for LiF - NaF - KF. In a separate investigation, Hoffman and Cohen [21] performed heat transfer experiments in circular tubes with the molten salt $NaNO_3$ - $NaNO_2$ - KNO_3 and arrived at the conclusion that correlations derived from other fluids were able to capture the experimental results.

Huntley and Gnadt [22] designed and tested an experimental loop with NaF - $NaBF_4$ to investigate corrosion between the salt and Hastelloy N. Their study included heat transfer experiments, which exhibited good agreement with conventional correlations. Ignat'ev et al [23] studied heat transfer of LiF - NaF - KF in circular tubes with good agreement with correlations. Wu et al [24] examined heat transfer of molten salt $LiNO_3$ and $NaNO_3$ - $NaNO_2$ - KNO_3 [25] in circular tubes across different flow regimes, with results consistent with conventional correlations.

Heat transfer experiments have also been conducted with fueled molten salts. Fueled molten salts consist of molten salts mixed with fissile material. Salmon [26] studied heat transfer in a double-tube heat exchanger using NaF - ZrF_4 - UF_4 and NaK, and obtained results that aligned with correlations. Amos et al [27] tested two fueled molten salts, LiF - BeF_2 - UF_4 and NaF - ZrF_4 - UF_4, in a heat exchanger configuration. Cooke and Cox [28] investigated heat transfer in fueled molten salt, LiF - BeF_2 - ThF_4 - UF_4, with good agreement with conventional correlations. Silverman et al [29] also studied forced convection with a fueled molten salt, LiF - BeF_2 - ThF_4 - UF_4, and an eutectic NaF - $NaBF_4$, and concluded that both salts behaved as normal heat transfer fluids.

Initial discrepancies between experimental results of molten salt heat transfer and conventional correlations have been attributed to factors such as uncertainty in the thermophysical properties of the salts, impurities in the salt, or the formation of a resistance layer [23]. Furthermore, advancements in measurement techniques and instrumentation have facilitated more complex experimental endeavors in the field of molten salt experiments [30]. Although Table 2.1 does not encompass the entirety of heat transfer experiments conducted with molten salts, as some reports are classified or not accessible, every experiment documented in the literature employs conventional correlations and matches nondimensional parameters for comparison with molten salt results. Moreover, the majority of literature focuses on simple geometries and forced convection in a circular pipe. These observations underscore the challenges associated with performing heat transfer experiments using molten salts.

The following section discusses how a surrogate fluid can be used to match nondimensional parameters of interest of molten salts to perform heat transfer experiments at lower operating temperatures.

2.2 Methodology

Surrogate fluids are sought out that match nondimensional numbers of interest obtained by nondimensionalizing the conservation equations, with further derivation available in Appendix A.1, to obtain the Reynolds, Prandtl, Euler, and Froude numbers. The objective of employing various scaling techniques is to achieve matching values for these numbers between the heat transfer component and the experimental settings. A more detailed discussion of the different scaling techniques can be found in Appendix A.2. Different techniques are employed to study different physical phenomena, thus the appropriate technique must be chosen based on the desired focus.

Surrogate fluids have been employed to scale down heat transfer components. Bardet and Peterson [31] utilized Therminol VP-1, Drakesol 260AT, and water to scale down experimental components

Table 2.1: Summary of heat transfer experiments using molten salts found in literature

Authors [Ref] - Year	Molten Salt	Comments
Grele and Gedeon [19] - 1954	NaF - KF - LiF	Forced convection on a pipe.
D. F. Salmon [26] - 1954	NaF - ZrF_4 - UF_4	Double tube heat exchanger studies using a molten salt and a liquid metal.
Hoffman and Jones [20] - 1955	NaF - KF - LiF	Forced convection on a pipe.
Amos et al [27] - 1958	LiF - BeF_2 - UF_4 and NaF - ZrF_4 - UF_4	Studied heat transfer of two molten salts in a shell and tube heat exchanger.
Hoffman and Cohen [21] - 1960	$NaNO_2$ - $NaNO_3$ - KNO_3	Forced convection on a pipe.
Cooke and Cox [28] - 1973	LiF - BeF_2 - ThF_4 - UF_4	Forced convection on a pipe, horizontal and vertical.
Huntley and Gnadt [22] - 1973	NaF - $NaBF_4$	Initially desined to study corrosion, but heat transfer experiments matched conventional correlations.
Silverman et al [29] - 1976	LiF - BeF_2 - ThF_4 - UF_4 and $NaBF_4$	Heat transfer studies of a proposed fueled-coolant molten salt pair.
Ingat'ev et al [23] - 1984	NaF - KF - LiF	Forced convection on a pipe.
Wu et al [24] - 2009	$LiNO_3$	Forced convection on a pipe.
Wu et al [25] - 2012	$NaNO_2$ - $NaNO_3$ - KNO_3	Forced convection on a pipe.

for various molten salts. Zweibaum et al [32] used Dowtherm A to scale down an experimental facility to study models created for Fluoride Salt-Cooled High-Temperature Reactors. Hughes [33] also used Dowtherm A as a surrogate fluid to scale down an experimental facility for studying models developed for Fluoride Salt-Cooled-High-Temperature reactors' heat exchanger and a directional direct reactor auxiliary cooling systems. Huddar et al [34] employed simulant oils to explore the frequency response of transient behavior in molten salt reactors. Liu et al [35] also utilized Dowtherm A to investigate natural convection behavior in Fluoride Salt-Cooled High-Temperature Reactors.

This work specifically addresses forced convection heat transfer for molten salt components, focusing on the Nusselt number, where the dominant nondimensional numbers are the Reynolds number and the Prandtl number. To ensure consistency, a linear scaling technique was employed, as described by Yadigaroglu et al [36]. It is important to note that other nondimensional parameters must be considered depending on the specific phenomena under investigation. For instance, in oscillating flows, the Strouhal number is matched, and in buoyancy-driven flows, the Rayleigh number is matched. However, these considerations are beyond the scope of this work.

Nusselt number, Nu is a function of Reynolds number and Prandtl number, Re and Pr:

$$Nu = f(Re, Pr). \tag{2.1}$$

The Reynolds number is defined as:

$$Re = \frac{\rho \cdot U_0 \cdot L_C}{\mu} = \frac{\rho \cdot V \cdot D}{\mu}, \tag{2.2}$$

where ρ and μ are the fluid's density and dynamic viscosity, respectively, U_0 and V are characteristic velocities, and L_C and D are characteristic lengths.

The Prandtl number is defined as:

$$Pr = \frac{\mu \cdot c_P}{k}, \tag{2.3}$$

where c_P and k are the fluid's specific heat at constant pressure and the thermal conductivity, respectively.

The Prandtl number was the first nondimensional number used to match a surrogate fluid with molten salts. This work focused on using water as a surrogate fluid to build an experimental loop to study the heat transfer phenomena of molten salt components. The molten salts consisted of five different molten salts used and considered in energy industries such as solar and nuclear. The molten salts are listed in Table 2.2 with their molar composition, approximate melting temperature, and industry. It's important to note that different molar compositions can vary the thermophysical properties of molten salts. The molar compositions reported in Table 2.2 consisted of those found in the literature.

2.2.1 Thermophysical Properties

Accurate thermophysical properties of the surrogate fluid and molten salts are required in order to properly scale the surrogate fluid and molten salt, as shown by the two nondimensional numbers in

Table 2.2: Molten salts selected with their molar composition, melting temperature, and industry.

Molten salt	Molar Composition (%)	Approximate melting temperature (^oC)	Industry
LiF - NaF - KF (FLiNaK)	46.5 - 11.5 - 5.42	454	Nuclear
$NaNO_3$ - KNO_3	66 - 34	222	Solar
$NaNO_3$ - $NaNO_2$ - KNO_3	0.07 - 49 - 44	142	Solar
LiCl - KCl	59.5 - 40.5	355	Nuclear
NaF - $NaBF_4$	58 - 42	385	Nuclear

Equations 2.2 and 2.3. There exists a variety of literature reviews summarizing existing experimental data and correlations of molten salts' thermophysical properties [6, 37–39]. This work focused on only selecting specific data sets and correlations to calculate their respective Reynolds numbers and Prandtl numbers.

The density of FLiNaK was obtained from experimental data of Cherenkova et al [40] with the corresponding correlation to match the data used. FLiNaK's viscosity was calculated from Cohen and Jones' correlation [41]. FLiNaK's thermal conductivity was obtained from Williams [42] and specific heat from Serrano-Lopez et al review article [37]. The density and viscosity of $NaNO_3$ - KNO_3 was obtained from Nissen [43]. The thermal conductivity of $NaNO_3$ - KNO_3 was obtained from [37] and its specific heat from [44].

$NaNO_3$ - $NaNO_2$ - KNO_3's density was obtained from the National Renewable Energy Laboratory's System Advisory Model [45], and its viscosity from Yang and Garimella [46]. $NaNO_3$ - $NaNO_2$ - KNO_3's thermal conductivity was obtained from [47] and its specific heat from [37]. Williams [42] was also used to obtain LiCl - KCl's density, viscosity, thermal conductivity, and specific heat. Koger [48] was used to obtain NaF - $NaBF_4$'s density, viscosity, thermal conductivity, and specific heat. Cabral et al [8] summarizes the correlations used to calculate the thermophysical properties of these salts, among others, and adjusts the correlations to have outputs in SI units.

Figure 2.1 plots the Prandtl number as a function of the temperature of the molten salts summarized in Table 2.2 with their temperature plotted in the top x-axis alongside water with temperature in the bottom x-axis. From this figure, it is clear that the Prandtl number of water is similar to the Prandtl number of the other molten salts at lower temperatures.

2.2.2 Model Example

A theoretical example of scaled molten salt components with water was done to further assess the capabilities of surrogate fluids scaling. A circular pipe was linearly scaled to study forced convection and calculate parameters of interest, such as friction factor and Nusselt number. The Darcy friction factor, f, is calculated in the laminar regime as:

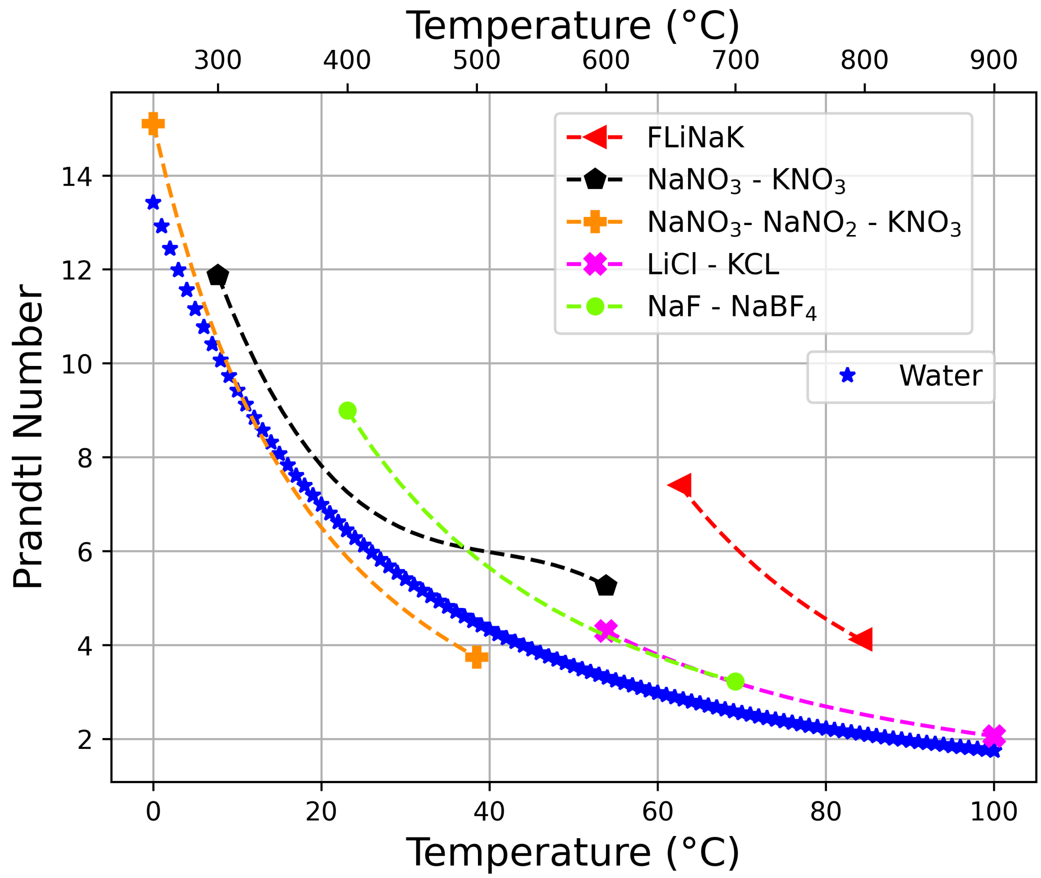

Figure 2.1: Comparison of Prandtl numbers between molten salt (top horizontal axis) and surrogate fluid, water, (bottom horizontal axis)

$$f = 64/Re, \tag{2.4}$$

where Re is the Reynolds number. For the turbulent regime, the Haaland [49] correlation is used, Equation 2.5:

$$\frac{1}{\sqrt{f}} = -1.8 \cdot log(\frac{6.9}{Re} + (\frac{\epsilon}{3.7 \cdot D_h})^{1.11}), \tag{2.5}$$

where ϵ is the roughness of the pipe (for simplicity, this work considers ϵ to be equal to 0).

In this work, transitional flows were not considered for this model example. The friction factor was calculated at temperature values at which the molten salt and water matched their Prandtl numbers. Nusselt number was calculated based on the Dittus-Boelter correlation [50]. For the Nusselt number calculations, a fixed Reynolds number was chosen (10,000) and the temperature was varied between the molten salts and water to better observe the distortions created by the Prandtl number distortion.

While the Prandtl number was matched through temperature selection, the Reynolds number was matched based on a linear scaling technique. The Reynolds number is matched between molten salt, ms, and surrogate fluid, sf, based on Equation 2.6.

$$Re_{ms} = Re_{sf} \leftrightarrow (\frac{\rho VD}{\mu})_{ms} = (\frac{\rho VD}{\mu})_{sf} \leftrightarrow \frac{D_{ms}V_{ms}}{D_{sf}V_{sf}} = \frac{\rho_{sf}\mu_{ms}}{\rho_{ms}\mu_{sf}}. \tag{2.6}$$

Equation 2.6 arranges the different variables in a form in which the temperature-dependent components are on the right-hand side of the equations and the geometric and operating components are on the left-hand side. Thus, the Reynolds number is matched by the geometry selection, linear scaling, operating conditions, and flow rate.

2.2.3 Distortions

Scaling components between molten salts to surrogate fluids inherently introduces distortions, and quantifying these distortions is a crucial aspect of scaling analysis. These distortions arise from adjustments made to geometric parameters, laboratory settings, temperatures, and pressures to ensure safety and cost-effectiveness. Liu et al [35] emphasized the lack of an established methodology for accounting for distortions in surrogate fluids. Understanding and quantifying scaling distortions are vital for accurately interpreting experimental data in scaled heat transfer experiments. Failure to properly account for distortions can lead to misinterpretation of experimental data and potentially overlook or misinterpret important phenomena. This work focused on the distortions that occur between Prandtl numbers. The technique used for quantifying Prandtl number distortions can potentially be extended to evaluate other types of distortions in future studies.

Distortions between Prandtl numbers were calculated for selected temperature ranges spanning the molten salts and water. The distortions were calculated based on a technique from Kairos Power [51]:

$$D_{Pr,i} = \frac{Pr_{ms,i} - Pr_{sf,i}}{Pr_{ms,i}}, \tag{2.7}$$

where the subscripts ms and sf stand for molten salt and surrogate fluid, respectively, and i is the Prandtl number at a specific temperature. To compare the distortions across a temperature range, a nondimensional temperature range was calculated based on Equation 2.8:

$$\theta_{i,ms} = \frac{T_{i,ms} - T_{min,ms}}{T_{max,ms} - T_{min,ms}} \tag{2.8}$$

The minimum and maximum temperatures, min and max, were obtained based on matching Prandtl number ranges between the molten salt and water.

As the Reynolds number was directly scaled and matched through geometric and operating conditions, these distortions do not propagate to the friction factor calculations, as will be shown in the results. However, the Nusselt number is dependent on the Prandtl number and the differences between the molten salt and water created further distortions when the Nusselt number was calculated.

The largest distortion is then further analyzed with uncertainty in the thermophysical properties accounted for. This was done in order to analyze the impact of the uncertainty of the molten salts' thermophysical properties on the distortions. The uncertainties in the Prandtl numbers were quantified based on the uncertainties in the thermophysical properties and using the least squares uncertainty [52].

2.3 Results

2.3.1 Prandtl number matching

Figures 2.2 to 2.6 plot the Prandtl numbers of water matched with the various molten salts across different temperature ranges. From these plots, it is more evident how the Prandtl number of water matches well with each individual molten salt. Water's Prandtl number matches well with the Prandtl numbers of FLiNaK, $NaNO_3$ - $NaNO_2$ - KNO_3, LiCl - KCl, and NaF - $NaBF_4$ to a very precise degree. While for $NaNO_3$ - KNO_3's Prandtl number there is a strange behavior occurring, in which the Prandtl number dips and then it follows similar trends as the other Prandtl numbers of the other fluids. One possible explanation comes from the correlation chosen to calculate the viscosity of $NaNO_3$ - KNO_3 [37] as the curve can be seen in different experimental results. While this phenomenon can cause complications when using surrogate fluids for heat transfer experiments, the chemistry behind the nature of this phenomenon is out of the scope of this work. Instead, this phenomenon will be studied as distortions between the Prandtl numbers.

Friction factor and pressure drop were calculated for a circular pipe (inner diameter of 2.54 cm and length of 1 meter) using surrogate fluids and molten salts by matching the Reynolds and Prandtl numbers. Reynolds number scaling was done using Equation 2.6 and by selecting a Prandtl number that matched between the molten salts and water. Table 2.3 summarizes the parameters between water and the molten salts for each Prandtl number, alongside operating ratios between water and molten salts. Pumping and heating power are of interest when designing a scaled-down thermal hydraulic experimental facility. They are used to size pumps and the type of heaters required. This work compares pumping and heating power ratios as a method to compare the pumping and heating requirements between the surrogate fluid and the molten salt. The derivation of the pumping and

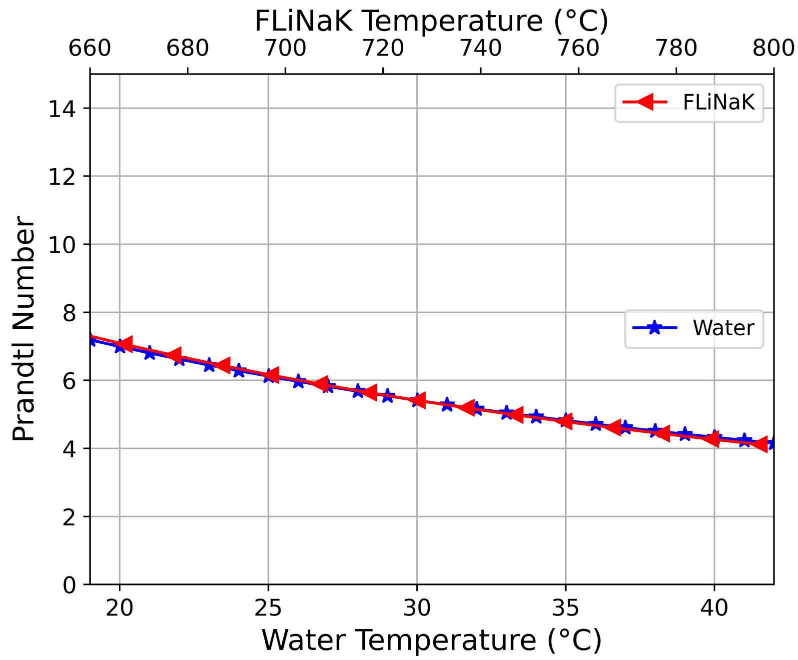

Figure 2.2: Comparison of Prandtl numbers between molten salt, FLiNaK, (top horizontal axis) and surrogate fluid, water, (bottom horizontal axis)

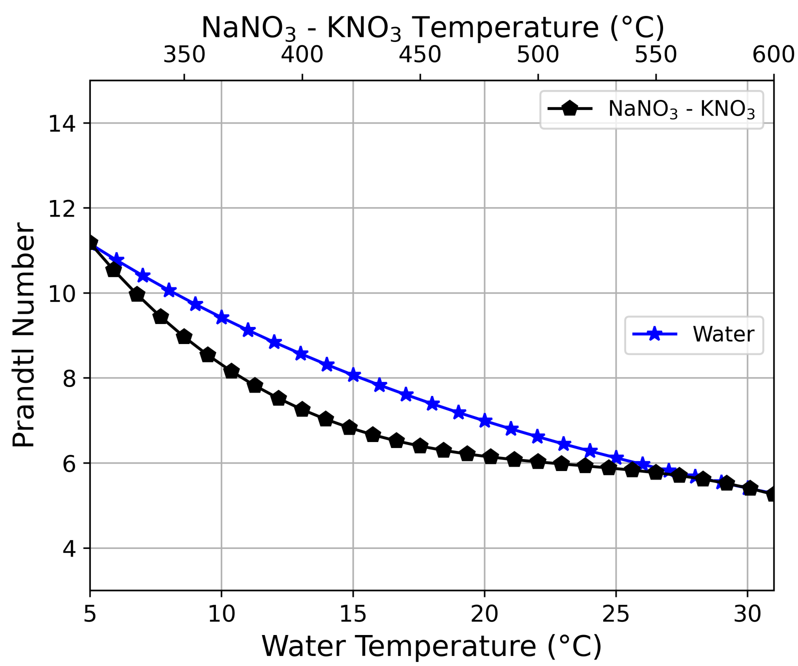

Figure 2.3: Comparison of Prandtl numbers between molten salt, $NaNO_3$ - KNO_3, (top horizontal axis) and surrogate fluid, water, (bottom horizontal axis)

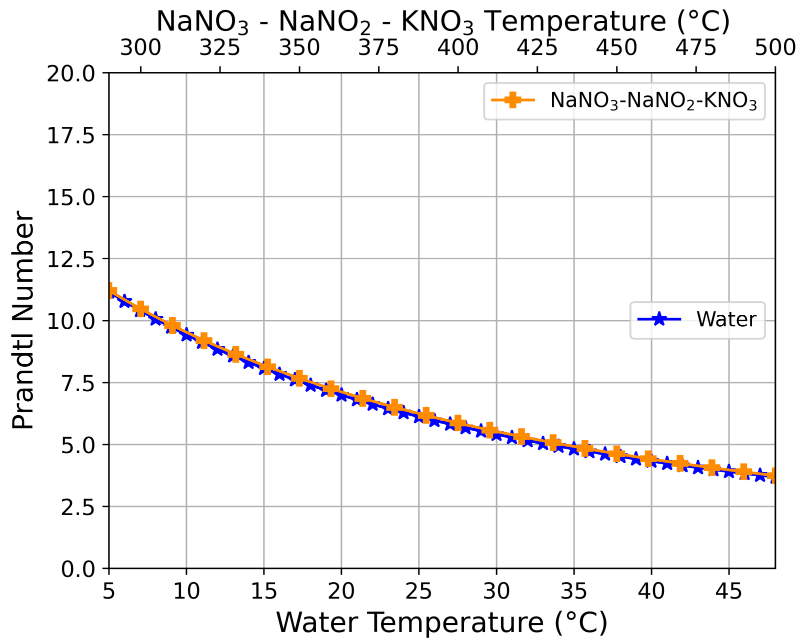

Figure 2.4: Comparison of Prandtl numbers between molten salt, $NaNO_3$ - $NaNO_2$ - KNO_3, (top horizontal axis) and surrogate fluid, water, (bottom horizontal axis)

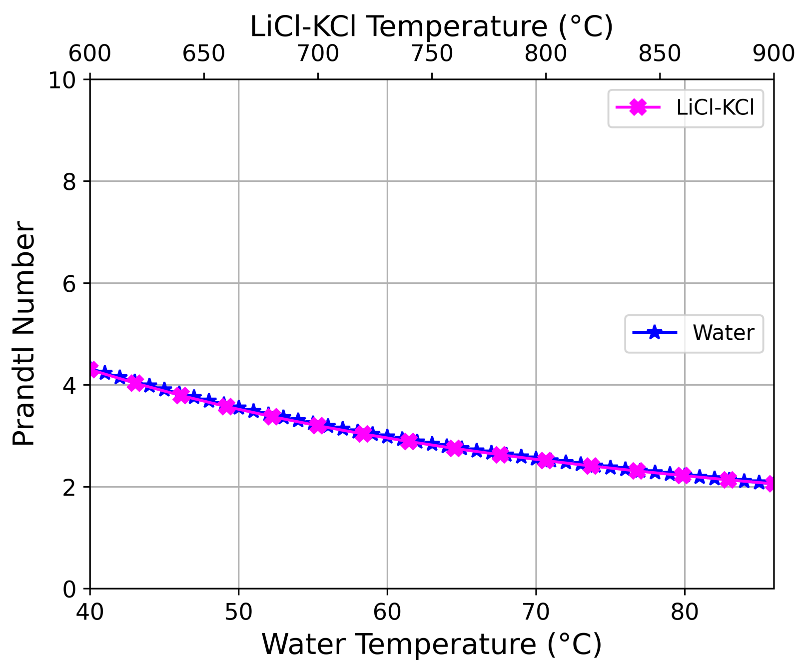

Figure 2.5: Comparison of Prandtl numbers between molten salt, LiCl - KCl, (top horizontal axis) and surrogate fluid, water, (bottom horizontal axis)

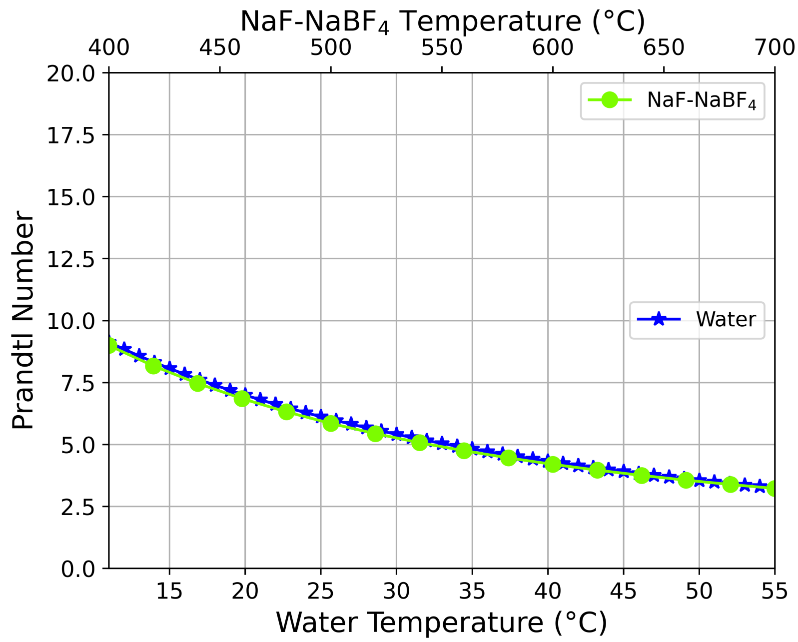

Figure 2.6: Comparison of Prandtl numbers between molten salt, NaF - $NaBF_4$, (top horizontal axis) and surrogate fluid, water, (bottom horizontal axis)

heating power ratios can be found in Appendix A.3. The pumping and heating power ratios are smaller than one, this shows that it is cheaper to pump and heat water in a scaled-down test section when compared to molten salts.

Table 2.3: Water scaled parameters for friction factor and pressure drop with matching Prandtl numbers.

Parameter	FLiNaK	$NaNO_3$ - KNO_3	$NaNO_3$ - $NaNO_2$ - KNO_3	LiCl - KCl	NaF - $NaBF_4$
Prandtl number	5	7	7	3	7
Water temperature (^{o}C)	33	20	20	59	20
Molten salt temperature (^{o}C)	746	411	366	724	455
Reynolds number ratio	1	1	1	1	1
Velocity ratio (V_{sf}/V_{ms})	0.61	0.86	0.84	0.56	1.02
Hydraulic diameter ratio	1	1	1	1	1
Pumping power ratio ($Q_{p,sf}/Q_{p,ms}$)	0.11	0.34	0.33	0.14	0.54
Heating power ratio ($Q_{h,sf}/Q_{h,ms}$)	0.03	0.06	0.07	0.13	0.06

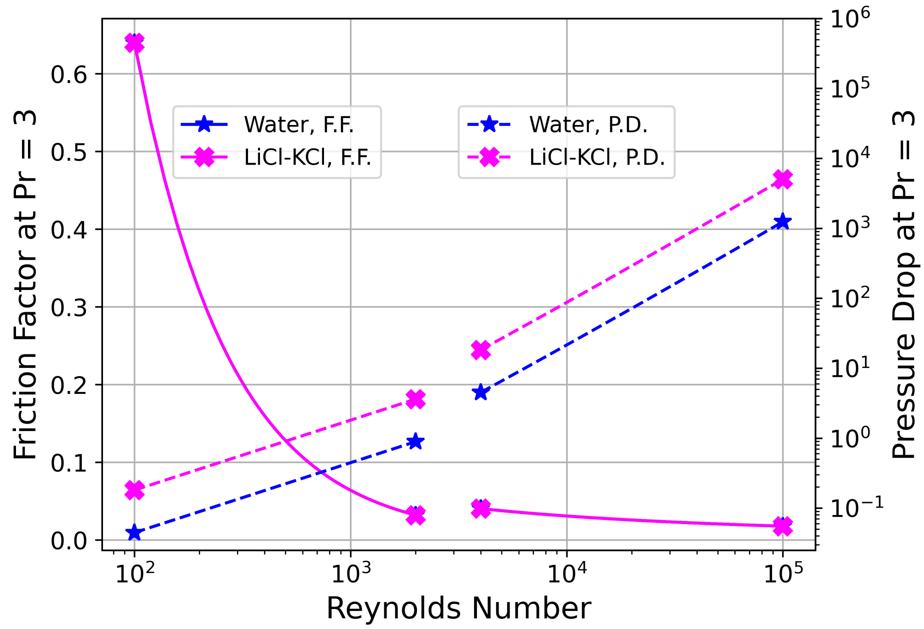

Figure 2.7: Friction factor and pressure drop comparisons (F.F. friction factor, P.D. pressure drop) between LiCL - KCl and water at Prandtl number of 3.

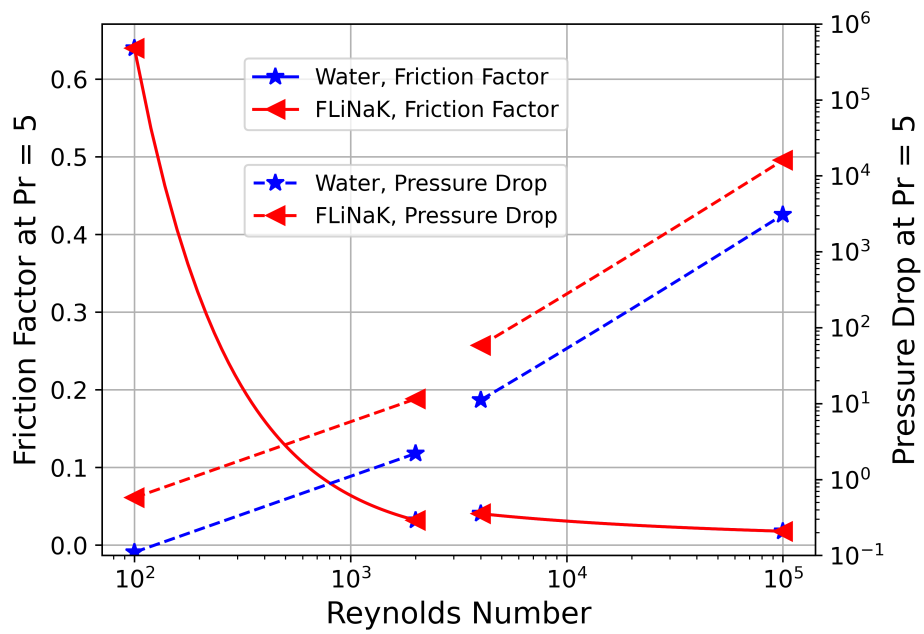

Figure 2.8: Friction factor and pressure drop comparisons (F.F. friction factor, P.D. pressure drop) between FLiNaK and water at Prandtl number of 5.

Figures 2.7 to 2.9 plot the friction factor and pressure drop between the molten salts and water over various Reynolds numbers. The friction factor is plotted on the left y-axis while the pressure drop is plotted on the right y-axis. For all the figures, the friction factor matches between the molten salts and water, while the pressure drop is smaller for water than for the other molten salts. These figures show how a surrogate fluid matches the friction factor characteristics of the molten salts while operating at lower pressure drops. Lower pressure drops further lead to smaller pumps and pumping powers when using surrogate fluids instead of molten salts for laboratory settings while preserving the nondimensional characteristics of interest.

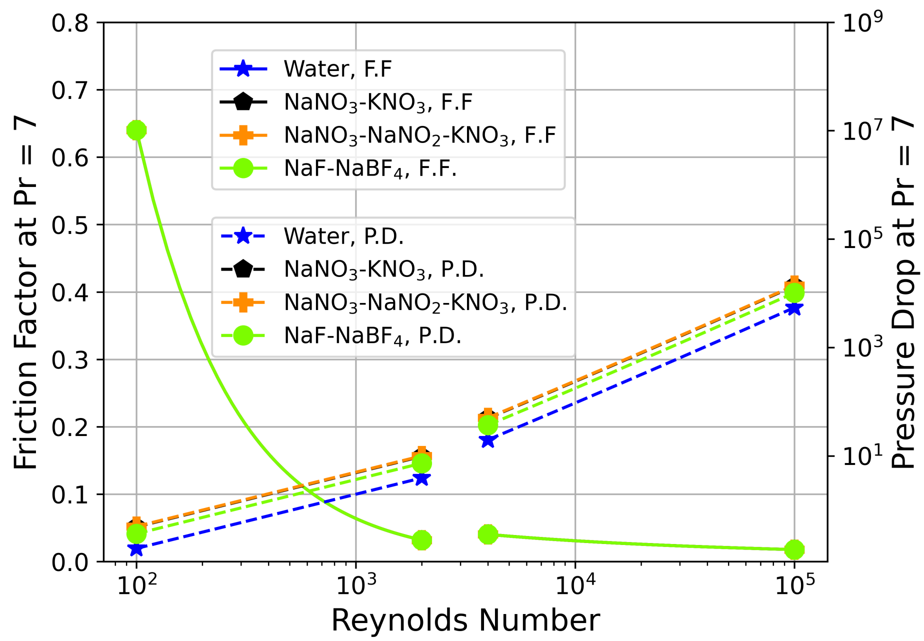

Figure 2.9: Friction factor and pressure drop comparisons (F.F. friction factor, P.D. pressure drop) between molten salts and water at Prandtl number of 7.

The Nusselt number was calculated using the Dittus - Boelter correlation [50] for the molten salts and water, as shown in Figures 2.10 to 2.14. The Nusselt number was obtained by varying the temperatures of the molten salts and water while maintaining the same Reynolds number creating a similar trend to the Prandtl number figures, Figures 2.2 to 2.6. The differences in Nusselt numbers between the molten salt and water are similar to the ones from the Prandtl numbers. This shows that by carefully scaling the molten salt components using a surrogate fluid, forced convective terms can be matched.

2.3.2 Scaling Distortions

Distortions were calculated for Prandtl numbers to understand how well surrogate fluids emulate the molten salts, specifically for forced convection applications. Equation 2.7 was used to calculate the Prandtl number distortions between water and the molten salts plotted in Figure 2.15, with θ calculated using Equation 2.8. In Figure 2.15 when the distortion calculated is positive, the Prandtl

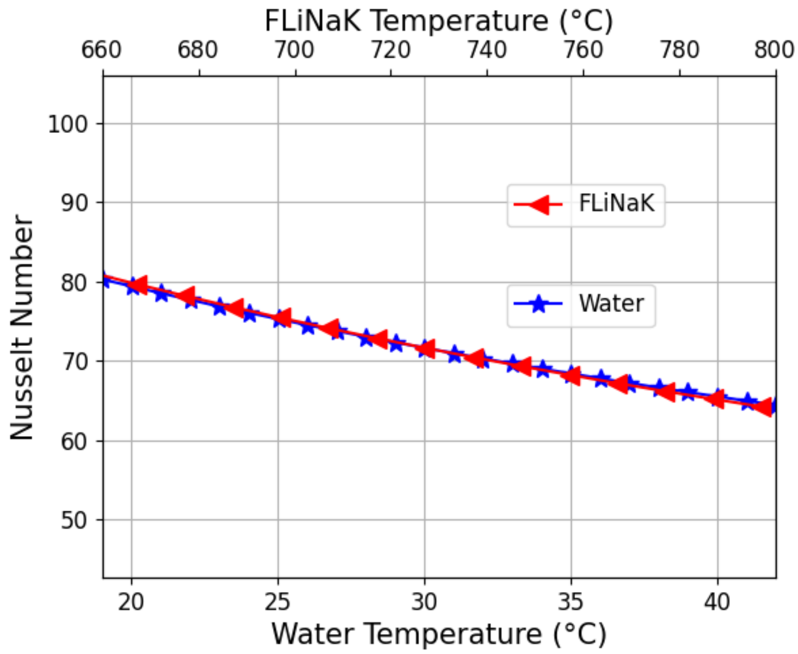

Figure 2.10: Comparison of Nusselt numbers between molten salt, FLiNaK, (top horizontal axis) and surrogate fluid, water, (bottom horizontal axis)

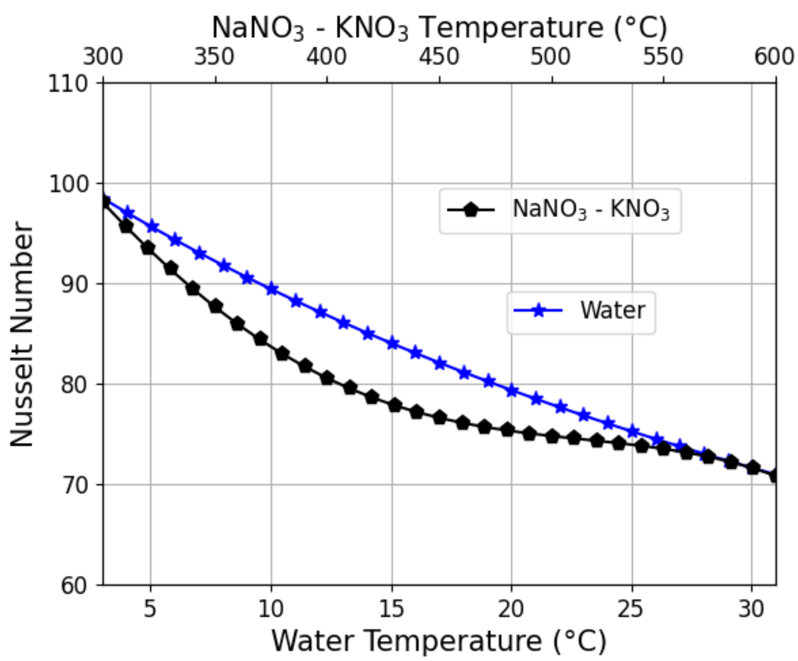

Figure 2.11: Comparison of Nusselt numbers between molten salt, $NaNO_3$ - KNO_3, (top horizontal axis) and surrogate fluid, water, (bottom horizontal axis)

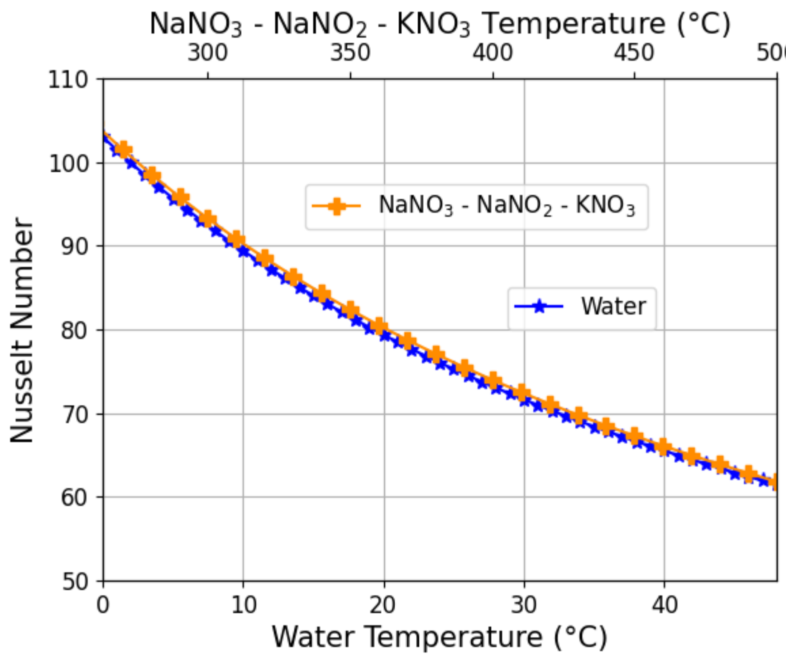

Figure 2.12: Comparison of Nusselt numbers between molten salt, $NaNO_3$ - $NaNO_2$ - KNO_3, (top horizontal axis) and surrogate fluid, water, (bottom horizontal axis)

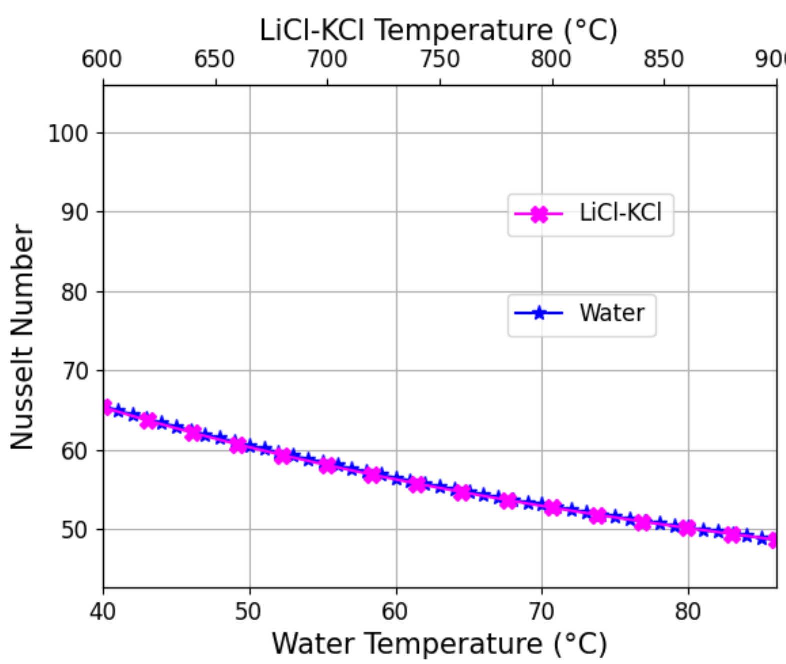

Figure 2.13: Comparison of Nusselt numbers between molten salt, LiCl - KCl, (top horizontal axis) and surrogate fluid, water, (bottom horizontal axis)

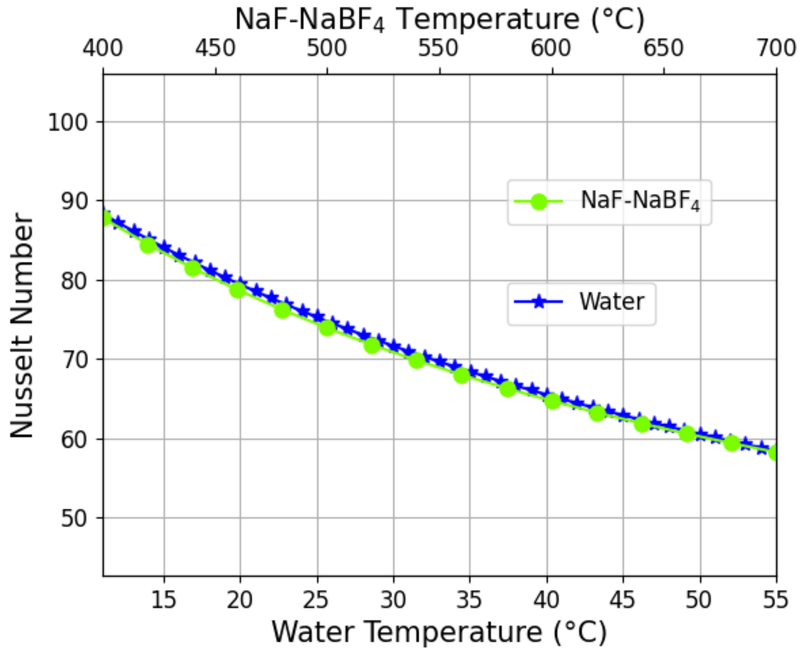

Figure 2.14: Comparison of Nusselt numbers between molten salt, NaF - $NaBF_4$, (top horizontal axis) and surrogate fluid, water, (bottom horizontal axis)

number of the molten salt is greater than that of the surrogate fluid. The inverse is true, in which a negative distortion correlates to a lower Prandtl number for the molten salt. The mismatches in Prandtl numbers shown in Figures 2.2 to 2.6 directly correlate to the shape of the distortions. This is more apparent for $NaNO_3$ - KNO_3, in which the viscosity behavior greatly impacts the overall distortion.

Based on the methodology used to match the Prandtl numbers between the molten salts and surrogate fluids, the expected distortions in Nusselt number predictions will follow a similar trend to the one plotted in Figure 2.15, with the smaller distortions occurring at the end of the temperature range and the largest near the center of the temperature range.

The largest distortion observed was from $NaNO_3$ - KNO_3, thus to better quantify the distortion an uncertainty analysis was done by propagating the uncertainty of thermophysical properties into the distortion calculations. Figure 2.16 plots the distortion between water and $NaNO_3$ - KNO_3 with uncertainty from $NaNO_3$ - KNO_3's thermophysical properties across nondimensional temperature, θ. Throughout θ's range, the uncertainty's magnitude is as large as the distortion in various locations. This observation highlights the need for more experimental data on the thermophysical properties of molten salts with more accuracy. Given the current state of the available data, the distortion between the molten salt and surrogate fluid were quantified; however, the uncertainty in the distortion was greater than the distortion itself.

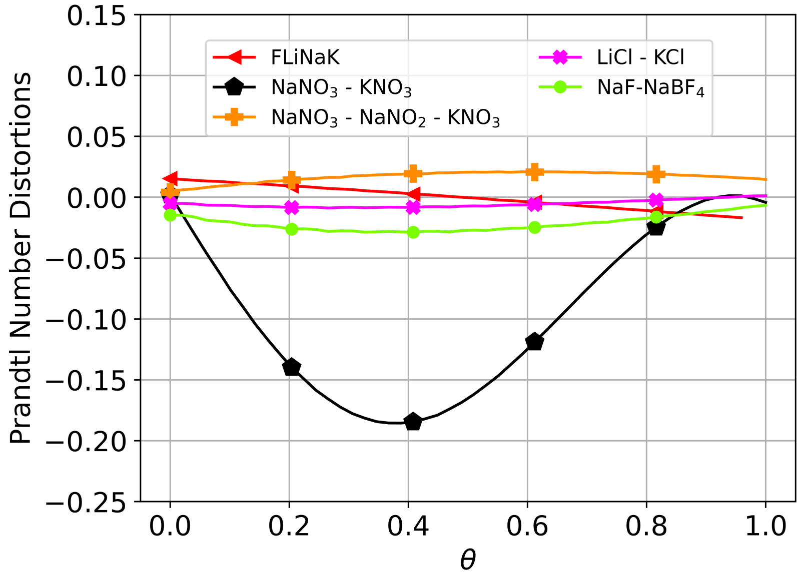

Figure 2.15: Calculated Prandtl number distortions for water and molten salts

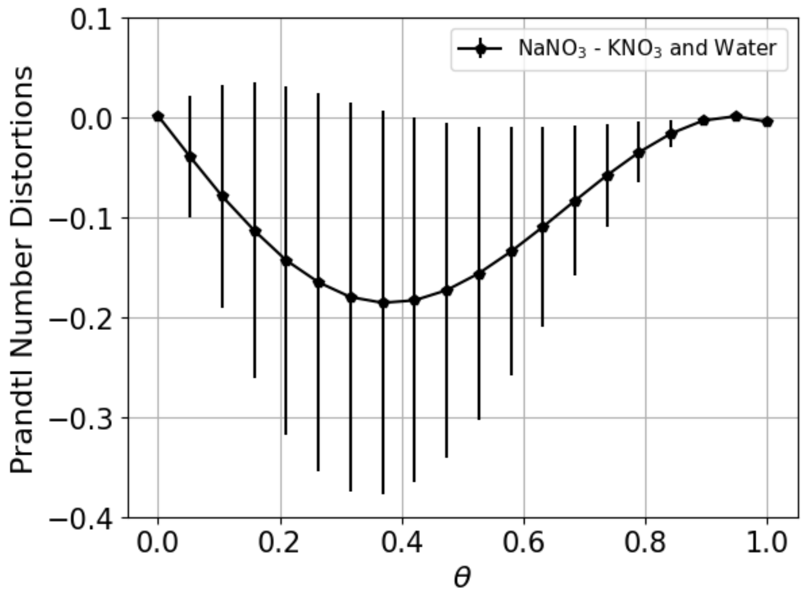

Figure 2.16: Calculated Prandtl number distortions for water and $NaNO_3$ - KNO_3 with uncertainty from thermophysical properties.

2.3.3 Experimental Distortions

To investigate the distortions that arise when using surrogate fluids for molten salt applications, experimental data for Nusselt number at a Reynolds number of 20,000 was utilized. The distortions and associated uncertainty were quantified using methods previously presented to calculate uncertainty in simulations of jet engine thrust [53]. The Nusselt number experimental data were obtained on a circular pipe with constant heat flux, and detailed information regarding the methodology, instrumentation, and procedure can be found in Section 3.2.5. The results of the experimental Nusselt number are depicted in Figure 3.18. For the experimental data, water was employed as the surrogate fluid with an inlet temperature of $\approx 21^{o}C$, and based on Table 2.3, the three molten salts that directly scale down at that Prandtl number are $NaNO_3$ - KNO_3, $NaNO_3$ -$NaNO_2$ - KNO_3, and NaF - $NaBF_4$. Table 2.4 summarizes and tabulates the distortions between water and the respective molten salts, this is a numerical representation of Figure 2.15.

Table 2.4: Tabulated Prandtl number distortions for water and molten salts from Figure 2.15

Molten salt	Minimum	Maximum
FLiNaK	-0.0169	0.0152
$NaNO_3$ - KNO_3	-0.1856	0.0017
$NaNO_3$ - $NaNO_2$ - KNO_3	0.0041	0.0208
LiCl - KCl	-0.0090	0.0011
NaF - $NaBF_4$	-0.0287	-0.0067

A cumulative distribution function (CDF) was chosen as the visual representation of the uncertainty and distortion. A CDF shows the probability of a Nusselt number to be that value or less and it was chosen as a method for uncertainty and distortion as they can be treated in a different manner. Roy and Balch [53] used the CDF to represent the different forms of uncertainty that were encountered in simulations. In their work, they used to visually understand the different forms of uncertainty in their results that come from the model form, model inputs, and numerical uncertainty. This work only focused on two different types of uncertainty, distortion, and experimental uncertainty. To create the original CDF, the probabilistic distribution, 100,000 random samples with a normal distribution centered on the mean of the Nusselt number and a standard deviation of 5% of the Nusselt number mean. The standard deviation of 5% was chosen as a non-conservative value to portray a small standard deviation of the Nusselt number, as most experimental data found in the literature with Nusselt number are usually presented with 10% uncertainty. An initial study with 10% standard deviation for the probabilistic distribution was done, but this uncertainty would trump the distortion and experimental uncertainty, thus a smaller value was chosen. Table 2.5 summarizes the parameters used for the CDF.

The distortions in the Prandtl number were directly propagated to the Nusselt number, assuming a one-to-one relationship. However, it is important to note that this approach tends to overestimate the actual Nusselt number distortion since the relationship between the Nusselt number and Prandtl number is typically nonlinear, often described by an exponent less than 1 [50, 54]. The decision to employ a one-to-one distortion between the Nusselt number and the Prandtl number was made to emphasize the effects of distortions observed in the Prandtl number and to showcase the worst-case

Table 2.5: Parameters chosen for the distortion quantification studies.

Parameter	Value
Reynolds number	20,000
Nusselt number	144.17
Number of Samples	100,000
Nusselt number standard deviation	7.21
Experimental uncertainty	12.41

scenario when using surrogate fluids. In reality, the distortion in the Nusselt number would be much lower than the values presented herein. The Nusselt number distortion is thus quantified based on:

$$D_{Nu} = D_{Pr}^{n}, \tag{2.9}$$

which n is equal to one for a one-to-one relationship. In reality, this exponent is equal to the one found through the Nusselt number correlation, often described by a value much less than one.

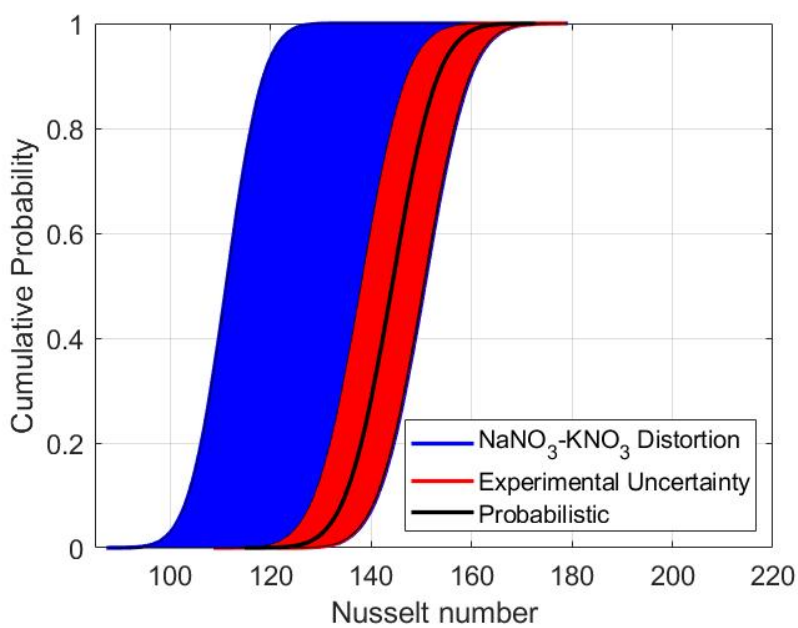

Figure 2.17: Cumulative probability of experimental Nusselt number with experimental uncertainty, $NaNO_3$ - KNO_3 distortion and probabilistic uncertainty obtained using water.

The probabilistic uncertainty, experimental uncertainty, and the three distortions were combined to create three CDFs shown in Figures 2.17 to 2.19. The CDFs shown can be interpreted as how the uncertainty is compounded between the different types of uncertainty. The different areas in the different colors are stand-alone areas, meaning they do not overlap but are meant to show the magnitude of the uncertainty in an area format. The larger the uncertainty the larger the area in the CDF. All three figures have the same probabilistic and experimental uncertainty with varied distortion depending on which molten salt was used. Figure 2.17 plots the cumulative probability versus Nusselt number for $NaNO_3$ - KNO_3's distortion. $NaNO_3$ - KNO_3 had the largest Prandtl number distortion and this can be seen in the CDF. The distortion is skewed in the lower Nusselt number values, as the distortion is heavily negative in Figure 2.15. The blue area in Figure 2.17 represents what the Nusselt number distribution for $NaNO_3$ - KNO_3 would be when using water as a surrogate fluid. From this figure, it is clear that the largest area represents the distortion found between water and $NaNO_3$ - KNO_3 when comparing the experimental uncertainty and the probabilistic uncertainty, but this was the case with the largest distortion and using a linear relationship between the Prandtl number and Nusselt number.

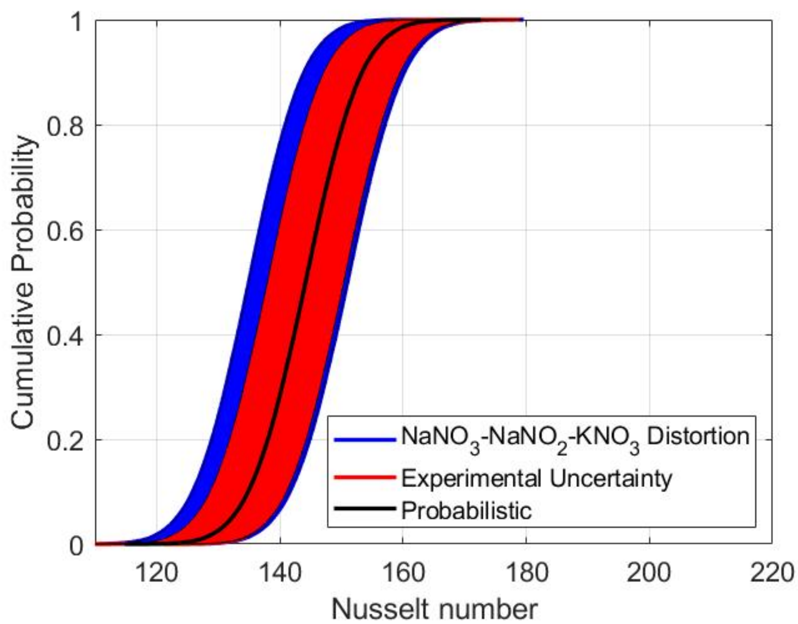

Figure 2.18: Cumulative probability of experimental Nusselt number with experimental uncertainty, $NaNO_3$ - $NaNO_2$ - KNO_3 Distortion and probabilistic uncertainty obtained using water.

Figure 2.18 shows the cumulative probability for the experimental Nusselt number obtained using water with the Prandtl number distortions from $NaNO_3$ - $NaNO_2$ - KNO_3. This figure shows smaller blue areas in comparison with the experimental uncertainty. In addition, the blue area covers the two sides of the Nusselt number but is skewed in the lower Nusselt numbers. This figure shows better promise when using surrogate fluids for molten salt scaled components as the distortion is much smaller in comparison with Figure 2.17. Figure 2.19 plots the cumulative probability with Prandtl number distortion of NaF - $NaBF_4$. This figure shows how water is also a good surrogate for

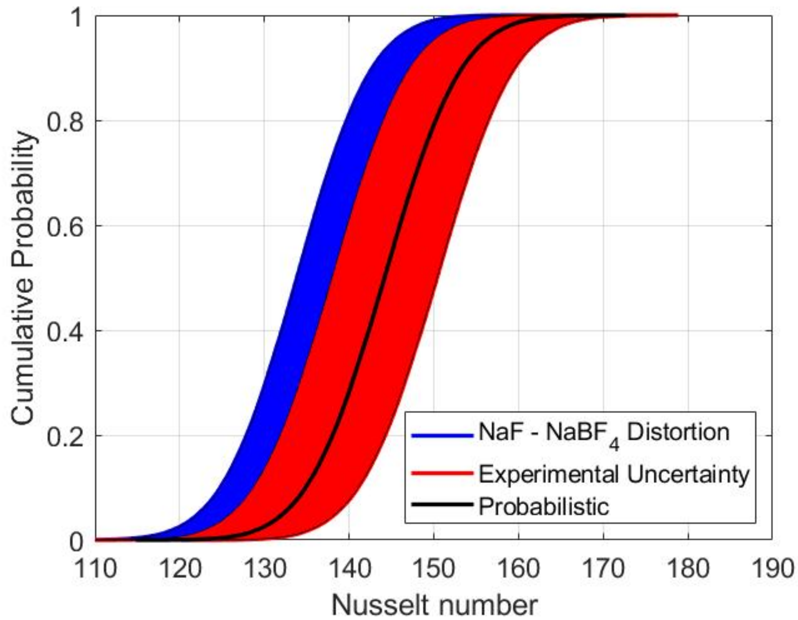

Figure 2.19: Cumulative probability of experimental Nusselt number with experimental uncertainty, NaF - $NaBF_4$ Distortion and probabilistic uncertainty obtained using water.

NaF - $NaBF_4$ as the distortion is small in comparison with the experimental uncertainty. Overall, the Figures 2.17 to 2.19 show the cumulative probability of experimental Nusselt number with the different distortions for the different molten salts, with the largest distortion found with $NaNO_3$ - KNO_3. Even with the largest distortion, the water showed to be a good surrogate fluid for scaled heat transfer experiments. As was concluded in Section 2.3.2, this large distortion could be mitigated with more accurate thermophysical properties of the molten salt to further reduce the Prandtl number distortion. Finally, the Nusselt number distortions were quantified based on a linear relationship with the Prandtl number distortion, but the Nusselt number distortions are expected to be much lower than the Prandtl number distortions.

2.4 Discussion and Conclusion

Molten salts have garnered attention and found applications in the energy industry due to their favorable thermophysical properties and ability to operate at high temperatures. However, studying heat transfer systems involving molten salts can be challenging and costly. To overcome these challenges, surrogate fluids have been proposed and demonstrated as viable alternatives for laboratory-scale heat transfer experiments. Despite the Prandtl numbers of the discussed surrogate fluids aligning with the requirements, there is room for further optimization of the temperature ranges for Prandtl number matching. Additionally, more accurate calculations of distortions can be achieved with improved molten salt thermophysical property data.

Moreover, uncertainty in the thermophysical properties significantly contributes to the overall uncertainty in the distortions observed in scaled-down surrogate fluid experiments. While distortions are to be expected when scaling down heat transfer components, the distortions arising from the Prandtl number are relatively small compared to the uncertainties associated with the thermophysical properties of the molten salts. To further explore this, actual experimental heat transfer data were employed to calculate the theoretical Nusselt number distortion using a one-to-one relationship with the Prandtl number. The Nusselt number distortions showed to be smaller than the experimental uncertainties for $NaNO_3$ - $NaNO_2$ - KNO_3 and NaF - $NaBF_4$, while for $NaNO_3$ - KNO_3 the distortion exceeded the experimental uncertainty. This was expected as the large distortion found in the Prandtl number was concluded to be created from the thermophysical properties of $NaNO_3$ - KNO_3. Thus, for more accurate scaled-down experiments with surrogate fluids, enhanced precision in the thermophysical property data of molten salts is imperative.

In this work, water has been identified as a potential surrogate fluid for five molten salts, FLiNaK, $NaNO_3$ - KNO_3, $NaNO_3$ - $NaNO_2$ - KNO_3, LiCl - KCl, and NaF - $NaBF_4$. Water has been demonstrated to have lower operating costs than molten salts through lower pumping and heating powers, as well as lower material costs as it has lower operating temperatures for experimental settings. Further along in this work, water was used as a surrogate fluid as the operating fluid in a heat transfer experimental facility, Section 3.2.1.

Chapter 3

PASSIVE HEAT TRANSFER ENHANCEMENTS - TWISTED TAPE INSERTS

Improving heat transfer has been an ongoing task in engineering research, design, and development [55, 56]. This is usually achieved by passive techniques [57], active techniques[58], or a combination of both [59]. Passive heat transfer enhancement techniques consist of changing the geometry to alter the heat transfer surface area to induce turbulence, such as twisted tubes, rifled tubes, coils, or fluid additives. An active heat transfer technique uses an external source such as mechanical power [60, 61] or inducing an electric or magnetic field [62, 63]. Some heat transfer enhancement techniques aim to combine active and passive approaches to further enhance heat transfer. In this work, the focus is specifically on passive heat transfer enhancement techniques. Passive heat transfer enhancements have been demonstrated to increase heat transfer but are accompanied by higher pressure drops [64]. Quantifying this trade-off has been an ongoing effort in various engineering fields [65]. The present work concentrates on investigating a passive heat transfer enhancement technique that is currently considered for molten salt energy applications, namely twisted tape inserts.

Twisted tape inserts are currently studied as a method to improve heat transfer. They were initially studied over a century ago to improve heat transfer in boilers [66]. The renewed interest in twisted tape inserts stems from their application in high heat flux environments such as molten salt reactors [67], fusion reactors [68], and solar power applications [69, 70]. The twisted tape inserts swirl the coolant and create secondary flows, thereby inducing fluid mixing and enhancing heat transfer [71]. The heat transfer is increased due to the mixing and swirling motion of the tape, creating longer flow lengths and higher velocities. Due to the twisted tape inserts' geometric variety and applications, extensive literature reviews have been conducted. Converse et al [72] summarized pressure drop and heat transfer predictions alongside experimental data of twisted tapes and other passive heat transfer enhancements. Manglik [73] performed an extensive review on the friction factor and Nusselt numbers of twisted tape inserts for their dissertation, providing derivations for friction factor and Nusselt numbers. Clark [74] provided a comprehensive summary of experimental work on twisted tape inserts, with a particular focus on computational efforts and geometric modifications. In more recent efforts, Hasanpour et al [75], Varun et al [76], and Madariya et al [77] conducted extensive literature reviews of friction factor and Nusselt number data of twisted tape inserts with a lot of work on modified twisted tape geometries. Modifications to twisted tape inserts include wing-like features [78], perforations [79], combinations of wings and perforations [80], or the addition of multiple twisted tape inserts in a single geometry [81–83].

While these modifications have demonstrated enhanced thermal performance, traditional twisted tape inserts, created by twisting a metallic strip into a spiral and inserting it into a pipe, are still preferred in various applications due to their simplicity in manufacturing [84, 85]. Figure 3.1 provides a comparison between traditional twisted tape inserts and common modifications.

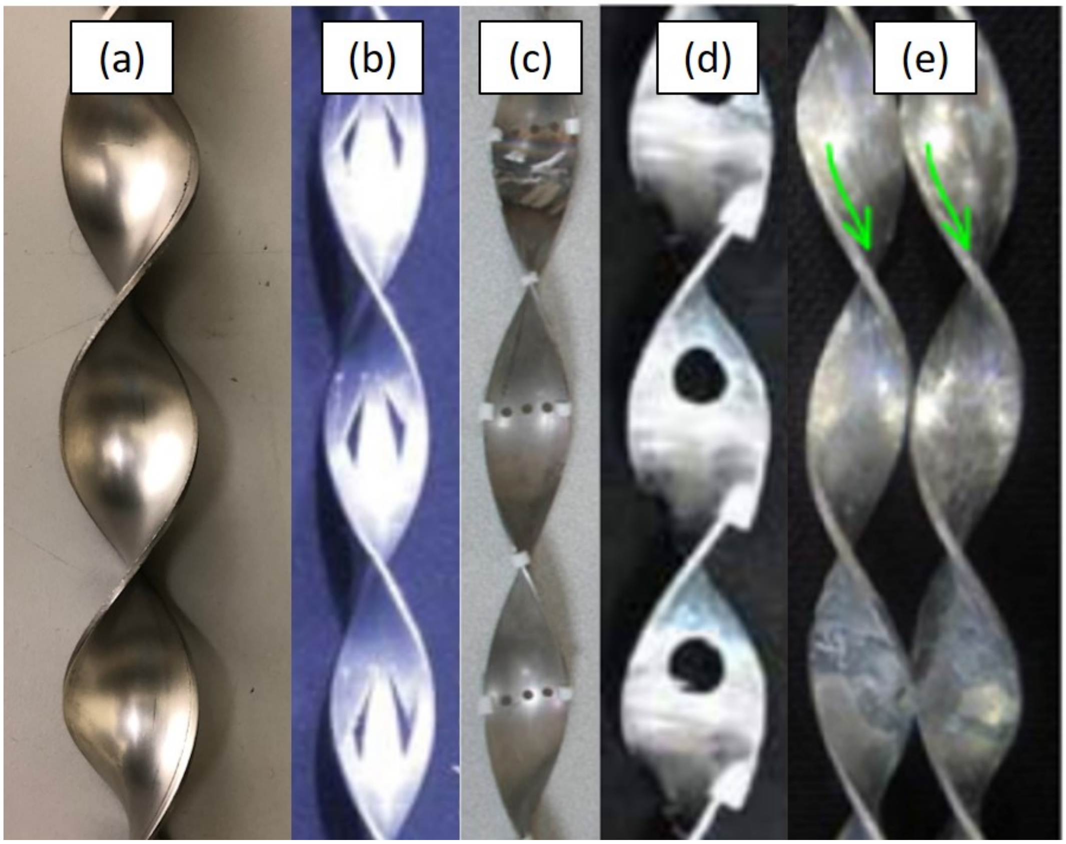

Figure 3.1: Comparison between a (a) traditional twisted tape insert, (b) wing-like features [78], (c) perforated [79], (d) combination of wings and perforations [80], and (e) multiple twisted tape inserts in a single tube [81].

A great deal of effort has been accomplished in changing the geometric parameters of the twisted tape inserts to obtain friction factor and Nusselt number correlations [72–77]. Figure 3.2 shows these relevant geometric parameters of a twisted tape insert. Here, D is the inner diameter of the pipe, w is the tape width, δ is the tape thickness, and H is defined as the length of a 180^o turn. The twisted tape pitch, y, is defined as the 180^o turn divided by the diameter of the pipe, i.e.:

$$y = \frac{H}{D}. \tag{3.1}$$

Unfortunately, as highlighted by Manglik and Bergles [86], the majority of the correlations can only be accurately applied to specific operating and geometric conditions. Manglik and Bergles derived

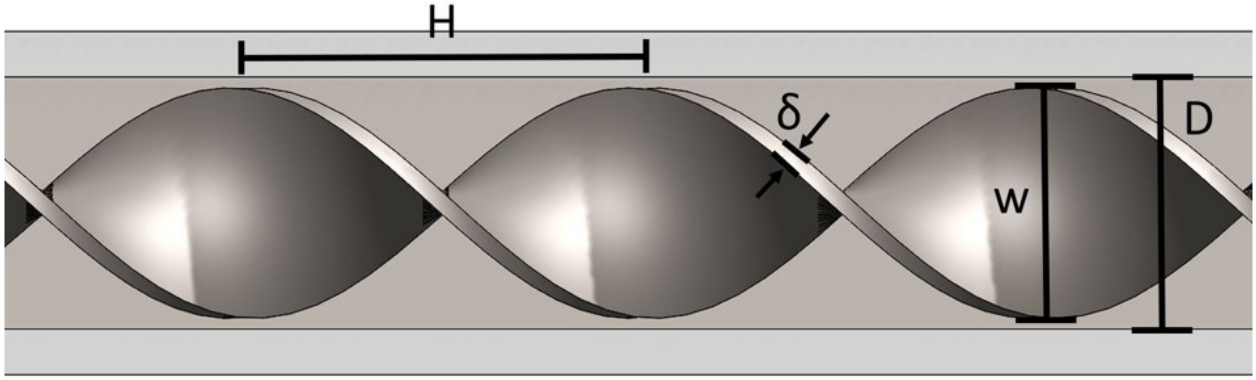

Figure 3.2: Diagram of twisted tape insert with relevant geometric parameters.

the most widely used friction factor and Nusselt number correlations for twisted tape inserts for laminar [87] and transitional and turbulent regimes [86]. The correlations were developed across a range of Reynolds numbers and investigated the impacts of varying the parameters of the twisted tape insert as well as studied the fluid flow phenomena on the friction factor and Nusselt number, with experimental data from Marner and Bergles [88].

In recent work with twisted tape geometries for which the width of the twisted tape w is smaller than the pipe's inner diameter D, it was noted that the pressure loss was changing with the twisted tape's width [89]. Loose-fitting twisted tapes, when $w < D$, are often employed due to their ease of installation [84]. Al-Fahed and Chakroun [90] studied the effects of twisted tape width with friction factor and Nusselt number. Al-Fahed and Chakroun observed a friction factor and Nusselt number dependence with the twisted tape width, though the friction factor results were not as clear with a direct relationship of twisted tape width. Bas and Ozceyhan [91] varied the distance between the twisted tape insert and the wall and studied their friction factor and heat transfer. Bas and Ozceyhan concluded that the twisted tape pitch y had a larger dependence on the thermal performance of the twisted tape insert than the width, w. Wiggins et al [92] showed that the correlations by Manglik and Bergles [86, 87] were over-predicting the experimental data for loose-fitting twisted tape inserts.

Other methods of deriving the friction factor and Nusselt number in twisted tape inserts have also been attempted. A different method of deriving correlations consists of analytical derivations, which are derived using conservation equations. Smithberg and Landis [93] developed friction factor and heat transfer correlations with the help of measured axial velocity. Smithberg and Landis probed the exit of twisted tapes in air and water to obtain axial and tangential velocities. An implicit friction factor correlation was derived from boundary layer theory and the measured exit flow velocities, while their heat transfer correlations were developed using Colburn-type analysis. Smithberg and Landis' simplified friction factor results are used herein to compare friction factor results. Smithberg and Landis [93] concluded that three effects are leading to the heat transfer phenomena, the additive effects of the tube wall boundary layer, the energy exchange from the vortex mixing and the effects of the twisted tape acting as a fin. Thorsen and Landis [94] expanded from Smithberg and Landis' work [93] to account for curvature effects and tighter twisted tapes. Sarma et al developed a turbulent [95] and a laminar [96] correlation based on van Driest eddy diffusivity to account for the effects of centrifugal forces and secondary flows. Sarma et al [97] then summarized both correlations and used asymptotic matching from Churchill [98] to obtain continuous curves for friction factor and Nusselt number.

In an effort to better understand twisted tape inserts in one-sided heat flux environments, such as in fusion reactors, Dedov et al [99] studied the friction factor and heat transfer in twisted tape inserts. Dedov et al created one sided heating using an electron beam to mimic heat flux environments expected to occur in the ITER thermonuclear reactor. Dedov et al, along with work from Varava et al [100, 101], derived friction factor and Nusselt number correlations by transforming the geometry based on the hydraulic diameter and twisting phenomena to treat it as conventional channel flow. Wiggins et al [92] showed that this methodology has been successful in predicting friction factor in loose-fitting twisted tape inserts at turbulent Reynolds numbers.

The current work focused on calculating the friction factor, Nusselt number, and thermal performance factor of loose-fitting twisted tape inserts. Friction factor data were obtained for eight different twisted tape geometries, for pitches of $y = 1.9$ and 3.81 three different widths were explored, $w/D = 0.95$, 0.85, and 0.75, while for a pitch $y \approx 2.86$, two widths of $w/D = 1.0$ and 0.95 were explored with water as a working fluid. The width of $w/D = 1.0$ is considered a tight-fitting twisted tape insert as the width is equal to the diameter. A subset of the twisted tape inserts explored for friction factor were studied for Nusselt number and thermal performance factor data, $y = 1.9$, 2.86, and 3.81, with a width of $w/D = 0.95$. The Reynolds number varied between the laminar to turbulent regime in the twisted tape inserts, $Re \approx 3,000 - 40,000$ for friction factor and 3,000 to 24,000 for Nusselt number. This chapter describes the leading friction factor and Nusselt number correlations of twisted tape inserts used to compare the current experimental data with. It then describes the experimental facility, MSETF-1, used to obtain the scaled experimental data. The geometric and operating conditions are then summarized for the different twisted tape sections. Friction factor, Nusselt number, and thermal performance results are presented and discussed with a final section deriving a loose-fitting twisted tape insert factor that can be used to predict friction factor in the loose-fitting twisted tape inserts.

3.1 Theory

This section describes the selected correlations to compare the current friction factor and Nusselt number data. Due to the extensive literature reviews that have been conducted on twisted tape inserts [72–77], and Manglik and Bergles' conclusion on the applicability of most correlations [86], it is evident that most twisted tape correlations are applicable only under specific operating and geometric conditions. Therefore, correlations were chosen that were relevant to the current work and are the ones most widely used throughout the literature.

3.1.1 Selected Correlations

The selected friction factor correlations are summarized in Table 3.1, while the Nusselt number correlations are summarized in Table 3.2. The correlations selected consisted of the Manglik and Bergles laminar and turbulent correlations [86, 87] as they are the most common twisted tape insert correlations. Smithberg and Landis [93] and Sarma et al [95–97] were chosen as they were derived analytically. For friction factor, the Lopina and Bergles correlation [102] was chosen as it has been used in the literature previously, while for the Nusselt number, the Hong and Bergles' correlation [103] was chosen as the experimental data was obtained using similar wall boundary conditions as this current work, constant heat flux.

Table 3.1: Selected friction factor correlations

Authors - Year [Ref]	Correlation
Manglik and Bergles Lam. - 1993 [87]	$f = \frac{15.767}{Re}(1 + 10^{-6}Sw^{2.55})^{1/6}[1 + (\frac{\pi}{2y})^2](\frac{\pi+2-\delta/D}{\pi-4\delta/D})^2 \cdot (\frac{\pi}{\pi-4\delta/D})$
Manglik and Bergles Turb. - 1993 [86]	$f = \frac{0.0791}{Re^{0.25}}(\frac{\pi}{\pi-4\delta/D})^{1.75}(\frac{\pi+2-\delta/D}{\pi-4\delta/D})^{1.75}(1 + \frac{2.752}{y^{1.29}})$
Lopina and Bergles - 1969 [102]	$f = \frac{0.1265}{y^{0.406}Re^{0.2}}(\frac{\pi+2-\delta/D}{\pi-4\delta/D})^{1.2}(\frac{\pi}{\pi-4\delta/D})^{1.8}$
Smithberg and Landis - 1964 - [93]	$f = [0.046 + 2.1(\frac{2H}{D} - 0.5)^{-1.2}]Re_x^n$; $n = 0.2[1 + 1.7(\frac{2H}{D})^{-1.2}]$
Sarma et al Lam. - 2003 [96]	$f_L = 1.5(1 + \frac{D}{2H})^{3.37}Re^{-0.565}$
Sarma et al Turb. - 2002 [95]	$f_T = 0.021Re^{-0.116}(1 + \frac{D}{2H})^{4.216}$

In the case of Smithberg and Landis' [93] and Sarma et al's [95–97] correlations, they define a twisted tape pitch based on a 360^o turn, thus the correlations showed in Tables 3.1 and 3.2 are adjusted accordingly to the current terminology of a 180^o turn to calculate the pitch. Smithberg and Landis also derived an implicit friction factor correlation,this work focused on their simplified approximate friction factor correlation for simplicity [93]. In addition, the inconsistency of variables defined between papers caused the equations in Tables 3.1 and 3.2 to be adjusted to the current

Table 3.2: Selected heat transfer correlations

Authors - Year [Ref]	Correlation
Manglik and Bergles Lam. - 1993 [87]	$Nu = 4.612 \cdot \{[(1+0.0951Gz^{0.894})^{2.5} + 6.413 \cdot 10^{-9} \cdot (Sw \cdot Pr^{0.391})^{3.835}]^2 + 2.132 \cdot 10^{-14} \cdot (Re_{ax} \cdot Ra)^{2.23}\}^{0.1} \cdot (\frac{\mu_b}{\mu_w})^{0.14}$
Manglik and Bergles Turb. - 1993 [86]	$Nu = Nu_{y=\infty}(1+\frac{0.796}{y})$; $Nu_{y=\infty} = 0.0236Re^{0.8}Pr^{0.4}(\frac{\pi}{\pi-4\delta/D})(\frac{\pi+2-2\delta/D}{\pi-4\delta/D})^{0.2}(\frac{\mu_b}{\mu_w})^{0.18}$
Hong and Bergles - 1976 [103]	$Nu = 5.172[1+5.484 \cdot 10^{-3}Pr^{0.7}(\frac{Re_{ax}}{y})^{1.25}]^{1/2}$
Smithberg and Landis - 1964 - [93]	$Nu = \frac{Re_x Pr}{1+\frac{700}{Re_x f}(\frac{D}{2H})(\frac{D_h}{D})Pr^{0.731}}[\frac{50.9(\frac{D}{2H})}{Re_x\sqrt{f}} + 0.023(\frac{D}{D_h})Re_x^{-0.2} \cdot Pr^{-2/3}(1+\frac{0.0219}{(\frac{2H}{D})^2 f})^{1/2}]$
Sarma et al Lam. - 2003 [96]	$Nu_L = 0.2036[1+(\frac{D}{2H})]^{4.12}Re^{0.55}Pr^{1/3}$
Sarma et al Turb. - 2002 [95]	$Nu_T = 0.1012[1+(\frac{D}{2H})]^{2.065}Re^{0.67}Pr^{1/3}$

definition of twisted tape parameters.

The main difference occurs in how the Reynolds numbers are defined between correlations. The first Reynolds number was defined based on empty pipe mean velocity and geometric parameters, where the mean velocity was defined as:

$$V = \frac{\dot{m}}{\rho \cdot \pi \cdot (D/2)^2}, \tag{3.2}$$

where $\dot{m}$ is the mass flow rate in kg/s. The velocity is then used for the Reynolds number empty pipe definition:

$$Re = \frac{D \cdot \rho \cdot V}{\mu}. \tag{3.3}$$

Manglik and Bergles defined a swirl Reynolds number as:

$$Re_{sw} = \frac{D \cdot V_s \cdot \rho}{\mu}, \tag{3.4}$$

where V_s was a swirl velocity defined as:

$$V_s = \frac{\dot{m}}{\rho \cdot (\frac{\pi D^2}{4} - \delta D)} \cdot \sqrt{1+(\frac{\pi}{2y})^2}, \tag{3.5}$$

which uses the cross-sectional area of the twisted tape insert with the width equal to the inner diameter ($w = D$).

The swirl Reynolds number, Equation 3.4, was used to define a swirl parameter, Sw, that balanced the viscous, convective inertia and centrifugal forces, defined as:

$$Sw = \frac{Re_{sw}}{\sqrt{y}}. \tag{3.6}$$

An axial velocity of the twisted tape insert was defined as:

$$V_{ax} = \frac{\dot{m}}{\rho \cdot (\frac{\pi D^2}{4} - \delta D)}, \tag{3.7}$$

and the axial Reynolds number as:

$$Re_{ax} = \frac{D \cdot V_{ax} \cdot \rho}{\mu}. \tag{3.8}$$

This was slightly different then the axial Reynolds number defined by Smithberg and Landis [93], as the axial velocity does account for the width of the twisted tape insert. That axial Reynolds accounting for the width of the twisted tape insert was calculated as:

$$Re_x = \frac{D \cdot \rho}{\mu} \cdot \frac{\dot{m}}{\rho \cdot (\frac{\pi D^2}{4} - \delta w)}. \tag{3.9}$$

It is important to note that while Equation 3.8 and Equation 3.9 are both axial Reynolds number correlations, they come from different sources and are calculated differently. These were only used to calculate the correlations and no results are presented using either Reynolds number terminology, but it highlights the multiple definitions and slight changes of terminology found in literature.

Manglik and Bergles' correlations [86, 87] were asymptotically matched in order to be applied to all Reynolds numbers using the following equation:

$$f = (f_{lam}^{10} + f_{turb}^{10})^{1/10}, \tag{3.10}$$

while for Sarma et al's correlations [95, 96] were combined based on the following equation [97]:

$$f = (f_{lam}^{5} + f_{turb}^{5})^{1/5}. \tag{3.11}$$

Sarma et al's Nusselt number correlations [95, 96] were combined through asymptotic matching based on the following equation [97]:

$$Nu = (Nu_L^5 + Nu_T^5)^{1/5}. \tag{3.12}$$

3.1.2 Channel Flow

A different method was explored to calculate friction factor and Nusselt number in twisted tape inserts, developed by Dedov et al [99] and Varava et al [100, 101]. This method considered the twisted tape geometry by treating it as conventional channel flow that "twists" in a rotating frame and can be addressed with traditional channel flow correlations accordingly. To start, a swirl coefficient, k, was defined as:

$$k = \frac{\pi}{2y}. \tag{3.13}$$

A modified mean velocity is then calculated based on:

$$V^* = \frac{\dot{m} \cdot \sqrt{1 + k^2}}{\rho \cdot A_x}. \tag{3.14}$$

A_x is the actual cross section of the twisted tape insert taking into account the difference in width and inner diameter:

$$A_x = \frac{\pi \cdot D^2}{4} - \delta \cdot w. \tag{3.15}$$

In the case of tight-fitting twisted tape inserts, the width is the same as the diameter, ($w = D$).

With the modified mean velocity, V^*, a new Reynolds number is defined as:

$$Re^* = \frac{V^* \cdot \rho \cdot D_h}{\mu}, \tag{3.16}$$

where D_h is the hydraulic diameter defined as:

$$D_h = \frac{4 \cdot A_x}{P_w}, \tag{3.17}$$

where P_w is the wetted perimeter accounting for all geometric parameters of the twisted tape insert.

With the new defined Reynolds number, Re^*, a twisting channel friction factor, f^* can be calculated based on the pressure drop:

$$\Delta P = f^* \frac{1}{2}\rho \cdot V^* \cdot \frac{L^*}{D_h}. \tag{3.18}$$

Where L^* was the adjusted length to account for the untwisting of the twisted tape insert:

$$L^* = L \cdot \sqrt{1 + k^2}. \tag{3.19}$$

The Nusselt number for the channel flow methodology, Nu^* was calculated based on two independent mechanisms, a forced convection and a centrifugal convection:

$$Nu^* = Nu_{forced} + C \cdot Nu_{centrifugal}. \tag{3.20}$$

The forced convection term uses a conventional channel flow Nusselt number correlation with adjusted parameters, in this case, Dedov et al [99] use the one from Petukhov et al [104]:

$$Nu_{forced} = \frac{Re^* Pr(\zeta/8)}{1 + \frac{900}{Re^*} 12.7\sqrt{\zeta/8}(Pr^{2/3} - 1)}, \tag{3.21}$$

where ζ was the friction factor based on Filonenko's equation for smooth pipes [105].

While the centrifugal Nusselt number term used a modified natural convection Nusselt number correlation:

$$Nu_{centrifugal} = [(Re_x k)^{1/3}(\frac{D_h}{D})\beta\Delta T Pr]^{1/3}, \tag{3.22}$$

where Re_x is the Reynolds number based on the axial velocity defined in Equation 3.9, and β is the volumetric expansion coefficient, and ΔT is the difference between the temperature of the wall and the bulk temperature of the fluid.

The C value in Equation 3.20 is a weighting coefficient determined from experimental data. The original formulation of Equation 3.20 grouped the C coefficient with the centrifugal component in Equation 3.22, but it is extracted here for simplicity in future discussions.

3.1.3 Thermal Performance

Thermal performance in twisted tape inserts has not been well studied in the literature. The thermal performance consists of studying how well a heat transfer enhancement technique improves the overall heat removal efficiency. This is done by considering the two competing effects encountered in these systems, increased heat transfer and friction factor. Thermal performance factor, η, was used to determine the overall efficiency of a heat transfer enhancement technique [106, 107]:

$$\eta = \frac{Nu/Nu_0}{(f/f_0)^{1/3}}, \tag{3.23}$$

where f_0 and Nu_0 are the friction factor and Nusselt number respectively of the non-modified geometry, empty pipe, and f and Nu are the friction factor and Nusselt number of the twisted tape insert.

In literature, an increase in twisted tape pitch has been observed to increase thermal performance. Murugesan et al [108] calculated the thermal performance factor with twisted tape inserts using water as working fluid, and reported thermal performance factors larger than 1. Chokphoemphun et al [109] observed a trend of decreasing thermal performance factor with increasing Reynolds numbers, with a majority of their data reaching $\eta \approx 1.0$ at Reynolds number of 15,000. Piriyarungrod et al [110] used air as a working fluid and determined the overall thermal performance of the twisted tape inserts was less than 1. Naga Sarada et al [111] calculated the thermal performance factor using air for different twisted tape insert pitches and widths and observed a trend of decreasing thermal performance with increasing Reynolds number and an increase of thermal performance with increased twisted tape width. Table 3.3 summarizes the thermal performance factor, with their experimental data points obtained using WebPlotDigitizer [112]. While other thermal performance factor data have been reported in the literature, the main focus consisted of modified twisted tape inserts which are outside the scope of this work.

Table 3.3: Summary of operating conditions and geometric characteristics of twisted tape inserts for thermal performance factor comparisons found in the literature.

Author [Ref]	Reynolds number range	Working fluid	Twisted tape pitch (y)
Murugesan et al [108]	3,000 - 11,000	Water	2.0, 4.4 and 6.6
Chokphoemphun et al [109]	5,000 - 24,000	Air	4.0 and 5.0
Piriyarungrod et al [110]	6,000 - 20,000	Air	3.5, 4.0 and 4.5
Naga Sarada et al [111]	6,000 - 13,500	Air	3.0, 4.0, and 5.0

The thermal performance factor is used as a method to compare the overall pumping power requirements with the effectiveness of the heat transfer enhancement. This method only considers the pressure loss and heat transfer gain solely in the test section or region of interest. The benefits of using the heat transfer enhancement at a systems level are left out for future work, as this would require further exploration of the pressure loss in the entire system and possible size reductions created from the heat transfer enhancement.

3.2 Methodology

This section describes the experimental facility designed to calculate the thermal performance of scaled-down molten salt passive heat transfer enhancement components. It describes the overall experimental setup with the data acquisition software and technique used to collect data and it ends with a detailed description of the twisted tape geometries and operating conditions used to calculate the friction factor and Nusselt number.

3.2.1 Experimental Setup

Scaled thermal hydraulic experimental facilities can be designed in two matters depending on the phenomena of interest. The two methods consist of studying separate effects [113] or integral effects [114]. Separate effects tests isolate physical phenomena of interest to study them independently within a system, while integral effects tests study how a physical phenomenon affects and changes the overall heat transfer system. In this work, the separate effects of pressure drop and heat transfer are studied for a passive heat transfer enhancement system.

At Virginia Commonwealth University, the Fluids in Advance Systems and Technology research group has designed and built a separate effects testing facility named the Modular Separate Effects Test Facility - 1st Loop (MSETF-1). MSETF-1 was designed to study the thermal performance of heat transfer enhancement methodologies using water as a surrogate fluid for advanced energy applications that use molten salts as the operating coolant. This is achieved by studying the pressure drop and heat transfer of the components separately. MSETF-1 was designed to have a swappable test section in order to facilitate the switching of the geometries of interest and expedite the number of tests that could be done in the facility.

MSETF-1 has shown to be versatile and easily adjustable to study a variety of thermal hydraulic concepts, such as traditionally manufactured test sections, additively manufactured test sections, flow straighteners, and air and water injections. Due to the versatility and changes to the facility, it has gone through various iterations to optimize and improve it. Figure 3.3 shows a schematic of MSETF-1 with its various components, while Figure 3.4 has the loop dimensions in centimeters, with Figure 3.5 showing MSETF-1 in the experimental laboratory. MSETF-1 was built on top and supported by unitstrut tables, as shown in Figure 3.4 and in Figure 3.5.

The water tanks consisted of two 70-gallon water tanks of Part Number LP0068SWSS, Inlet Tank

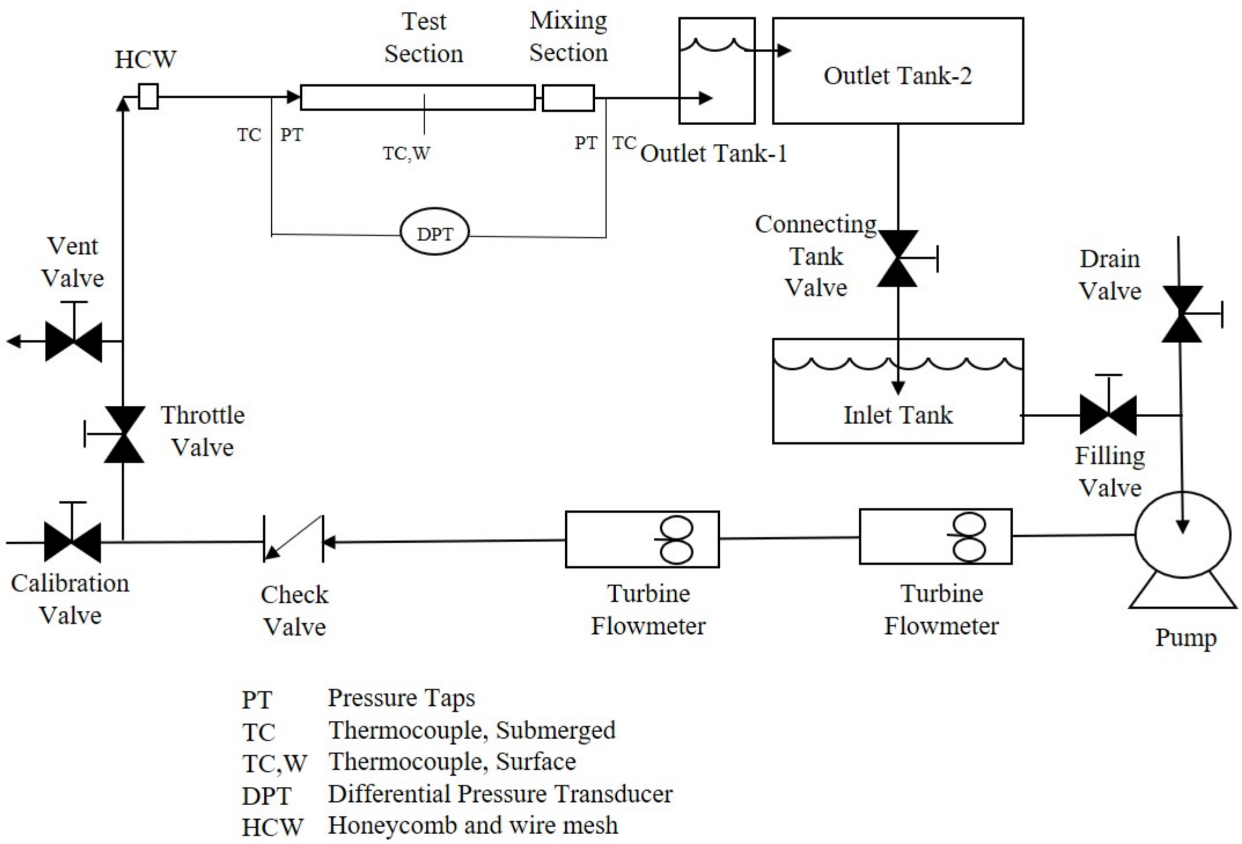

Figure 3.3: MSETF-1 Schematic

and Outlet Tank-2, and one 7-gallon water tank Part Number SP00007SWLN, Outlet Tank-1. Each tank served different purposes. Inlet Tank and Outlet Tank-2 were designed to store water during experimental runs, while Outlet Tank-1 served as a method to keep constant hydrostatic pressure in the loop and in the test section. Pressure was kept hydrostatic by maintaining a constant water level in Outlet Tank-1 with the use of three connecting hoses at the top of the water tank that would drain excess water into Outlet Tank-2, this connection is shown in Figure 3.6 with dimensions in centimeters. Water was circulated using a Pentair SUPERFLOWVS variable speed control pump.

MSETF-1 had a total of six valves: the Vent Valve, Throttle Valve, Calibration Valve, Drain Valve, Filling Valve, and Connecting Tank Valve. Each valve was opened or closed depending on different MSETF-1s operating procedures. For a detailed explanation of each valve configuration in MSETF-1's procedures refer to Appendix B.

The length of MSETF-1 varied depending on the test being conducted. Heat transfer tests require a mixing section shown in Figure 3.3 directly after the test section and before the pressure and thermocouple taps. However, for pressure tests, the mixing section was removed to solely investigate

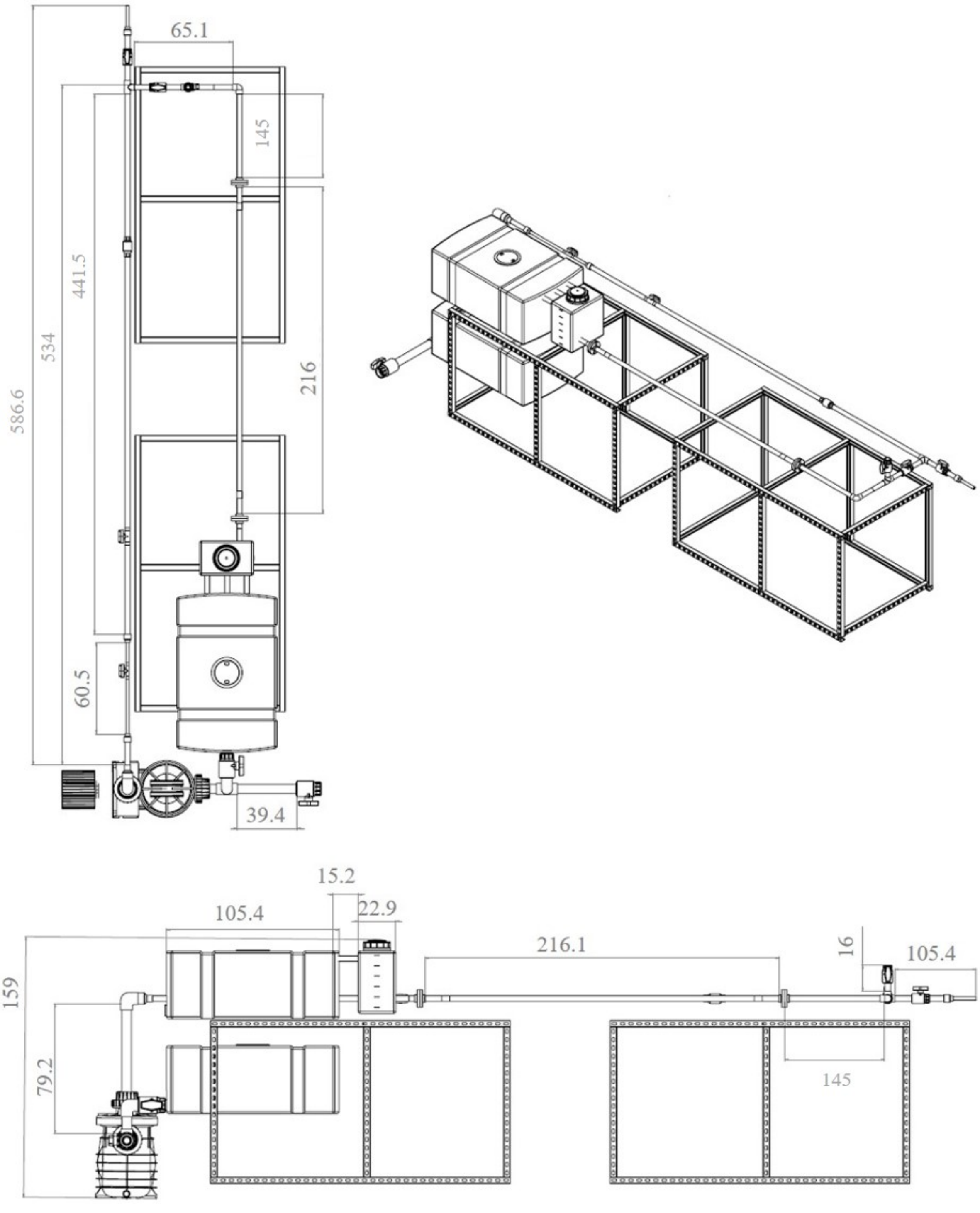

Figure 3.4: MSETF-1 Dimensions in centimeters

the region between the test section and the pressure taps. The dimensions illustrated in Figure 3.4 represent the pressure drop experimental configuration, thus no mixing section was added in this schematic.

Figure 3.5: MSETF-1 loop at Virginia Commonwealth University

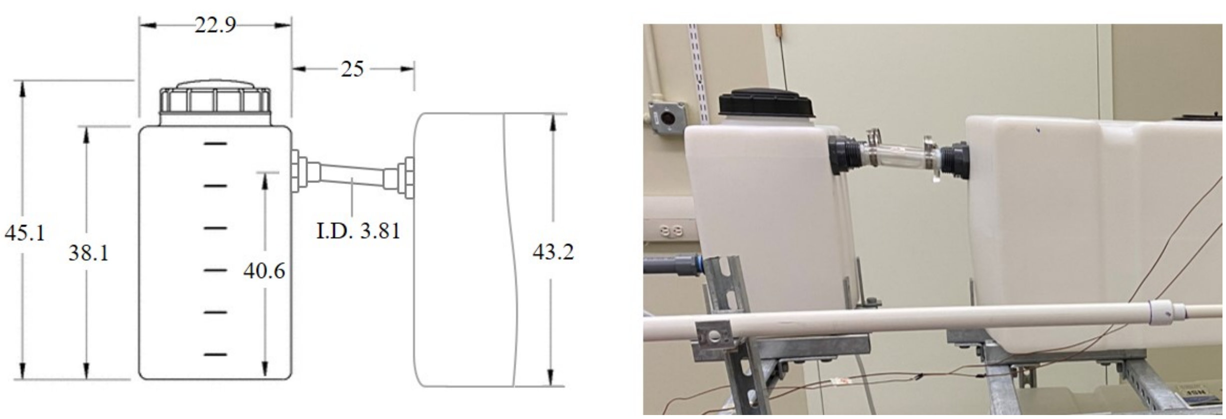

Figure 3.6: Schematic with units in centimeters (Left) and image (Right) of the tank connections.

Following the Throttle and Vent valves, a 90^o elbow guided the water into the test section region. After the 90^o elbow, a flow straightener consisting of a honeycomb and wire-mesh was set to aid with flow development, as well as 1.35 meters (53 pipe diameters) of pipe length to ensure the flow was fully developed before it entered the test section. This length was kept constant throughout the different experiments. The mixing section consisted of an in-house static mixer built by welding a 10 cm twisted tape insert of pitch y = 1.9 on a 15 cm long 1" nominal inner diameter pipe.

3.2.2 Data Acquisition Setup

This section describes the data acquisition for pressure drop and heat transfer. Data was collected using the software, from National Instruments (NI), LabVIEW VERSION 2017 SP1 (32-bit), and acquired using a combination of voltage drop (NI-9205, C-series Voltage Input Module) and temperature (NI-9213, C-series Temperature Input Module) modules mounted on a cDAQ-9174 compact chassis. The NI modules, NI chassis, power supply for a pressure transducer, and computer for data acquisition are shown in Figure 3.7. A grounding section was added due to the limited space near the NI module terminals and the proper grounding techniques between signals described in the NI module user guides. The grounding section connected all grounds from the various instruments and modules to a common ground connected in parallel with a $1M\Omega$ resistor. This was used to remove any oscillating signals that were not random noise from the instrumentation.

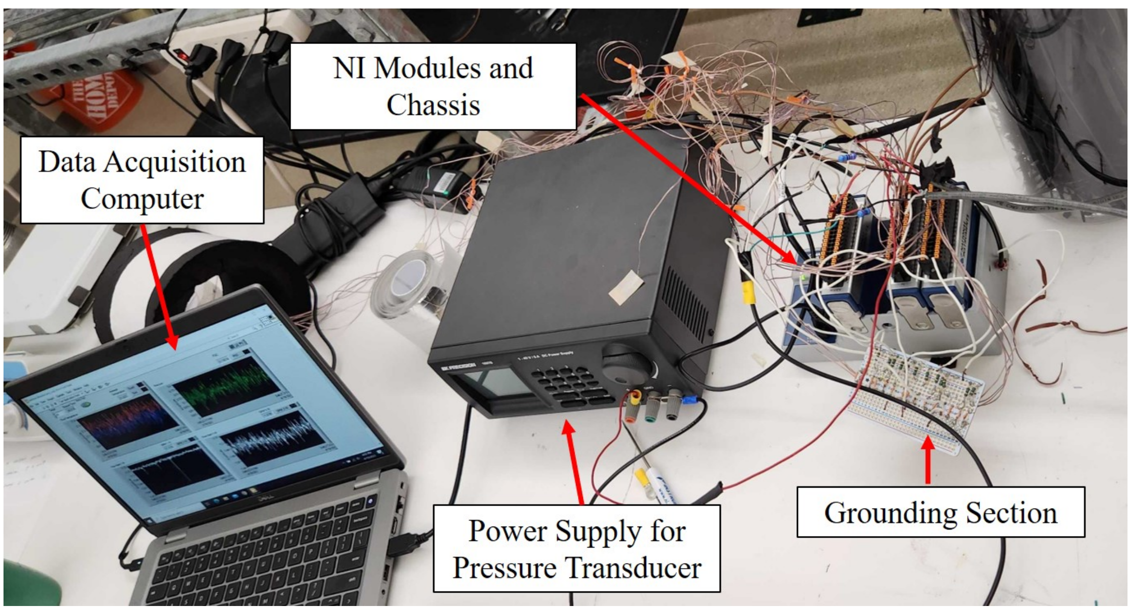

Figure 3.7: NI setup with power supply and data acquisition computer

The LabVIEW software consists of a Front Panel and Block Diagram. The Front Panel is used to monitor the data acquisition and define user inputs, in this case, experimental target time and a Boolean option to write the data to a file. A figure of LabVIEW's Front Panel is shown in Figure 3.8. The Block Diagram is the component where the user creates and constructs the underlying software and architecture of the data acquisition code. The code written for the pressure and heat transfer experiments consisted of a while-loop that runs the data collection until a user-defined target time has been reached. All of the code functions are contained within this while-loop. This includes the DAQ Assistant, a function to edit, add, and remove signals obtained from the modules, the Write to File function, where the file directories are edited, and controls. A schematic of the Block Diagram is shown in Figure 3.9.

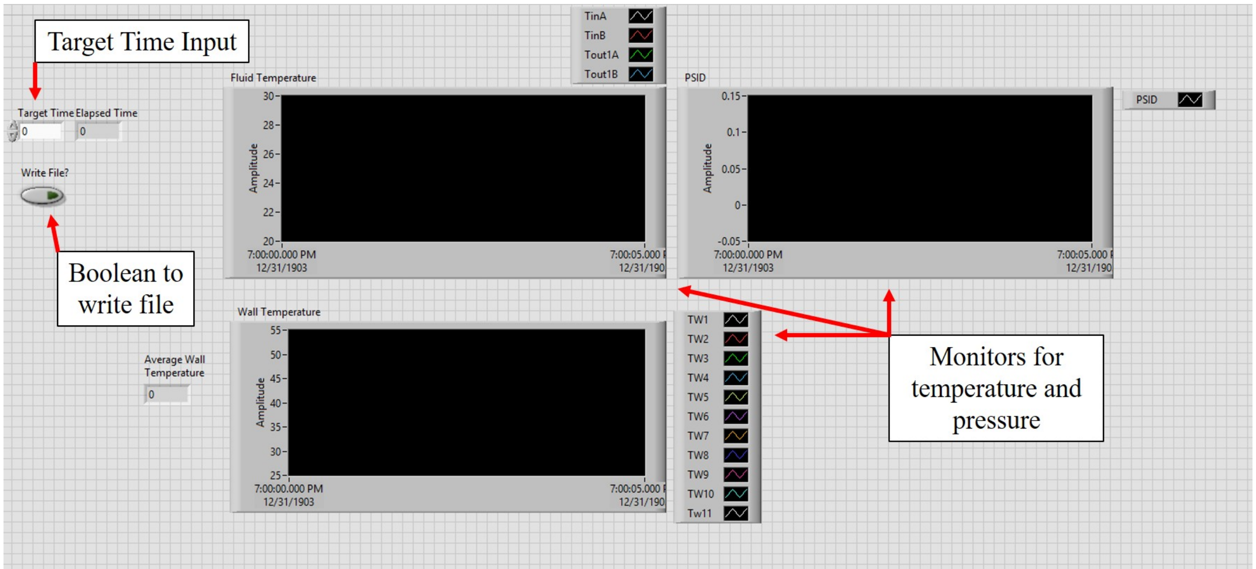

Figure 3.8: LabVIEW's Front Panel for pressure drop and heat transfer experiments

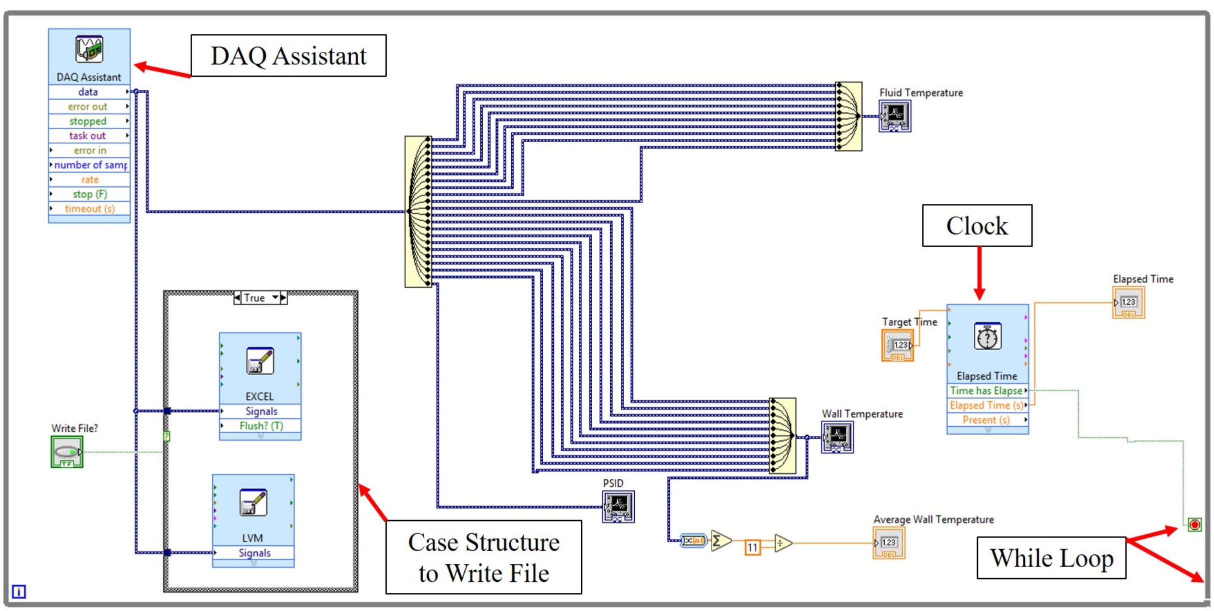

Figure 3.9: LabVIEW's Block Diagram showing the code's architecture.

3.2.3 Instrumentation

Flow rate was measured with two inline flow meters consisting of a low and high flow rate of ranges 3.8 -38 liters per minute (lpm) and 19 - 190 lpm respectively. The flow meters had NIST Certificate of accuracy of ± 3 %. The low flow rate flow meter had a Part Number of 2400T431 and the high flow rate flow meter of 2400T451. The high flow rate flow meter is shown in Figure 3.10 installed in MSETF-1 with dimensions from McMaster-Carr.

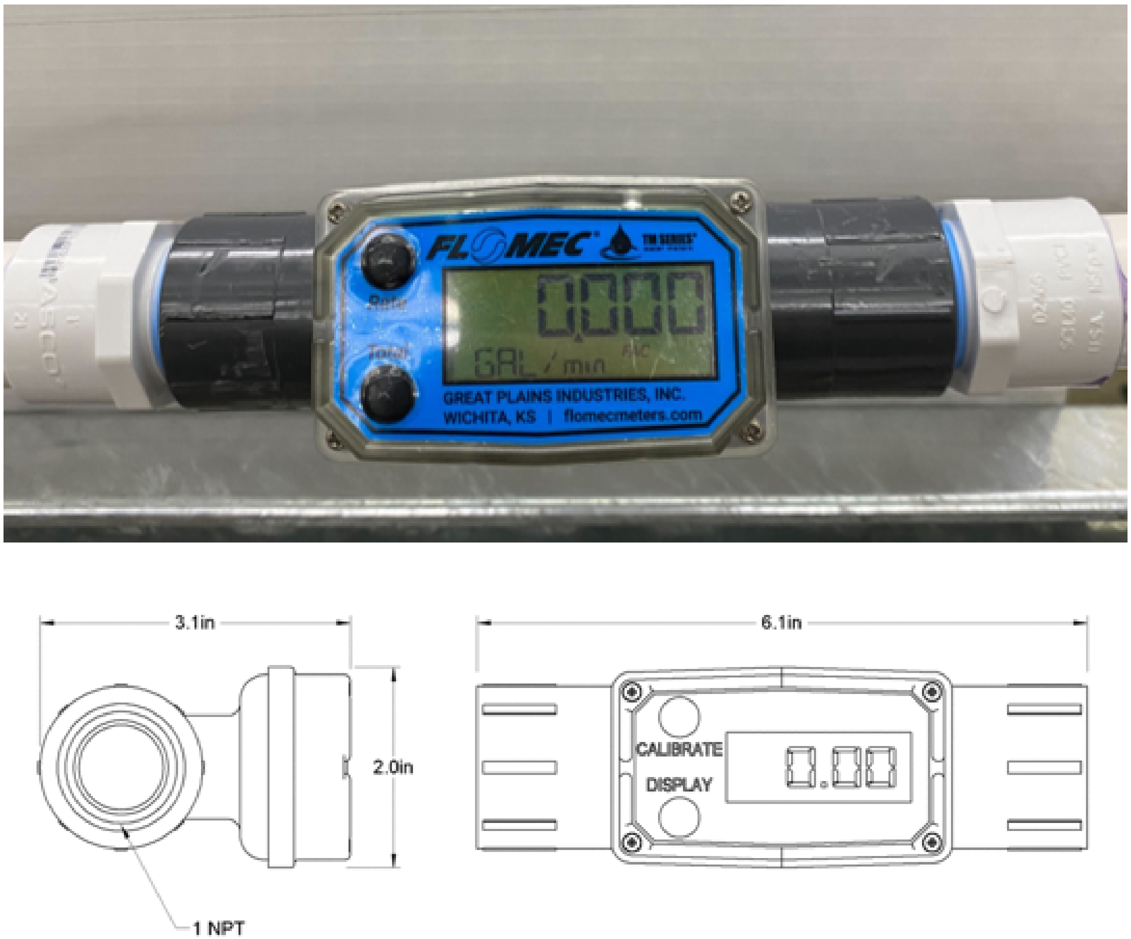

Figure 3.10: Flow meter installed in MSETF-1 (Top), and schematic of flow meter from McMaster-Carr with units in inches (Bottom).

The pressure transducer consisted of an Omega oil-filled differential pressure sensor with an accuracy of 13.8 Pa and Item Number PX409-2.5DWU5V. The pressure taps were installed upstream and downstream of the test section as shown in Figure 3.4. The pressure taps were connected to the pressure transducer using a combination of Yor-Loks, a form of compression fittings, and water hoses. The water hoses for the upstream and downstream pressure taps were measured to be the same length in order to remove any pressure loss biases created by the length of the water hoses.

The pressure taps were tapped 3.8 cm from the end of one-inch pipes with 1/8 inch NPT threads. Figure 3.11 shows the installed pressure transducer used in MSETF-1 with water lines to each side of the pressure transducer ports and the unit strut used to support it.

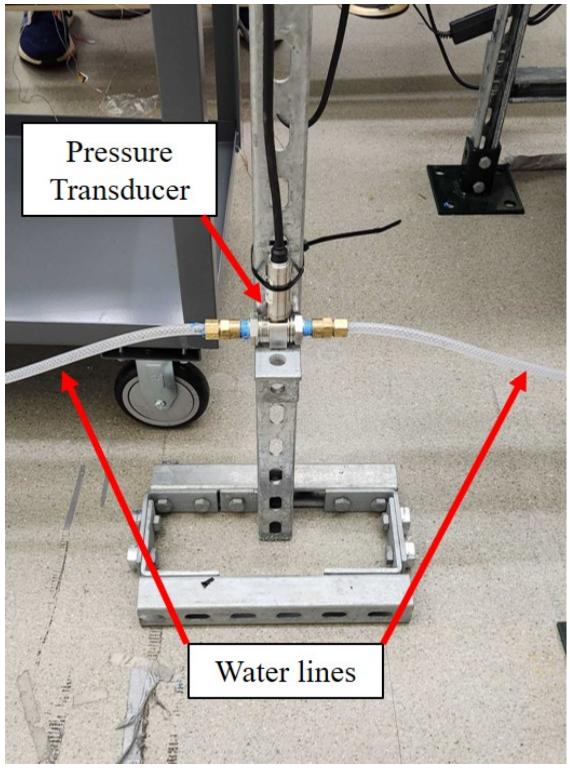

Figure 3.11: Pressure transducer used in MSETF-1, with water lines and installation mount.

Two different types of thermocouples were used to measure the fluid and wall temperatures for heat transfer experiments. To measure the fluid's temperature, T-Type thermocouples were installed downstream and upstream of the test sections with the same connections as the pressure taps. The range in which the submerged thermocouples were placed radially in the fluid was varied to ensure statistically different tests, more details of the radial location of the thermocouples can be found in Appendix B.3.1. The second type of thermocouples used consisted of T-Type thermocouples with an adhesive side to measure the wall temperatures. A total of eleven evenly-spaced surface thermocouples were used to average the wall temperature. The azimuthal location of the thermocouples was varied to obtain statistically different tests. Figure 3.12 shows the difference between a surface thermocouple and a submerged thermocouple.

Heat transfer experiments consisted of a constant heat flux boundary condition at the wall, which was achieved using ten heaters wrapped around the test section. The heaters consisted of a combination of Fisherbrand High Temperature Heating cords (of diameter 4.8 mm with a length of 1.8 meters rated for 120 Volts and 8.3 Amps, Part No. FHWC1180 and Fisher number of 11476084) and

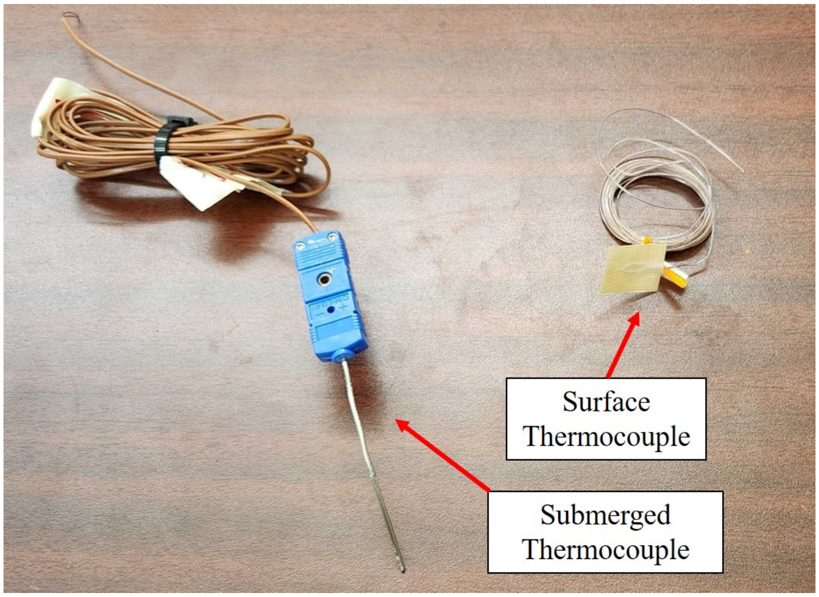

Figure 3.12: Comparison between a surface and submerged thermocouple

Briskheat heating cords (Model HTC451002 with same specifications as the Fisherbrand heating cord). The heaters were plugged into AC variable power supplies from Circuit Specialists Model Number TDGC-2KM, shown in Figure 3.13. The variable power supplies vary the voltage output by turning a dial on its top, with the voltage output displayed on a small screen. The voltage output was limited to 110 Volts during experiments. For further details of the installation and procedures refer to Appendix B.3.1.

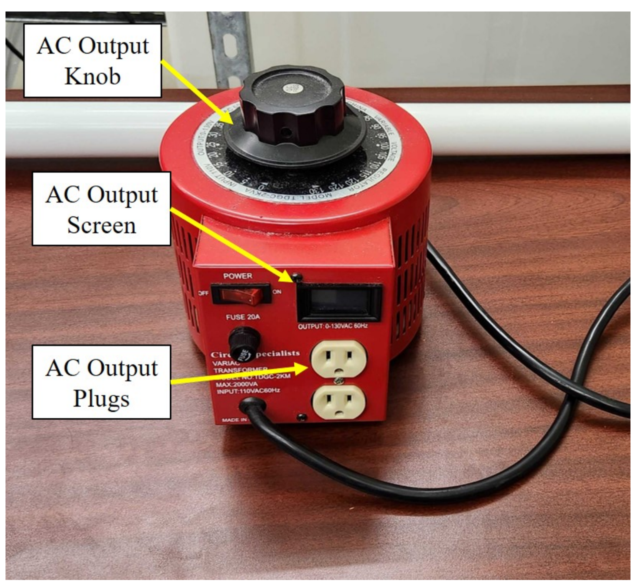

Figure 3.13: AC Power supply for heating elements with output window and output knob.

3.2.4 Description of Experiments

This section outlines the experiments performed to calculate the friction factor and Nusselt number for twisted tape inserts. It includes details on the methodology, instrumentation, and the explored twisted tape geometries. The twisted tape inserts were welded to the ends of 1.83 m long stainless-steel pipes of 1" nominal diameter (26.67 cm) as shown in Figure 3.14 with the three main twisted tape pitches studied. Three initial twisted tape geometries were studied for friction factor and heat transfer. Table 3.4 provides a summary of the geometric parameters and experimental conditions of the twisted tape inserts. The Reynolds numbers explored consisted of laminar, transitional, and turbulent regimes. The twisted tape inserts have been shown to act as turbulent suppressors, thus a Reynolds number of 3,000 is considered laminar in these geometries.

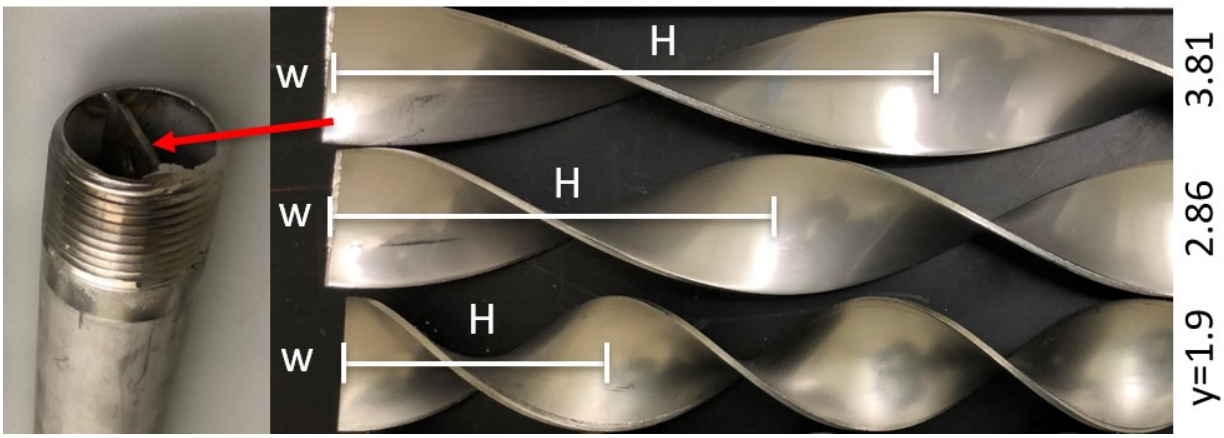

Figure 3.14: Welded twisted tape insert (Left) and twisted tape inserts with different pitches (Right).

Table 3.4: Geometric and experimental conditions of twisted tape inserts for friction factor and Nusselt number experiments

Parameter (Unit)	Value
Inner diameter, D (mm)	26.67
Hydraulic diameter, D_h (mm)	15.05
Ratio of width and diameter, w/D (-)	0.95
Test section length, L (m)	1.83
Twisted tape width, w (mm)	25.4
Twisted tape thickness, δ (mm)	1.6
Inlet temperature, (^oC)	≈ 21
Pitch, y (-)	1.9, 2.86, and 3.81
Reynolds numbers, Re (-)	3,000 - 48,000

The initial friction factor results revealed an intriguing phenomenon related to the width of the twisted tape. This observation prompted further investigations, which are discussed in further detail in Section 3.3.1. Subsequent friction factor experiments were conducted with additional twisted tape geometries to explore this phenomenon. Specifically, the width of the twisted tape was varied, and four new twisted tapes with two different widths and two different pitches were studied. Figure 3.15 illustrates the varying width configurations of the different twisted tape inserts. Table 3.5 summarizes the new geometric and experimental conditions of the four additional twisted tape inserts for friction factor experiments.

Table 3.5: Geometric and experimental conditions of twisted tape inserts for friction factor experiments with different widths

Parameter (Unit)	Value
Inner diameter, D (mm)	26.67
Hydraulic diameter, D_h (mm)	15.82 and 16.61
Test section length, L (m)	1.83
Twisted tape width, w (mm)	22.58 and 19.94
Ratio of width and diameter, w/D (-)	0.85 and 0.75
Twisted tape thickness, δ (mm)	1.6
Inlet temperature, (^{o}C)	$\approx$ 21
Pitch, y (-)	1.9 and 3.81
Reynolds numbers, Re (-)	$\approx$ 3,000 - 48,000

Figure 3.15: Twisted tape inserts with varying widths and pitches.

The Fluids in Advanced Systems and Technology (FAST) Research Group at VCU has been exploring additive manufacturing techniques to further explore the geometric characteristics of passive heat transfer enhancements. Thus, in the efforts to push the boundaries encountered by traditional manufacturing techniques, some of the geometries that were initially intended to study were not feasible with current manufacturing techniques, i.e. tighter twisted tape pitches. To overcome some of these shortcomings, additive manufacturing was explored to build twisted tape test sections. A detailed description of the methodology derived and executed by the FAST Research

Table 3.6: Geometric and experimental conditions of additively manufactured twisted tape inserts for friction factor experiments.

Parameter (Unit)	Model	Measured
Inner diameter, D (mm)	26.67	26.51
Test section length, L (cm)	91.4	93.3
Twisted tape width, w (mm)	26.67	26.51
Ratio of width and diameter, w/D (-)	1.0	1.0
Twisted tape thickness, δ (mm)	2.54	2.41
Pitch, y (-)	2.86	2.86
Flange thickness, (mm)	20.32	21.03

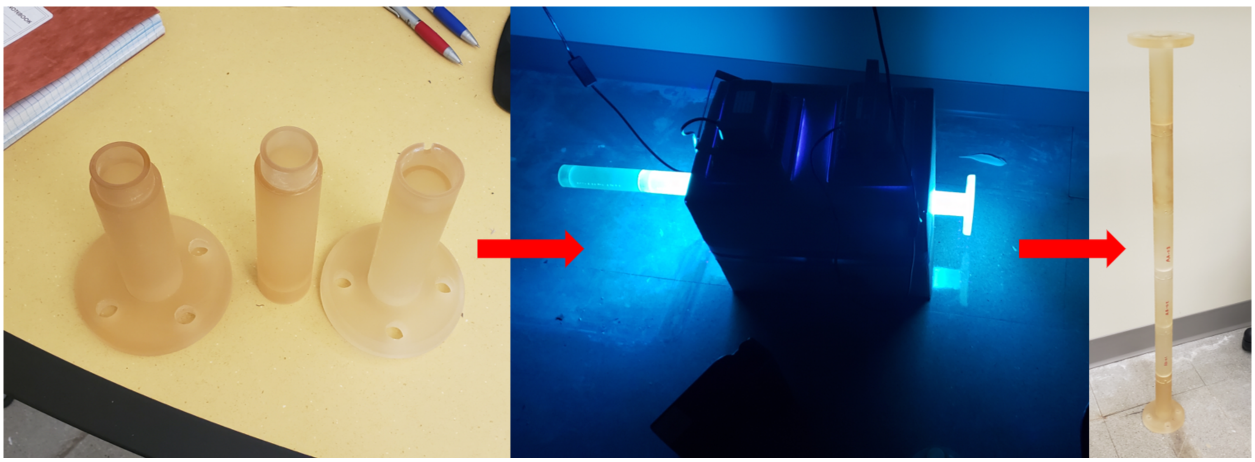

Figure 3.16: Current methodology to create additively manufactured test sections of printing different parts and gluing them together via UV light exposure to create longer test sections.

Group to obtain test sections that can be long enough to have fully developed flow and withstand MSETF-1 operating conditions can be found in Appendix D with the current iteration and working methodology in Appendix D.2. Figure 3.16 shows the current methodology of gluing small parts together via UV light exposure to create test sections that are long enough to experience fully developed flow.

Additive manufacturing technology is still in its developing stages, and further research is required to fully explore its potential. For this work, only one geometry was explored to assess the feasibility of this technology. The exploration of geometries otherwise unfeasible with traditional manufacturing using additive manufacturing will be left for future work. Table 3.6 summarizes the geometric parameters of the additively manufactured twisted tape insert for the 3D models and the actual measured value. The 3D printing technique used to create the test section consists of Stereolithography (SLA) printing, further discussion can be found in Appendix D, and this method of printing requires a curing procedure once it has been printed. The curing procedure can cause small changes in the 3D printing as it is heat treated, thus a model and measured value are presented in Table 3.6.

3.2.5 Calculations

This section discusses the major equations used to calculate the friction factor and Nusselt numbers. The raw data obtained from LabVIEW had to be post-processed and analyzed to obtain the results shown in Section 3.3. A detailed discussion of the post-processing methodology and discussions to calculate friction factor and Nusselt number can be found in Appendices C.2 and C.3 respectively, with uncertainty quantification in Appendices C.4.1 and C.4.2. A Matlab in-house code was developed to post-process the data from LabVIEW to analyze the friction factor and heat transfer.

The friction factor was calculated based on the pressure drop obtained from the Omega Pressure transducer. The following equation was used to calculate the Darcy friction factor:

$$f = \frac{2 \cdot \Delta P \cdot D}{L \cdot \rho \cdot V^2}, \tag{3.24}$$

where ΔP is the pressure drop, ρ is the density of the water at bulk temperature, D is the diameter of the pipe and V is the average velocity based on circular pipe geometry, Equation 3.2.

The twisting channel friction factor was calculated in a similar manner:

$$f^* = \frac{2 \cdot \Delta P \cdot D_h}{L^* \cdot \rho \cdot V^{*2}}, \tag{3.25}$$

where L^*, and V^* are the adjusted length and velocity that accounts for the untwisting of the twisted tape insert. The mean velocity was calculated based on Equation 3.14, and the adjusted length was calculated based Equation 3.19.

For Nusselt number calculations, the heat transfer coefficient was calculated based on the energy equation. The total heat transfer by convection, UA, equals the enthalpy change of the fluid:

$$UA \cdot (T_w - T_b) = \dot{m} \cdot c_P \cdot (T_{out} - T_{in}), \tag{3.26}$$

where T_w, T_b, T_{in}, and T_{out} are the average temperatures obtained at steady state. Simplifying Equation 3.26 yields:

$$UA = \frac{\dot{m} \cdot c_P \cdot (Tout - T_{in})}{(T_w - T_b)}. \tag{3.27}$$

The heat transfer coefficient, h, that accounts for the conduction through the wall was defined as:

$$\frac{1}{h \cdot A_i} = \frac{1}{UA} - \frac{ln(D_o/D)}{2 \cdot \pi \cdot k_{ss} \cdot L_{heated}}, \tag{3.28}$$

where A_i is the inner heated surface area of the pipe, D_o is the outer diameter, and k_{ss} is the thermal conductivity of stainless steel. Finally, the heat transfer coefficient was found with:

$$h = (\frac{1}{UA} - \frac{ln(D_o/D)}{2 \cdot \pi \cdot k_{ss} \cdot L_{heated}})^{-1} \cdot \frac{1}{\pi \cdot D \cdot L_{heated}}. \tag{3.29}$$

The Nusselt number, in terms of empty pipe, was calculated by:

$$Nu = \frac{h \cdot D}{k_w}, \tag{3.30}$$

where k_w is the thermal conductivity of water.

The channel flow Nusselt number was calculated with:

$$Nu^* = \frac{h \cdot D_h}{k_w}. \tag{3.31}$$

3.2.6 Experimental Procedure - An Overview

Friction factor and heat transfer experiments required multiple experimental procedures. These procedures were developed through a literature review and through trial and error. Some of them were developed by an exhausting number of error experiments and learning through some of the overall physics governing the experimental loop, the data acquisition, and the instrumentation. This led to major changes in MSETF-1. The initial version of MSETF-1 consisted of a continuous loop with a single tank. The majority of the piping remained the same, but the single tank setup did not allow for accurate heat transfer experiments. The outlet water temperature would create a sort of feedback through the loop and would not allow for a steady state to occur in the test section. The feedback was created by the heat up of the water mixing in the initial tank and propagating to the rest of the loop. This would create a transient inlet water temperature and a true steady state was not achievable. This led to the changes and the current version of MSETF-1 as briefly discussed in Section 3.2.1.

In general, to obtain both the friction factor and heat transfer data, the system had to reach a steady state. This consisted of adjusting the pump to a desired pre-known frequency and waiting for the flow to reach a steady state by monitoring the flow meters. Afterward, through the LabVIEW software, the data was monitored until it seemed to reach a steady state in which the oscillations were random and not following a visible trajectory. Once the steady state was observed, data acquisition began by collecting the data through the LabVIEW software and documenting the flow rate of the flow meters. This description is brief for simplicity, but further descriptions of the operation of MSETF-1 such as degassing, filling up, and the different procedures to obtain the experimental data can be found in Appendix B.

3.3 Results

Initial experimental data were taken in a circular pipe test section to qualify the experimental loop, instrumentation, procedures, and post-processing codes were working properly by comparing the data against well-known circular pipe friction factor correlations. These data are shown in Figure 3.17 for friction factor with correlations from Moody [115], Filonenko [105], and Blasius [116]. Figure 3.17 also plots the friction factor of a circular pipe test section made with additive manufacturing to test the printing technique and ensure the connections between test sections were assembled properly. The experimental data was plotted with $\pm 2\sigma$ error bars. The results shown in this section consist of steady-state values calculated from the experiments, thus one does not need to consider the Nyquist frequency.

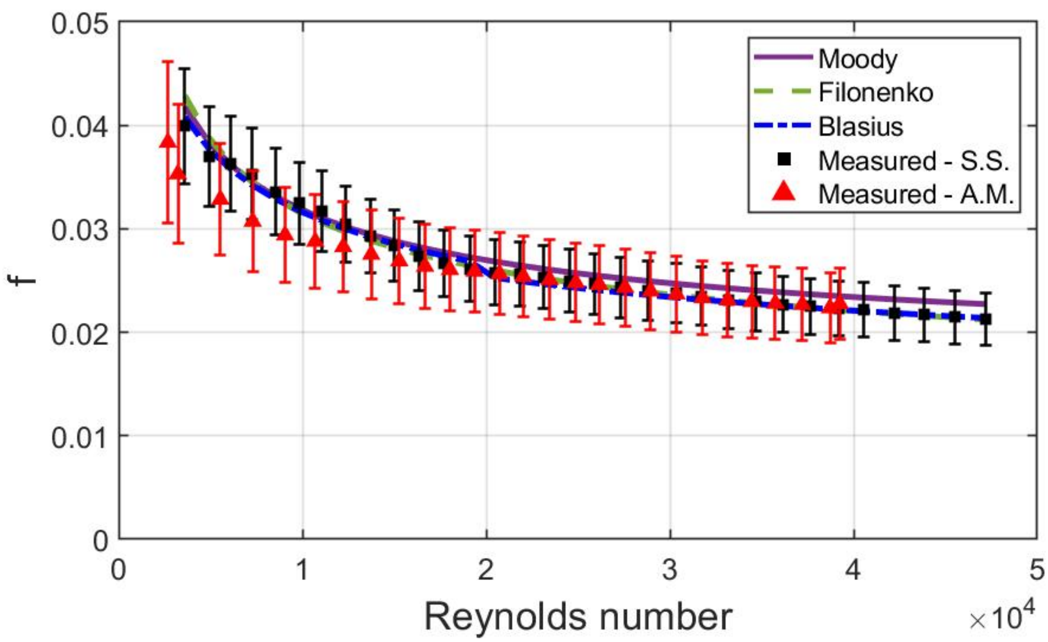

Figure 3.17: Friction factor versus Reynolds number of measured stainless-steel test section (Measured - S.S.), additively manufactured test section (Measured - A.M.), and correlations from Moody [115], Filonenko [105] and Blasius [116].

Figure 3.17 shows that the methodology, instrumentation, and codes are working accordingly as all the data points for the stainless steel test section (Measured - S.S.) match well with the other correlations at all Reynolds numbers. For the additively manufactured test section (Measured -

A.M.) the data matches well in the turbulent regime, but the laminar data was lower than the other experimental measured data and the correlations (Re ≤ 10,000). This low friction factor can be attributed to different factors, such as the printing methodology and surface roughness of the prints. The test sections were printed in the same orientation to maintain constant surface roughness as previous work has shown different printing orientations change the surface roughness [117]. Currently, the friction factor of the additively manufactured test section is compared with the stainless-steel friction factor and correlations using the surface roughness of stainless steel. In order to obtain more accurate comparisons, the quantification of the surface roughness of these test sections is required, but this is left for future work.

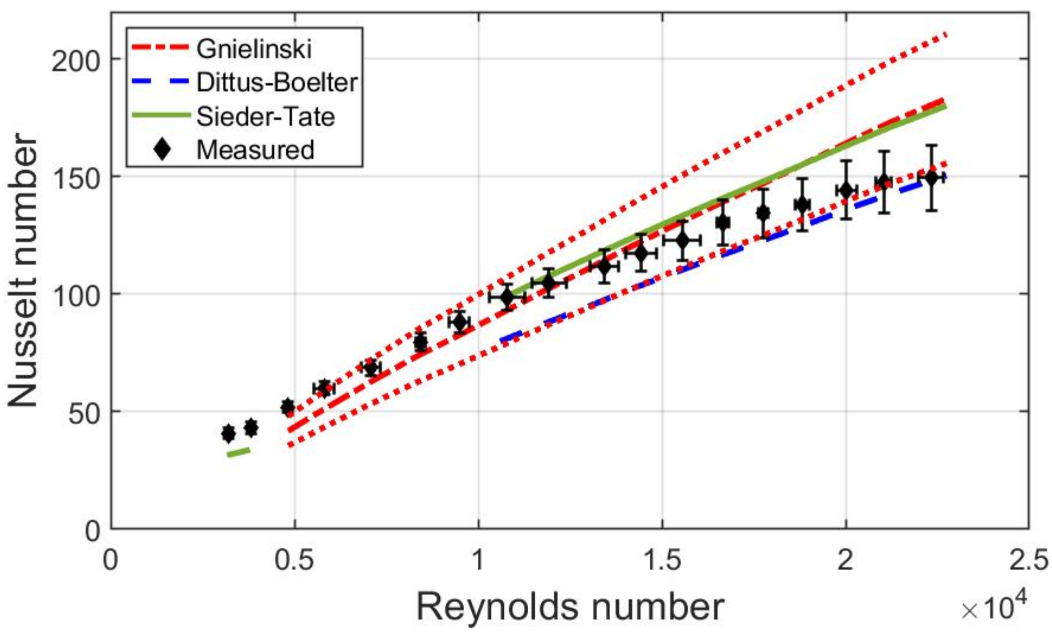

Figure 3.18: Nusselt number versus Reynolds number of measured empty pipe with correlations from Gnielinski [54], Sieder-Tate [118], and Dittus-Boelter [50].

In a similar manner, heat transfer experimental data were obtained on a circular empty pipe to test the methodology, codes, instrumentation, and test procedures. The data were also compared with well-known empty pipe correlations. These data are shown in Figure 3.18 with correlations from Gnielinski [54], Dittus-Boelter [50] and Sieder-Tate [118] at their respective Reynolds number operating range, in addition with Gnielinski's correlation with ±15% uncertainty. Experimental data points fall outside the Reynolds number ranges of the correlations as those Reynolds numbers were explored for the twisted tape inserts and validation data was required. The experimental data points match within ±15% of Gnielinski's correlation indicating the viability and accuracy of the flow loop and instrumentation. As the Reynolds number increases the measured Nusselt number starts deviating from Gnielinski's correlation, though it starts matching with Dittus-Boelter's correlation. This phenomenon might be attributed to the thermal loss encountered by the sticky side of surface thermocouples. This thermal loss was not accounted for in Equation 3.28. Further work should be done to quantify this value, but for the current experimental results, the impact was not as meaningful as the data matches, within uncertainty, with the selected correlations at the explored Reynolds numbers.

3.3.1 Friction Factor

The friction factor results presented in this section are expressed as Darcy friction factors, whereas many correlations are based on Fanning friction factors. To convert the friction factor correlations provided in Table 3.1, one can simply multiply them by four. Friction factor was obtained on the first set of twisted tape inserts with pitches of y = 1.9, 2.86, and 3.81 with data shown in Figures 3.19 to 3.21 with selected friction factor correlations. The correlations consisted of two experimental correlations, Manglik and Bergles [86, 87] and Lopina and Bergles [102], and two analytically-derived correlations from Smithberg and Landis [93] and Sarma et al [97]. For all three twisted tape pitches, the Manglik and Bergles correlation overpredicted the current experimental data for all three pitches. The Lopina and Bergles' correlation accurately predicts the pitch of y =1.9 at the turbulent regime, but it seems the correlation is not as strongly dependent on the pitch as by varying the pitch the correlation didn't vary as consistently. For y = 2.86 and 3.91, it completely overpredicted the current data, with the former slightly overpredicting it more than the Manglik and Bergles correlations. In the case of the two analytical correlations explored, both of them underpredicted the measured experimental data for the three different pitches, but agreed with each other.

Manglik and Bergles' correlations [86, 87] follow a similar trend of the measured friction factor throughout the different Reynolds numbers. The leading theory consisted of the fact that the correlations don't account for loose-fitting twisted tapes. Further work was performed with twisted tapes that had smaller widths to explore this phenomenon of the over-prediction of loose-fitting twisted tape insert's friction factor. Friction factor data was obtained for twisted tapes with widths of w/D = 0.85 and 0.75 for y =1.9 and 3.81, with results shown in Figures 3.22 and 3.23. The results from w/D = 0.95 consisted of the original data set collected shown in Figures 3.19 and 3.21. Figures 3.22 and 3.23 only plot a single Manglik and Bergles correlation as changing the width didn't change the calculated friction factor prediction. It can be observed that as the width decreases the overall friction factor decreases, and this is not accounted for in the Manglik and Bergles' correlation.

An additively manufactured twisted tape insert with pitch y =2.86 was printed and assembled to

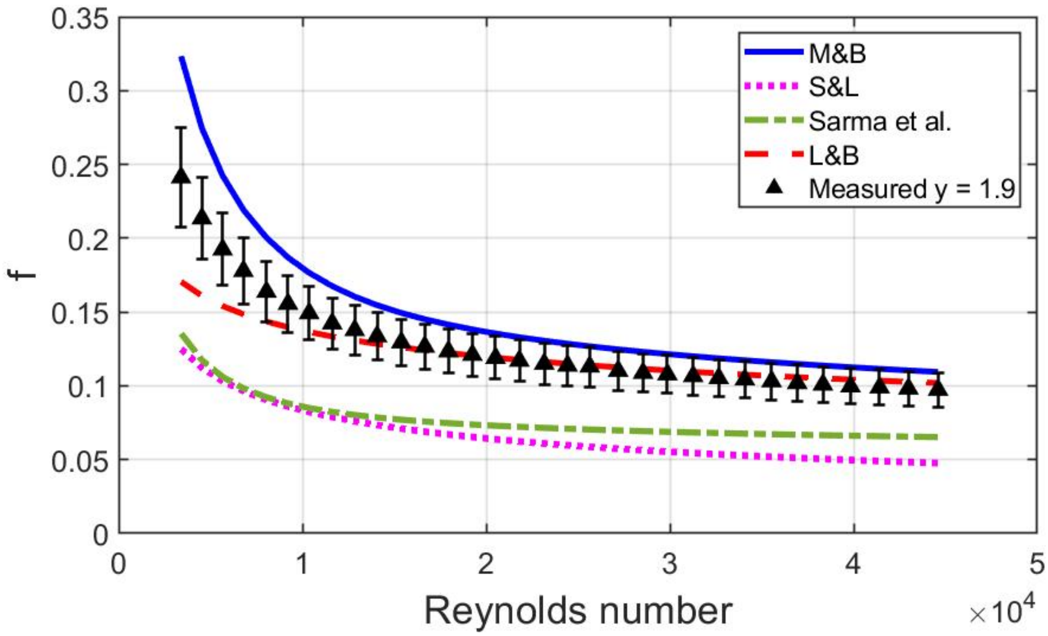

Figure 3.19: Friction factor versus Reynolds number of measured twisted tape with correlations from Manglik and Bergles (M&B) [86, 87], Smithberg and Landis (S&L) [93], Sarma et al [97] and Lopina and Bergles (L&B) [102] for a pitch of y = 1.9.

collect friction factor for a tight-twisted tape insert geometry. The test section was printed with the twisted tape insert attached to the walls of the circular tube, creating a perfect fit between them. Figure 3.24 plots the friction factor data obtained from the additively manufactured twisted tape and Manglik and Bergles' correlation [86, 87]. For the tight-fitting twisted tape insert, the Manglik and Bergles correlation completely matches the experimental data. This showed that the correlation predicts friction factors for tight-fitting twisted tape inserts, but it fails to predict loose-fitting twisted tape friction factor data.

Another method to calculate friction factor based on a twisting channel, f^*, was also explored and considered. This was initially explored by Varava et al [100, 101] and Dedov et al [99]. It also showed good promise in predicting loose-fitting twisted tape insert friction factor at turbulent numbers [92]. Figure 3.25 plots the channel flow friction factor, f^*, versus channel flow Reynolds number, Re^*, measured for twisted tape inserts of width $w/D = 0.95$ with Filonenko's correlation [105]. This method also incorporates the hydraulic diameter of the twisted tape and circular pipe. The experimental friction factor data collapses into a common form when accounting for the hydraulic diameter and transforming the geometry into conventional channel flow, as shown in Figure 3.25.

The modified channel flow friction factor matches well with the Filonenko correlation at the

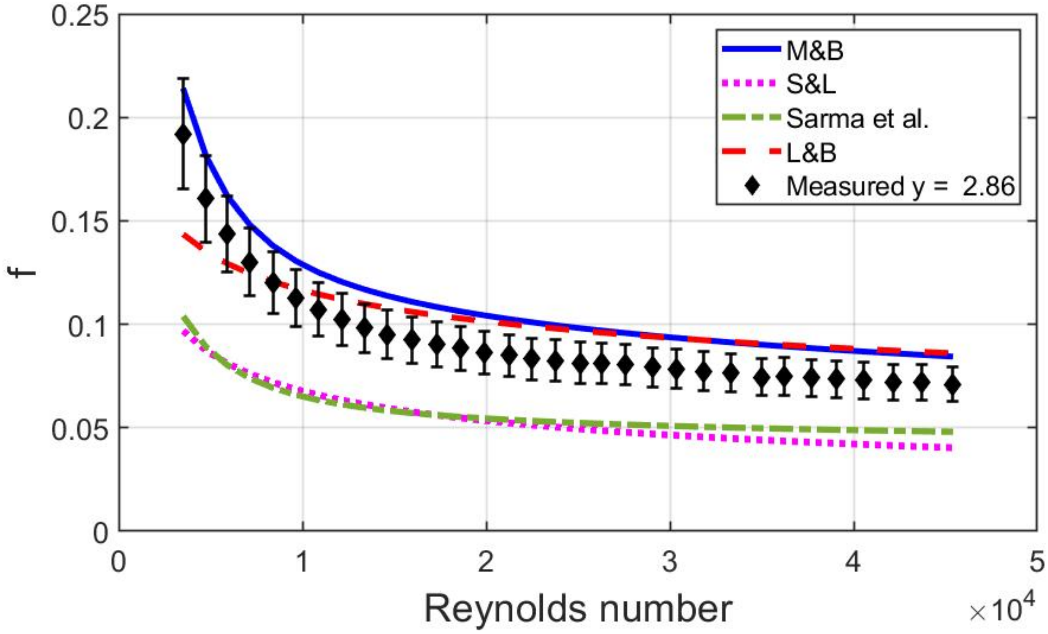

Figure 3.20: Friction factor versus Reynolds number of measured twisted tape with correlations from Manglik and Bergles (M&B) [86, 87], Smithberg and Landis (S&L) [93], Sarma et al [97] and Lopina and Bergles (L&B) [102] for a pitch of y = 2.86.

modified Reynolds number, Re^* above 10,000. While at lower Reynolds numbers the correlation underpredicts the current data. This methodology was capable of predicting friction factor of the loose-fitting twisted tape inserts better than the other four correlations explored, Manglik and Bergles [86, 87], Smithberg and Landis [93], Sarma et al [97], and Lopina and Bergles [102]. Figure 3.26 plots the channel flow friction factor, f^*, versus Reynolds number, Re^*, for the different widths, w/D = 0.95, 0.85, and 0.75, for the twisted tape pitches of y =1.9 and 3.81. Similarly to the data in Figure 3.25, all the experimental data collapses to a common form and matches well with Filonenko's correlation [105]. From this data set, it seems that Filonenko's correlation starts under predicting the experimental data at a lower Reynolds number, $Re^* < 500$. This data reinforces the channel flow methodology for loose-fitting twisted tape inserts, especially at the turbulent regime.

Finally, the channel flow method was applied to the additively manufactured twisted tape insert with friction factor data shown in Figure 3.27. At this point, it is unclear why the channel flow methodology failed to match Filonenko's correlation, but it perfectly matched Manglik and Bergles' correlations [86, 87] as shown in Figure 3.24. One possibility for the underprediction of the channel flow correlation can be the surface roughness of the additively manufactured test section. One possibility could be the incorporation of a correlation that includes the surface roughness of the additively manufactured test section, but this is left out for future work. This shows a limitation

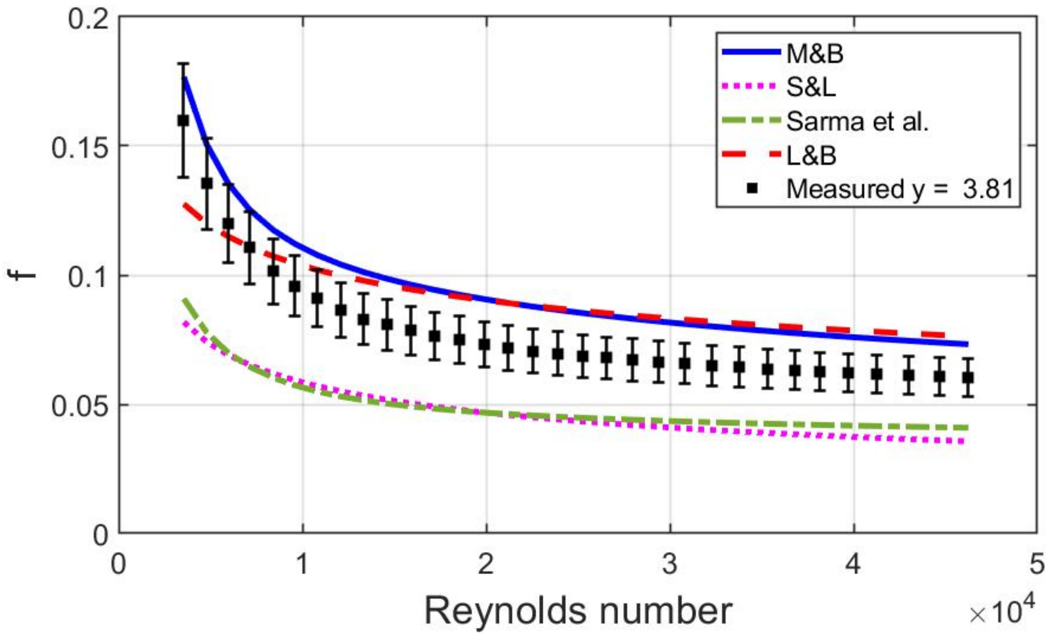

Figure 3.21: Friction factor versus Reynolds number of measured twisted tape with correlations from Manglik and Bergles (M&B) [86, 87], Smithberg and Landis (S&L) [93], Sarma et al [97] and Lopina and Bergles (L&B) [102] for a pitch of y = 3.81.

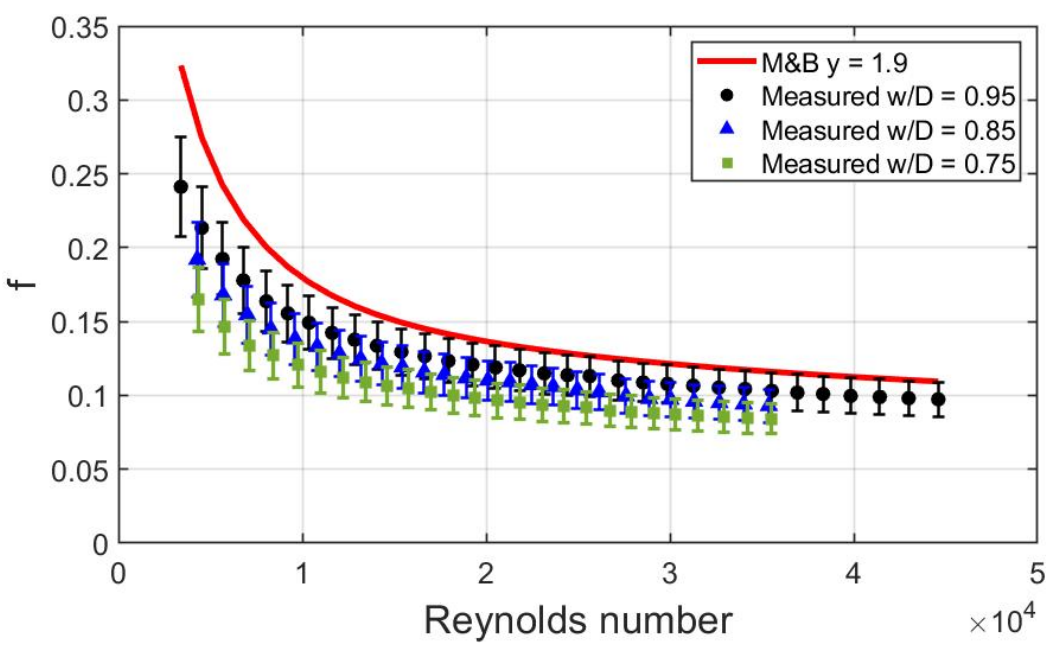

Figure 3.22: Friction factor versus Reynolds number of twisted tape inserts with y = 1.9 and varying widths, (w/D = 0.95, 0.85, and 0.75) with Manglik and Bergles' correlation [86, 87].

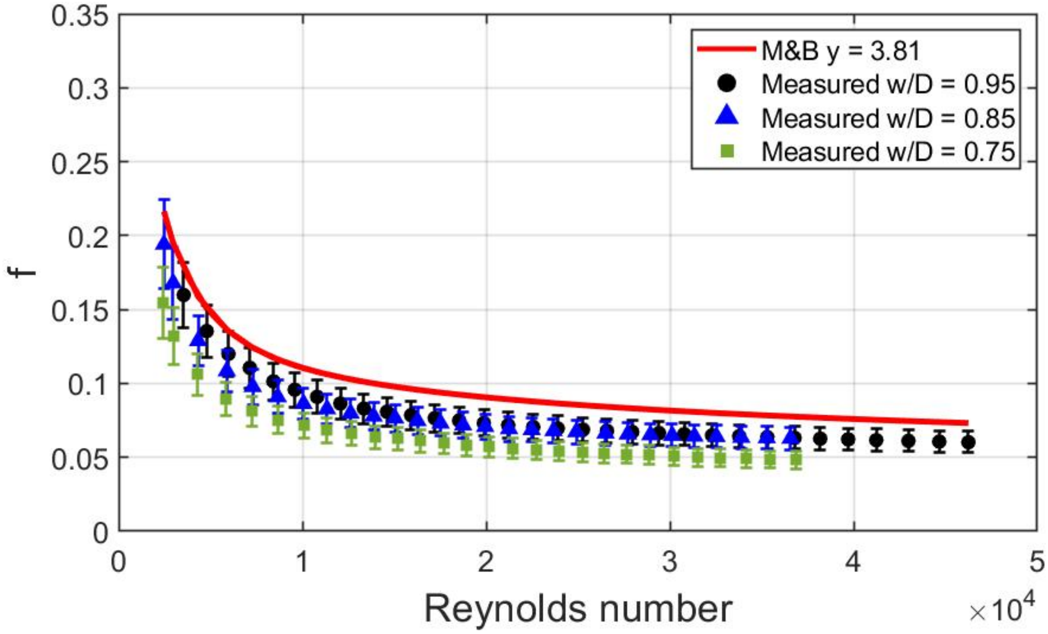

Figure 3.23: Friction factor versus Reynolds number of twisted tape inserts with y = 3.81 and varying widths, (w/D = 0.95, 0.85, and 0.75) with Manglik and Bergles' correlation [86, 87].

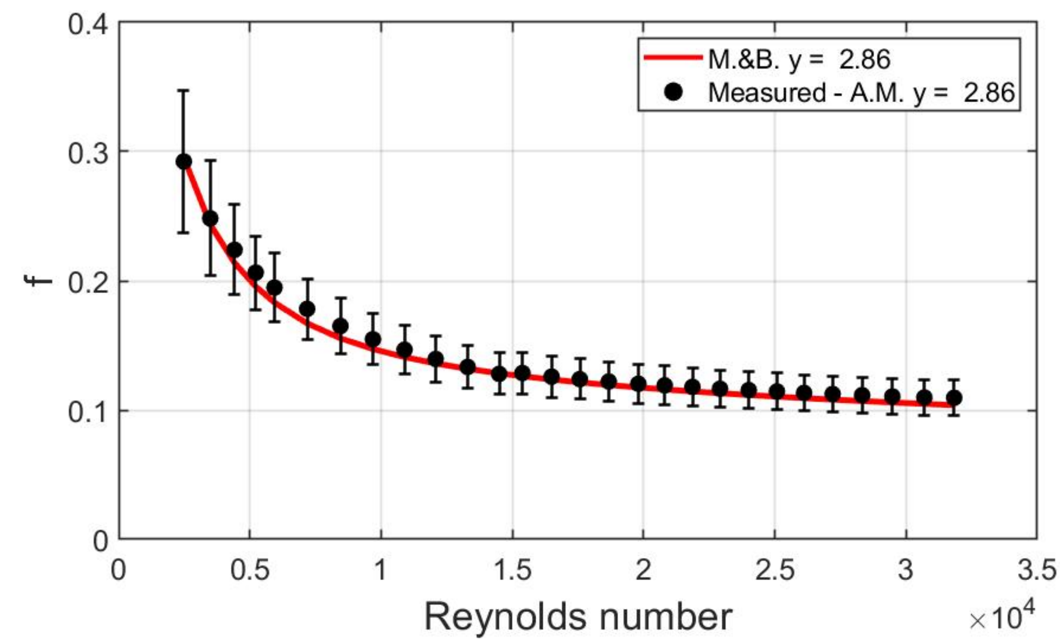

Figure 3.24: Friction factor versus Reynolds of the additively manufactured test section of pitch y = 2.86 with Manglik and Bergles' correlation [86, 87].

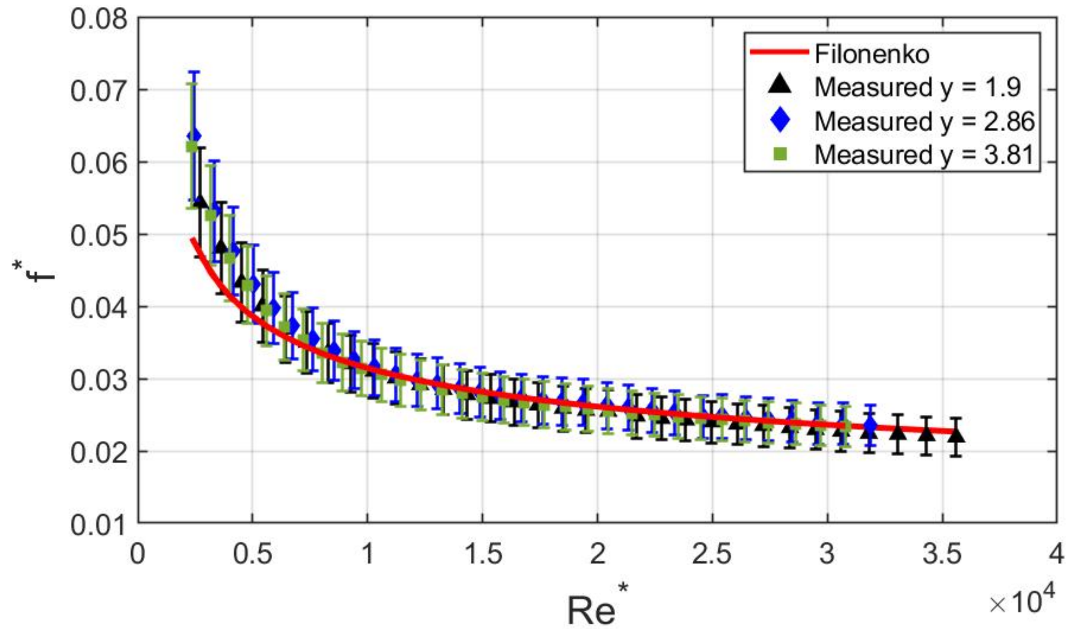

Figure 3.25: Friction factor versus Reynolds number using channel flow for the twisted tape inserts with w/D = 0.95 with friction factor correlation from Filonenko [105].

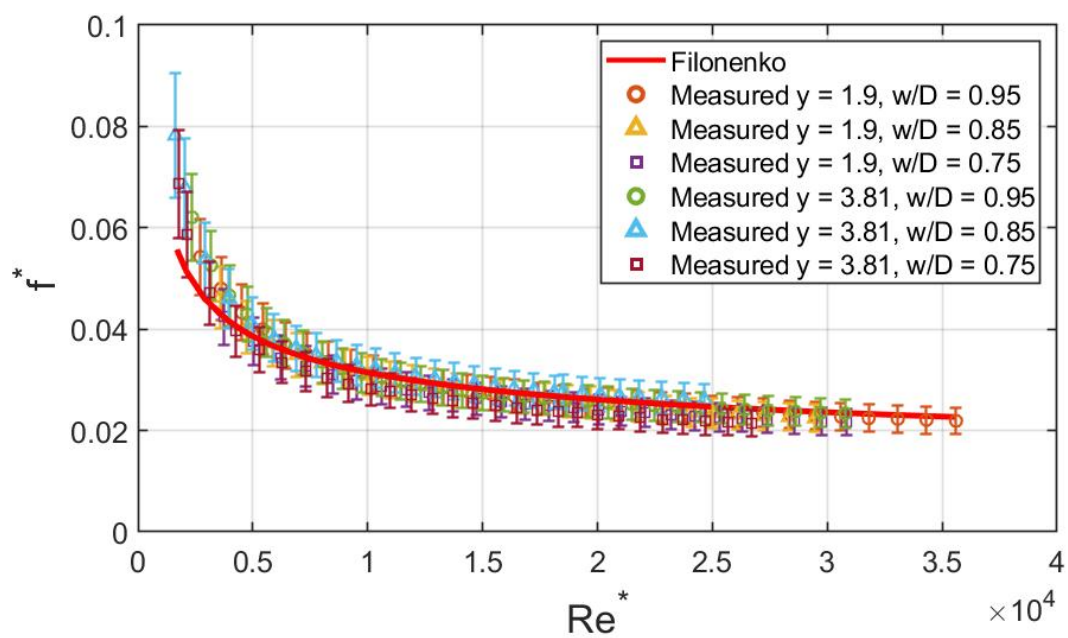

Figure 3.26: Friction factor versus Reynolds number using channel flow methodology for different widths, w, and pitch y. with Filonenko's correlation [105].

of the channel flow methodology, and further work should be performed to fully understand this phenomenon.

Wiggins et al [92] suggested a modification to Manglik and Bergles' laminar correlation [87] to account for the friction factor at low Reynolds numbers for the channel flow methodology. They used asymptotic matching [98] to combine the Manglik and Bergles correlation with the channel flow method. This improved the channel flow predictions at low Reynolds numbers, Re^*, but at tighter twisted tape pitches, in their case y =1.9, the new correlation overpredicted the experimental data. With the current experimental data, it is clear that the channel flow method collapses all friction factor data into a common form for loose-fitting twisted tape inserts, but it fails the capture the friction factor for tight-fitting twisted tapes. This led this work to focus instead on adding a loose-fitting factor to Manglik and Bergles' correlations [86, 87], refer to Section 3.3.4. Additionally, it is interesting to note that the channel flow friction factor does not increase with smaller pitches.

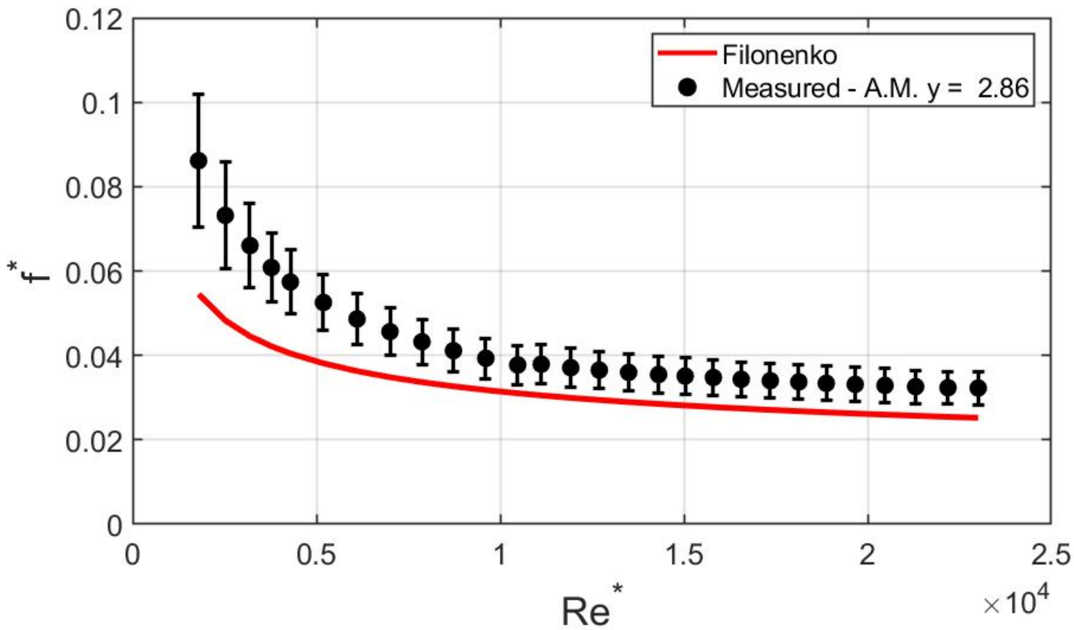

Figure 3.27: Friction factor versus Reynolds using channel flow method for the additively manufactured test section with Filonenko's correlation [105].

3.3.2 Heat Transfer

Heat transfer experimental data were obtained on three twisted tape insert geometries, y =1.9, 2.86, and 3.81 with widths of w/D = 0.95. Heat transfer experiments required various data sets to not only ensure the repeatability of the measured experimental data but also decrease the uncertainty in the measurements. For further discussion and derivation of the uncertainty in the heat transfer measurements please refer to Appendix C.3 and C.4.2. The heat transfer on the twisted tapes with smaller widths, w/D = 0.85 and 0.75, was left out for future work. In addition, for the heat transfer data in the additively manufactured twisted tape insert, further work has to be done to fully quantify the thermal conductivity of the resin. Collins et al [119] concluded that the lack of thermophysical properties data in 3D printed materials created a challenge in accurately predicting thermal performance when calculating heat transfer in 3D printed microchannels. Thus, this work does not include heat transfer for the additively manufactured test sections and future work should focus on accurately characterizing the important thermophysical properties of the resin used in heat transfer experiments, specifically the thermal conductivity. In addition, study the effects of printing direction with heat transfer.

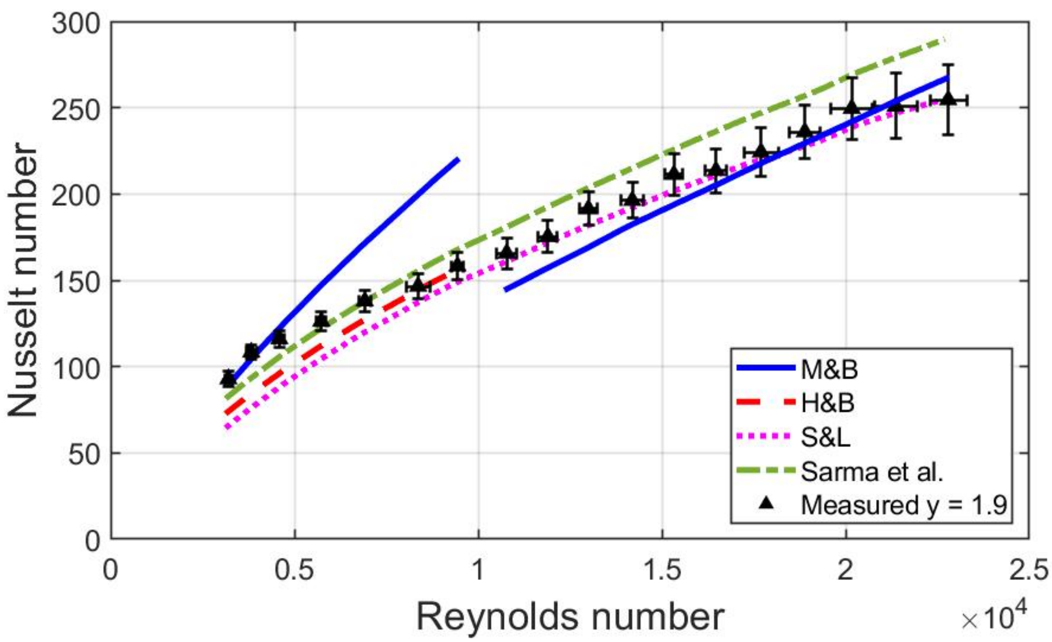

Figure 3.28: Nusselt number versus Reynolds number of measured twisted tape insert with pitch y = 1.9 with correlations from Manglik and Bergles (M&B) [86, 87], Hong and Bergles (H&B) [103], Smithberg and Landis (S&L) [93], and Sarma et al [97].

Figures 3.28 to 3.30 plot the measured Nusselt number for the different twisted tape inserts with four different correlations, Manglik and Bergles (M&B) [86, 87], Hong and Bergles (H&B) [103], Smithberg and Landis (S&L) [93], and Sarma et al [97]. The correlations from Manglik and Bergles' are plotted in their respective Reynolds number ranges, one laminar and one for transitional and turbulent regimes. One clear observation of the correlations from Manglik and Bergles consists of the discontinuity observed between the laminar and turbulent correlations, especially at the tighter pitches. This can be observed by the trend of the laminar Nusselt number correlation [87], as it tends to have a more pronounce upwards trend than the other correlations, more noticeable at tighter twisted tape pitches, y.

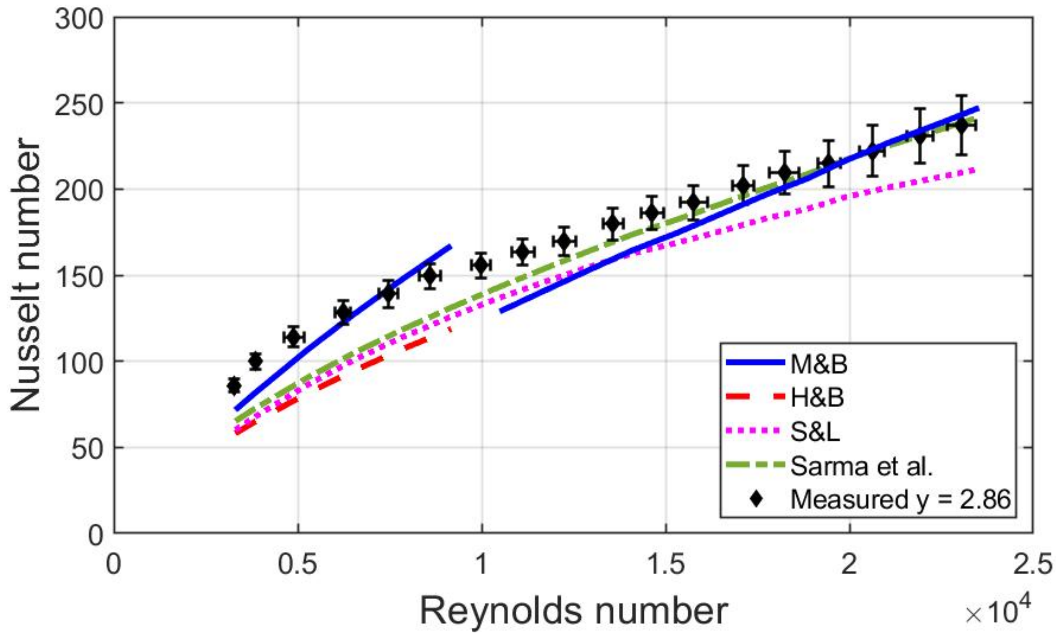

Figure 3.29: Nusselt number versus Reynolds number of measured twisted tape insert with pitch y = 2.86 with correlations from Manglik and Bergles (M&B) [86, 87], Hong and Bergles (H&B) [103], Smithberg and Landis (S&L) [93], and Sarma et al [97].

Manglik's thesis [73] explored the heat transfer dependence between loose-fitting and tight-fitting twisted tapes and showed no difference between the two heat transfer data. Manglik discusses how the heat transfer fin-effects of the twisted tape insert were mitigated by isolating the twisted tape from the heated walls to reduce conduction between the circular tube and the twisted tape. The current work with loose-fitting twisted tape inserts didn't properly isolate the twisted tapes from the circular thus some conduction is expected between the tube walls and the twisted tape insert, but the current methodology was not sensitive enough to measure those conduction effects. Low Reynolds numbers are expected to have more dominant conduction effects between the circular tubes and the twisted tape creating an additional fin effect, but this is not evident with the current experimental results. It is not clear why the Nusselt number data at low Reynolds numbers follow the trends from the other correlations. At the other pitches, y = 1.9 and 3.81, the data matches better with the selected correlations.

Hong and Bergles [103] obtained heat transfer data for twisted tape inserts using constant heat flux, similar to wall boundary conditions as this experimental data, but the correlations significantly underpredict the current experimental data. Smithberg and Landis [93] and Sarma et al [97] follow similar Nusselt number trends as the current experimental data. The Smithberg and Landis correlation [93] was accurate at the tighter pitch, y =1.9, it was accurate at the turbulent regime

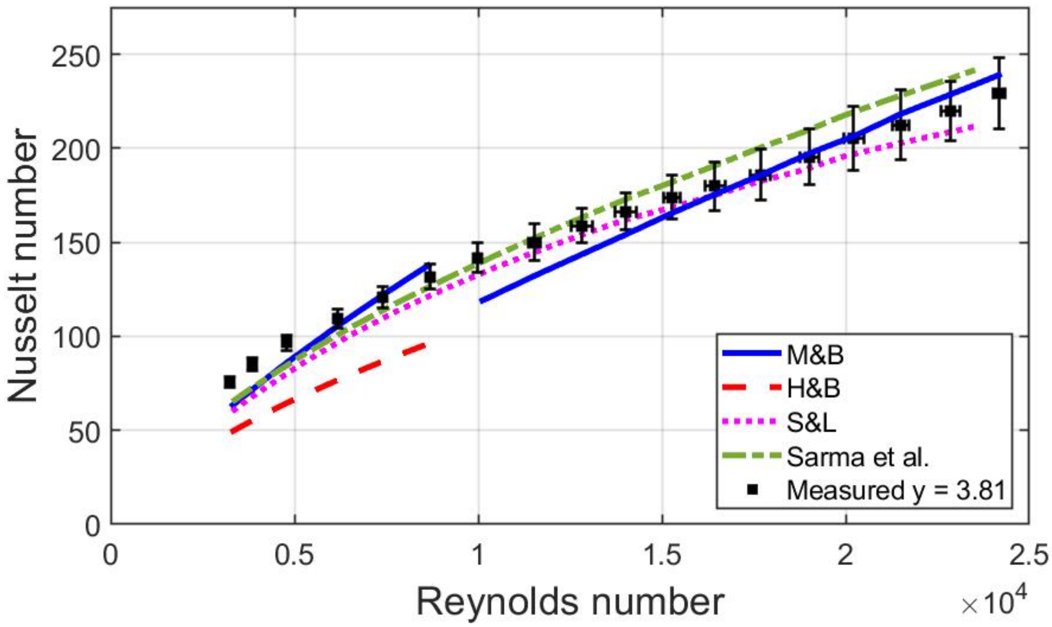

Figure 3.30: Nusselt number versus Reynolds number of measured twisted tape insert with pitch y = 3.81 with correlations from Manglik and Bergles (M&B) [86, 87], Hong and Bergles (H&B) [103], Smithberg and Landis (S&L) [93], and Sarma et al [97].

for a pitch of y =3.81, but it was consistently under-predicting for a pitch of y =2.86. The Nusselt number correlation from Sarma et al [97] has an interesting phenomenon for pitches of y = 1.8 and 3.81, in which it under-predicts the current experimental data at low Reynolds numbers and over-predicts at higher Reynolds numbers, but it is accurate in the transitional regime. While for the pitch of y = 2.86, it is accurate at higher Reynolds numbers while underpredicting the other regimes.

The channel flow correlation was also applied for heat transfer in the three twisted tape inserts, with data shown in Figure 3.31 with Dedov's derived correlation for channel flow heat transfer [99]. The Nusselt number experimental data collapses to a common form when transformed into a channel flow geometry. Similar to previous observations with friction factor at this twisted tape width, w/D = 0.95, the calculated Nusselt number matches well with the channel flow correlation for values of $Re^* > 10{,}000$, while at low Reynolds numbers the correlation under predicts the transformed Nusselt number data, Nu^*. In this transformed geometry, the transition between laminar to turbulent is better observed. Further work should be performed in understanding the channel flow behavior at the lower Reynolds numbers ($Re^* < 10,000$).

The channel flow Nusselt number correlation uses an experimentally derived coefficient in Equation 3.20. Dedov et al [99] and Varava et al [101] derived a C coefficient equal to 0.2 applicable to

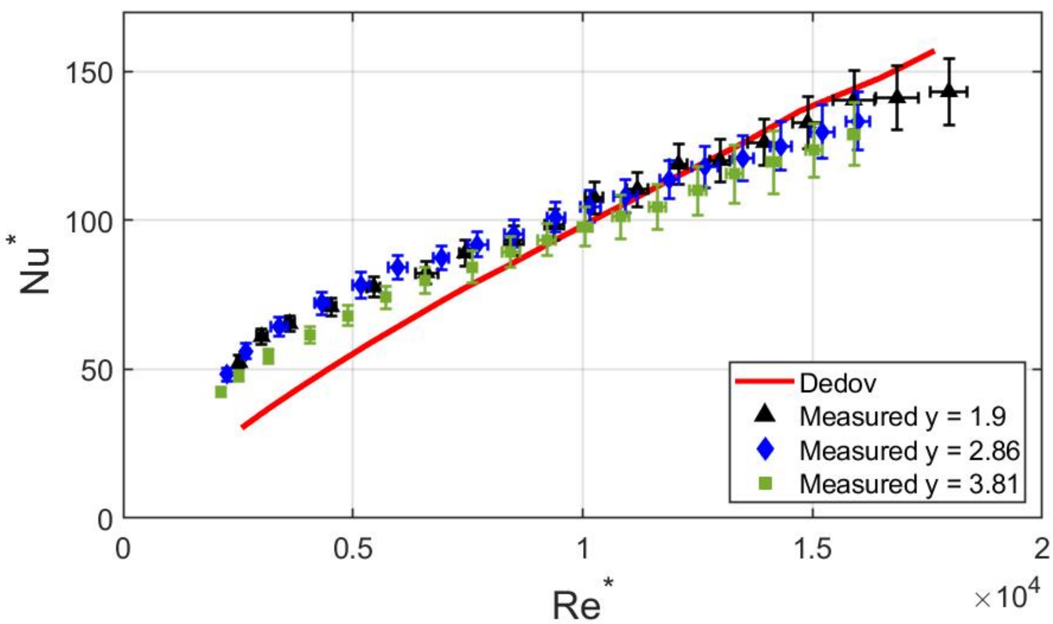

Figure 3.31: Nusselt number versus Reynolds number of channel flow methodology with Dedov's derived correlation [99].

turbulent flows and was used in all Reynolds numbers in Figure 3.31. However, the channel flow Nusselt number underpredicts the measured channel flow Nusselt number for all three twisted tape insert geometries. As the Reynolds number decreases, the heat transfer effects due to the centrifugal force in the twisted tape insert are expected to dominate when compared to the forced convection heat transfer. However, in the laminar regime, Varava et al [100] reported a higher C coefficient of $C = 0.47$, indicating some variability of this weighting coefficient with Reynolds number. Due to this, the C coefficient was adjusted to $C = 0.6$ for the laminar regime, as shown in Figure 3.32 to better match the channel flow Nusselt number for $Re^* < 10{,}000$. This updated C coefficient for the centrifugal convection term better matches the experimental data for Reynolds numbers up to $Re^* \approx$ 7,000. This further implies that the centrifugal force in the lower Reynolds number has a stronger presence than in the turbulent regime. The transition that occurs between the lower Reynolds numbers and the turbulent regime, in which the forced convection term dominates, requires further studies and better understanding. This in order to group both channel flow correlations to a common form to encompass the different Reynolds numbers.

3.3.3 Thermal Performance

Thermal performance factor, η, was calculated for three twisted tape insert geometries, $y = 1.91$, 2.86, and 3.81 with a width of $w/D = 0.95$ utilizing Equation 3.23. The thermal performance factor plots were divided into their respective fluids, with water shown in Figure 3.33 and air in Figure 3.34

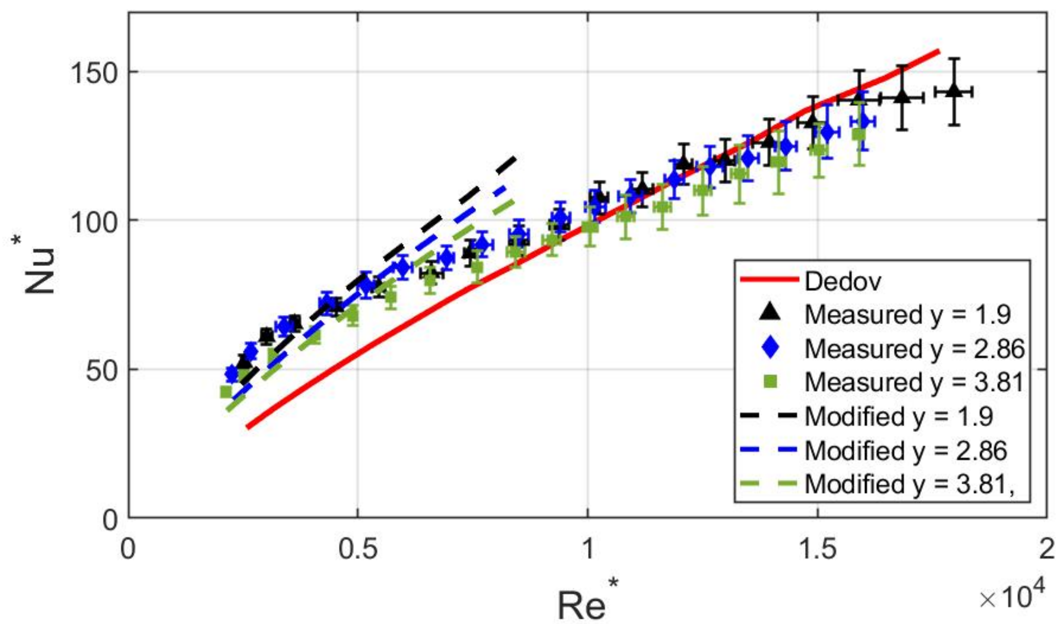

Figure 3.32: Nusselt number versus Reynolds number of channel flow methodology with Dedov's derived correlation [99] with modified C coefficient at lower Reynolds numbers.

with data from the literature summarized in Table 3.3. The thermal performance factor calculated for y = 1.9 matches well with Murugesan's data [108] for y = 2, but the data are more dissimilar at larger pitches. In addition, the phenomena observed in the current measured data in which at lower Reynolds numbers the thermal performance factor is higher than at high Reynolds numbers is not observed in Murugesan's data. The dependence on the Reynolds number is not as clear in Murugesan's data, but their thermal performance factor is more dependent on the twisted tape pitch. As with smaller pitches, the thermal performance factor increases. The current uncertainty in the thermal performance factor, in Figure 3.33, does not show the dependence of the thermal performance from the twisted tape pitch. Due to how uncertainty is propagated between values to calculate the thermal performance factor uncertainty, refer to Appendix C.4.3, the uncertainty is more or less constant throughout the different Reynolds numbers, or at least it seems to be constant.

At higher Reynolds number (Re > 10,000), the thermal performance factor is only slightly higher than 1 for current data and Murugesan's data [108], indicating a small enhancement over the smooth pipe case when using water as a working fluid. Figure 3.34 shows the thermal performance factor when air is a working fluid, and the majority of the thermal performance factor is slightly below 1. The exception is Naga Sarada's data for thermal performance factor in air. The remaining data indicate an overall decrease in thermal performance ($\eta < 1$), for Re > 15,000 for all cases. This may imply a negative benefit of using twisted tape inserts for fluids with low Prandtl numbers, but

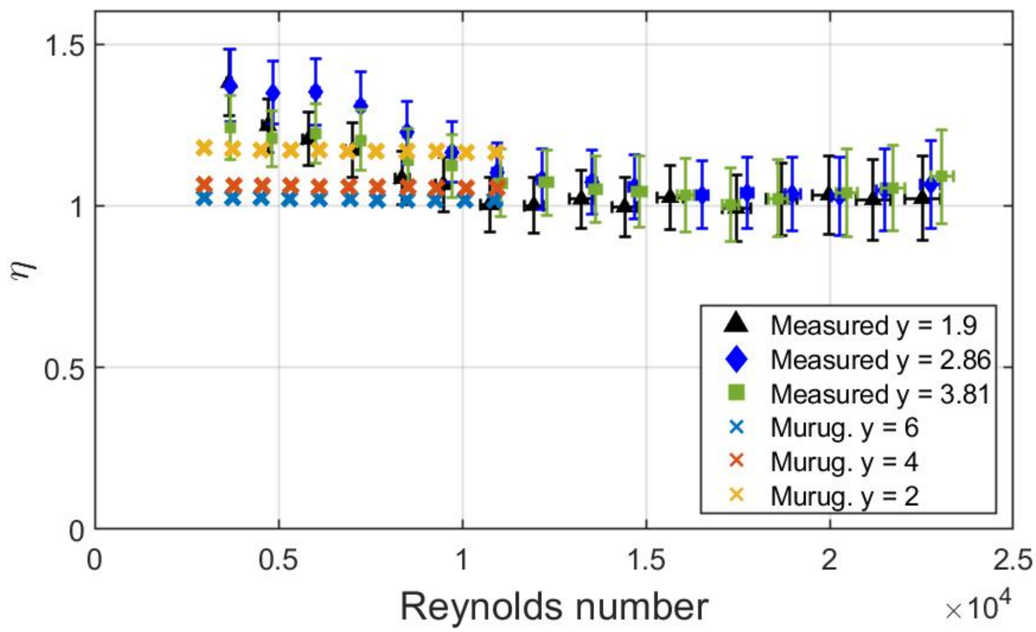

Figure 3.33: Measured thermal performance factor versus Reynolds number of twisted tape inserts with Murugesan (Murug.) data [108] obtained with water as a working fluid.

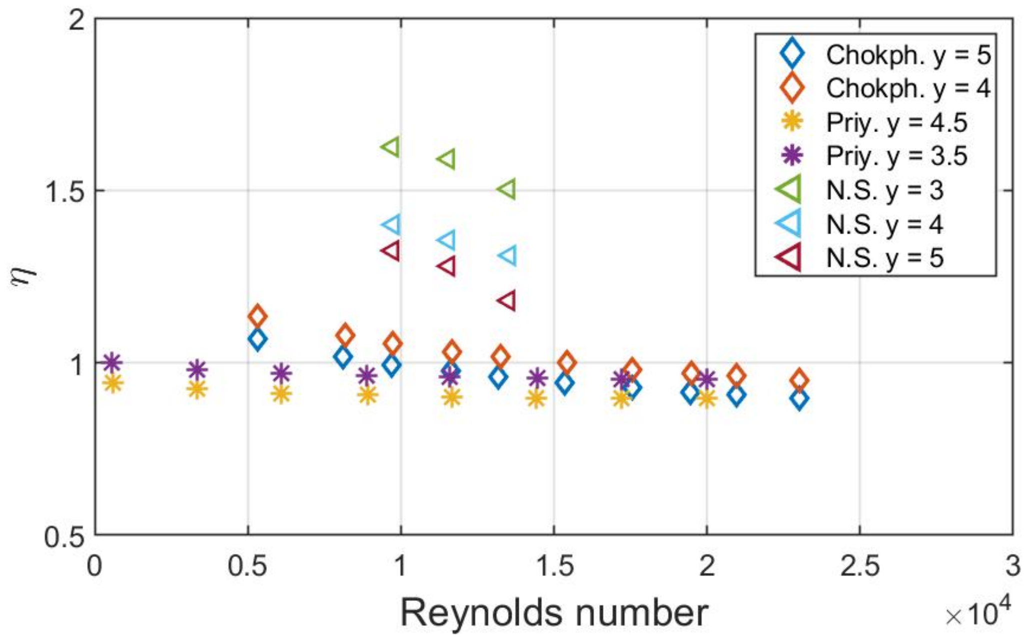

Figure 3.34: Thermal Performance factor versus Reynolds number of twisted tape inserts obtained using air as working fluid from Chokphoemphun et al (Chokph.) [109], Priyarungrod et al (Piry.) [110], and Naga Sarada et al (N.S.) [111].

a benefit when using high Prandtl number fluids, such as molten salts. Further work is required to fully quantify and understand the thermal performance factor for twisted tape inserts at higher Prandtl numbers.

3.3.4 Derivation of friction factor correlation factor

A great deal of effort has been carried out in deriving correlations for friction factor and Nusselt number of twisted tape inserts. Manglik and Bergles [86, 87] derived the most widely used correlations for friction factor and Nusselt number of twisted tape inserts. Section 3.3.1 shows how their correlations over predict the friction factor of loose-fitting twisted tape inserts, (i.e. when $w \neq D$). This section discusses the derivation of a "loose-fitting" factor that can be added to the Manglik and Bergles correlations in the form of:

$$f = f_{M.B.} \cdot \phi, \tag{3.32}$$

where $f_{M.B.}$ is the asymptotically matched correlation from Equation 3.10 and ϕ is the adjusted factor to account for loose-fitting twisted tape inserts.

A previous attempt was performed to change two components in Manglik and Bergles' correlations:

$$(\frac{\pi}{\pi - 4\delta/D})^m \tag{3.33}$$

and

$$(\frac{\pi + 2 - 2\delta/D}{\pi - 4\delta/D})^n, \tag{3.34}$$

where m and n are exponents of different values.

These factors appear in various correlations found in the literature for friction factor and heat transfer starting as early as 1961 with Ibragimov et al [120], with most of the correlations derived afterward consisting of varying the exponents m and n to match individual experimental data. For a full list of friction factor correlations with these components and different coefficients refer to [73], with eleven of thirteen friction factor correlations changing the exponents m and n according to their current results.

These factors can be derived by relating the overall area of the pipe and the actual cross-sectional area of the pipe as well as the hydraulic diameter nondimensionalized by the diameter of the pipe. Accounting for loose-fitting twisted tape inserts the new factors obtained were:

$$(\frac{\pi \cdot D^2}{\pi \cdot D^2 - 4\delta \cdot w})^m, \tag{3.35}$$

and

$$(\frac{D(\pi \cdot D + 2w - 2\delta)}{\pi \cdot D^2 - 4\delta w})^n, \tag{3.36}$$

with efforts focused in varying the m and n components to match experimental data with different pitches, y, and widths, w. While preliminary work using this methodology showed initial success, due to the fear of simply creating another correlation that is not applicable to all the parameters of the twisted tape insert, the author decided to try a different route and focus on the ϕ component in Equation 3.32.

This was done as a method in which, if the twisted tape insert consisted of a tight-fitting twisted tape insert, the correlations derived by Manglik and Bergles would be applicable to the current experimetnal data, as shown in Figure 3.24 with the tight-fitting twisted tape results. And in the case in which the twisted tape insert consisted of a loose-fitting twisted tape insert, the user would simply need to multiply the results by a loose-fitting twisted tape factor.

After different derivations and trial and error, the following ϕ factor was chosen:

$$\phi = (\frac{\pi - 4\delta w/D}{D_h})^{n - D_h/D}. \tag{3.37}$$

The derivation follows a similar pattern to the efforts done previously in using the actual cross-sectional area normalized by the hydraulic diameter instead of the pipe's inner diameter.

The n component was then varied and the Norm, defined as the length or distance between vectors, versus the experimental data, was used to calculate the best n value to fit the loose-fitting data. Figure 3.35 plots the norm of the difference between the adjusted Manglik and Bergles correlations and the experimental data summarized in Section 3.3.1.

From Figure 3.35 one can observe how the norms calculated behave in a similar pattern and have a minimum close to 0.5. Figures 3.36 to 3.38 plot the Manglik and Bergles correlation with the loose-fitting factor, ϕ, with an exponent $n = 0.5$, showing good agreement with current experimental data for loose-fitting twisted tape inserts for different pitches and widths.

The adjusted correlation performs best for the pitch of y = 2.86, Figure 3.37, as it matches all Reynolds numbers. While for a pitch of y =1.9, the tightest pitch is shown in Figure 3.36, the adjusted correlation matches well at high Reynolds numbers ($Re > 10,000$) while at the laminar

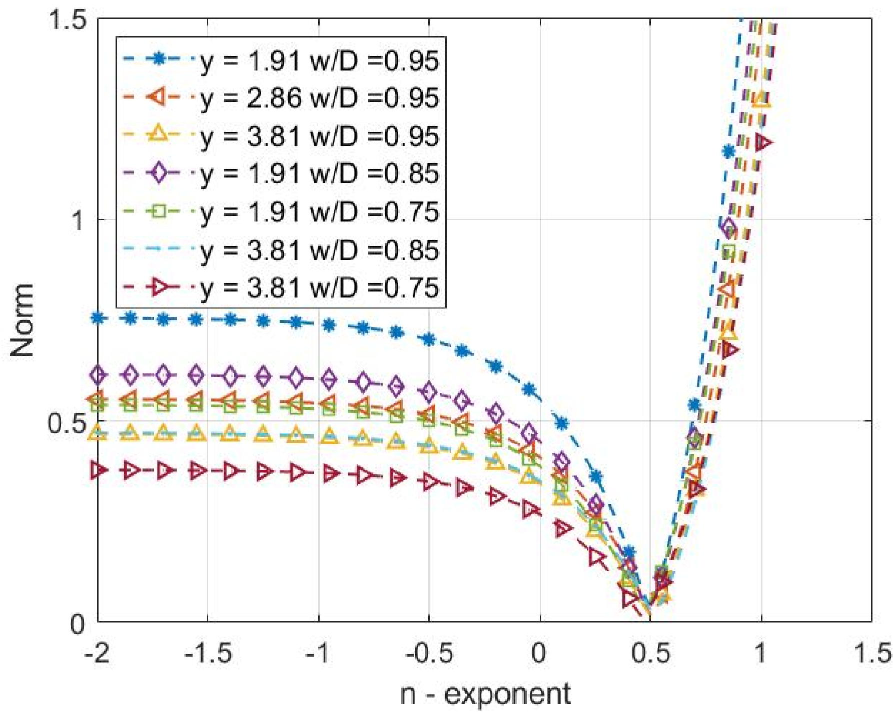

Figure 3.35: Norm versus exponent studied to add a width component to Manglik and Bergles correlations [86, 87].

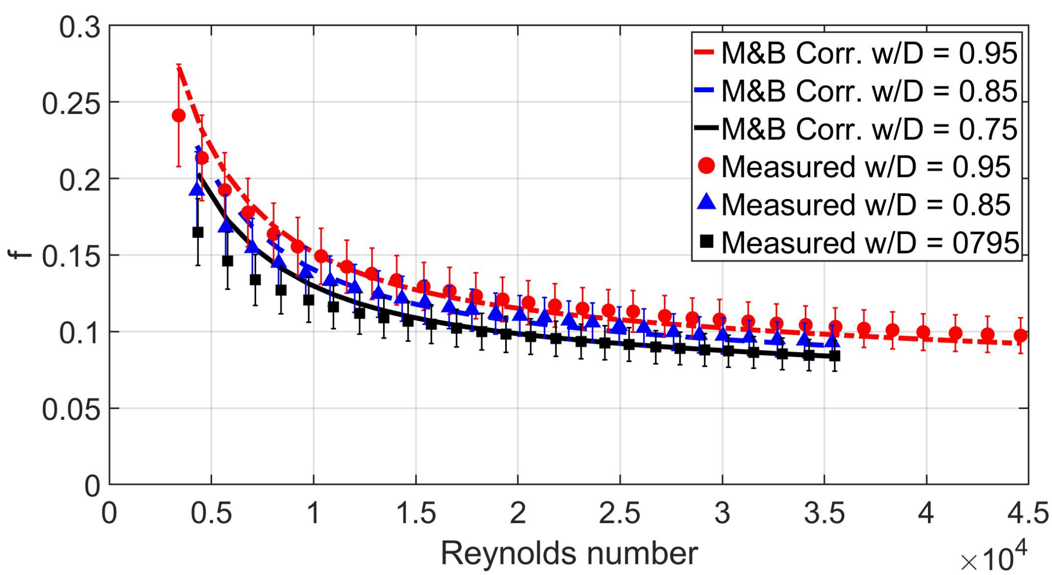

Figure 3.36: Friction factor versus Reynolds number of twisted tape inserts with pitch $y = 1.9$ with adjusted Manglik and Bergles correlation [86, 87] using ϕ in Equation 3.37 and $n = 0.5$.

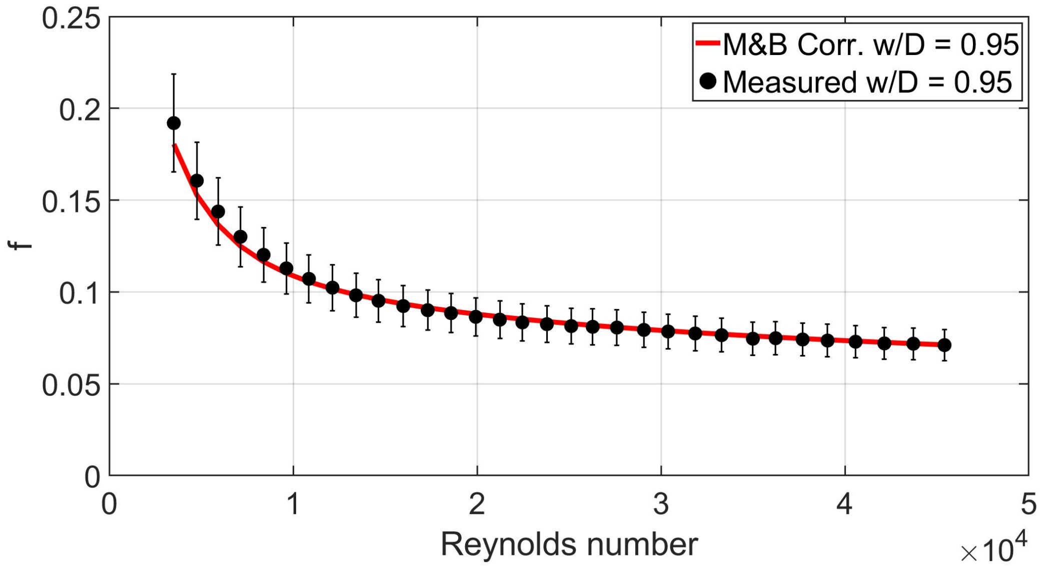

Figure 3.37: Friction factor versus Reynolds number of twisted tape inserts with pitch $y = 2.86$ with adjusted Manglik and Bergles correlation [86, 87] using ϕ in Equation 3.37 and $n = 0.5$.

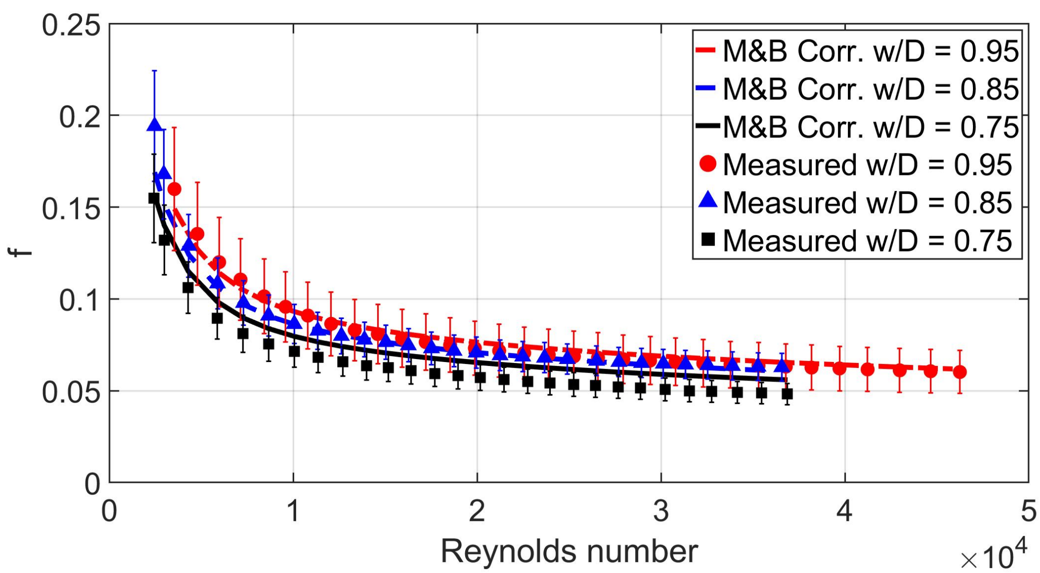

Figure 3.38: Friction factor versus Reynolds number of twisted tape inserts with pitch $y = 3.81$ with adjusted Manglik and Bergles correlation [86, 87] using ϕ in Equation 3.37 and $n = 0.5$.

region, it slightly overpredicts the data within the uncertainty of the experimental data. Finally, for the pitch of $y = 3.81$, Figure 3.38, the data matches well with all Reynolds numbers for the widths of $w/D = 0.95$ and 0.85, but it consistently overpredicts the smallest width of $w/D = 0.75$, but, again, within the uncertainty of the experimental data.

3.4 Conclusion and Discussion

Friction factor, Nusselt number, and thermal performance data were collected and analyzed for a variety of twisted tape insert geometries of interest. Friction factor data were obtained for eight different twisted tape geometries, with one built using additive manufacturing technologies (refer to Appendix D). The geometries consisted of twisted tape widths of w/D = 0.95, 0.85, and 0.75 for twisted tape pitches of y = 1.9 and 3.81, as well as a pitch of y =2.86 for widths of w/D = 1.0 and 0.95. The friction factor correlation from Manglik and Bergles [86, 87] predicted well the friction factor for the tight fitting twisted tape insert, the additively manufactured twisted tape insert of y = 2.86 and w/D = 1.0, but it over predicted the rest of the twisted tape insert's friction factor. The friction factor was also observed to depend on the width of the twisted tape insert, w, something not accounted for in the correlation. It was observed that with decreasing width, the friction factor also decreased, which agrees with less surface contact with the fluid causes less drag and thus less pressure loss. In general, the selected correlations also failed to consistently predict the friction factor of the twisted tape inserts. The other experimentally-derived correlation, Lopina and Bergles [102], matched well with the turbulent friction factor of a pitch of y = 1.9, but the small dependence on twisted tape pitch was observed as the rest of the predictions didn't match the experimental data. The analytically-derived correlations from Smithberg and Landis [93] and Sarma et al [95–97] consistently underpredicted the friction factor data. It was theorized that the low prediction might have been caused by the misunderstanding in the twisted tape parameter definitions, but the heat transfer data showed relatively good agreement with the correlations thus this theory was scrapped. There is an overwhelming amount of discrepancies between the literature on how to define different twisted tape parameters, thus some confusion can be made when defining and calculating some of these phenomena.

The channel flow methodology [99–101] was also used to predict the transformed friction factor, f^*, for twisted tape inserts. Good agreement was observed with the loose-fitting twisted tape insert's friction factor data and Filonenko's correlation [105] at high Reynolds numbers ($Re^* > 10,000$). While at low Reynolds numbers, the correlation underpredicted the transformed experimental data. In general, it was observed that the loose-fitting twisted tape transformed friction factor was collapsing to a common form. Unfortunately, the tight-fitting twisted tape insert manufactured using additive manufacturing failed to collapse to the same common form. The methodology was adjusted to account for the same width-to-diameter ratio, w/D = 1.0, but Filonenko's correlation underpredicted the entirety of the data set. Further work on the roughness of the additively manufactured test sections should be done to account for the surface roughness in the channel flow methodology for this tight-fitting twisted tape insert.

Previous work by Wiggins et al [92] explored the possibility of adjusting Manglik and Bergles' laminar correlation [87] to better predict the laminar friction factor using the channel flow methodology. This work focused on exploring a different route, in which a factor (ϕ) was added to the Manglik and Bergles' laminar and turbulent correlations [86, 87] to be better applicable to loose-fitting twisted tape inserts. Good agreement was observed, within the experimental uncertainty, when the new factor was applied to the Manglik and Bergles correlations.

Nusselt number data was collected for twisted tapes of pitch $y = 1.9$, 2.86, and 3.81, across Reynolds numbers of 3,000 to 24,000. The experimental data were compared to leading Nusselt number correlations to assess the performance of each prediction at laminar to turbulent Reynolds numbers at varying pitches. While the correlations from Manglik and Bergles [86, 87] were obtained using tight-fitting twisted tape inserts, it was found that their correlations were applicable to the current loose-fitting twisted tape inserts for twisted tape pitches similar to those in which their experimental correlations were derived from. This can be attributed to how Manglik and Bergles performed their experiments by eliminating conduction from the pipes into the twisted tape insert and minimizing heat transfer fin effects. This methodology of twisted tape insert installation also explains why their friction factor correlation overpredicts the loose-fitting twisted tape insert data. While the width of the twisted tapes Manglik and Bergles used is not a tight-fitting twisted tape ($w < D$), it behaves as one due to the addition of the multiple buffers between the twisted tape and the circular pipe. The current work allowed for some heat transfer fin effects as the twisted tape insert was not isolated from the walls and some conduction was allowed to happen between the twisted tape and the walls. Unfortunately, the current methodology was not sensitive enough to measure the heat transfer fin effects that Manglik and Bergles were avoiding. The fin effects are more dominant at lower Reynolds numbers, as the large temperature gradients allow for higher heat transfer through conduction between the walls of the pipe and the twisted tape insert, but more measurements are required to better understand this phenomenon. In addition, the current experimental methodology is not sensitive enough to measure those conduction effects. This could provide reasoning for some laminar experimental predictions of the Nusselt number to be higher than the correlations. Although the Nusselt number correlations are lower in comparison with the experimental data only for the pitches of $y = 2.86$ and 3.81 at the low Reynolds numbers, the discrepancy cannot be solely attributed to these fin effects. In addition, Manglik showed no perceptible difference when measuring heat transfer between loose-fitting and tight-fitting twisted tape inserts [73]. In addition, for the twisted tape pitch outside of their geometric bounds of applicability ($y < 3$), the laminar correlation over predicting the current data, while the turbulent regime matched with current data. The correlation from Hong and Bergles [103] was explored as it used similar boundary conditions, specifically in the laminar regime, though it did not predict the current experimental work. The analytical correlations of Smithberg and Landis [93] and Sarma et al [95–97] predicted the Nusselt number trend in which no discontinuity was observed as the twisted tape inserts transitioned from their laminar to the turbulent regime, but agreement with current experimental data varied through the different pitches.

The channel flow transformation [99–101] proved to be a good tool to predict turbulent Nusselt number, Nu^*, for loose-fitting twisted tape inserts. The channel flow methodology collapsed the experimental data to a common form independent of twisted tape pitch, as it used the hydraulic diameter and adjusted Reynolds number, Re^* to describe and relate the data. When transformed to channel flow, experimental data matched well with Dedov's Nusselt number correlation [99] at $Re^* > 10,000$. For the lower Reynolds number, an adjustment to the centrifugal convection term in the channel flow methodology was provided. The C coefficient used by Dedov et al [99] and Varava et al [101] was obtained from the experimental results in the turbulent regime. Varava et al [100] reported a higher C coefficient at lower Reynolds numbers to better match their experimental results. This work adjusted the C coefficient to match current experimental data for $Re^* < 8{,}000$. This can lead to prior knowledge in channel flow being applicable to the twisted tape insert geometry, such as studies, data, and predictions for fouling and surface roughness.

Thermal performance factor, η, was calculated for the same three geometries and Reynolds numbers of Nusselt number experimental data. Twisted tape inserts proved to improve heat transfer across all Reynolds numbers when in comparison with a circular pipe geometry. Although, an increase of thermal performance ($\eta > 1.0$) was only observed for low Reynolds numbers ($Re < 10,000$). In addition, a dependence of working fluid was observed for thermal performance prediction. In which for higher Prandtl number fluids, an increase of thermal performance was observed implying the benefits of using twisted tape inserts for high Prandtl number fluids (i.e. molten salts). Further work should be done to better understand and quantify this Prandtl number dependence, in particular for molten salt applications.

Additionally, the ambiguous transition between laminar and turbulent Reynolds numbers has been an ongoing work and discussion throughout the literature. The channel flow transformation, and the collapse of experimental data in both friction factor and Nusselt number, leads to the conclusion of a critical Reynolds number not defined in circular pipe parameters, but defined by incorporating the entire parameters of the twisted tape inserts. Thus, a critical turbulent Reynolds number is defined in this work as $Re^*_{cr} = 10,000$ for twisted tape inserts. Though the offset from the laminar regime is not clear from the current work, the channel flow methodology could provide further insight in the fluid flow regimes to better determine and characterize those values.

Chapter 4

FLUID FLOW IN TWISTED TAPE INSERTS - POSITRON EMISSION PARTICLE TRACKING

The further understanding of fluid flow in complex engineering heat transfer geometries can contribute to their improved design and further optimization. With the advancements in computational power, computational fluid dynamics (CFD) has emerged as a valuable tool for studying and analyzing flow structures in these complex geometries by numerically solving the Navier-Stokes equations. Direct numerical simulations (DNS) involve solving a discretized version of the Navier-Stokes equations, but they can be computationally demanding as they require resolving all the fluid flow scales, both spatial and temporal. Consequently, DNS can become computationally expensive. To mitigate this computational cost, various turbulence modeling techniques that filter fluid flow phenomena have been developed, but they necessitate rigorous validation, typically through experimental data.

There are various techniques and instrumentation used to obtain experimental fluid flow data for proper computational validation. These range in complexity from a hot wire probe [121] to a combination of lasers and cameras [122]. Complications arise when the region of interest has a complex geometry or access window, the flow is opaque, or the measuring technique causes fluid flow alterations as it's interrogating the flow. There are other methods of fluid flow measuring techniques that do not need direct optical access and are non-intrusive, which consist of ultrasonics [123], magnetic resonance [124], gamma ray tomography [125], radiography [126], or positron emission particle tracking (PEPT) [127]. PEPT interrogates the flow velocity by tracking radiolabelled fluid tracers through the detection of two coincident 511 keV gamma rays. Making it ideal for complex geometries or opaque fluids as the gamma rays penetrate through the geometry. PEPT is explored in this work as a method to calculate the velocity fields in twisted tape inserts.

Flow regimes within the twisted tape insert geometry have been theorized and found in literature, in which the fluid flow is affected by different dominant flow phenomena. Manglik and Bergles [86, 87] described four different flow regimes of the twisted tape insert, in which different flow phenomena are dominant. These regions consist of a viscous flow, swirl flow, swirl-turbulent transition, and turbulent swirl flow. In the viscous flow regime, the inertial and viscous forces are balanced creating a longer effective flow path. In the second region, swirl flow, the addition of the convective inertia force is balanced with the centrifugal and viscous forces. In the swirl-turbulent transition region, turbulent fluctuations are forming, but the centrifugal forces suppress the fluctuations further. In the fourth region, the turbulent swirl flow, the main forces consist of fluctuating velocities and centrifugal forces. This last region is characterized by swirl-induced vortex mixing.

There has been little work done to further understand and quantify these regions. Experimental fluid flow studies of twisted tape inserts are not as common in literature, with only a handful of papers found. The complex geometry affects the visual access for most visual flow measuring techniques. The first reported velocity data were obtained by Smithberg and Landis [93]. Smithberg and Landis obtained axial velocity at the exit of the twisted tape insert's geometry using static and impulse probes in the air. They characterize the flow in two regions, a twisting boundary layer flow and a helicoidal core flow modified by secondary circulation effects [93]. Smithberg and Landis [93] define a "vortex mixing" in which both regions are constantly being mixed through a vortex pattern which causes an increase in friction factor and pressure drop. Seymour [128] observed the secondary flows created by the twisted tape insert using radioactive gas tracing. Backshall and Landis [129] studied the boundary layer of the twisted tape insert and observed that the total velocity follows the universal logarithmic velocity profile. Cazan and Aidun [130] used Laser Doppler Velocimetry to study the flow in a twisted tape insert by varying the twisted tape pitch and Reynolds number. Cazan and Aidun were focused on studying the swirl flow induced after a short twisted tape insert, with the twisted tape consisting of only one pitch in length. They were mainly focused on the swirl flow effects in the freestream flow caused by the twisted tape insert, and not necessarily in the flow inside the twisted tape insert but in the downstream flow. In more recent work, Wiggins et al [131] used PEPT to study the fluid flow 20 diameters downstream of the entrance of the twisted tape insert and they observed that the flow was not fully developed. Wiggins reported axial and radial velocities at 20 and 30 diameters. The turbulent kinetic energy was measured from the average and instantaneous velocities from PEPT with noticeable regions of high and low turbulent kinetic energy. PEPT was capable of detecting the secondary flows previously predicted in experiments, with one additional secondary swirl observed in one channel of the twisted tape insert.

As can be concluded from the limited fluid flow experimental data in twisted tape inserts, obtaining velocity profiles in these geometries is complicated and complex with most experimental efforts focused in flow studies after the twisted tape insert. Other efforts to obtain velocity structures in twisted tape inserts consist of computational simulations, or computation fluid dynamics (CFD) simulations. Though Clark [74] concludes that the majority of the efforts done through CFD are specifically focused on thermal hydraulic design, i.e. determining the friction factor and Nusselt number. In addition, most of the CFD work consists of using various turbulence models that require further experimental validation and there is a lack of agreement between which turbulence model to use for the simulations. Though this is beyond the scope of the current work, the data gathered should help provide insight into appropriate turbulence model selection and further CFD validation. Furthermore, Clark et al [74, 85] identified secondary flow structures that arise with the usage of the twisted tape inserts that can lead to local hot spots in the material. Secondary flows were further confirmed by Wiggins et al [131, 132] using PEPT. These secondary flows resulted in local lower heat transfer at the wall with higher surface temperatures.

This work focused on obtaining fluid flow data using PEPT at three different Reynolds numbers, Re = 4,000, 8,000, and 17,700 for three different twisted tape geometries to further explore and understand the different flow regions in twisted tape inserts. The Reynolds numbers were defined as the circular pipe Reynolds numbers, Equation 3.3. Three different twisted tape geometries were studied, the additively manufactured twisted tape insert of width w/D = 1.0, and two traditionally manufactured twisted tape inserts with width of w/D = 0.95 and 0.85. Velocity contours of the different twisted tape inserts were obtained to study the effects of the twisted tape width on the velocity behavior. Azimuthally averaged velocity profiles were obtained which averaged the velocity in both θ and z dimensions. Velocity plots at three different angles were obtained to further interrogate the flow and observe the influence of the twisted tape width on the velocities. Finally, the vorticity and Reynolds stresses were obtained for the additively manufactured twisted tape insert to further interrogate the flow. The vorticity allowed for the location of helical vortices previously described in the literature and the identification of high vorticity regions near the twisted tape insert. The turbulent kinetic energy was found to be higher near the walls of the circular pipe and the twisted tape insert.

4.1 PEPT

Positron Emission Particle Tracking (PEPT) was initially postulated by Shaw in 1984 in a U.S. Patent to study blood flow around the heart [133]. While little work has been done on this specific application of PEPT, PEPT has been used extensively in studying flows in engineering applications, specifically those that are too complex or opaque for other fluid flow measuring techniques.

PEPT works by the detection of two coincident 511 keV gamma rays. The detection is made by an array of detectors housed in a positron emission tomography (PET) scanner. The collection of the coincident gamma ray's detection at a given time step can be used to create coincident lines. Coincident lines are created based on the detection of gamma rays by the PET scanner as lines connecting the location of detection. Coincident lines are grouped near the location of the tracer and are used to determine the location of the tracer. The radiotracer consists of a macroscopic particle coated through activation by a radioactive isotope, in this case, Fluorine-18 (^{18}F), which decays through positron emission. The positron travels through the medium before interacting with an electron, thus annihilating themselves and creating two back-to-back coincident gamma rays that are detected by the PET scanner. The detections are collected together to find the location of the radiotracer. This procedure is illustrated in Figure 4.1. Due to its uniqueness, complexity, and novelty, a great deal of effort has been done to develop reconstruction methodologies of the raw PET data. Six methodologies have been found in literature, the Birmingham method [127], the Cape Town method [134], the Bergen method [135], the G-means method [136], the Spatiatemporal B-spline reconstruction method [137], the feature point identification method [138], and a machine learning clustering method [139]. Windows-Yule et al [140] recently compared the leading PEPT reconstruction methodologies without a clear finding of which reconstruction method was the "best." Each reconstruction algorithm proved to be efficient at specific tasks and depending on the application, different algorithms were recommended. This work used the feature point identification method (FPI), as a large number of particles were tracked, and it has been used previously in twisted tape geometries [131].

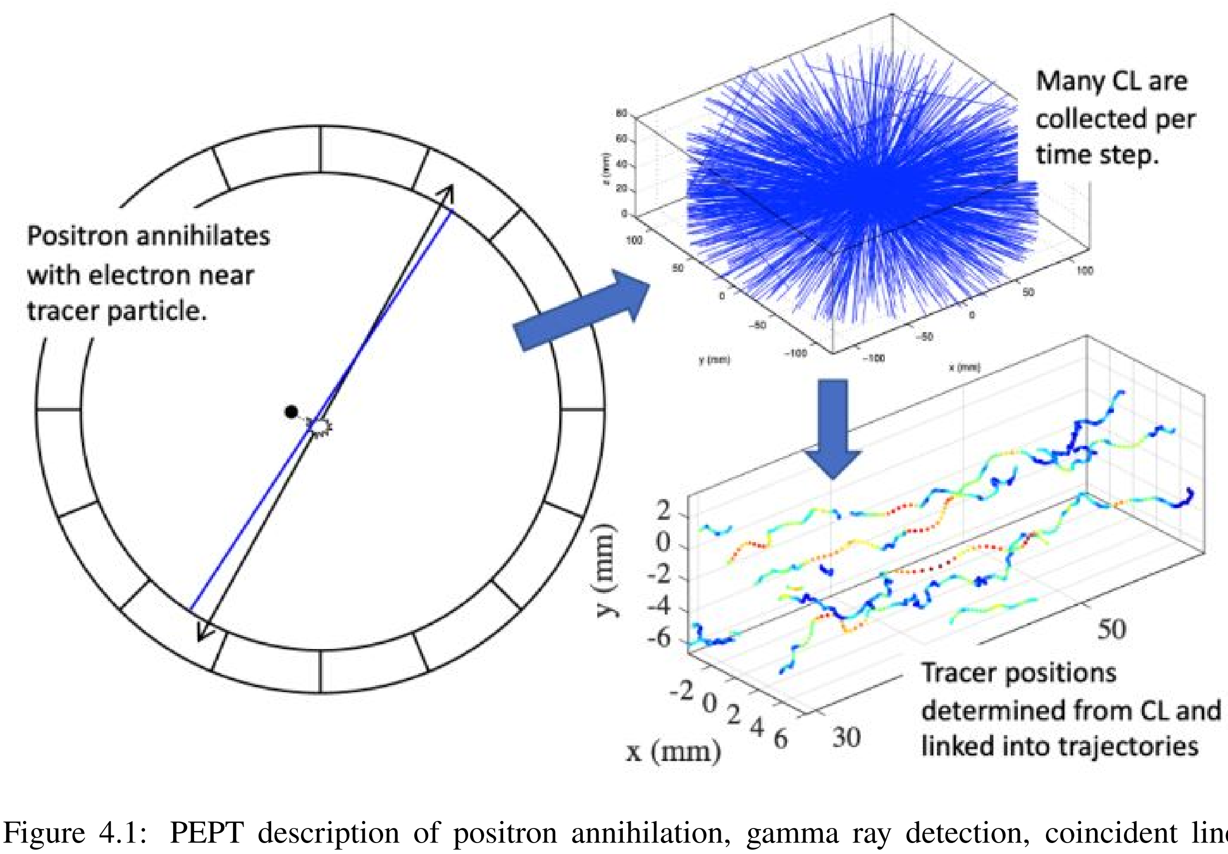

Figure 4.1: PEPT description of positron annihilation, gamma ray detection, coincident lines reconstruction and linking from Wiggins et al [141].

PEPT has been used in a variety of engineering geometries to provide further insight into their fluid flow structures. Pérez-Mohedano et al [142] used PEPT to study flow structures in a dishwasher with a priori knowledge of the number of particles. Wiggins [132] used the Lagrangian nature of the PEPT data to study Lagrangian Structure Functions on pebble beds. Wiggins et al [143] used PEPT to study wall-bounded flow and the turbulence characteristics of a circular pipe. Houston et al [144] used PEPT to study the development length of a flow straightener. PEPT was used to calculate the velocity fields inside two tanks with rotating impellers and the data was comparable to laser Doppler anemometry data [145]. Chiti et al [145] discussed methods of treating the trajectory Lagrangian data and turning it into Eulerian velocity fields. Their Eulerian spatial averaging methods were used in this work for time-averaged results. Pianko-Oprych [146] compared PEPT results with particle image velocimetry on a spinning blade turbine in a tank, showing good agreement between both velocity measuring techniques. Savari et al [147] used the Lagrangian trajectories to further calculate the turbulent kinetic energy, dissipation rate, and turbulent diffusion coefficients in a similar geometry, a tank vessel with a rotating impeller. Similarly, Fishwick et al [148] used PEPT to study the hydrodynamics of a propeller moving vertically in a vessel. PEPT has been used to study multi-phase flows. Sommer et al [149] used PEPT to study the fluid-flow interactions created by air bubbles in the tracer particles while Waters et al [150] used PEPT to follow particles in pulp to help develop mathematical models in froth flotation. Easa and Barigou [151] compared PEPT and CFD results in solid-liquid interactions for non-Newtonian fluids showing good comparisons in the velocity profiles between the CFD and PEPT results. Perin et al [152] used Monte Carlo simulations to study the ability of PEPT to measure flow behavior in turbulent multiphase flow. PEPT has been used to interrogate fluid flow phenomena in different complex geometries and for different applications, making it an ideal fluid flow measuring technique for twisted tape inserts.

4.2 Methodology - PEPT at VCU

This section describes the methodology used to run PEPT experiments at Virginia Commonwealth University (VCU). The methodology greatly derives from the work done at the University of Tennessee Knoxville.

4.2.1 PET Scanner - Mediso LFER

The Bioimaging and Applied Research Core (BARC) at VCU has a MultiScan Large Field of view Extreme Resolution (LFER) large bore research PET/CT scanner originally used for imaging mice or small primates [153]. Figure 4.2 shows the Mediso LFER Scanner at VCU in its original and vertical configurations. The LFER is a scanner with a cylindrical field of view that houses a PET and CT scanner that allows it to share the same field of view, as the CT camera and PET crystals can move inside the scanner. The Mediso LFER was bought with two different extensions to hold the small primates or mice, a Mobil Cell (depicted in Figure 4.2) and a monkey chair. The scanner can pivot in different orientations allowing it to be vertical, horizontal, or at a given angle. When the

Mediso LFER scanner was adjusted for PEPT experiments, its vertical configuration, the monkey chair had to be plugged into the scanner. The PET scanner is arranged into 3 rings with 18 detectors in each ring detectors made of lutetium yttrium oxyorthosilicate (LYSO) crystals. The individual crystals consist of 1.59 mm × 1.59 mm crystals arranged in a 29 × 29 matrix array [141].

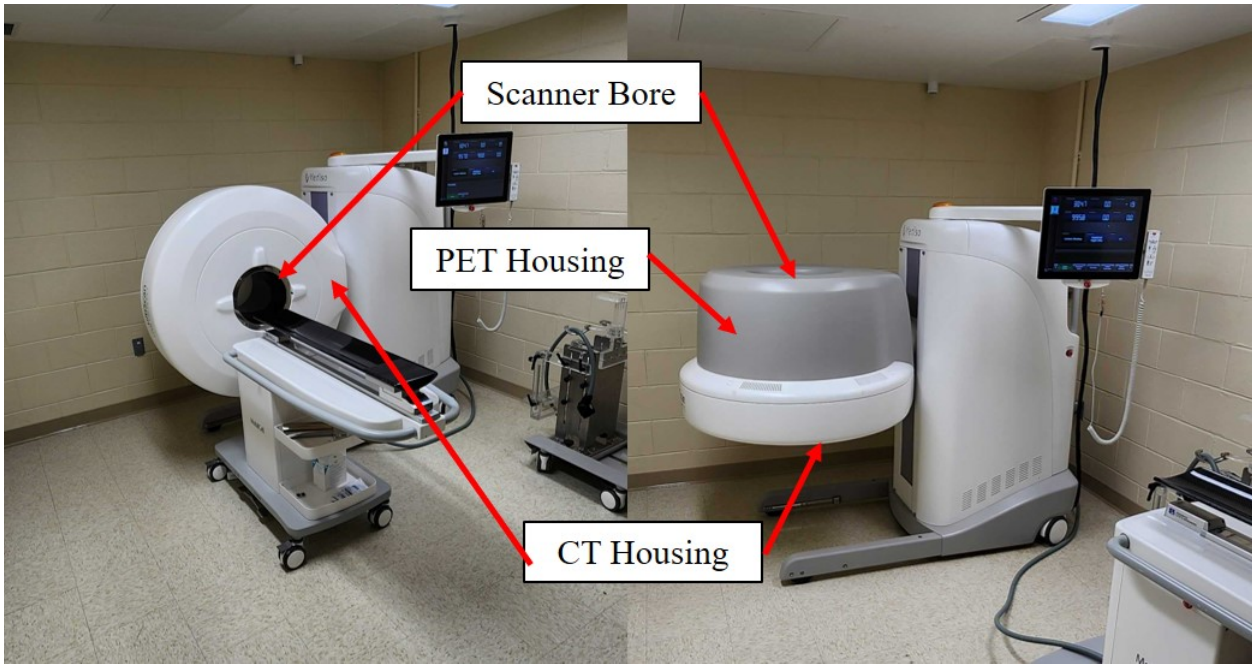

Figure 4.2: BARC's Mediso LFER Scanner at VCU shared with the FAST research group at VCU in its original configuration (Left) and the vertical configuration for PEPT experiments (Right).

4.2.2 Tracer Particles and Radiolabelling

The tracer particles consisted of OH-form anion exchange resin from BIO-RAD AG 1-X8 Anion Exchange Resin, biotechnology grade, 100-200 mesh, with Part Number 1432445. The tracer particles had bead size of 106 - 180 μm diameter and a density of approximately 1200 kg/m^3. Figure 4.3 shows the anion exchange resin used for the PEPT experiments next to the Fisher Scientific Scale used to weigh the particles for the radiolabelling procedure. Further details on the radiolabelling procedure can be found in Appendix E.2.

In order to test if the particles were proper tracers, the Stokes number was evaluated. The Stokes number, St, is defined as the ratio between the relaxation time, τ_R, of the particle relative to the Kolmogorov time scale of the fluid, τ_η. [154] :

$$St = \frac{\tau_R}{\tau_\eta}. \tag{4.1}$$

Previous PEPT work done on wall-bounded flow defined Stokes number as [143]:

Figure 4.3: BIO-RAD AG 1-X8 Anion Exchange Resin next to the Fisher Scientific Scale used to weigh the particles.

$$St = \frac{1}{18}\frac{\rho_p}{\rho_f}(\frac{d_p}{\eta})^2, \tag{4.2}$$

where η is the Kolmogorov length scale estimated to 80 μm. This gave a Stokes number of 0.33, which is less than 1. Showing the capabilities of these tracers to follow the fluid in wall-bounded flow. Different methods of calculating the Stokes number were found in literature, with one dependent on the velocity of the fluid, V, [155]:

$$St = \frac{1}{18}\frac{\rho_p}{\rho_f}\frac{d_p^2}{D}\frac{V}{\nu}, \tag{4.3}$$

where ρ_p and ρ_f are the density of the particle and the fluid, respectively, d_p is the diameter of the particle, and D is the diameter of the pipe. Figure 4.4 plots the different Stokes numbers for the two maximum and minimum diameters of the particles with relationship to Reynolds number using Equation 4.3. The highest Reynolds number explored in this work is Re = 17,700, and based on Figure 4.4, the Stokes number is << 1, showing that the particles follow the fluid motion like a tracer.

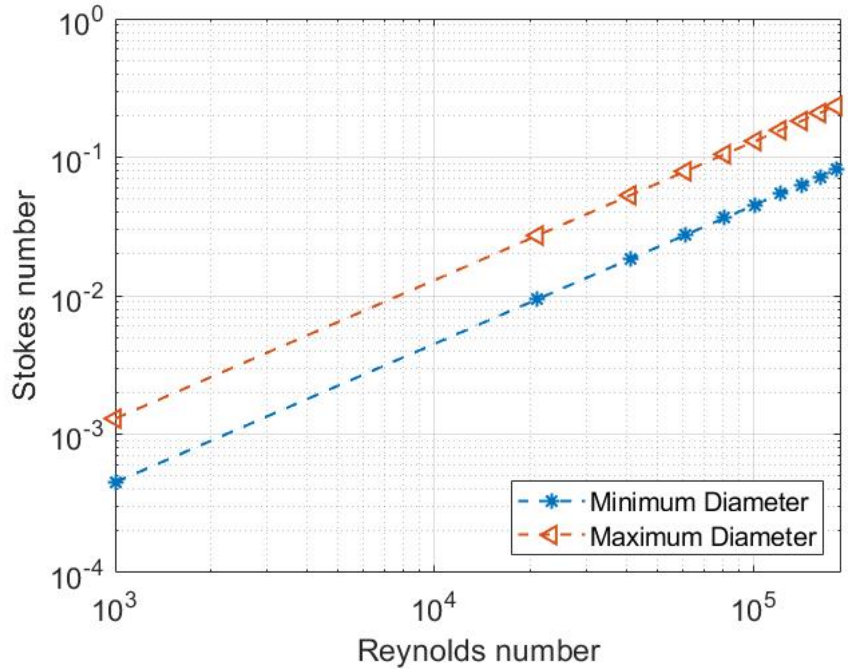

Figure 4.4: Stokes number versus Reynolds number of anion exchange resin with minimum and maximum diameter using Equation 4.3.

Fluorine-18 (^{18}F) was used to activate the radiotracers. The ^{18}F ions were attached to the OH-form anion resin's ions through a process called radiolabelling. ^{18}F was ordered a day prior to the experiments from Sofie Biosciences, Inc. to arrive at 11:30 a.m. on the day of the experiment in the form of an aqueous solution of volume less than 200 μL. This varied for each experiment, but different methods to mitigate the inconsistency of ^{18}F delivered were created. The success of the radiolabelling greatly depended on the amount of volume received, as the higher concentration of ^{18}F in the sample allowed for less ^{18}F wasted and more activated particles. Further details can be found in Appendix E.2.

One method to mitigate the inconsistency of the deliveries from Sofie consisted of an increase in activity ordered. Initial ^{18}F orders consisted of 30 mCi to arrive at 11:30 a.m., but as arrival time was not guaranteed the order was increased to 35 mCi. Figure 4.5 shows a comparison of the activity of ^{18}F versus time. As average arrival times were close to 12:00 p.m., the order of 35 mCi would arrive close to the initial desired activity of 30 mCi. There is no current mitigation for the inconsistency of the volume delivered. Unfortunately, this has been found to greatly impact the success of the radiolabelling procedure and further impact the PEPT experiment. On one occasion, a volume of 1 mL was delivered. This was handled by creating two solutions with lower concentrations of particles. The results shown in this dissertation consist of data obtained from the delivery of 1 mL of ^{18}F.

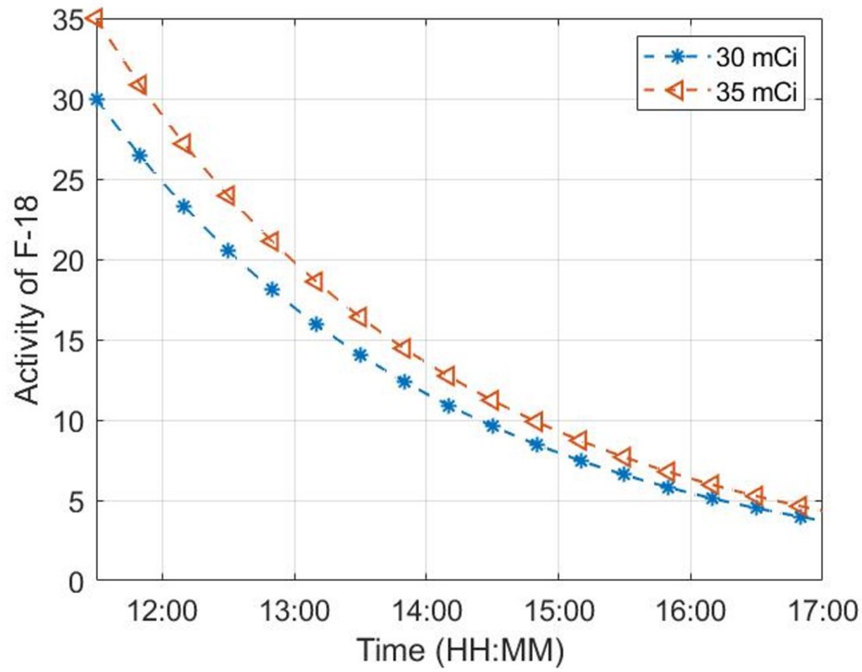

Figure 4.5: ^{18}F activity comparison between the initial order activity of 30 mCi and the adjusted order of 35 mCi.

^{18}F has a half-life of 109.8 minutes and decays via positron and neutrino emission. The emitted positron travels an average distance of 0.66 mm in water before annihilating with an electron [156] creating two 511 keV gamma rays. The half-life allows for data collection to last in the range of minutes to a couple of hours, with good radiolabelling practice, while short enough to allow for clean up in a couple of days and avoid contamination with the instrumentation and equipment. In addition, the short distance traveled by the positron in water allows for more accurate detection of the physical location of the radiotracer [156].

4.2.3 PEPT Loop

An experimental flow loop was designed and built to perform PEPT experiments at VCU. The flow loop had constraints of having a limited set of space as the Mediso LFER scanner was housed in a small room initially intended to interrogate small primates or mice. The room consisted of a 3.04 by 4.12-meter room with ceilings of 2.23 meters tall, thus a large experimental facility similar to MSETF-1 was not possible. In addition, the Mediso LFER scanner is currently owned by BARC and the facility would have to be moved in order to accommodate other types of experiments. The experimental loop had to be easily adjustable and transportable between locations. The locations consist of the Mediso LFER scanner room and a separate room used to check for leaks in the flow loop and experimental conditions.

The experimental flow loop was designed and built to meet all those requirements [157]. The flow loop was constructed using PVC pipe with a 1.5” nominal inner diameter (40.9 mm) with parts connected using PVC unions for easy installation and disassembly. Figure 4.6 shows a schematic of the experimental flow loop built to fit in the Mediso LFER scanner room.

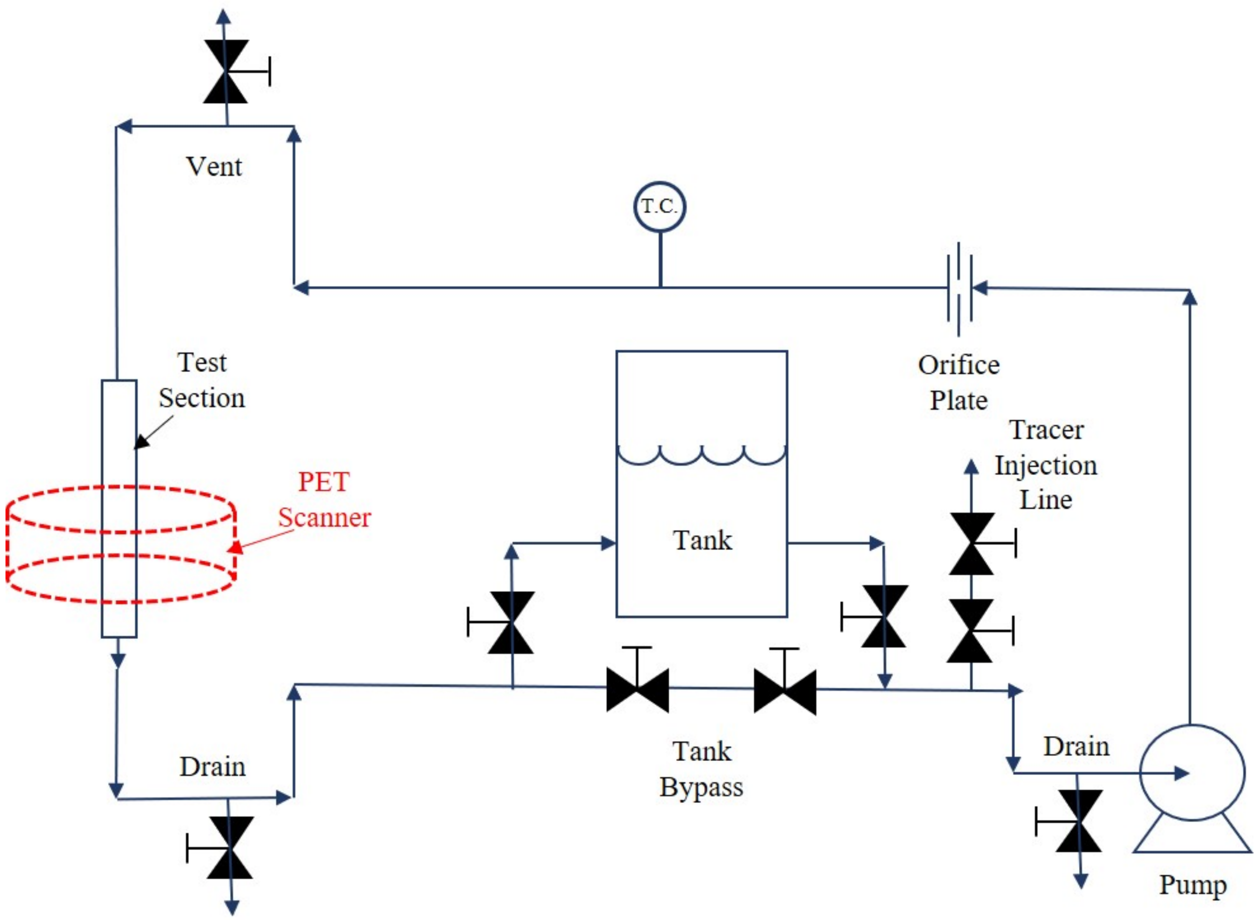

Figure 4.6: PEPT flow loop schematic.

The PEPT loop circulates water using a Pentair SUPERFLOW VS variable speed control pump, similar to MSETF-1, that has been modified to remove sections that could cause the radiotracers to possibly get stuck. From the pump, the water traveled upward in a vertical pipe until it met a 90^o elbow to a horizontal PVC pipe. An orifice plate flow meter and T-Type thermocouple were located in this horizontal pipe. The orifice plate flow meter consisted of a TE-E-2 PTFE orifice plate flow meter for a 1.5” nominal inner diameter pipe (40.9 mm). The orifice plate is connected to an Omega 1 psi differential pressure transducer of Item Number PX409-001DWU5V. The orifice plate flow meter was used rather than a turbine flow meter to prevent tracer losses by the turbine flow meter. After the flow passed through the horizontal pipe with the thermocouple and orifice plate, the water flow was directed upwards. For mass flow rates below the range of the orifice plate, a low flow rate flow meter was employed to measure the flow, a King Instrument Company Part Number 720501513W flow meter. Subsequently, the water flowed horizontally to a vent positioned at the highest point of the loop to facilitate degassing of the system. The flow was then redirected in a downward vertical manner towards the bore of the PET scanner, where the vertical test section was located. After the flow passed through the test section, the flow traveled back up towards the tank and the tracer injection line.

The flow loop was designed in a manner in which the water tank was isolated during the experiments. It initially was used to fill up the flow loop, but for actual PEPT experiments, the flow would bypass the tank. Next to the tank, the tracer injection line was located. This consisted of a T-connection with two valves. This section was used to introduce the radiotracers into the loop without having the need to use the tank. The tank was avoided as it was a location for tracers to settle down. In this method, the tracers were constantly in circulation.

4.2.4 PEPT Loop Modifications

This section discusses the modifications done to the PEPT loop from its original design by Dr. Cody Wiggins. Exploratory PEPT experiments were performed to test the capability of the current facility to obtain significant data at low Reynolds numbers with the test sections summarized in Table 3.4 and 3.5. The low mass flow rates experienced by the laminar regime of these twisted tape inserts caused the majority of the tracer particles to get stuck or settle in different parts of the facility. This led to very few particles passing through the field of view of the PET scanner. To mitigate this, the test sections were increased to have a 1.5” nominal inner diameter (40.9 mm), with previous test sections consisting of a 1” nominal inner diameter. This increase in inner diameter allowed for larger mass flow rates that would allow particles to flow through the field of view while maintaining a laminar regime in the twisted tape inserts. This also led to an increase in the development length required to have a fully developed flow at the entrance of the twisted tape inserts’ test section. Due to the limiting size of the scanner room, and the vertical orientation of the test sections, there was not enough length to have a fully developed empty pipe flow before the twisted tape insert was introduced. To overcome this, a flow straightener was added immediately downstream of the 90^o elbow that feeds into the test section.

A flow straightener was built using the design from Laws [158] who observed a fully developed flow within 5.5 diameters of two 90^o elbow bends. Laws’ design was based on a plate with holes arranged in a circular configuration. This design showed minimal pressure loss with small development lengths. The constructed flow straightener consisted of a similar hexagonal configuration with holes arranged in a 1:6:12 ratio with a porosity of 53% [144]. Houston et al [144] collected PEPT data downstream of the flow straightener from a partially closed valve and observed fully developed flow around 4.5 diameters downstream of the flow straightener. Houston et al [144] described the flow straightener as having a thickness of 6.35 mm, with a center hole diameter of 7 mm, an inner ring diameter of 17.99 mm with holes of 6.65 mm, and an outer ring diameter of 30.00 mm, with each hole in the outer ring having a size of 5.5 mm. Figure 4.7 shows the schematic of the flow straightener designed by Houston et al [144] with a picture of the flow straightener mounted between two flanges.

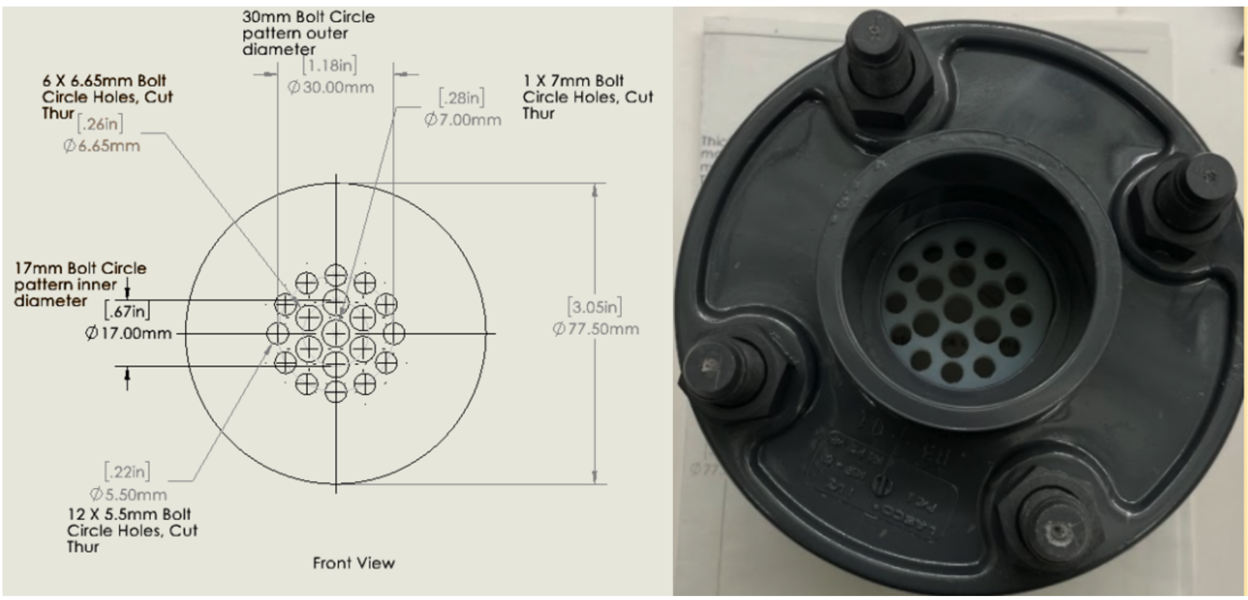

Figure 4.7: Flow straightener schematic designed by Houston et al [144] (Left), with flow straightener mounted between flanges (Right).

The same flow straightener was repurposed for the modifications of the PEPT loop. The flow straightener was installed 3 diameters (12 cm) from the 90^o elbow and the flow traveled downstream for 6.2 diameters (25.4 cm) before being introduced to the twisted tape insert geometries. Houston et al [144] observed fully developed flow at 4.5 diameters from this flow straightener at a Reynolds number of 37,700, a much higher Reynolds number than the Reynolds numbers explored in this work and at a smaller distance than the updated design. Thus the flow was fully developed before the twisted tape insert test section.

In addition, the overall length of the test section increased from 1.44 meters to 1.54 m to increase the scanning window. Adjustments to the piping were done to reduce and increase different components to accommodate the new length of the test section and the addition of the flow straightener upstream of the test section. The new design had to have a maximum height of 2.16 m (5 cm lower than the ceiling of the scanner room). Figure 4.8 shows the before and after of the modifications done on the PEPT loop. It also shows the limiting height the flow loop can extend before reaching the ceiling.

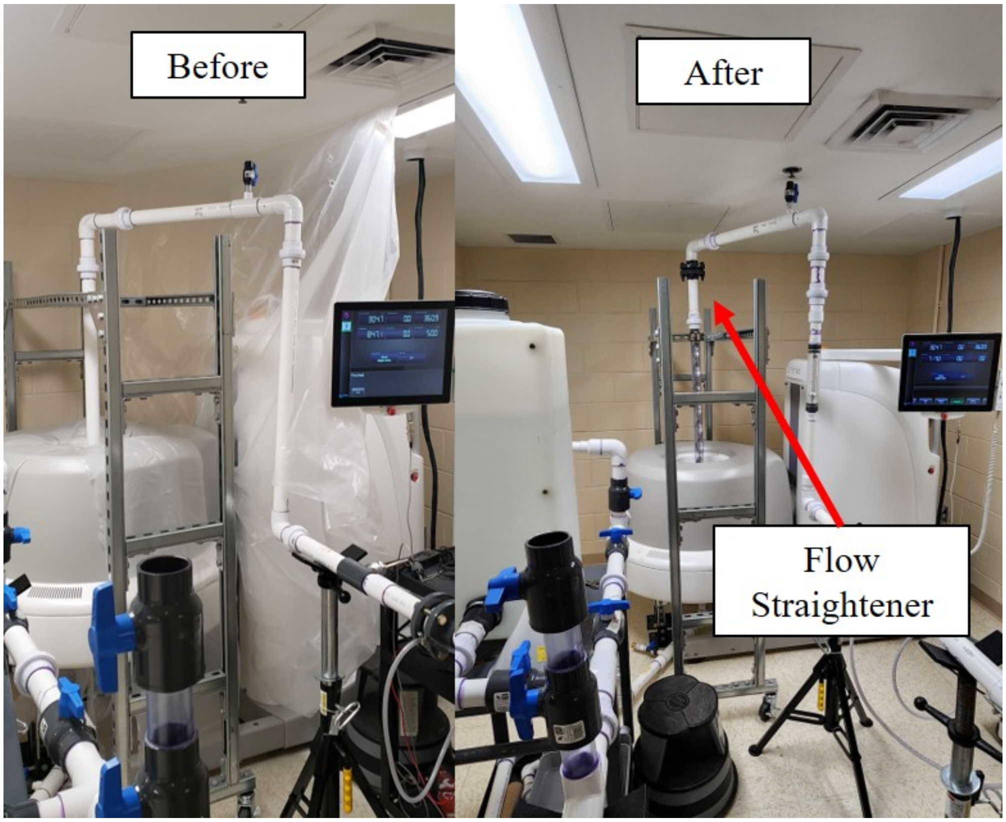

Figure 4.8: PEPT flow loop in scanner room before modifications (Left), and after modifications (Right).

4.2.5 Description of Experiments

Initial PEPT exploratory experiments were performed with twisted tape inserts of the same geometry as those for the friction factor experiments, summarized in Table 3.4. Unfortunately, the low Reynolds numbers proved to be problematic as the majority of the particles were settling down or getting stuck at various locations of the PEPT loop. Thus, these new test sections were manufactured and tested. In addition, the original flow loop had to be redesigned to obtain fully developed pipe flow at the entrance of the twisted tape inserts, further discussion on the modifications can be found in Section 4.2.4.

Two test sections were manufactured using a clear PVC pipe of 1.5" nominal inner diameter (40.9 mm) and a new order of twisted tape inserts with larger widths (but keeping the same width-to-diameter ratios w/D = 0.95 and 0.85). Instead of welding the twisted tape inserts to stainless-steel pipes, as was previously done for the friction factor and Nusselt number experiments, a stainless steel plate of similar thickness as the twisted tape and length of 12.7 mm was welded to the end of the twisted tape insert. The width of the plate was ≈ 44 mm (smaller than the outer diameter of the PVC pipe). The PVC pipe was then cut to fit the stainless-steel plate in place with the twisted tape insert inside the PVC pipe, with Figure 4.9 showing the two final twisted tape insert test sections. Table 4.1 summarizes the geometric and experimental conditions of the new test sections manufactured for PEPT experiments, with Reynolds number defined as the empty pipe Reynolds number.

Table 4.1: Geometric and experimental conditions of twisted tape inserts for PEPT Experiments

Parameter (Unit)	Value
Inner diameter, D (mm)	40.9
Twisted tape width, w (mm)	38.9 and 34.8
Ratio of width and diameter, w/D (-)	0.95 and 0.85
Test section length, L (m)	1.55
Twisted tape thickness, δ (mm)	1.52
Inlet temperature, (^{o}C)	≈ 22
Pitch, y (-)	≈ 2.42
Reynolds numbers, Re (-)	4,000, 8,000, and 17,700

Figure 4.9: Twisted tape inserts used for PEPT experiments with different widths (w/D = 0.95 and 0.85).

Furthermore, PEPT experiments were conducted on the additively manufactured test section described in Table 3.6. For this test section, only the Reynolds number of 17,700 is presented in this work as experiments at the lower Reynolds numbers did not produce significant data. The lower flow rates for this test section did not push enough particles to pass through the field of view of the scanner. To ensure the additively manufactured test section was suitable for the PEPT experiments, a smaller test section known as the Tesseract was 3D printed and subjected to a higher dose of radiation than the ones experienced in the actual PEPT experiments. This was done to study the effects of radiation in the gluing mechanism of the test section and verify that the material would not fracture or become compromised due to exposure to gamma rays. It was essential to protect the Mediso LFER scanner, as the test sections are positioned at its center, and any breakage or compromise could result in water damage. For further details on the Tesseract and the test done to study the effects of the radiation on the additively manufactured parts, refer to Appendix D.3.

Figure 4.10: Additively manufactured twisted tape insert of pitch $y \approx 2.42$ for twisted tape experiments (Left and Middle), and the test section installed in the PEPT loop (Right).

With the success of the Tesseract project and no observable damage or fractures that could pose harm to the scanner, PEPT experiments were performed for the additively manufactured twisted tape insert. Figure 4.10 shows the additively manufactured twisted tape inserts with it installed in the PEPT loop.

4.2.6 Experimental Procedures - An Overview

The PEPT experimental procedures are complex and required multiple days to prepare, set up, and clean up. This consisted of an entire week of experimental efforts. All experiments were performed on Fridays with the preparation and setup occurring on Wednesday and Thursday. Finally, the clean-up of the flow loop would occur on Mondays the week after the test to ensure the radioactivity of the ^{18}F had decayed. This section goes over important steps and procedures done to obtain the experimental data. For a clear overview of the procedures, the different tasks are divided by days.

The Wednesday procedure consisted of building the flow loop in an adjacent room to the Mediso LFER room to check the various unions and fittings of the PEPT flow loop. The flow loop was built and filled with deionized water provided by VCU's Sanger building. During this day, an operating test was carried out to ensure the desired flow rates to be tested on Friday were achievable by the flow loop, as well as to determine the pump frequency required to achieve those flow rates. After the pump frequencies were determined, the flow loop was drained and disassembled. This allowed for the parts to dry out before being assembled in the scanner room.

The Thursday procedure consisted of building the flow loop in the Mediso LFER scanner room. The Mediso LFER scanner had to be adjusted to its vertical bore configuration. In addition, the water tank was filled with fresh deionized water. The water remained in the water tank for the rest of the day, with the fill-up of the loop occurring the day of the experiments. This allowed for purer deionized water to be used for the actual experiments. If the water used for PEPT was not deionized, there was a high risk for the ^{18}F to leak into the water. This would create random radioactive spots in the water that would be confused by the code. Furthermore, the ^{18}F order was placed during this day to arrive at 11:30 a.m. the next day, Friday. Finally, the CT protocol in the Mediso LFER scanner was used to ensure the test section was in its most vertical orientation. This was initially done with a toolbox level, but true precision could not be achieved with cavemen eyeballs and a bubble of air, thus a CT scan was taken to further check the straightness of the test section. Figure 4.11 shows the CT scan obtained from a twisted tape insert test section to check for the true level of the test section. In cases in which a true level was not achievable, the angle was off by less than 0.5 mm in the 150 mm of field of view. This was estimated to be less than 0.2^os.

On Friday, before the flow loop was filled with water a set of covers were placed around the scanner. Initial procedures covered the entirety of the scanner to avoid any water spills getting inside the scanner. This procedure was then changed to a form of "tent" that would be created between the flow loop and the scanner. This was done as some of the vents were covered and would cause overheating of the crystals when PET data was collected. When the crystals' temperature would reach near 100^oC, the crystals would automatically turn off and would stop detecting the gamma rays. A figure of the procedure to create the tent in the scanner room is shown in Figure 4.12 with the vents left without covers. After the flow loop and scanner were separated by the tent, the flow loop was filled with water. Temperature measurements of the water were obtained to determine the correct flow rates for the desired Reynolds numbers, as they are dependent on the water's temperature. The flow loop was constantly under supervision to ensure the fittings and unions were watertight. The pump was then run at 1500 RPMs to degas the facility. This consisted of a procedure known as "DJ-ing" the flow loop. The two valves next to the water tank were partially opened and closed at random intervals to create a shock in the water and help any gas bubbles escape. In cases where small bubbles would accumulate in the pump, the valves were continuously partially closed and opened to remove further air bubbles. The water of the loop was maintained at a maximum of 23 ^{o}C. The high pump frequency of the degassing procedure would cause the water

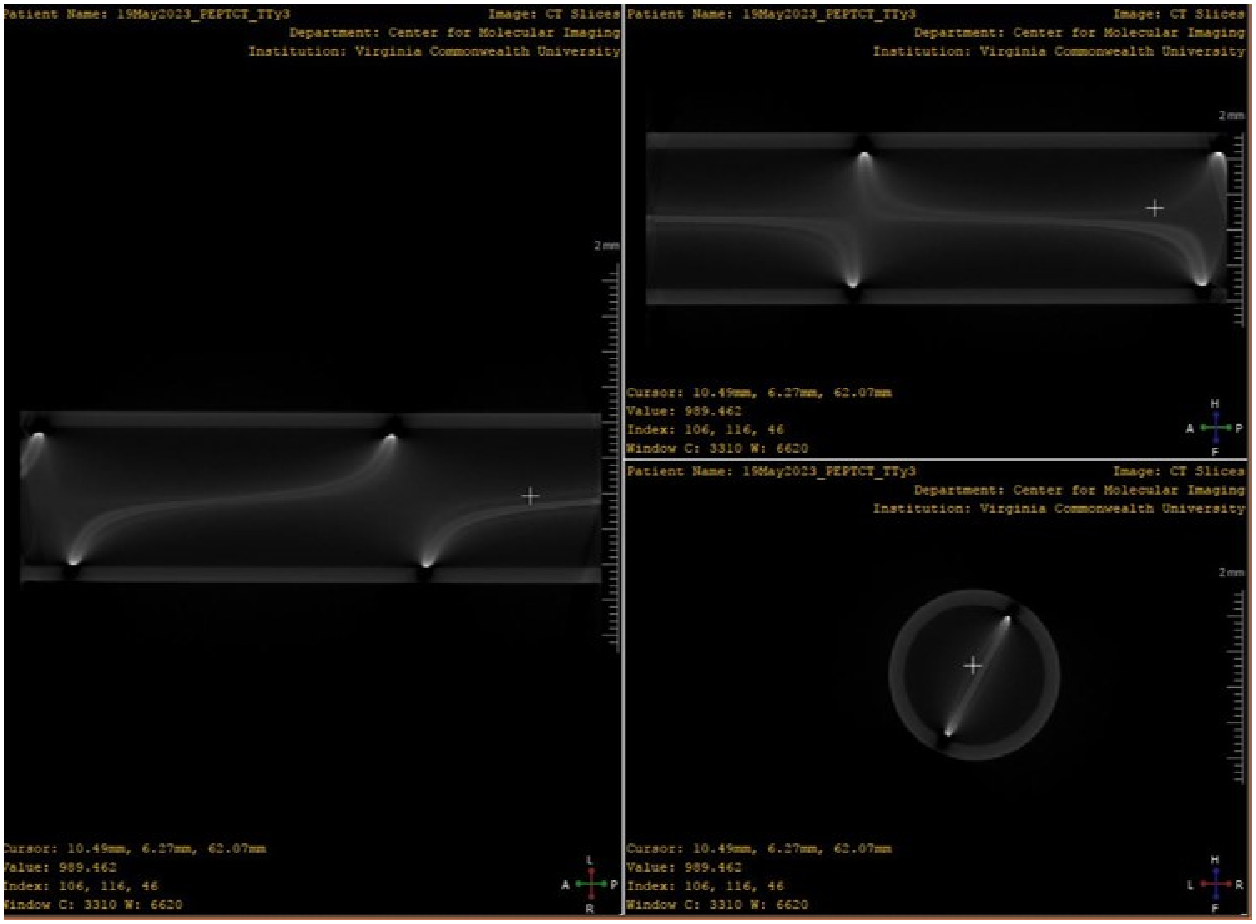

Figure 4.11: CT scan of twisted tape inserts with 3 different geometric views to check for vertical straightness and unsure it was not leaning in any angle.

to heat up, thus a quick degassing methodology was required.

Once the flow loop was degassed and the desired flow rate was achieved, a baseline survey of the room, flow loop, and the shielded lead blocks was taken with the Geiger Counter. This baseline survey was used to ensure the activity had decayed back to background levels on Monday, as this survey was done before the radiation arrived. The shielded lead blocks were known as "The Castle" and are shown in Figure 4.13. The instrumentation to perform the radiolabelling was set up inside the castle, Figure 4.14, which consisted of a centrifuge, DI water, Eppendorf, filter tubes and waste bottle. For a detailed description of the radiolabelling procedure refer to Appendix E.2. After the radiolabelling was performed, the radiotracers were inserted inside the flow loop through the particle injection line.

The PEPT experiments started by running the LabVIEW software inside the Mediso LFER room and initializing the PET data collection in the Nucline LFER's Software. Table 4.2 summarizes the different data acquisition target times for LabVIEW and the Nucline LFER Software for PEPT

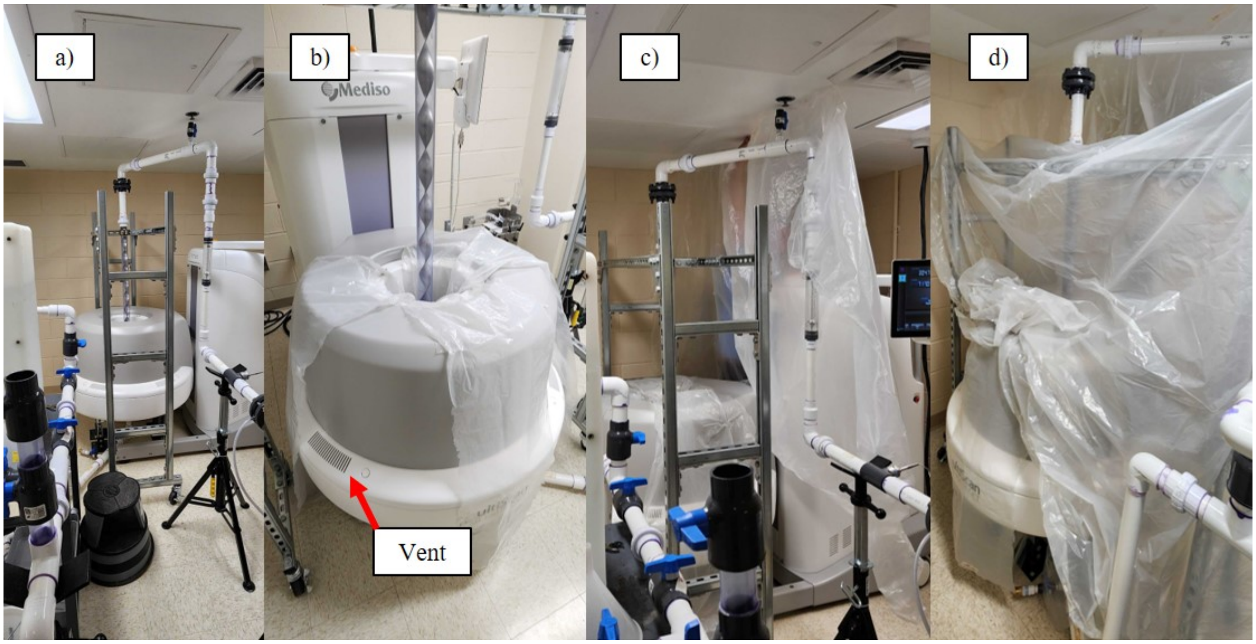

Figure 4.12: Procedure to protect the scanner from any water leaks while leaving the scanner vents open; (a) initial with no covers, (b) covering the bore, (c) isolating loop from the scanner, (d) final cover set up.

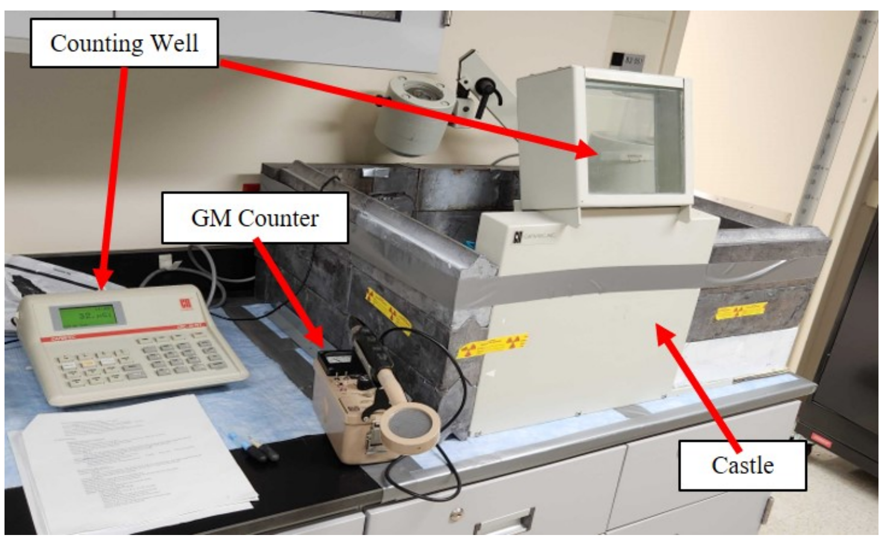

Figure 4.13: Shielded lead blocks, the castle, where the radiolabelling took place alongside the counting well and GM Counter.

experiments. LabVIEW data acquisition times were kept at 90 seconds as the important data collected from it consisted of the average temperature and the flow rate. Since the system was not affected during data collection times, the 90 seconds were sufficient to extract the important information. The target times of the Mediso were varied depending on which Reynolds number

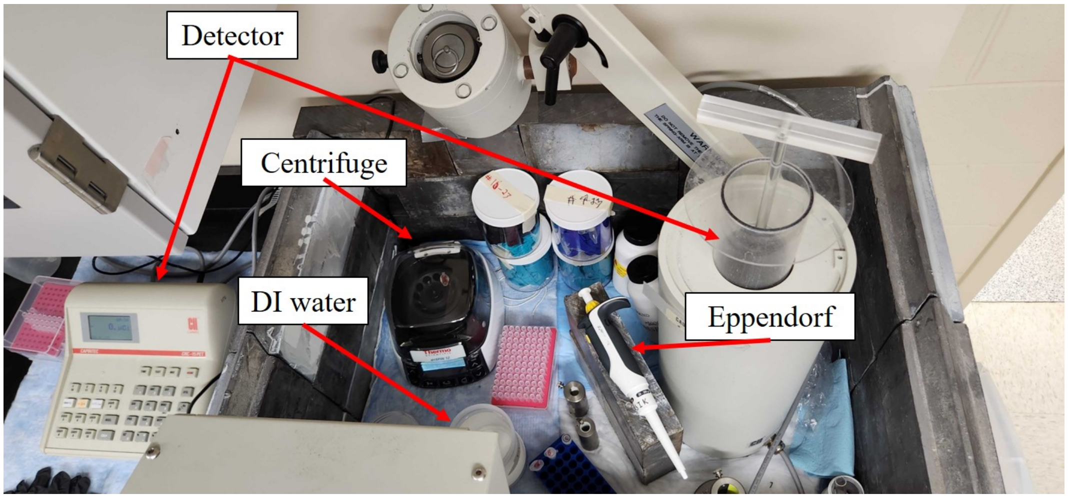

Figure 4.14: Instrumentation set up inside the castle to perform radiolabelling.

was tested. The low Reynolds numbers had an average data acquisition time of 2 minutes and 30 seconds, as with the low flow rate the radiotracers would begin to settle in the pump and get stuck in the different fittings and valves across the loop. As time went by, fewer and fewer particles were observed across the field of view of the scanner. Once the 4,000 Reynolds number test was finished, the flow rate was increased and the valves were opened to allow any trapped particles to get released. In addition, during this time, the flow loop was disturbed by tapping wrenches at different locations, such as valves, corners, or T's, to release any particles stuck in the flow loop.

Table 4.2: Summary of data acquisition times for PEPT experiments for twisted tape inserts.

Reynolds number	LabVIEW Data Acquisition Target Time (s)	Nucline LFER Software Target Time (mm:ss)
4,000	90	2:30
8,000	90	5:00
17,700	90	5:00 - 20:00

The entire data collection consisted of a couple of hours, depending on how well the radiolabelling was performed. After the final test was collected, the pump was turned OFF, the data transfer from the Nucline LFER Software to the computer was started, and the experimentalists surveyed themselves with the Geiger Counter before leaving the building.

On Monday, the clean-up consisted of collecting a survey to ensure all the activity had reached background levels and performing a swipe test. After ensuring the activity was back in the background, the loop was drained and disassembled. Finally, the data was added to the FAST Research Group's Google Drive and the Mediso LFER was adjusted to its original horizontal configuration.

4.3 Data Handling

PEPT requires a variety of data post- and pre-processing techniques and codes. Due to this, this section describes some of the parameters chosen for the reconstruction of the PET raw data, as it comes in list-mode files, through a C++ code, as well as the filtering and data manipulation done afterward through Matlab and C++ codes. Different laptops were used for both the pre-and post-processing, not to study the computational effects but due to the availability of working laptops.

4.3.1 M-PEPT

This section describes the steps done to obtain the tracer particle trajectories by running the C++ code MultiPEPT_V2.0.cpp (M-PEPT). M-PEPT is a code initially developed at the University of Tennessee Knoxville [132, 159] to read raw PET data and reconstruct and link particle locations through time. The reconstruction algorithms employed in the M-PEPT code allow it to track any number of particles at a given time step [136, 138], a unique capability as previous PEPT reconstruction algorithms required prior knowledge of the number of particles in the field of view. This code uses image-processing techniques to identify the particles that pass through the field of view of the PET scanner. The code requires multiple user inputs in order to fine-tune the different techniques to locate and link the particles through different time steps. The M-PEPT code creates a 3-dimensional grid that is segmented into voxels. Voxels are the base 3-dimensional units in space that are used to locate the particles. The locations of the detections in the PET scanner from the 511 keV gamma rays are used to create coincident lines between the detections. These are lines that connect the paired locations in a straight line, since the two coincident 511 keV gamma rays travel in opposite directions, back-to-back. The coincident lines are grouped into different time steps, a user input, in order to estimate the location of the particle. Similar to intensity in an image, the number of coincident lines in a voxel is used to estimate the location of the particle as a higher number of coincident lines relates to a high probability of a particle in that voxel. The code then fits 3 one-dimensional Gaussian normal probability curves in which the center is the location of the particle to locate the particle location at a specific time step. The particle locations are then linked based on the most-likely connection between particles across different time steps based on a cost-effective matrix. A further summary of the inputs chosen for the M-PEPT code and their function follows.

The initial parameters inputted in the M-PEPT code consisted of the voxel size and time discretization for line density calculations. These were kept constant through the various experiments and are summarized in Table 4.3. Initial studies were done to determine the optimal time and spatial discretization, with the parameters in Table 4.3 determined as the optimal ones or the ones that resulted in the largest linkage between particles. Consistency in this discretization was chosen to remove any biases in the post-processing or over complications, as some of these parameters are used down the line and could cause confusion in the calculations, or further user error. Furthermore, the option of Overlapping time steps was chosen to better locate the particle through different time steps. The overlapping time step works by adding the original time step and the overlapping time step as the new time step window to estimate the location of the particles, but the original time step for line densities is the actual jump between time steps. These can be viewed as, in the case of a Reynolds number of 4,000, the first 12 milliseconds are used to determine the initial location of the particle (5 + 7 = 12), the next time step is from 5 to 17 milliseconds, the next time step is from 10 to 22 milliseconds, and so on until the collecting time of the PEPT experiment has come to an end.

Table 4.3: Spatial and temporal discretization used for the M-PEPT code dependent on Reynolds number.

Reynolds number	Voxel size (mm)	Time step for Line Density (msec)	Overlapping time step (msec)
4,000	2	5	7
8,000	2	3	6
17,700	2	1.5	4.5

The next input consisted of the linking methodology of particles across time steps. The linking methodology chosen was Munkres's nearest neighbor based on the Kuhn-Munkres algorithm [160, 161]. This method consisted of creating a cost matrix of the displacement in the position of the particles between time steps. A maximum velocity, an input by the user in the M-PEPT code, was used to determine if the displacement between particles in the cost matrix was realistic or not, thus creating links through time steps for particle pairs, a more detailed description of the linking methodology can be found in Wiggins [132]. The next M-PEPT parameter consisted of the detection method. Particles were detected based on image processing techniques in which the density of coincident lines was analogous to pixel intensities in images, feature point identification (FPI) [138]. FPI functions by tracing the coincident lines at a given time step and from the 3D voxel mesh, it detects particle position based on the largest concentration of coincident lines in a voxel or the largest intensity based on the nearest neighbors.

The next parameter consisted of the minimum peak voxel (MPV) value for time step consideration. This parameter was a threshold of coincident lines crossings through a voxel to determine if there are any particles observed at any given time step. In other words, to determine if the code was going to search for a particle at a given time step or move on to the next time step. This value was determined through a plot of coincident lines per time step, one of the outputs of the M-PEPT code, to observe what was the peak grid element when no particle was passing through the field of view. This value ranged between 4 and 7, depending on the test and the time the test was taken, or the order of the test. As the ^{18}F leached from the particles into the deionized water, the minimum peak voxel background would go higher, and the code would take longer to locate the particles, in addition, it could identify false positive particle locations. The first tests required an MPV value of 4, while for the later tests, the value was raised to 6 or 7. Figure 4.15 shows the plot of peak grid element versus time for the first 10 seconds of data to decide on an MPV value, in this case, the value of 5 was used. To interpret the plot, the troughs are time steps in which no particle is passing through the field of view, where some minimums occur as high as 4, which would cause the user to select an MPV of 5.

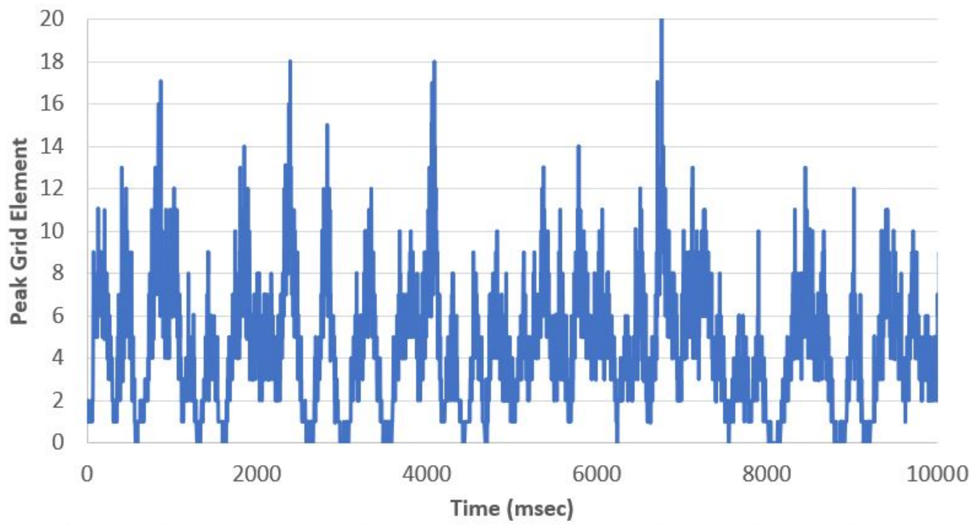

Figure 4.15: Plot of peak grid element versus time (msec) of the first 10 seconds of data for a twisted tape insert.

FPI further requires two inputs from the user, a particle intensity threshold and the number of voxel neighbors to consider for particle detection. The particle intensity threshold value, a fraction value between 0 to 1, was multiplied by the peak voxel value, and only voxels with higher values than the result of this product were considered particles. The particle intensity value was the one that varied the most between tests. When not enough particles were found, specifically at the end of the field of view of the scanner, the particle intensity threshold was lower. While for cases in which too many particles were found, the value was increased. The number of voxel of neighbors consisted of how many voxel neighbors were going to be used to determine which voxel had the particle in a high-density coincident line cloud. This parameter was not adjusted by the user and remained the default value throughout all tests, in which the default value was 0.3. Finally, the last input that was varied consisted of the maximum expected velocity that is used for the Munkres nearest neighbor linking. This was heavily dependent on the Reynolds number and geometry of the test section. For example, if the mean expected velocity was 0.5 m/s, the maximum velocity was chosen as 1.5 m/s, as advised by the creator of the code. This was suggested in order to allow any fast-moving particles, in which the movement was physical, to be linked between time steps. This would differentiate any fast-moving particles from those that had an unrealistic jump between time steps.

4.3.2 Dewarping

Warping is a phenomenon observed in PET scanners, as noted by Moses [162], as a form of astigmatism defect. This is created by the depth of interaction of the gamma rays in the LYSO crystals. As the coincident gamma rays travel through the detectors they create a radial bias the further away they are from the center. This occurs as the gamma rays enter through one crystal and may cause no detection until it travels further in the crystal lattice until it is detected in a different LYSO crystal. This requires a PET radial correction from the original trajectories outputted from the M-PEPT code. To correct this warping phenomenon, calibration was done using point sources at different radial locations within the Mediso LFER's field of view. Further details on the dewarping efforts of the Mediso LFER can be found in Wiggins et al [141]. The particle locations were dewarped before the other post-processing techniques.

4.3.3 Filtering

Filtering and adjusting techniques were performed to properly analyze and interpret the PEPT data. The first adjustment consisted of centering the data for proper Lagrangian and Eulerian data analysis. After the dewarping, discussed above, the true center of the test section was found. This was done using three different methods, as the true center of the field of view can be complicated to find based on the raw PET data. Different methods have been discussed and theorized on how to find the real center of the data set.

The first method to find the real center consisted of averaging all the $x-$ and $y-$ positions. This method proved to be effective in most twisted tape experimental data, as any outlier particle position that went out of the real geometry would be hidden within this average. Unfortunately, this method doesn't properly work in cases in which particles are unevenly distributed in the $x-y$ plane. This is the case for data sets with geometries such as flow straighteners, as the flow is developing particles might be biased in one direction which causes this method to be less effective in finding the true center.

The second method consisted of obtaining the center based on the maximum and minimum x and y. This work consisted of flows traveling in the $z-$direction, making the x and y, the azimuthal directions of the flow. This method provided a very biased center and it was prone to errors as any false particle trajectory would lead to an erroneous estimated center. This method was used as a guide and as an informant of particles that would be "detected" outside the geometry, but the centering calculation was not based solely on this method. Any particles found outside the geometry were considered as false-positive from the M-PEPT code.

The third method consisted of obtaining a center based on the 2 subsequent maximum and minimum x and y positions. This means that the next two maximum and minimum, not taking into consideration the ones used for the second method, were averaged and a different true center was obtained from the difference. This method was devised as the possibility of one particle trajectory affecting the maximum and minimum in the second method can occur frequently, but the possibility of 3 false-positive trajectories that have gone outside the true geometry is less likely.

In reality, the true center was obtained based on the three methods. In the case in which there was a bias in the data passing through a region in the $x - y$ plane, methods two and three were used to find the true center. In the case in which a particle trajectory was outside the real geometry, a false positive, the first and third methods were considered to find the true center. In most cases, all three methods were used together as they had a difference of less than 1 mm between them, in cases without a bias in the $x - y$ plane and no fake trajectories. Figure 4.16 shows the $x - y$ plane of the first 600 particle trajectories for the additively manufactured twisted tape insert before and after the centering methodology. For this geometry, it is clear that the center of the field of view has zero particles passing by since the twisted tape is rotating in the center. Figure 4.17 plots the same particle trajectories in three dimensions before and after centering. The centering is less apparent in Figure 4.17 than in Figure 4.16, but it is intended to show the centering in the three planes and how the z plane was unaffected from the centering of the data.

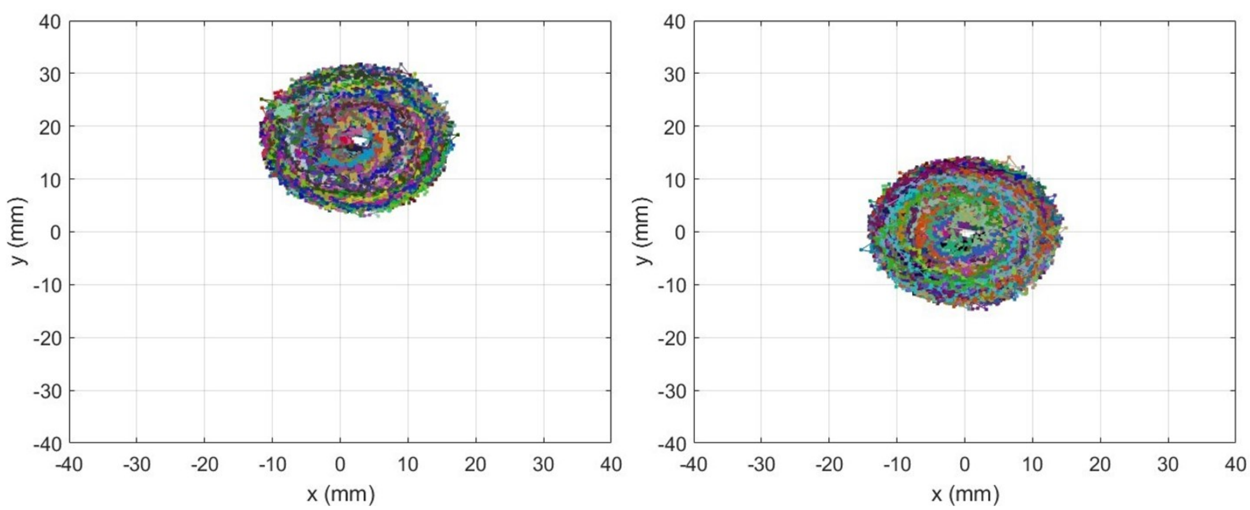

Figure 4.16: Plot of the centering methodology in the $x - y$ plane for the additively manufactured twisted tape insert before centering (Left) and after centering (Right) for 600 particle trajectories.

To facilitate the Eulerian frame of reference calculations, and observe the flow in its rotation frame of reference, the position trajectories were untwisted. This was done through two steps. The new

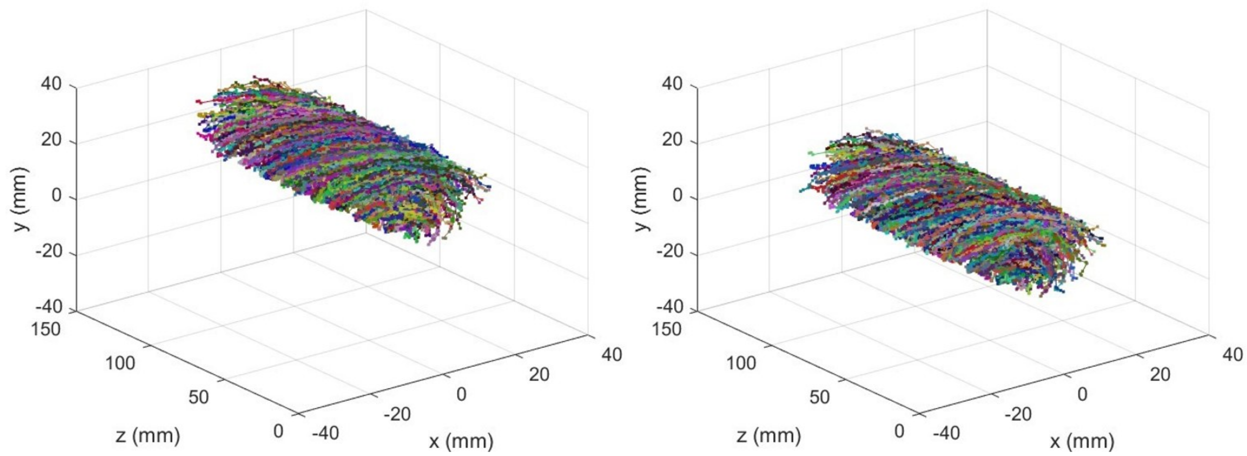

Figure 4.17: Particle trajectories in all three dimensions for twisted tape data before centering (Left) and after centering (Right) for 600 particle trajectories.

x and y untwisted positions were calculated based on:

$$x_{new} = x_{old} \cdot cos(\frac{\pi \cdot z}{H}) + y_{old} \cdot sin(\frac{\pi \cdot z}{H}), \tag{4.4}$$

$$y_{new} = -x_{old} \cdot sin(\frac{\pi \cdot z}{H}) + y_{old} \cdot cos(\frac{\pi \cdot z}{H}). \tag{4.5}$$

The particle locations were rotated by a different angle in order to view it in a horizontal view of the twisted tape insert. Figure 4.18 shows the untwisted particle trajectories for the additively manufactured twisted tape insert after both rotations, with the addition of a horizontal dotted line to represent the location of the twisted tape insert.

Wiggins [132] described the method used herein to obtain velocity and acceleration data from the Lagrangian trajectories of the radiotracers. This was done via filtering and differentiation of the trajectories through convolution with Gaussian kernels, as suggested by Mordant et al [163]. The Gaussian kernels consisted of:

$$k(\tau) = A \cdot exp(-\frac{\tau^2}{\sigma^2}), \tag{4.6}$$

$$k'(\tau) = A' \cdot \tau \cdot exp(-\frac{\tau^2}{\sigma^2}), \tag{4.7}$$

$$k''(\tau) = A''(\frac{2\tau^2}{\sigma^2} - 1) \cdot exp(-\frac{\tau^2}{\sigma^2}) + B. \tag{4.8}$$

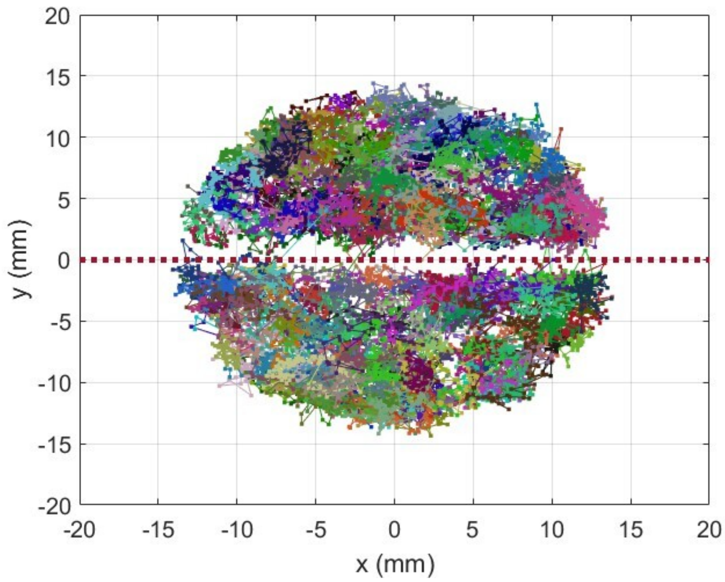

Figure 4.18: Untwisted particle trajectories in the $x-y$ plane for 300 particle trajectories for the additively manufactured twisted tape insert, with a dotted line through the center to represent the twisted tape insert.

The normalization constants were selected based on proper filtering through convolution operations for Equation 4.6 and proper differentiation of simple functions for Equations 4.7 and 4.8, as explained in Wiggins' dissertation [132]. The uncertainty in the position is further propagated to the uncertainty in the velocities through the convolution.

The kernel half-width filter, σ, was adjusted by varying it from 0.5 to 3.5 in 0.5 increments to find an optimal half-width filter. The optimal half-width filter consisted of one in which the data had been smoothed out, but real motions and fluctuations of the trajectories remained. Berg et al [154] suggested that the standard deviation of the velocity and acceleration versus the filter size will have an "elbow" to represent a visual representation of this phenomenon. Figures 4.19 and 4.20 plot the standard deviation of the velocity and acceleration, respectively, of the twisted tape trajectory data, versus the half-width filter. While an "elbow" is not observed in the standard deviation of the acceleration, one was observed in the velocity data of Figure 4.19. This elbow was observed, for the twisted tape data, at approximately σ = 1.5-time steps. All twisted tape data presented herein were filtered using a σ = 1.5 time steps half-width filter to smooth out the trajectories and calculate velocity and acceleration. This was done as the last step for both twisted and untwisted particle trajectory data.

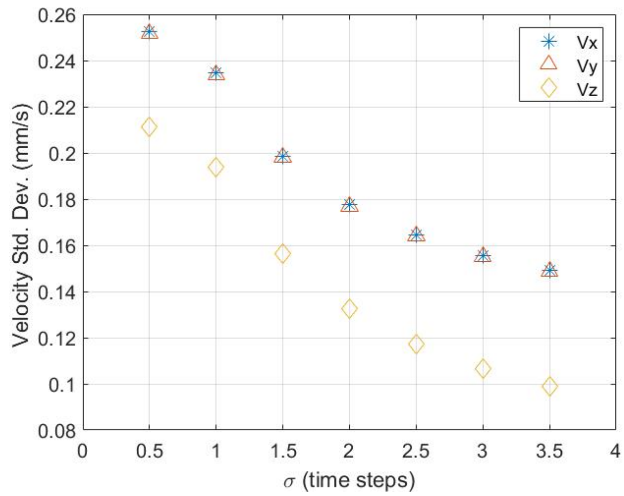

Figure 4.19: Standard deviation of the velocity versus filter width for twisted tape experiments.

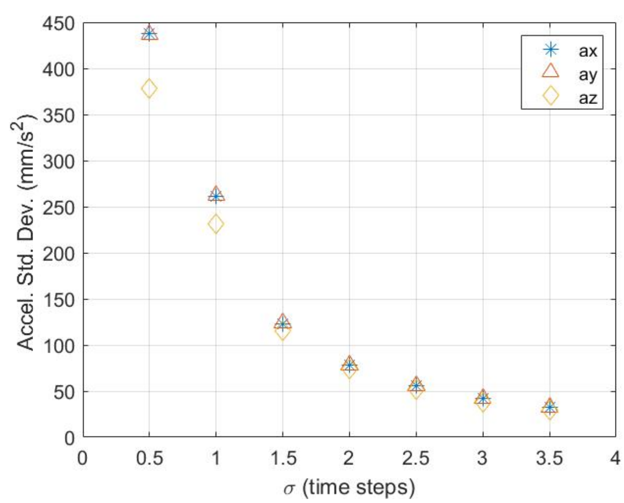

Figure 4.20: Standard deviation versus filter width for twisted tape experiments.

4.3.4 Eulerian Calculations

Post-filtering and untwisting of the data, the time−averaged and z−averaged Eulerian calculations, and contour plots were created based on the discretization of the geometry. This method consisted of equally spaced data points created in the $x - y$ plane. The averaging was done by averaging the velocities based on the number of particles that passed through a specific region of interest [145], based on Equation 4.9.

$$V_k(i, j) = \frac{\Sigma_{n=1}^{N_{particles}} V_k}{N_{particles}}, \tag{4.9}$$

where i, j are the $x - y$ spatial discretization regions, V is the velocity in an arbitrary direction k, where k could be in the x, y, z, r or θ direction, N is the total number of particles that pass through that specific region.

Additionally, the uncertainty of the velocity at each discretization region, $\sigma_{V_k}(i, j)$, was calculated based on the individual velocity uncertainty of each particle at each time step, σ_{V_k}, that was propagated from the uncertainty of the position through the convolution of the kernel filter. The uncertainty at each spatial discretized cell was calculated based on Equation 4.10.

$$\sigma_{V_k}(i, j) = \sqrt{\frac{\sum_{n=1}^{N_{particles}} \sigma_{V_k}^2}{N_{particles}}}. \tag{4.10}$$

4.3.5 Azimuthal Velocity Correction - Smaller widths

An interesting phenomenon was found in the Eulerian results for the twisted tape of width $w/D = 0.85$. This phenomenon consisted of particle trajectories not rotating with the twisted tape insert. The small width of the twisted tape allowed for a section of the flow to go untwisted. As a result, particle trajectories were found that would pass through the field of view outside the width of the twisted tape insert. This resulted in particle trajectories not twisting with the flow. The untwisting Matlab code does not differentiate between a particle rotating with the twisted tape and one that is simply passing through. Due to this, the code would add a twisting effect to the particles that would pass without twisting. The resulting Eulerian contour plots in the x, y, r and $\theta-$directions would result in biased velocity contours as the untwisted particles would gain artificial velocity due to the twisting motion. A couple of techniques were developed to address this issue. The first one consisted of removing the transaxial velocity based on the tangential velocity derived by Manglik and Bergles [86, 87]. This velocity is defined as the x and y components of the real velocity of the flow. Unfortunately, when the tangential velocity was removed from the x and $y-$velocities, it did not result in the same contour plots as observed in the other twisted tape inserts. The goal was to obtain velocity contours that replicated the region where the twisted tape insert is located, while not removing the real physical phenomena occurring in the gap. The second method obtained the average V_θ as a function of r to subtract the mean velocity from the transaxial flow. A plot of the mean θ-velocity as a function of r for the smaller width twisted tape insert is shown in Figure 4.21. As can be observed, the V_θ is higher as r increases and approaches the wall. This V_θ average was then used to adjust the x and y components based on Equations 4.11 and 4.12 in the untwisted trajectories. The $\theta-$velocity shown in Figure 4.21 was obtained from the artificially adjusted twisted velocity, which is different from the $\theta-$velocity shown in Figure 4.41. Further discussion follows on the difference between the two methods in the results sections.

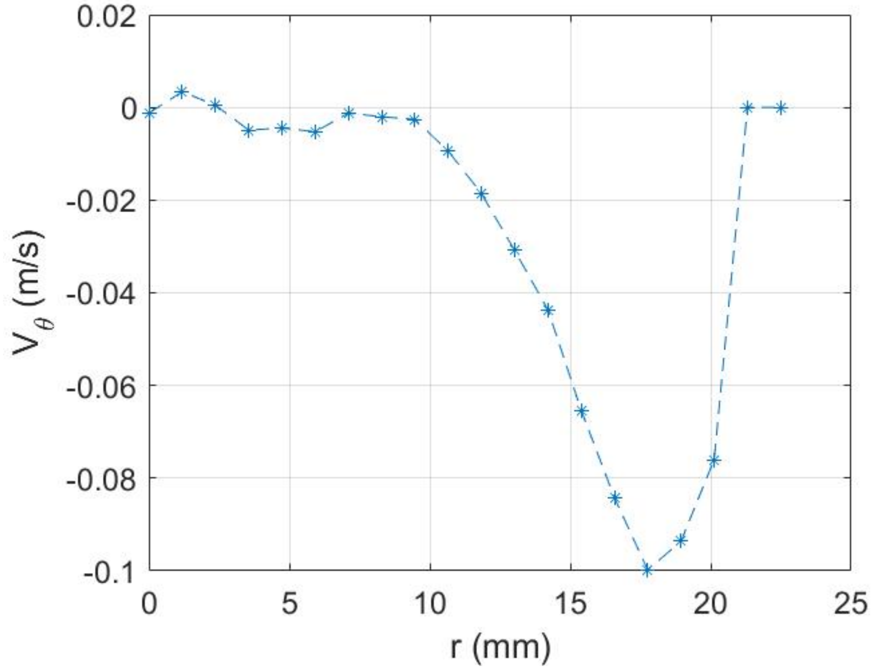

Figure 4.21: Azimuthal average of V_θ versus radius for twisted tape insert of w/D = 0.85 for Reynolds number = 17,700 to adjust radial velocities.

$$V_{x,new}(i,j) = V_{x,old}(i,j) + V_{\theta,mean}(r) \cdot \frac{y}{R}, \tag{4.11}$$

$$V_{y,new}(i,j) = V_{y,old}(i,j) - V_{\theta,mean}(r) \cdot \frac{x}{R}, \tag{4.12}$$

4.4 Results

This section summarizes the results obtained from PEPT for the three different twisted tape inserts (w/D = 1.0, 0.95, and 0.85) for the different Reynolds numbers. The Reynolds numbers used in this section consist of the circular pipe Reynolds numbers, similar to those in Equation 3.3. The Reynolds numbers were 17,700, 8,000, and 4,000. The twisted tape inserts have been shown to suppress turbulence, thus the 8,000 and 4,000 Reynolds numbers are considered to be in the transitional and laminar regime for these geometries. This section is divided into different subsections, contour plots, azimuthally averaged velocities, velocity profiles at different angles, vorticity, and Reynolds stresses. The contour plots, Section 4.4.1, were obtained from the untwisted velocity trajectories and averaged through time and space to obtain 2-D contour plots. These serve to provide further insight into the velocity structures occurring at the twisted tape inserts. The azimuthally averaged velocities, Section 4.4.2, were obtained from the twisting trajectories and averaged into radial bins.

Previous work done on PEPT to average the radial components into equally area-spaced bins has been explored for the geometry of a circular pipe, but this work focused on Eulerian discretization summarized in Section 4.3.4. The velocity profiles at different angles 4.4.3 were obtained from the contour plots in the twisting frame and linearly interpolated to match the radial and angle location.

Table 4.4: Summary of reconstruction results for each experiment, average estimated uncertainty in position, average number of coincident lines used for detection and estimated activity per particle in each experiment for additively manufactured test section (A.M.) and traditional.

Experiment	No. of Traj.	Δ x (mm)	Δ y (mm)	Δ z (mm)	No. of CL	Act. per Part. ($\mu Ci/particle$)
A.M., Re = 17,700	7,173	0.73	0.73	0.58	27	12.80
w/D = 0.95, Re = 17,700	5,322	0.96	0.96	0.76	15	7.11
w/D = 0.95, Re = 8,000	321	0.79	0.79	0.61	23	7.27
w/D = 0.95, Re = 4,000	974	0.64	0.65	0.51	41	9.72
w/D = 0.85, Re = 17,700	1,474	0.55	0.55	0.42	54	25.6
w/D = 0.85, Re = 8,000	1,040	0.48	0.49	0.35	73	23.08
w/D = 0.85, Re = 4,000	422	0.38	0.38	0.29	118	27.98

Table 4.4 summarizes the reconstruction results for each experiment with the number of trajectories reconstructed and filtered and the spatial uncertainty which is highly dependent on the average number of coincident lines (No. of CL), ($\sigma^2 \sim 1/\sqrt{CL}$) [127]. The number of coincident lines greatly affects the uncertainty of the location of the particle, as the higher number of coincident lines found in a time step allows for a better approximation of the particle location at that point in time. The number of radiolabelled particles, the amount of ^{18}F that was able to attach to each particle, the speed at which the particles are passing by the field of view, and the reconstruction parameters greatly affect the number of coincident lines found. The M-PEPT reconstruction parameters were kept at similar values for similar Reynolds numbers, but unfortunately, the volume of ^{18}F delivered was a bigger factor in how active the particles were created. The high uncertainty in the test consisting of Reynolds number 17,700 for the twisted tape width of w/D = 0.95 is further propagated in the results. The activity per particle and the number of particles passing through the field of view are much lower than the saturation limits of the Mediso LFER scanner [153], thus the dead time of the scanner did not affect the current results.

Figures 4.22 to 4.24 plot the velocity in the x, y and z direction obtained from 150 filtered trajectories for a twisted tape width of w/D = 0.95 and Reynolds number of 8,000. The particles are traveling from left to right with the swirling motion of the twisted tape insert clearly observed as they travel through the field of view of the scanner. Figures 4.22 to 4.24 plot the twisted instantaneous velocities of the particles. The data from the twisted Lagrangian velocity differs from the contour plots, as the velocity of the contour plots was obtained after the particle trajectories were untwisted and adjusted to have the twisted tape match the $x-$axis.

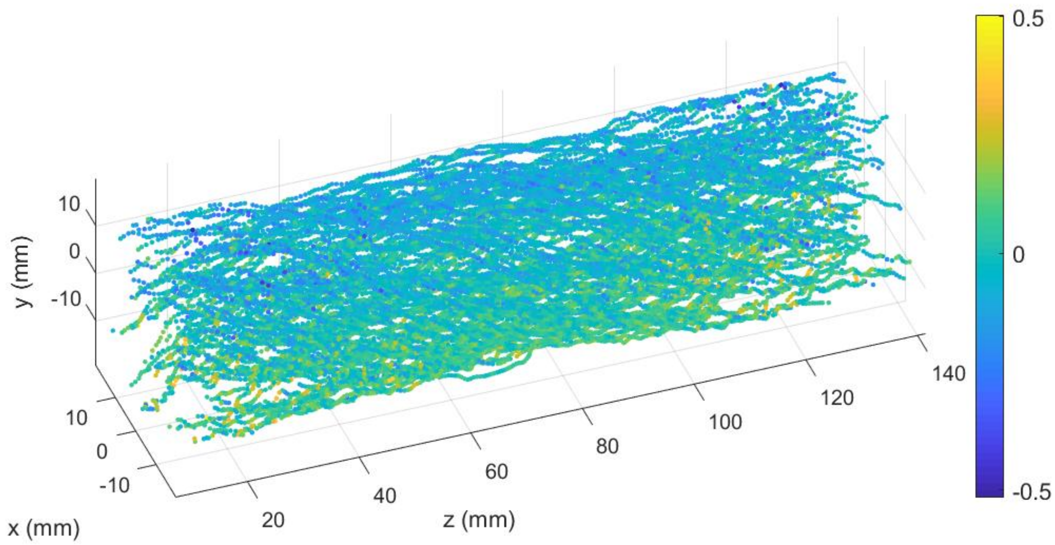

Figure 4.22: Velocity in the $x-$direction for 150 filtered trajectories from twisted tape of width $w/D = 0.95$ at a Reynolds number of 8,000.

4.4.1 Contour Plots

This section shows the contour plots for the twisted tape inserts which are of great interest based on literature [73, 74, 93]. In total, seven velocity contours are shown for the $z-$direction for the seven different twisted tape conditions. Afterward, a selection of velocity contours in the x and $y-$directions are shown in which interesting phenomena were observed. The contour plots show the velocity data in the $x-y$ planes with rotation of twist in the counter-clockwise direction. The first V_z contour plot consists of the additively manufactured twisted tape at a Reynolds number of 17,700, shown in Figure 4.25, as a nondimensionalized velocity divided by the maximum velocity found in the $z-$ direction, V_z. All the V_z contour plots can be interpreted as the positive V_z flowing out of the page. Figure 4.25 shows a clear distinction from where the twisted tape insert is located, horizontal in the $x-$axis. The velocity contour also shows two larger velocities occurring opposite from one another in the direction of the twist. These larger velocities have a form of tail that decreases in width the further away it goes from the location of the twist. In addition, the tight-fitting twisted tape ($w = D$) shows a clear distinction between the two semi-circles, with only small velocities

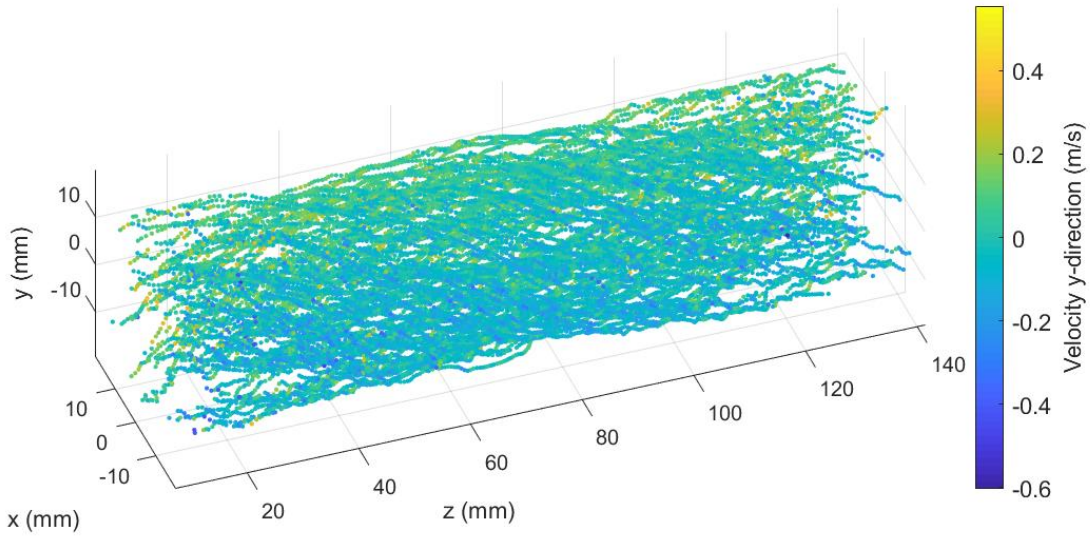

Figure 4.23: Velocity in the $y-$direction for 150 filtered trajectories from twisted tape of width $w/D = 0.95$ at a Reynolds number of 8,000.

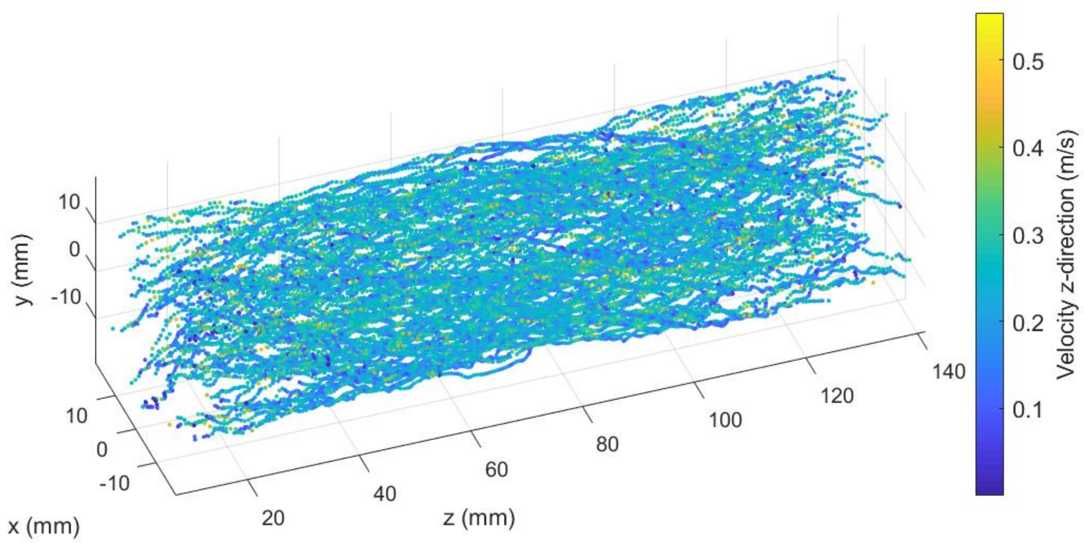

Figure 4.24: Velocity in the $z-$direction for 150 filtered trajectories from twisted tape of width $w/D = 0.95$ at a Reynolds number of 8,000.

(almost negligible) found at the width of the twisted tape. These are caused by the discretization methods described in Section 4.3.4, as small sections that encompass the twisted tape might also extend towards the flow. This is also a result of uncertainty in the trajectory reconstruction and the methods used to calculate the center of the geometry and untwisting. This phenomenon was also observed in a PEPT twisted tape velocity paper from Wiggins et al [131]. In addition, the clear distinction of the location of the twisted tape in comparison with the pipe allowed for better resolution near the twisted tape region. This phenomenon would be less effective with the loose-fitting twisted tapes ($w \neq D$). An inflow region at the center of the pipe is also observed that was previously described by Smithberg and Landis [93]. In this case, the inflow region was defined as the lower $z-$velocities found near $r = 0$. Smithberg and Landis used transaxial velocities to better approximate the inflow region, associated with lower velocities in the $z-$direction.

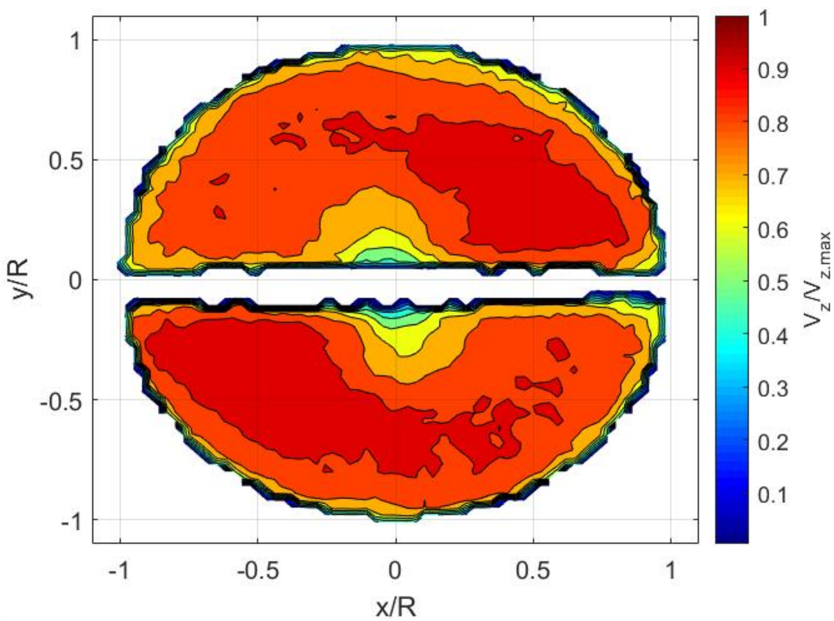

Figure 4.25: Nondimensionalized velocity contour of V_z for additively manufactured twisted tape insert ($w/D = 1$) at Re = 17,700.

Figure 4.26 plots the nondimensionalized velocity contour of V_z for the loose-fitting twisted tape insert for a width of $w/D = 0.95$, with a similar Reynolds number to the additively manufactured twisted tape insert, Figure 4.25, Re = 17,700. The first thing to note is how the twisted tape width makes it harder for the visualization of the twisted tape, as in Figure 4.26 the twisted tape appears to be leaning to the side of the left wall. The two velocity structures that appear in the additively manufactured twisted tape are also observed, but their shape is not as symmetric or as well defined. For easier discussion, the regions are divided into their respective quadrants. In the case of the loose-fitting twisted tape insert, the region that has the twisted tape touching the wall, the one located in the third quadrant, has better-defined structures than its counterpart, the one in the first quadrant. The one located in the first quadrant is experiencing the flow crossing between the two semi-circles thus not allowing it to develop properly. This is further shown as a large $z-$velocity near the right wall was formed.

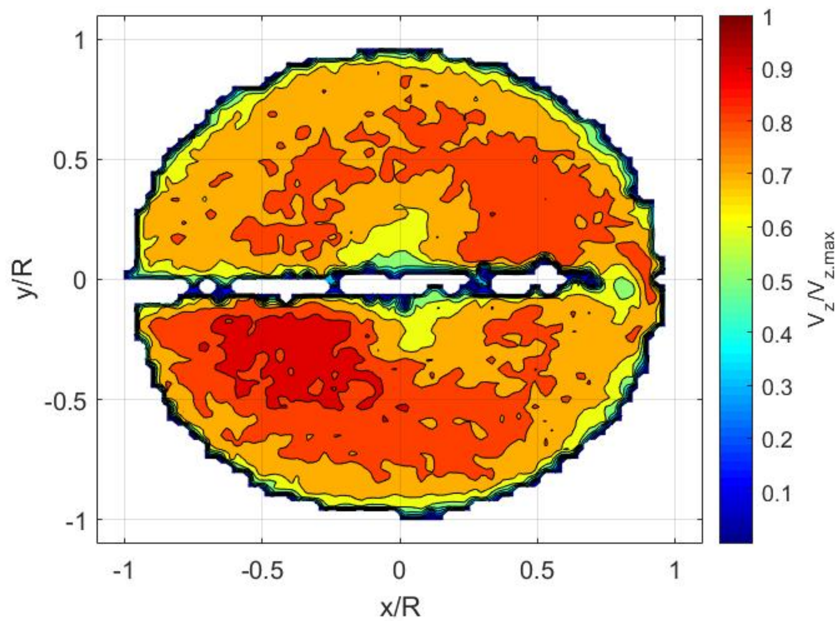

Figure 4.26: Nondimensionalized velocity contour of V_z for twisted tape insert of width w/D = 0.95 at Re = 17,700.

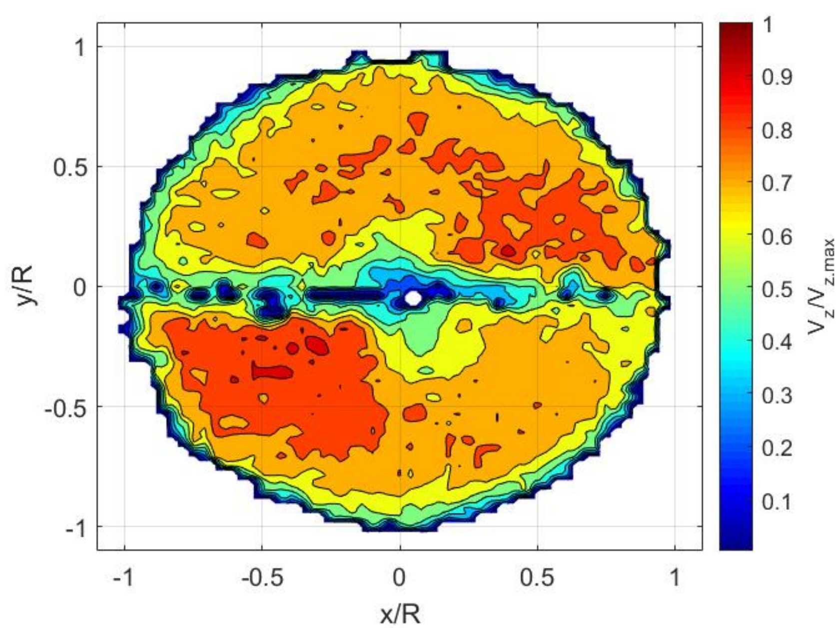

Figure 4.27: Nondimensionalized velocity contour of V_z for twisted tape insert of width w/D = 0.95 at Re = 8,000.

Velocity data was obtained at a Reynolds number of 8,000 and 4,000 for the twisted tape width of w/D = 0.95, with nondimensionalized velocity plots shown in Figures 4.27 and 4.28, respectively.

Both data sets were obtained on two different experimental days, thus the exact geometry of the twisted tape location was not matched, as small changes in the exact location of the twisted tape are expected. The velocity contours between tests match in general shape, with the exception of the exact location of the twisted tape insert. For a Reynolds number equal to 8,000, similar flow structures are observed as the turbulent Reynolds number but not as dominant or pronounced as those found in the higher Reynolds number, Re = 17,700. Smithberg and Landis [93] describe these regions as "high-velocity islands." These islands decreased in size when comparing the two Reynolds numbers. The high-velocity islands at the tail of the flow structure are smaller in size, in quadrants II and IV. Though, the higher velocity structure in the third quadrant is better defined and shaped than the one in the first quadrant. Further concluding that the twisted tape is resting near one of the walls allowing for the creation of a semi-circular division between Quadrants II and III, but allowing for flow to cross between semi-circles in Quadrants I and IV. In addition, the inflow region at the center of the pipe that was observed for the Reynolds number of 17,700 further decreased in size.

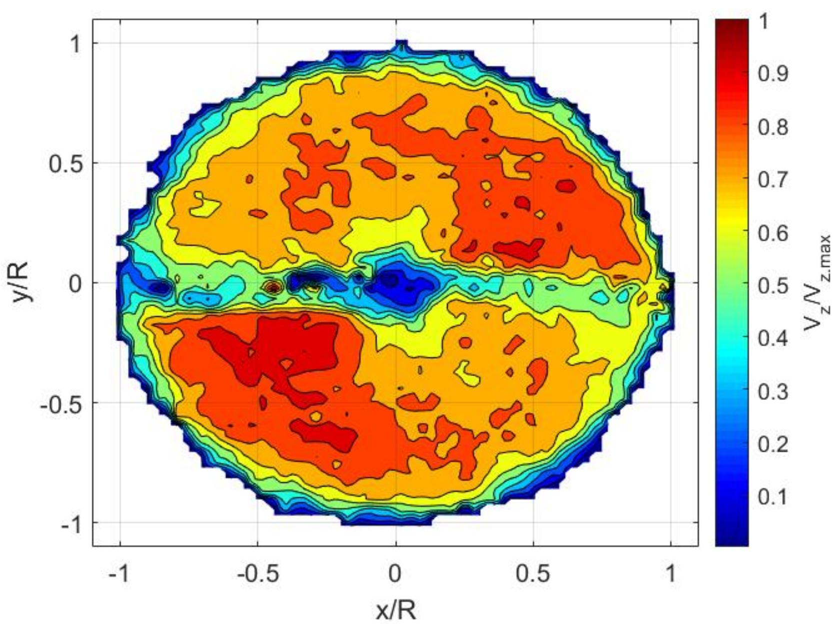

Figure 4.28: Nondimensionalized velocity contour of V_z for twisted tape insert of width w/D = 0.95 at Re = 4,000.

The twisted tape was harder to detect in the lower Reynolds number twisted tape data, as shown in Figures 4.27 and 4.28 with the lack of clear distinction in the twisted tape insert. The twisted tape thickness, δ, consisted of 1.55 mm, and the size of the discretization element for both cases was larger than half the thickness thus the spatial discretization near the twisted tape is not small enough to completely separate the twisted tape with the flow near it. Smaller discretization sizes were explored, but the limited number of particles made it hard to recover significant data. Thus for these plots, Figures 4.27 and 4.28, a clear distinction between the two semi-circles was not accomplished and connections in the flow are observed. Nevertheless, the contours provide important insight into the flow behavior at the lower Reynolds numbers. For the low Reynolds number, the appearance of "low-velocity islands" are also observed. These occur in regions of the flow that have lower velocities in comparison with their neighbors. Additionally, the inflow regions also decrease in size with lower Reynolds numbers.

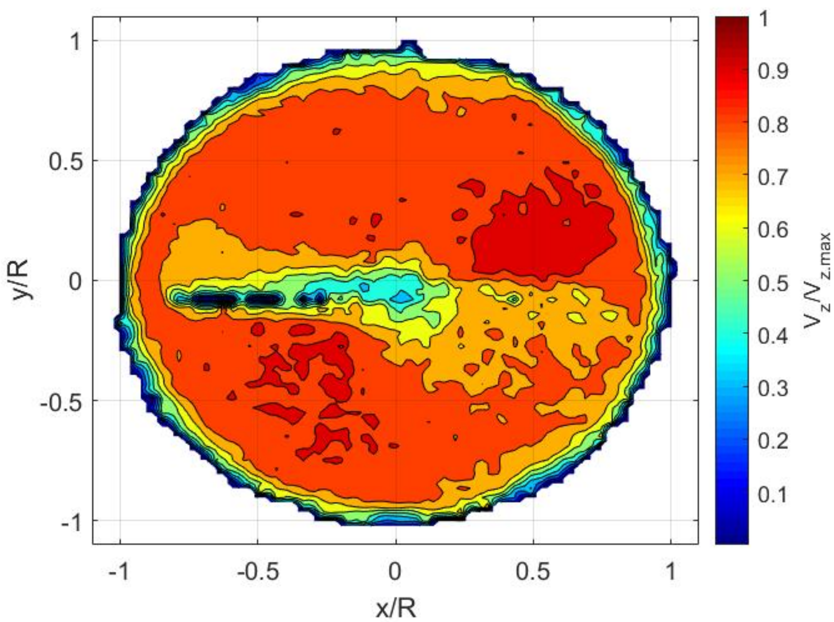

Figure 4.29: Nondimensionalized velocity contour of V_z for twisted tape insert of width w/D = 0.85 at Re = 17,700.

The $z-$velocity contour for the twisted tape width of $w/D = 0.85$ for a Reynolds number of 17,700 is shown in Figure 4.29. This plot shows the impact the width of the twisted tape insert has on the overall velocity contour. The larger wall-to-twisted tape clearance allows for more flow to pass between the two semi-circles. In addition, the exact location of the twisted tape with this width is harder to identify. While some flow structures reach a zero velocity near the negative $x-$axis, this is not the same case for the positive $x-$axis. The current averaging methodology in the $z-$direction causes some discrepancy where the twisted tape location is as it is moving across the circular pipe. Thus the discretization method and the vibrations that occur from the twisted tape, make it harder to identify the twisted tape from the particle trajectories. In addition, the two separate velocity structures found in the twisted tapes of width w/D = 1.0 and 0.95 are not as well defined in this case. Both structures seem to have merged together as the gap between the twisted tape and the inner diameter of the pipe was large enough. Additionally, the inflow region for this twisted tape insert is almost entirely gone. The overall flow contour expected from the previous flow velocity contours differs from the ones of the tighter twisted tape inserts.

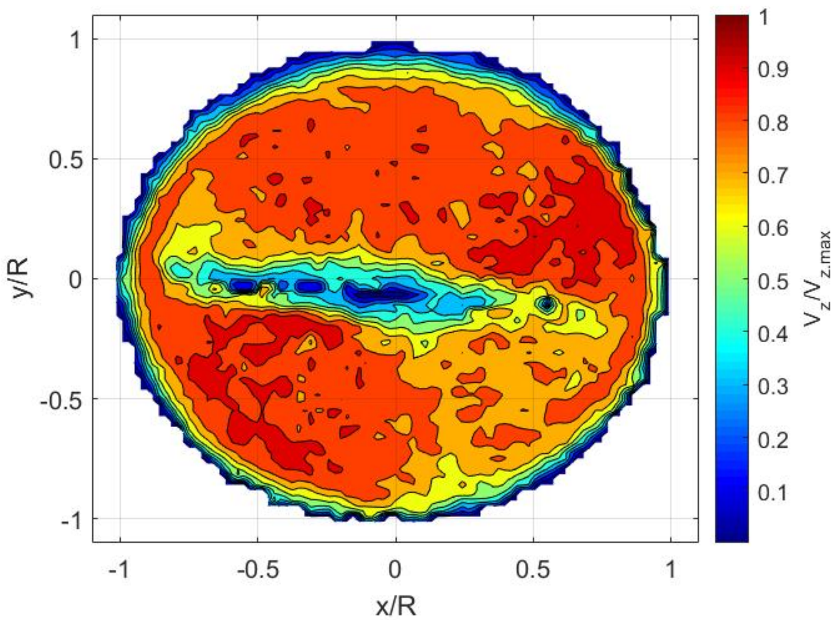

Figure 4.30: Nondimensionalized velocity contour of V_z for twisted tape insert of width w/D = 0.85 at Re = 8,000.

PEPT data was also obtained for the twisted tape width $w/D = 0.85$ at Reynolds numbers of 8,000 and 4,000, as shown in Figures 4.30 and 4.31 respectively. These plots also aid to show how the velocity contours previously observed for the larger twisted tape width and the additively manufactured twisted tape differ. One interesting thing to note consists of the velocity field near the twisted tape and the walls of the pipe. The large velocity islands previously observed for the larger widths of twisted tape inserts are not as well defined and formed in this geometry. More data should be acquired in these geometries to further understand the effects of the loose-fitting twisted tape inserts. Additionally, the inflow region is entirely gone. The overall contour plots for the $z-$velocity for the smaller twisted tape widths are more uniform due to the disappearance of the large velocity islands. The large velocity islands are not allowed to form in these geometries. Additionally, the effects of twisted tape width are clearly observed on the different velocity contours.

The nondimensionalized velocity contours in the x and y direction for the additively manufactured test section at a Reynolds number of 17,700 are shown in Figure 4.32. The velocity is normalized by the maximum velocity in the z direction to be consistent with the methodology of the V_z contour plots. Figure 4.32 shows the complexity of the transaxial velocity of the twisted tape inserts. In general, the larger magnitudes of velocity in the x direction are observed near the twisted tape

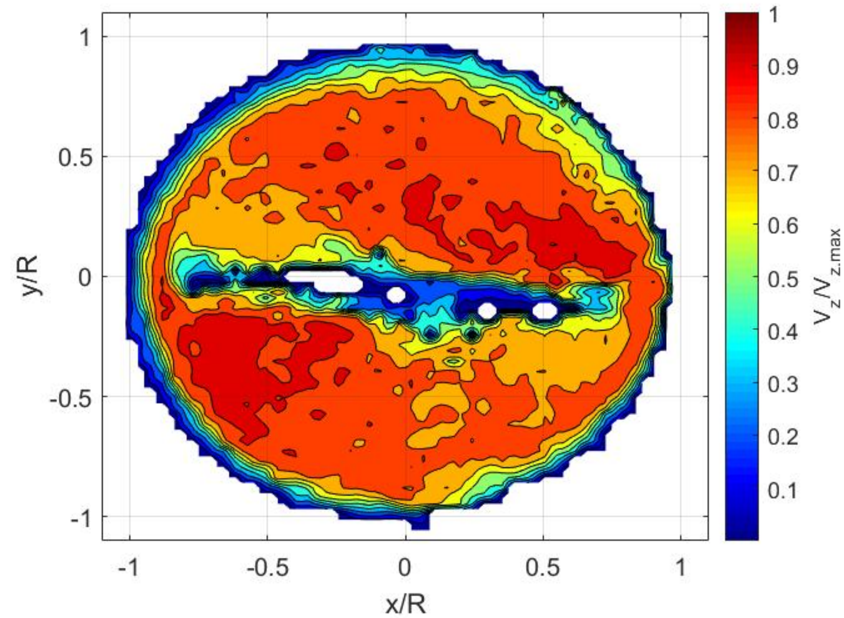

Figure 4.31: Nondimensionalized velocity contour of V_z for twisted tape insert of width w/D = 0.85 at Re = 4,000.

insert. The $x-$velocity also shows oscillatory velocities in which the direction changes depending on the location. While in the $y-$direction, no major velocities are observed, but instead a pattern is observed for the flow direction. This V_y pattern in the contour plot is not observed when comparing the velocity in the loose-fitting twisted tape inserts. Figure 4.33 plots the V_y velocity for Reynolds numbers of 4,000 and 8,000 for the twisted tape of width $w/D = 0.95$. The twisted tape insert is not as clearly defined, or observed, in these contours as the ones from the z Velocity, Figures 4.26 to 4.28, where a clear zero velocity is observed near the $x-$axis. Instead, the velocity magnitude is already low enough near it that it blends with the current discretization technique, as explained in the V_z contours above. Instead, focus is brought to what is physically occurring at the gaps between the twisted tape insert and the pipe's walls. The flow in the $y-$direction was of special interest due to the observation of the high-velocity spots created by the gap of the twisted tape insert. The velocity contours in the $x-$direction mainly showed the high velocities observed near the twisted tape that further create inflow regions near the center of the twisted tape. Thus, a further focus was brought to the velocity in the $y-$direction. The loose-fitting twisted tape creates a region in which the flow is allowed to cross between the two semi-circles at higher velocities than the average transaxial velocity, the red and blue regions in Figure 4.33. It is noted that the direction of the velocity is greatly affected by the twisting motion, in which the velocity is negative on the right side (since it is moving from the top semi-circle to the bottom semi-circle). The opposite is observed near $x/R = -1$, in which V_y is positive describing how the flow is moving from the bottom semi-circle to the top one. A similar phenomenon is observed in Figure 4.34, which plots the nondimensionalized V_y contours for the twisted tape widths of w/D = 0.85 on the left side and w/D = 0.95 on the right for a Reynolds number of 17,700. The contour plot for w/D = 0.85 was adjusted based on the methodology described in Section 4.3.5, and even with the azimuthal correction, a positive V_y is observed at $x/R = -1$. The effects that cause the azimuthal correction would have affected the entire gap, creating high-velocity spots in different locations, but this was not observed. It is also noted that the velocity pattern for V_y is not affected by the azimuthal correction, as the same pattern of changes in velocity direction is observed for the smaller width twisted tape as the additively manufactured velocity contour in Figure 4.32.

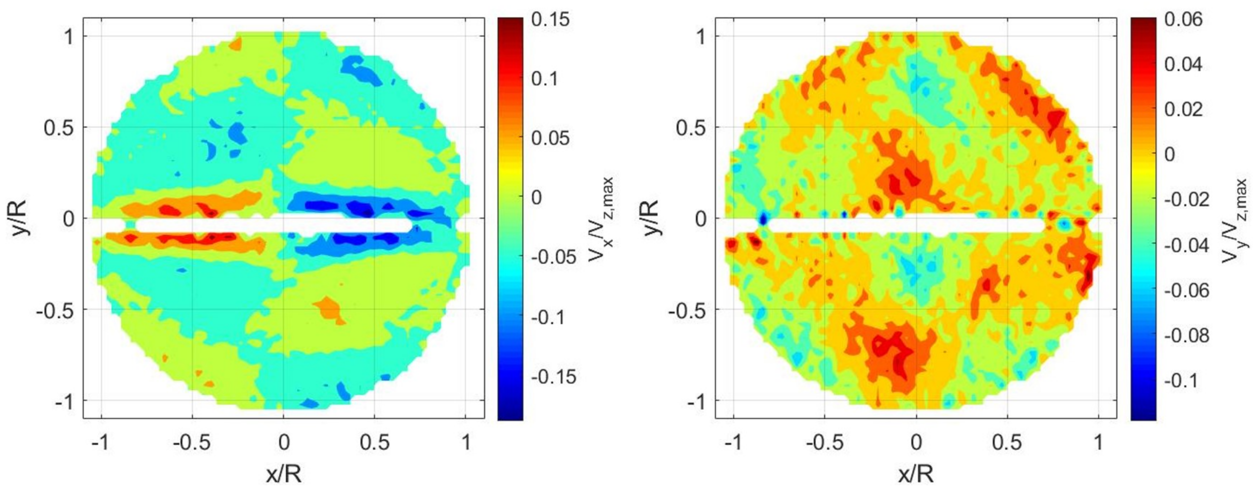

Figure 4.32: Nondimensionalized velocity contours of V_x (Left) and V_y (Right) for additively manufactured twisted tape insert at Re = 17,700.

It is noted that the reason why the negative velocity is not observed at x/R = 1 is due to the twisted tape resting on that side of the wall. This is further validated in the V_z contour plot shown in Figure 4.29 in which the velocity contour is not as continuous at that location. Additionally, the plot for the width of w/D = 0.95 for Reynolds number of 17,700, Figure 4.34 further proves the point in which in the occasion the twisted tape insert rests on one side of the wall, this will lead to the high velocity only appearing in one location, ($x/R \approx 1$). This further causes higher velocities in the transaxial direction when a loose-fitting twisted tape is used instead of a tight-fitting twisted tape.

Figure 4.35 plots the V_y contour for the twisted tape insert of width w/D = 0.85 for the Reynolds numbers of 4,000 on the left and 8,000 on the right. These two plots were also obtained by subtracting the averaged $\theta-$velocity, as discussed in Section 4.3.5, and shown on the left side of Figure 4.34. The velocity pattern is also observed in these plots even with the azimuthally average correction. One thing that is observed in all the smaller width transaxial velocities, is that both loose-

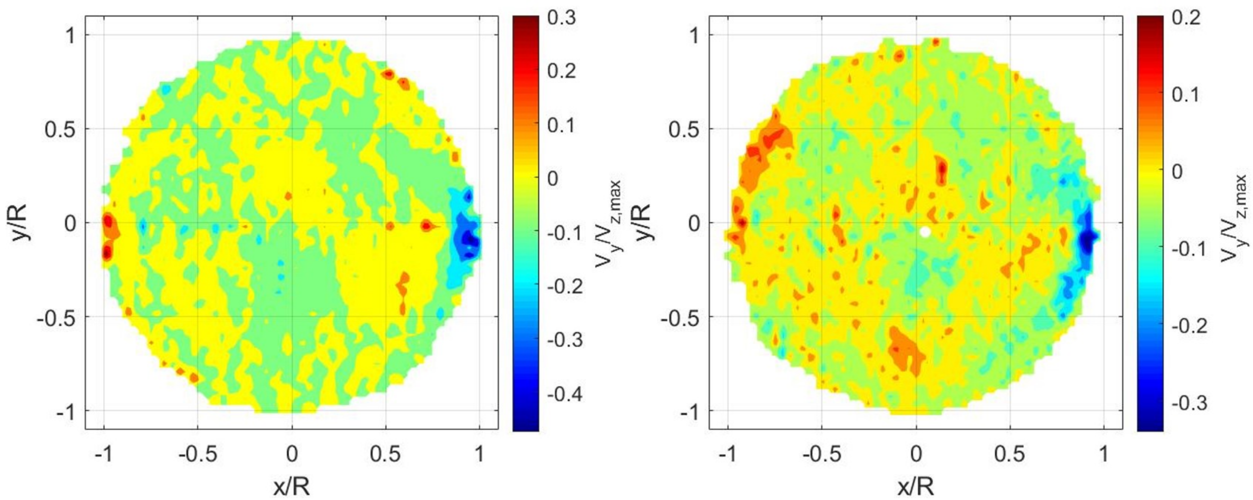

Figure 4.33: Nondimensionalized velocity contours of V_y for the twisted tape width of $w/D = 0.95$ for Reynolds numbers of 4,000 (Left) and 8,000 (Right).

fitting twisted tape inserts have flow crossing between the two semi-circles and that the velocity magnitude of this flow is consistently between 0.15 to 0.4 of the maximum $z-$velocity. This further highlights the need to further understand the velocity fields that occur for smaller-width twisted tape inserts, as that flow is hot spots occur due to the smaller twisted tape width. Furthermore, in applications that consist of loose-fitting twisted tape inserts and the distance between the walls and the twisted tape is large enough, there is a potential for larger transaxial velocities that were not previously identified near the gap of the twisted tape insert. This could lead to further cold and hot spots in the walls of the pipe at high heat flux environments, such as those in fusion or fission reactors.

The final velocity contour shown herein consists of the velocity in the $\theta-$direction. Only two plots are shown in Figure 4.36 for the additively manufactured twisted tape insert at a Reynolds number of 17,700, plotted on the left, with the velocity obtained from the twisted tape of width $w/D = 0.85$ at a Reynolds number of 8,000, plotted on the right. The 8,000 Reynolds number was chosen as it had the clearest representation of the phenomena on both sides of the gap between the twisted tape and the inner diameter of the pipe. While a clear distinction and pattern are observed for the additively manufactured twisted tape insert in which there is no flow crossing between the upper and lower semi-circles, the same can't be said of the counterpart. The $\theta-$velocity for the smaller twisted tape width is dominated by the velocities occurring near the clearance of the twisted tape insert.

A difference in the experimental contours was observed for the different geometries, as the flow was allowed to cross between the semi-circles, resulting in great dependence on the twisted tape

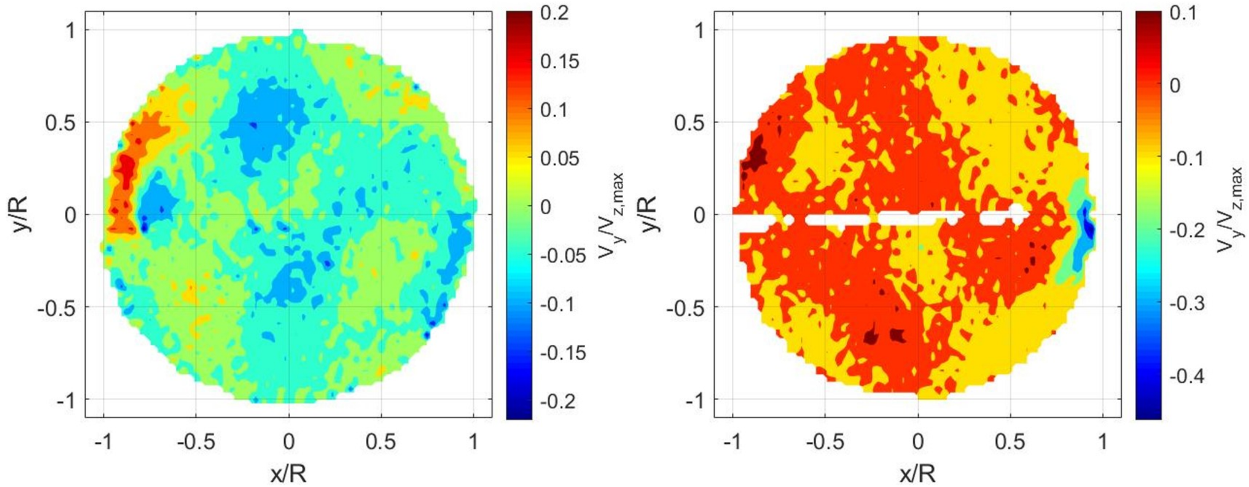

Figure 4.34: Nondimensionalized velocity contours of V_y for the twisted tape width of $w/D = 0.85$ (Left) and $w/D = 0.95$ (Right) for Reynolds numbers of 17,700.

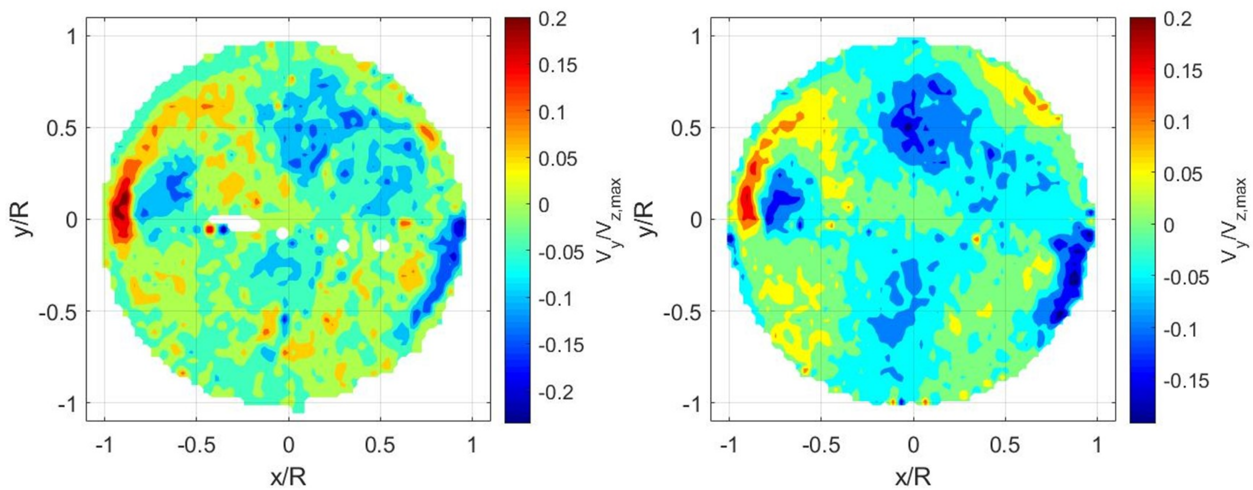

Figure 4.35: Nondimensionalized velocity contours of V_y for the twisted tape width of $w/D = 0.85$ for Reynolds numbers of 4,000 (Left) and 8,000 (Right).

flow with the twisted tape width. The velocity contour plot of the additively manufactured twisted tape insert is further compared with results found in the literature. Figure 4.37 shows the velocity contour comparison for the axial velocity obtained from the additively manufactured test section ($w/D = 1.0$) at a Reynolds number of 17,700 and a velocity contour obtained from Smithberg and Landis [93] at a Reynolds number of 140,000. The velocity contour for the additively manufactured test section has a flipped $x-$axis and negative velocity (to maintain constant axis configuration) to better match the swirl direction with the experiments from Smithberg and Landis [93]. The PEPT results show a qualitatively similar flow pattern to the one observed by Smithberg and Landis. A

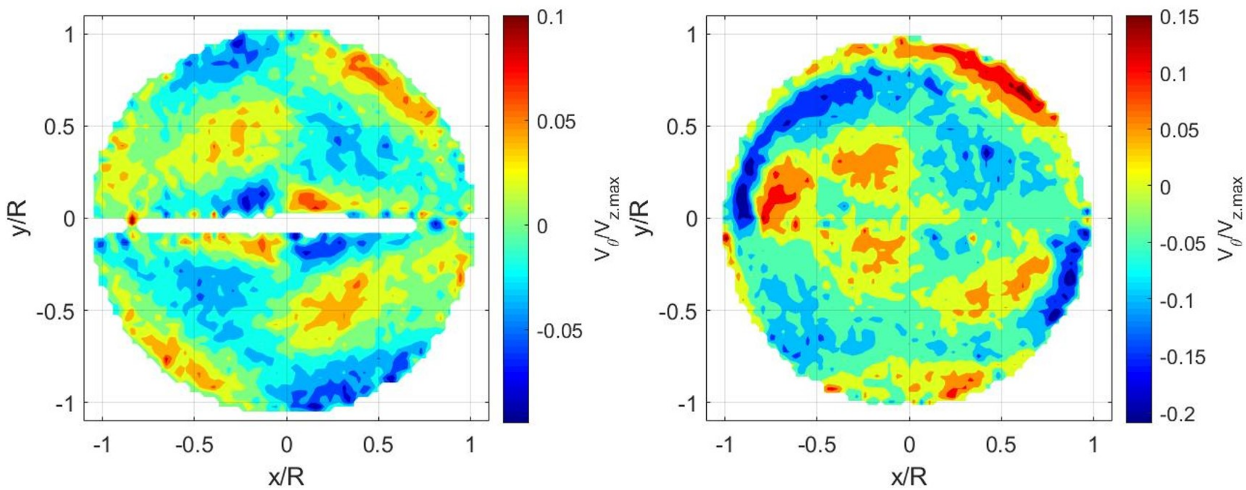

Figure 4.36: Nondimensionalized velocity contours of V_θ for the additively manufactured test section for Reynolds number of 17,700 (Left) and the traditional twisted tape insert of width w/D = 0.85 (Right) for a Reynolds number of 8,000.

higher velocity was observed next to the twisted tape insert, with a lower velocity region at the center of the pipe. Clark [74] noticed that this inflow region represents the secondary circulations in the fluid and this secondary flow mixes the boundary layer with the freestream fluid. The vortex flow is also responsible for the higher velocities observed near the twisted tape compared to the region near the walls of the circular pipe. Smithberg and Landis suggest the inflow region creates "high-velocity islands," as shown in their contour map. The high-velocity islands are higher velocities compared to their surrounding area. While the PEPT contour plots observed in this work do show the inflow vortex near the center of the twisted tape insert, it did not create the multiple islands observed by Smithberg and Landis, but instead, it created a large single velocity island next to the twisted tape in the direction of the flow. The flow velocity structures are not as grouped as the ones observed by Smithberg and Landis. In addition, the higher velocities observed near the twisted tape insert in comparison with the walls of the pipe can be observed by the PEPT results.

Clark [74] studied the effects the changing of the twisted tape pitch had on the velocity contour, but concluded that the flow was not observed to be fully developed for any of the cases except for the twisted tape of infinite pitch. Clark observed a dependence of the inflow structures observed by Smithberg and Landis when varying the pitch of the twisted tape insert. With larger inflow regions for the larger twisted tape pitch. Figure 4.38 shows the comparison of the same velocity contour plot of the twisted tape insert with one of the many contour plots shown by Clark [74] obtained through CFD and a velocity contour from Date [164] with a similar twisted tape pitch, y = 2.25 obtained using a numerical simulation with their derived transport equations. In this case,

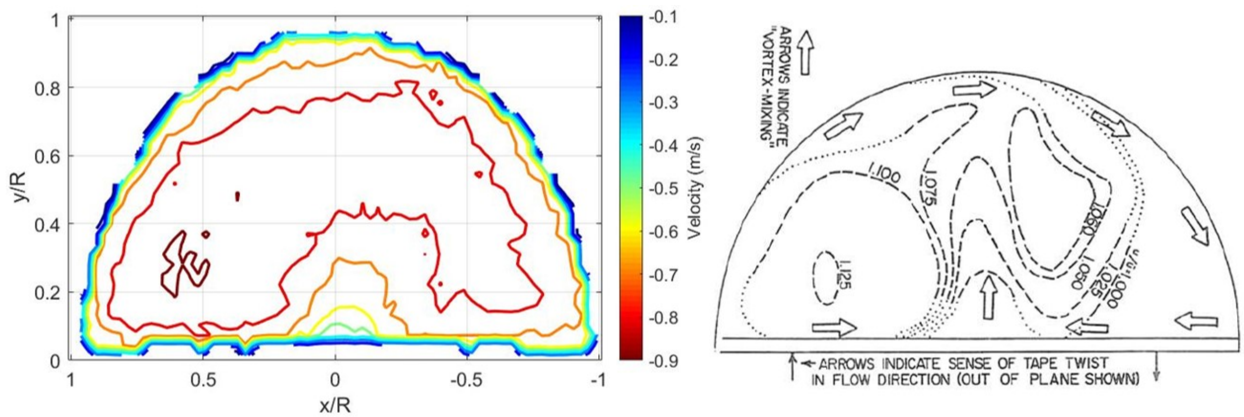

Figure 4.37: Velocity contour of axial velocity (V_z) for the additively manufactured twisted tape insert (w/D = 1.0) at a Reynolds number of 17,700 (Left) and the axial velocity contour from Smithberg and Landis [93] at Re = 140,000 and pitch of y = 5.15 (Right).

the contour plot of the additively manufactured test section is shown unflipped and unchanged. The PEPT data compares better with Clark's contour plot in the formation of the high-velocity region as it expands across the entire semi-circle, while Date's contour plot, shows a division of two different high-velocity islands. A higher velocity island next to the twisted tape insert is observed in both cases, though the computationally obtained velocity contours have a wider velocity island, as observed in the results from Clark and Date. Though the location of the high-velocity island in the case of Date's results is shown to develop at a higher location, not as near the twisted tape insert. The inflow region obtained by the PEPT data falls between the experimental data from Smithberg and Landis [93] and the simulations from Clark [74] and Date [164], in terms of the overall shape. Though it is noted that for the computational results, the inflow region is observed to be off-centered when compared to the experimental results shown in this work and in Smithberg and Landis [93].

4.4.2 Azimuthally - Averaged Velocities

Azimuthally averaged velocities were obtained by averaging the domain in z and θ through time and grouped into radial components. The data used in the azimuthally averaged velocities consisted of the twisting velocities, the same ones shown in Figures 4.22 to 4.24. In addition, the azimuthal average velocities' uncertainties were obtained based on the least squares method, similar to the uncertainty done for the friction factor and Nusselt number. Thus each radial data point is highly dependent on the number of particles that pass through it, as well as the original uncertainty in the position and velocity after the kernel filter was applied. Thus high uncertainties in Table 4.4 are propagated through the data and plotted in Figures 4.39 and 4.41. Data points that go beyond $r/R \approx 1$ are caused by the discretization and the uncertainty in the particle location.

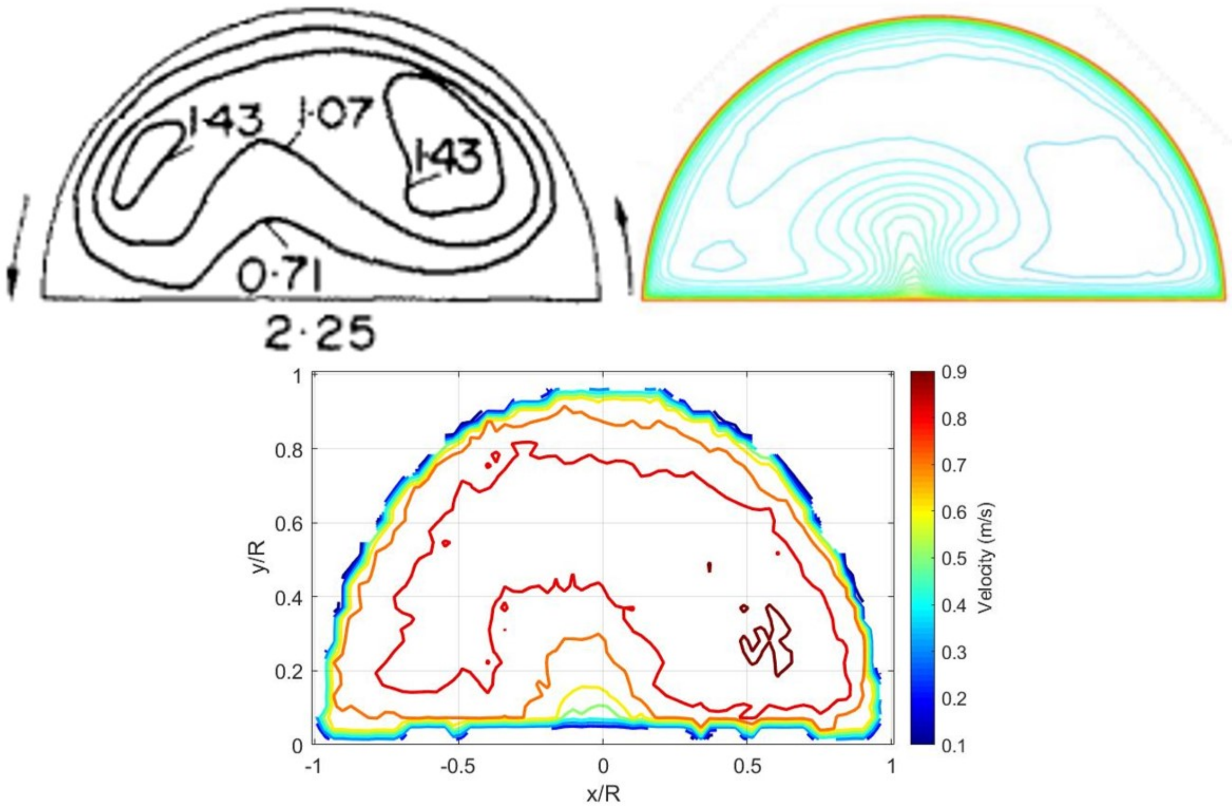

Figure 4.38: Velocity contour of axial velocity (V_z) for the additively manufactured twisted tape insert (w/D = 1.0) at a Reynolds number of 17,700 (Bottom) and the axial velocity contour from Clark [74] at Re = 80,000 (Right) and Date [164] at Re = 1,200 (Left).

The $z-$velocities in Figure 4.39 and 4.40 were normalized by the maximum velocity in the azimuthal average, $V_{z,max}$. This method collapsed the azimuthally average velocities into a common form. Figure 4.39 plots the V_z azimuthally averaged for the three twisted tape inserts at a Reynolds number of 17,700. This plot shows how the azimuthally averaged $z-$velocity collapses together at approximately r/R = 0.4 regardless of the width of the twisted tape. The major changes are observed earlier in the velocity plot, which is contradicting what the author would have originally expected. The $z-$velocity differs in shape as r/R approaches zero, since the geometry of the twisted tape insert is similar across the different tests, this region was the one expected to match across different twisted tape widths. This difference is attributed to the realization that the twisted tape is not as consistent in its z location as it is twisting in the pipe and it is not perfectly centered throughout the geometry. This leads to velocities occurring near the center of the pipe that gets averaged through the z and θ-directions. For the additively manufactured twisted tape insert, w/D = 1.0, the velocity does approach zero as r/R approaches 0. Additive manufacturing has proven to be precise in its manufacturing and installation, while for traditional manufacturing the twisted tape oscillates within the geometry in the $z-$direction. This leads to different parts of the twisted tape

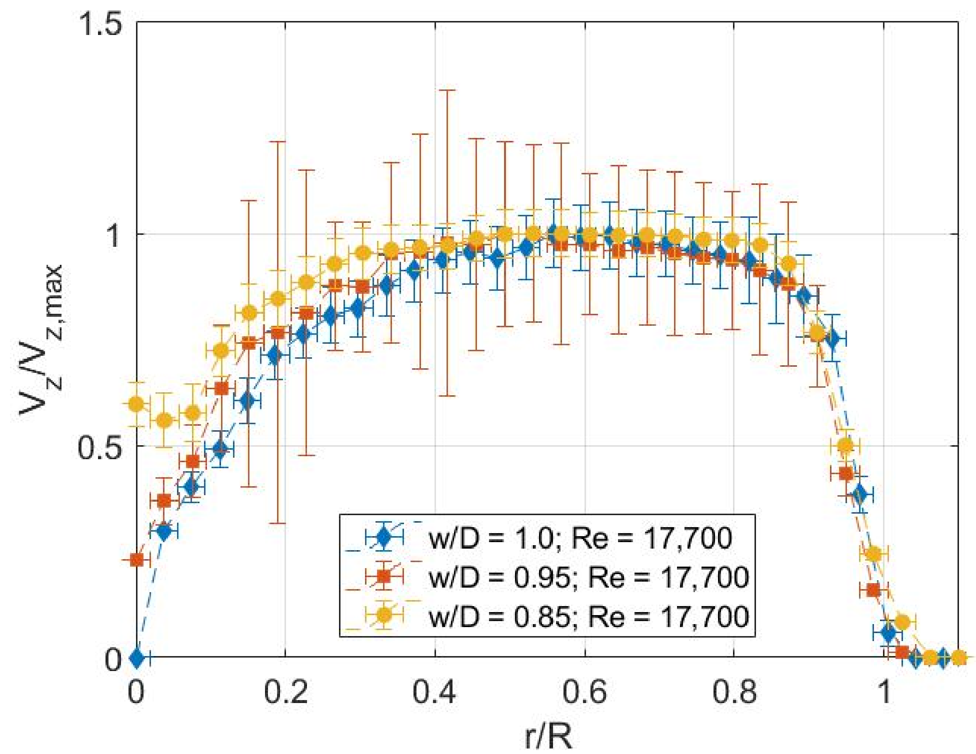

Figure 4.39: Averaged nondimensionalized azimuthal V_z for the three twisted tapes at Re = 17,700.

touching the walls at different z and θ locations. This affects the $z-$ velocity near the center of the pipe as observed in the azimuthally averaged plot in Figure 4.39, while it can also create higher transaxial velocities as discussed in Section 4.4.1. In addition, higher $z-$velocities were expected for the smaller widths as r/R approached one, but this was not observed. It is concluded, that while there is an increase in velocity at the gaps between the twisted tape and the circular pipe, as shown in the contour plots, the high velocities are averaged with the rest of the velocities to a common form similar to the tight fitting twisted tape insert.

This is further shown in Figure 4.40, which plots the azimuthally averaged V_z for the rest of the cases, twisted tape widths of w/D = 0.95 and 0.85 for Reynolds numbers of 8,000 and 4,000. Similarly to Figure 4.39, the velocities collapse together at $r/R \approx 0.4$ with the differences mainly observed with the velocities near the center of the geometry. Figure 4.40 also shows how only one velocity approaches zero at the center of the pipe, the $w/D = 0.95$ for a Reynolds number of 4,000. It is unclear with the current data if this is artificial or the actual velocity. More data should be gathered in these geometries to better understand the velocity near the twisted tape insert. The rest of the average velocities approach 0.5 $V_z/V_{z,max}$ as r/R approaches zero.

The final azimuthally average velocity plot consists of the $\theta-$velocity, shown in Figure 4.41. The

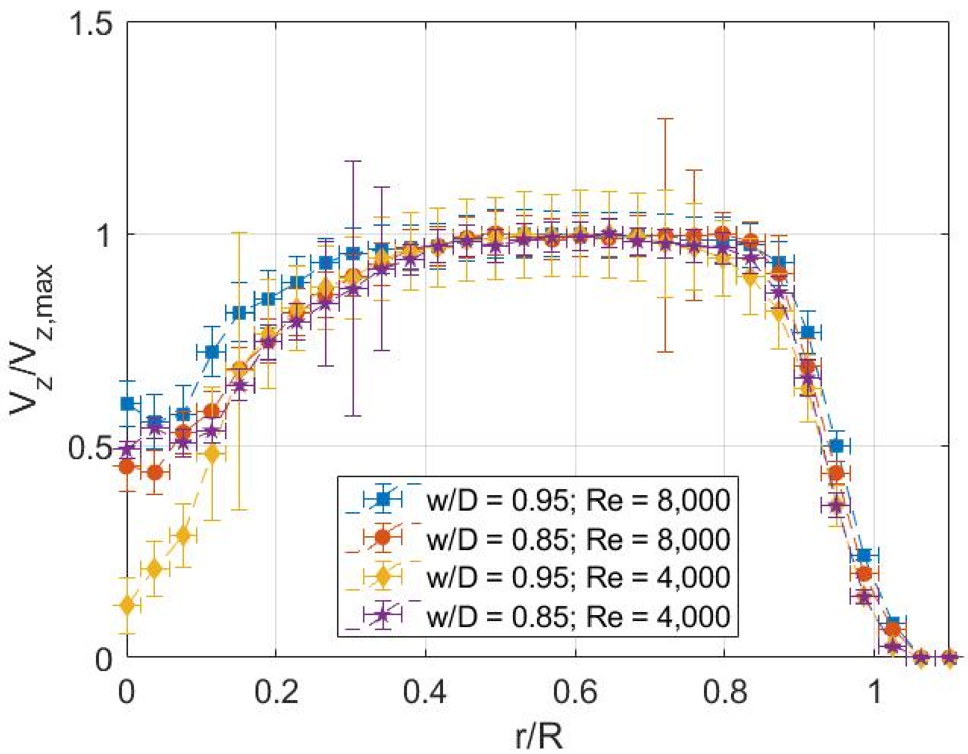

Figure 4.40: Averaged nondimensionalized azimuthal V_z for twisted tape widths w/D = 0.95 andd 0.85 at Re = 4,000 and 8,000.

$\theta-$velocities in this case were not corrected using the azimuthal correction of Section 4.3.5. For this case, a different normalization value was chosen as the V_{mean} of the empty pipe velocity. This empty pipe mean velocity is the same velocity used to define the Reynolds numbers. Normalizing the $\theta-$velocity with the mean empty pipe velocity results in the data collapsing to a common form. This is expected as the $\theta-$velocity is heavily dependent on the initial velocity before the twisted tape insert. The normalized θ-velocity has a similar trend for all twisted tapes as it travels from the center of the pipe toward the pipe's inner diameter. Additionally, the slope of the normalized $\theta-$velocity is the same regardless of Reynolds number and twisted tape geometry. The V_θ for the loose-fitting twisted tape inserts of width w/D = 0.85 are the first to break the observed slope as they start decreasing and trending downwards. The maximum V_θ for these twisted tapes occurs at approximately $r/R \approx 0.7$. A similar trend is observed for the loose-fitting twisted tapes of width w/D = 0.95, but the velocity starts decreasing at $r/R \approx 0.8$. The largest V_θ observed consisted of the additively manufactured test section, with the peak occurring at $r/R \approx 0.9$. The maximum V_θ for all cases doesn't occur at the edge of the twisted tape insert's width, but slightly earlier. For the additively manufactured geometry, the velocity decreases due to the wall effects, but it is not clear why the velocity decreases before the edge of the twisted tape insert in the loose-fitting cases.

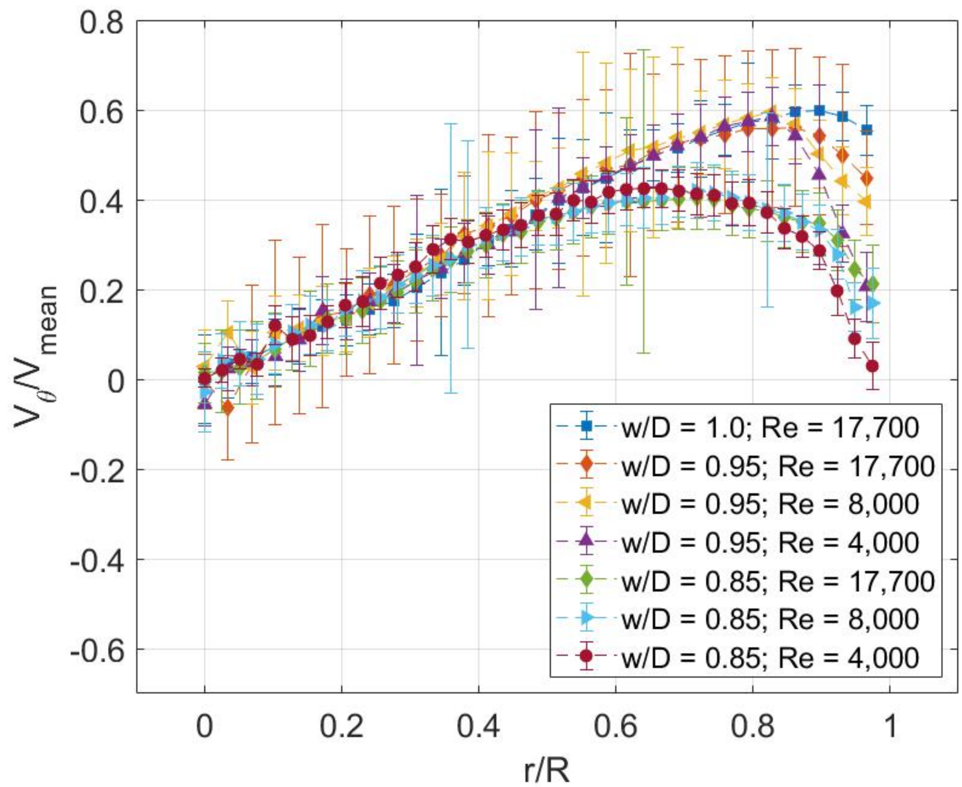

Figure 4.41: Averaged nondimensionalized azimuthal V_θ for the three twisted tape inserts of different widths for the three different Reynolds numbers, Re = 17,700, 8,000, and 4,000.

Additionally, the large uncertainties in Figure 4.41 are mainly occurring for the twisted tape of width w/D = 0.95 at Re = 17,700, as inspected individually the error bars are smaller in the other cases. This large uncertainty is propagated from the initial large uncertainty in the position of the particles by the M-PEPT code.

4.4.3 Velocity Profiles

In addition to the azimuthally average velocity plots shown in Section 4.4.2, velocity profiles were obtained at three different angles across the semi-circle. This means that a line was drawn through the contour plots in Section 4.4.1 at three different angles, 45^o, 90^o, and 135^o, to study the velocity behavior dependent on θ and r. These angles were chosen as they interrogated the fluid flow in equally distant locations. The highest velocities are not expected to occur in these regions. A schematic showing the different angles used to describe the velocity profiles with respect to the semi-circle is shown in Figure 4.42 to help visualize the velocity locations within the twisted tape insert geometry. The velocity profiles were obtained at the gray dashed lines. Due to the two semi-circles created in the twisted tape insert, the velocities were averaged between the two semi-circles.

Thus the 45^o angle contains both the 45^o and the 225^o angles since the 225^o is located at a 45^o from the horizontal plane opposite to the twisting direction. The 90^o angle was also averaged with the 270^o angle and the 135^o with the 315^o angle.

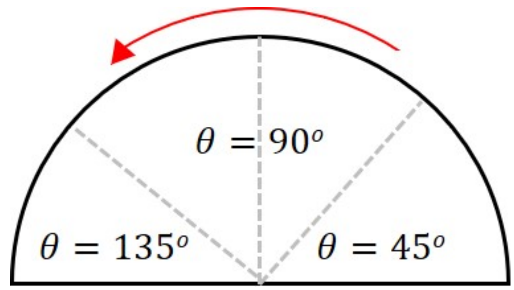

Figure 4.42: Schematic describing the linear locations based on the counter-clockwise angles with the red arrow in the direction of the twist.

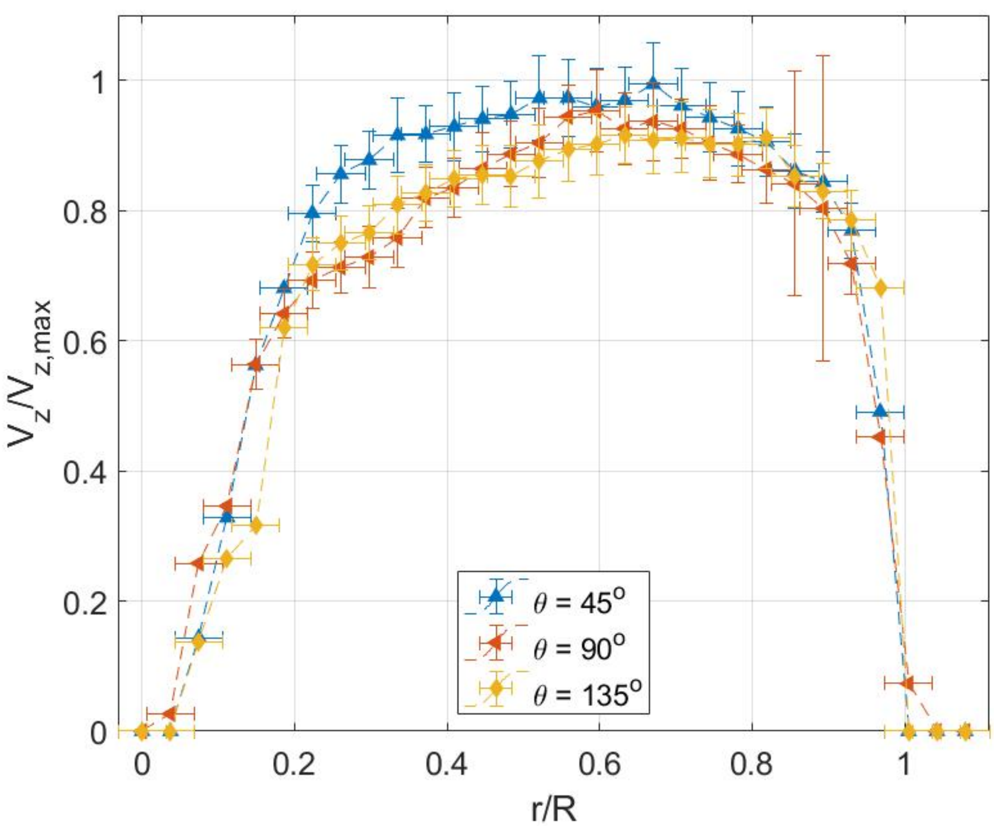

Figure 4.43: Nondimensional $z-$velocity profiles for the additively manufactured twisted tape insert (w/D = 1.0) at Re = 17,700 for 45^o, 90^o, and 135^o angles.

The nondimensionalized $z-$velocity for the additively manufactured twisted tape insert is shown in 4.43 normalized by the maximum velocity in the $z-$direction. While the three velocities have a similar trend, the highest velocity was found to be in the 45^o angle, or near the 45^o angle, in the direction of rotation. It is interesting to note that the velocity fields for the 90^o and 135^o angles follow the same trend as r is increasing. This phenomenon, and the contour plots, show a larger velocity is expected near the twisted tape insert in the direction of twist and it then becomes θ independent. All three velocities plots are also skewed towards the wall. Meaning that the maximum velocity occurs at a radial location $r/R > 0.5$. The maximum velocity occurs near r/R = 0.7 for the 45^o and the 135^o angles, while for the 90^o angle it occurs near $r/R = 0.6$. Additionally, the velocity is higher after the maximum velocity, or near the pipe's wall, than near the center of the geometry. This is contrary to what was observed in the contour plots, in which a higher velocity was observed near the twisted tape insert. This is still true in the $y-$direction, but the inflow region is in the radial location interpolated, thus it shows an increased velocity bias for the velocities near the wall instead of the twisted tape.

Similar linear velocity data were obtained at the same angles for the loose-fitting twisted tape inserts, with the velocity profiles for the same Reynolds number, Re = 17,700, shown in Figure 4.44 for the two different widths. The velocity profile of the twisted tape of width $w/D = 0.95$ follows a more similar trend to the one from the additively manufactured test section, in which a clear rise and fall near the wall and twisted tape insert are observed, with a higher velocity found for the 45^o than for the other two angles interrogated. The velocity trend for the bigger width also doesn't fully match the same pattern observed for the additively manufactured twisted tape insert. The shape is not as skewed towards the pipe's wall, but instead, it seems to have a more symmetric trend. Additionally, the location for the maximum velocity of each velocity profile is shifted closer to the center of the geometry. For the 45^o angle, the maximum velocity was found at $r/R \approx 0.6$, while for the 90^o and 135^o angles, it was found at $r/R \approx 0.5$.

The smaller width velocity data, $w/D = 0.85$ does not follow the same trend as the larger width and tight-fitting twisted tape insert. It is important to note, that these velocity profiles were obtained with the corrected azimuthal velocity, but the correction only affects the x and $y-$velocities. This trend was also observed for the contour plots in Section 4.4.1, in which the $z-$velocity contour plot was not showing the same velocity structures found for the tighter twisted tape inserts. Instead, the velocity plots for the smaller width, $w/D = 0.85$, are almost indistinguishable from one another, creating a smoother velocity profile that doesn't seem to be dependent on the angle. In addition, the velocity data for the smaller width has a flatter distribution with reaching a steady velocity, in relationship to r/R, at a smaller radial position ($r/R \approx 0.15$). The velocity profiles for all three angles for the smaller-width twisted tape also show no clear velocity maximum.

The $z-$velocity profiles for the twisted tape insert of width $w/D = 0.95$ for Reynolds numbers of 4,000 and 8,000 are shown in Figure 4.45. Similarly to the velocity shown in Figure 4.44 for the

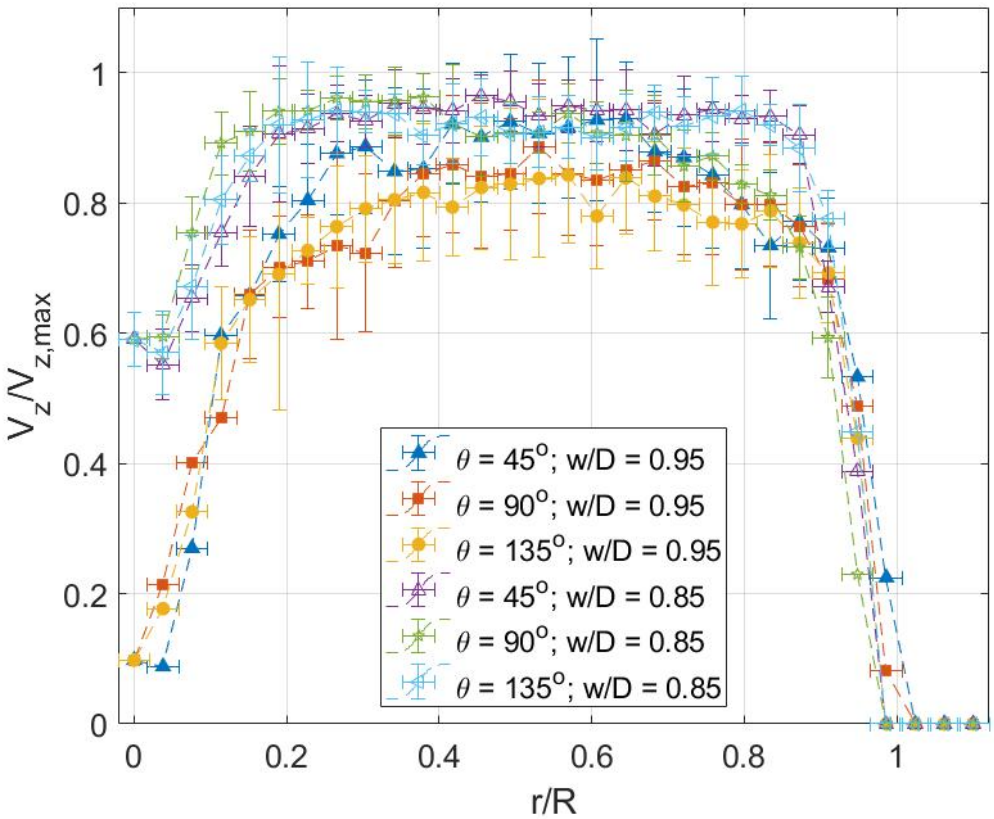

Figure 4.44: Nondimensional $z-$velocity profiles for the twisted tape widths w/D = 0.95 and 0.85 at Re = 17,700 for 45^o, 90^o, and 135^o angles.

same twisted tape width, a higher velocity was found at a 45^o angle in comparison with the other two angles independent of the Reynolds number. In addition, the same phenomenon was observed in which the 90^o and 135^o angles velocity profiles follow the same trend between them. While it wasn't as clear in the contour plots, the velocity profiles show a more apparent difference between the different Reynolds numbers. A higher velocity was observed near the twisted tape insert ($r/R <$ 0.5) for the 45^o angles for both Reynolds numbers, Re = 4,000 and 8,000. Additionally, the location of the maximum velocity is shifted closer to the center of the geometry, for the Reynolds number of 8,000 it is located at $r/R \approx 0.45$, while for the Reynolds number of 4,000, it is located at $r/R \approx 0.4$. The velocity profiles for the 90^o and 135^o angles are flatter and not as skewed toward the pipe's wall as was previously observed. The velocity profiles start differing near the twisted tape insert (r/R approaches zero), this highlights how the movement of the twisted tape insert inside the pipe creates further changes in the velocity fields.

The final $z-$velocity profiles are shown in Figure 4.46, for a twisted tape width of w/D = 0.85 at Reynolds numbers of 8,000 and 4,000 for the same angles. This plot also shows how the velocity

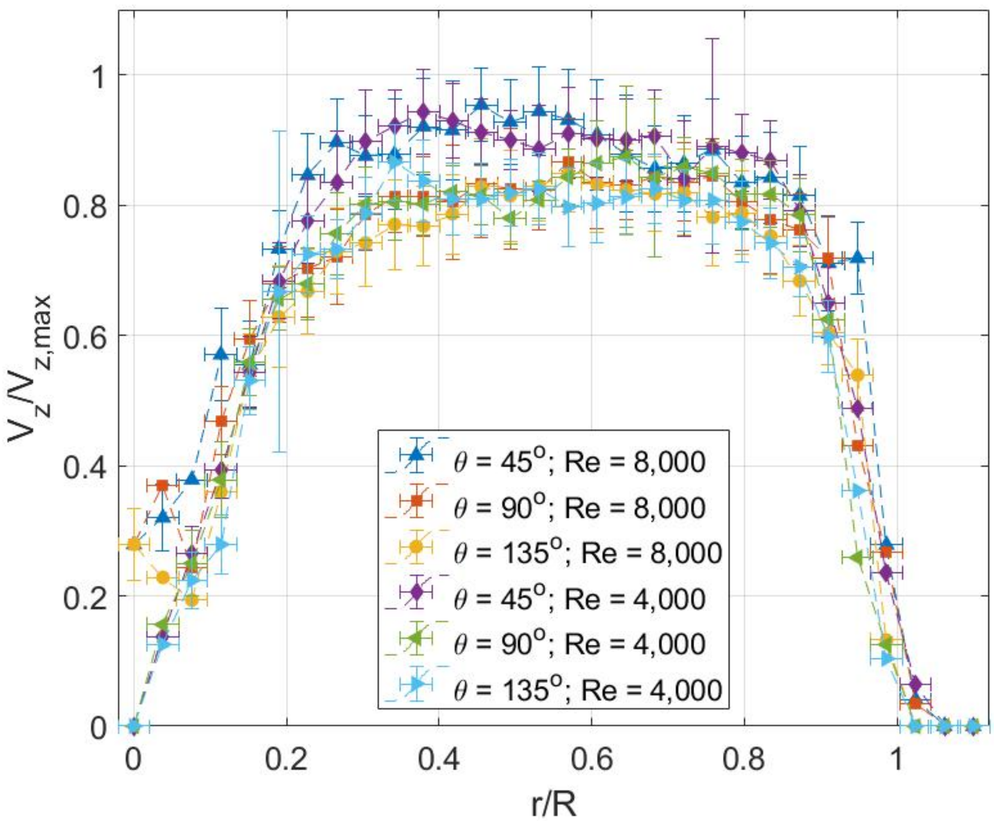

Figure 4.45: Nondimensional $z-$velocity profiles for the twisted tape width of w/D = 0.95 at Re = 8,000 and 4,000 for 45^o, 90^o, and 135^o angles.

profiles for the smaller width, w/D = 0.85, have a flatter top than the previous velocity profiles. The smaller width also creates a more uniform velocity profile across θ, as the velocity profiles do not show a higher velocity profile for the 45^o angle compared to the 90^o and 135^o angles.

Similarly to the azimuthal plots, the exact location of the twisted tape insert for both loose-fitting twisted tape inserts is not as apparent and clear as the additively manufactured twisted tape insert as the velocity near the center of the pipe does not reach zero. This was previously explained with how the twisted tape is moving around inside the pipe and through the $z-$averaging done to calculate the Eulerian velocities the exact location of the twisted tape insert is lost. This location of the twisted tape insert could be mitigated for PEPT experiments by adding supports to the twisted tape to maintain a constant location as it travels through the pipe. This kind of work has been done to study the friction factor and Nusselt number of twisted tape inserts, with the leading correlations obtained using this exact method in their experiments. This is usually not how they are introduced in the geometry and as it was concluded in Section 3, this creates a discrepancy when understanding the true phenomena that occur in twisted tape inserts. While having a perfect twisted tape insert

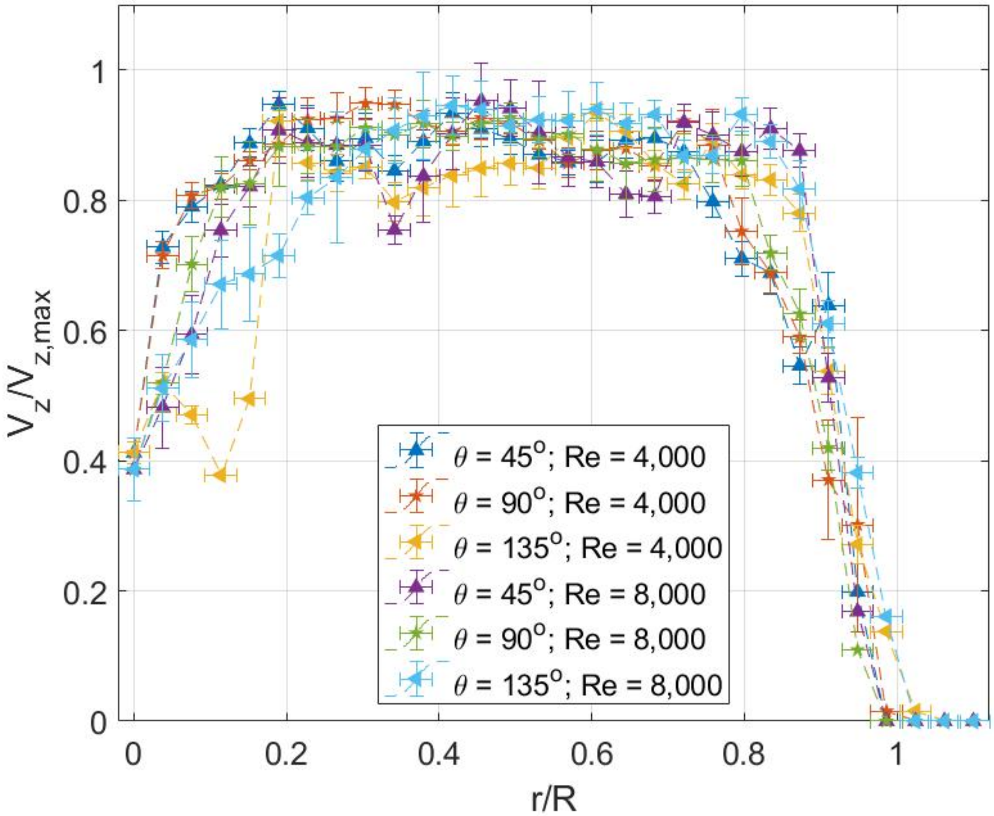

Figure 4.46: Nondimensional $z-$velocity profiles for the twisted tape width of w/D = 0.85 at Re = 8,000 and 4,000 for 45^o, 90^o, and 135^o angles.

might be ideal for real scenarios, most fabrication techniques, using traditional manufacturing, of twisted tape inserts create small variations between them and the method they are installed.

4.4.4 Vorticity

In order to better understand the vortices that occur in the twisted tape geometry, the vorticity in the $z-$direction was calculated for the additively manufactured twisted tape insert, defined as:

$$w = \frac{\partial V_y}{\partial x} - \frac{\partial V_x}{\partial y}. \tag{4.13}$$

Figure 4.47 compares the vorticity of the additively manufactured twisted tape insert with the vorticity calculated by Wiggins et al [131] for a twisted tape insert of pitch y = 3, Reynolds number of 20,000 and w/D = 0.93. The plot from Wiggins et al [131] has inverted x and $y-$axis when compared to the current results which can lead to differences in the direction of the vorticity compared between the two plots. While the vorticity magnitudes are different in the two twisted tape inserts, one thing to note is the regions of high vorticity. In both cases, the high vorticity regions appear near the twisted tape insert. In addition, the vorticity observed by the additively manufactured test section has a pattern behavior comparable with the one obtained by Wiggins et al [131]. The gap created by the loose-fitting twisted tape insert further

Additionally, Wiggins et al reported the visualization of two secondary flows occurring in the top half of the channel with a single one occurring in the bottom half. These secondary flows were heavily dependent on the location of measuring flows

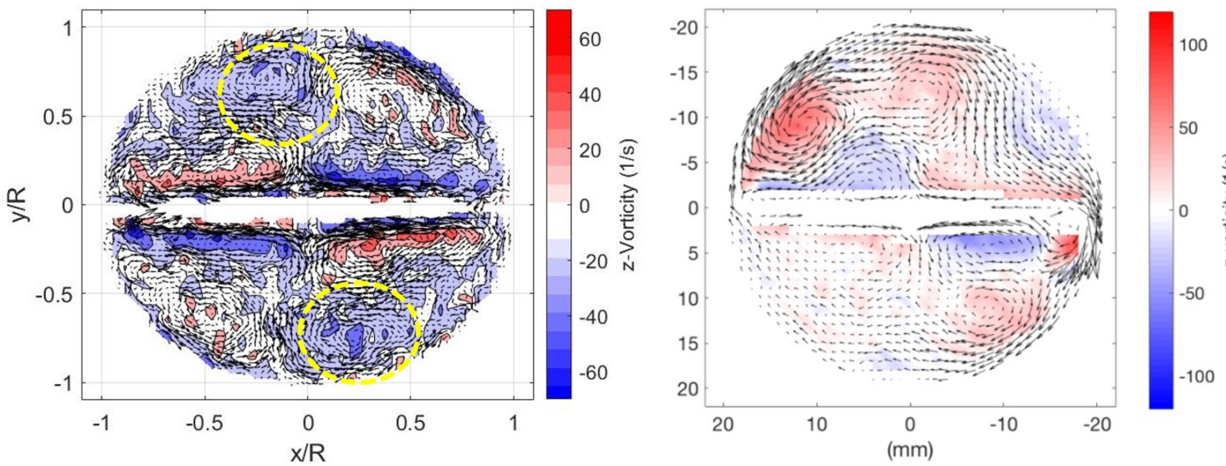

Figure 4.47: Vorticity with velocity quivers of additively manufactured twisted tape insert at Re = 17,700 (Left) with vorticity and velocity quivers from Wiggins et al [131] at Re = 20,000 (Right).

Two large regions of high vorticity are observed away from the twisted tape insert that allows for the formation of helical vortices. These regions are highlighted in Figure 4.47. The same helical vortices that Cazan and Aidun [130] observed in the free stream after the twisted tape insert. In addition, Cazan and Aidun observed the helical vortices originated near the twisted tape and drifted away toward the center of the semi-circle. It is theorized that the large $z-$velocities created by the twisted tape insert observed in the contour plots, Figure 4.25, push the helical vortices to be off-centered in the semi-circle towards the regions of lower $z-$velocity. The current data are obtained at more than 20 diameters from the inlet, thus the formation of these helical vortices is not captured, but their location away from the twisted tape insert is confirmed.

The vorticity in the smaller width twisted tape insert (w/D = 0.85) was also calculated and shown in Figure 4.48 for a Reynolds number of 4,000. The loose-fitting twisted tape insert creates a pair of swirls that initiate at the gap of the twisted tape insert. The clockwise vortex (red circles in the selection of Figure 4.48) that occurs is a direct creation of flow crossing between the two semi-circles. The vortex travels and dissipates as it travels from the origin source of the gap of the twisted tape insert. The red vortex then creates a counter-rotating vortex (the blue region to the right of the red one). The same phenomenon is observed on the opposite side of the twisted tape insert ($r/R = 1$), but not as pronounced as the highlighted one. The swirls that are occurring near the twisted tape gap dominate the rest of the transaxial flow in the twisted tape insert. This was observed in the contour plots in Section 4.4.1 and further highlighted by the disappearances of the previously identified vortex regions in Figure 4.47.

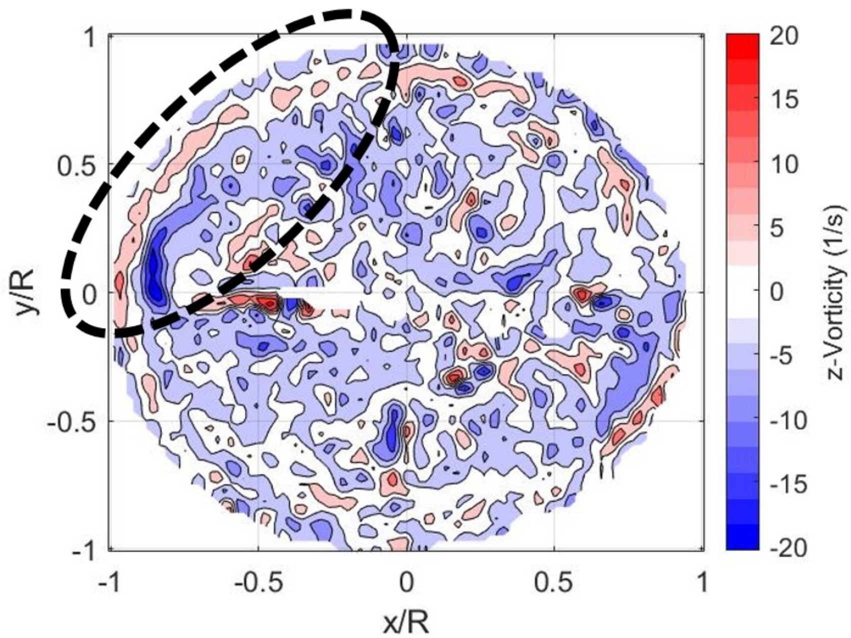

Figure 4.48: Vorticity of the loose-fitting twisted tape insert of width $w/D = 0.85$ at Reynolds number of 4,000.

This is further shown in Figure 4.49. Figure 4.49 plots the vorticity for the twisted tape insert of width $w/D = 0.85$ at Reynolds numbers of 8,000 and 17,700, respectively. The vortices created by the transfer between semi-circles are also observed at the higher Reynolds numbers in the same regions. The same clockwise and counter-clockwise vortex is formed at the gap of the twisted tape insert, but they are further propagated in the rest of the flow. While at the Reynolds number of 4,000, the vortices created by the gap between the twisted tape slowly dissipate to the rest of the flow, the vortices created at higher Reynolds numbers seem to dominate and propagate to the rest of the semi-circle geometry. The vortices previously observed for the additively manufactured twisted tape insert at a Reynolds number of 17,700 completely disappear for the smallest width geometry at the same Reynolds number. The loose-fitting twisted tape of width $w/D = 0.85$ creates a different pattern of mixing, as the two competing effects of the swirling motion of the twisted tape insert and the flow crossing between the two semi-circles are competing. It is interesting to note the change of direction of rotation of the swirls changes as the Reynolds number increases.

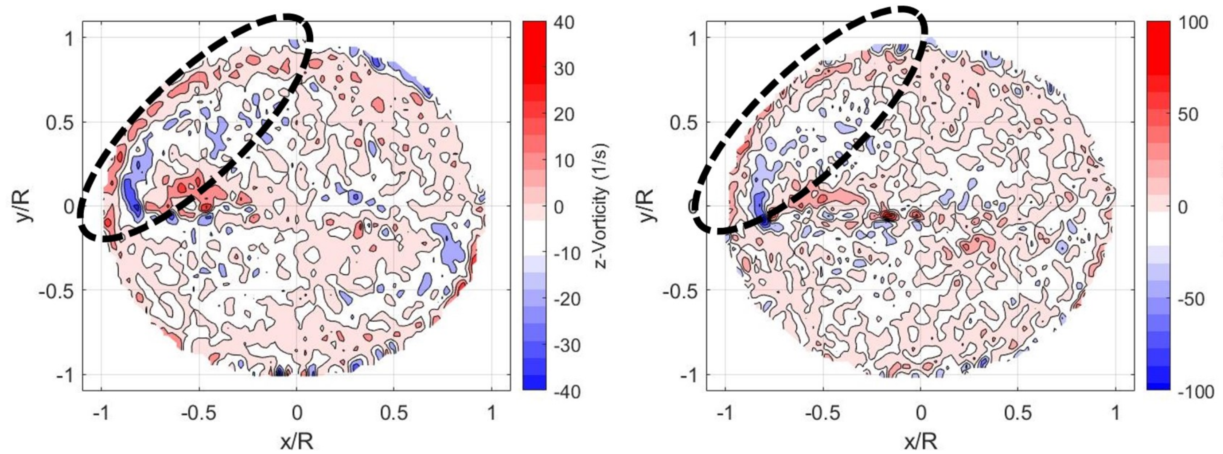

Figure 4.49: Vorticity of the loose-fitting twisted tape insert of width $w/D = 0.85$ at Reynolds number of 8,000 (Left) and 17,700 (Right).

The secondary flow observed by Clark et al [74, 85] that resulted in higher wall temperatures, lower localized heat transfer, and a thicker boundary layer was observed in the additively manufactured twisted tape insert at two opposite locations that are further pushed by the high-velocity islands created by the twisting motion. These secondary flows can result in localized hot spots in the material as the flow is not allowed to properly mix with the rest of the flow in high heat flux applications. The loose-fitting twisted tape insert of width $w/D = 0.85$ created secondary flows close to the wall that further propagated to the rest of the half channel. The vorticity contour for the Reynolds number of 4,000 shows that a transaxial flow separation is created by the flow crossing from the opposite channel. This flow separation can lead to larger hot spots in the material than those observed in the tighter twisted tape insert.

4.4.5 Reynolds Stresses and turbulent kinetic energy

Positron Emission Particle Tracking (PEPT) has been used previously to obtain Reynolds stresses in a circular pipe [141, 143] by radially binning the geometry. This method was initially explored to obtain Reynolds stresses and the turbulent kinetic energy of the twisted tape insert as a function of radius. Unfortunately, the radial binning used does not properly interrogate the flow as the geometry is not θ independent as it is in a circular pipe. Initial results did not show a clear representation of the flow structures in the twisted tape insert. This resulted in the same methodology used to obtain the contour plots in Section 4.4.1 to be implemented to obtain Reynolds stresses in the twisted tape insert. The Reynolds stress in the $z-$direction is defined as:

$$V_z(t) = \overline{V_z} + v'_z, \tag{4.14}$$

where $V_z(t)$ is the instantaneous velocity at time t, $\overline{V_z}$ is the averaged velocity, and v'_z is the fluctuating term of the velocity.

The turbulent kinetic energy was also explored for this work, which is defined as:

$$k = \frac{1}{2}(\overline{(v'_x)^2} + \overline{(v'_y)^2} + \overline{(v'_z)^2}), \tag{4.15}$$

where the $\overline{(v'_x)^2}$ and $\overline{(v'_y)^2}$ were obtained using Equation 4.14, but for the $x-$ and $y-$directions.

In this work, only the Reynolds stresses and turbulent kinetic energy of the additively manufactured twisted tape insert are presented. Figure 4.50 plots the Reynolds stress $v_z v_z$ nondimensionalized by the maximum velocity in the $z-$ direction with the turbulent kinetic energy nondimensionalized by the maximum velocity. Fully convergence issues are expected in these results, as more data is required to better converge higher statistical data. Only the results of the additively manufactured twisted tape insert show any concluding remarks as these variables were observed to be more dependent on the location of the twisted tape insert. A large region of high turbulent kinetic energy was observed at the corners of the semi-circle. The same region of high turbulent kinetic energy was observed by Wiggins et al [131] with loose-fitting twisted tape inserts. Higher turbulent kinetic energy was also observed in locations near the wall of the circular pipe, this was also noted by Wiggins et al [131], which agrees with higher turbulent kinetic energy near the walls for pipe flow. These higher turbulent kinetic energy spots allow for better mixing of the flow.

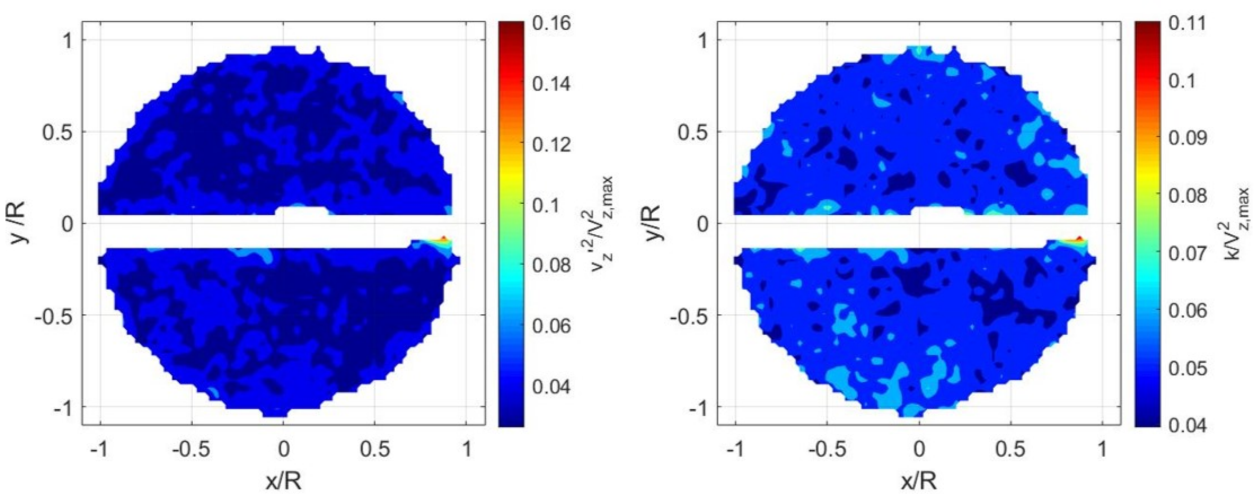

Figure 4.50: Reynolds stresses $v_z'^2$ (Left) and Turbulent Kinetic Energy, k, (Right) for additively manufactured twisted tape insert at Re = 17,700 normalized by the maximum V_z^2.

The Reynolds stresses in the x and $y-$directions are smaller in comparison with those in the $z-$direction, thus the contour of the Reynolds stress $v_z'^2$ is qualitatively similar to the one of the turbulent kinetic energy. No main conclusions could be drawn from this experimental set for either turbulent characteristics of interest. A much larger data set is required for a more meaningful conclusion and analysis. This is left for future work.

4.5 Conclusion

Positron emission particle tracking has been used to interrogate the velocity fields of complex geometry in a passive heat transfer enhancement technique, twisted tape inserts. Contour velocity data shows a clear dependence on the width of the twisted tape, a parameter that has been neglected in studying the majority of twisted tape insert experiments and computational efforts. Manglik [73] mainly explores the velocity contours that arise when the thickness of the twisted tape insert is varied in a non-twisting geometry. While the results show a clear flow pattern dependence, the effects caused by the gap between the twisted tape insert and the circular pipe showed to be more dominant in this work.

The velocity contours in Section 4.4.1 show a clear dependence in the velocity structures when the twisted tape width is varied. The velocity contour for the additively manufactured twisted tape insert represents the ideal scenario in which the perfect conditions of the twisted tape insert are achieved and thus create a flow velocity pattern that has been compared with others found in literature [74, 93, 164]. While the twisted tape width of $w/D = 0.95$ has qualitatively similar velocity contours, the flow that crosses between the two semi-circles further affects the formation of the large velocity islands and the inflow region previously described and identified in Smithberg and Landis [93]. The inflow region was observed to be dependent on the Reynolds number as the overall size of the inflow region increased with increased Reynolds number. Additionally, only a single velocity island was observed through the PEPT results in a semi-circle region, instead of the two main high-velocity islands observed by Smithberg and Landis. The same pattern in the high-velocity islands was also observed for the twisted tape insert of width $w/D = 0.95$ across three Reynolds numbers. Numerical simulations predict the creation of another velocity island further away from the motion of the twist, which was not observed in the current experimental work. Additionally, the large velocity islands and the inflow region are less apparent or as dominant in the loose-fitting twisted tape insert of width $w/D = 0.85$. The large velocity islands and the inflow region are not allowed to properly form due to the flow crossing between semi-circles. Additionally, the velocity contours in the x and $y-$directions showed a clear dependence on twisted tape width. The highest velocities observed for the additively manufacturing twisted tape insert were observed near the twisted tape, while for the loose-fitting twisted tape inserts, they were observed near the gap of the twisted tape width.

The difference in flow patterns is further observed with the azimuthally averaged velocity profiles and the velocity profiles obtained at different angles. A higher velocity was found near the 45^o angle for the additively manufactured twisted tape insert and the twisted tape of width $w/D = 0.95$, but a flatter velocity profile was observed in the smaller width twisted tape insert $w/D = 0.85$. Additionally, the $\theta-$velocity for all twisted tape inserts was observed to collapse to a common form regardless of Reynolds number when normalized by the mean velocity of the empty pipe before the twisted tape insert. This highlights that the main driving component of the $\theta-$velocity is the twisting of the flow. The azimuthally averaged $\theta-$velocity also shows a decrease in velocity not occurring at the edge of the twisted tape insert, but earlier in the geometry, which is counterintuitive to what would be expected with the highest velocity occurring at $r/R \approx w/R$. While for the additively manufactured twisted tape insert, the lower maximum $\theta-$velocity occurring before $r/R = w/R$ agrees with the no-slip boundary condition occurring at the wall, this does not explain why the velocity decreases before the end of the twisted tape. Instead, the velocity decreases due to the flow crossing between the two semi-circles. Additionally, the large $y-$velocities observed in the contour plots for the loose-fitting twisted tapes are not captured in the azimuthally averaged $\theta-$velocity, thus while it is higher at certain locations it does not fully affect the azimuthally averaged V_θ.

Manglik and Bergles [73, 86, 87] further predicted different flow structures and regimes of these twisted tape inserts that occur as the Reynolds number increases. The current work did not show or provide context for the differences in regimes that they initially predicted. The majority of the flow structures were dominated by the twisting motion and the width of the twisted tape insert. Future data should be collected in much lower Reynolds numbers. The Reynolds number of 4,000 provided a benchmark for the low Reynolds number, as the twisted tape inserts have been shown to suppress turbulence, but the data did not provide a reliable conclusion for the different flow regimes expected to have been observed.

The vorticity for the additively manufacturing twisted tape test section was similar to those observed by Cazan and Aidun [130]. Though their results mainly focus on the study of the free stream flow after the twisted tape insert, the formation of the swirling vortices in additive manufacturing agrees with their vortices. Additionally, smaller vortices are observed created near the walls of the twisted tape insert with opposite swirling motions highly dependent on the location of the twisted tape. These high vortices create instabilities in the location of the twisted tape insert. While they do not create changes in the location of the twisted tape insert in the additively manufactured test section, they further affect the stationary location of the twisted tape insert in the loose-fitting twisted tapes. The vorticity of the loose-fitting twisted tape insert of width $w/D = 0.85$ further shows the creation of two swirls counter rotating swirls that are born due to the cross-flow through the gap of the semi-circles. These small vortices propagate further into the geometry affecting the overall transaxial velocity behavior.

Finally, while Reynolds stresses and turbulent kinetic energy was obtained for the additively manufactured twisted tape insert, it does not fully capture these turbulent characteristics of the flow. Methodology previously done to obtain these quantities in a circular pipe was initially explored with little success. PEPT is capable of calculating these quantities as they have been reported previously in the literature [131, 141, 143]. The turbulent kinetic energy matches are qualitatively similar to the one obtained by Wiggins et al [131] with high turbulent kinetic regions near the walls of the pipe and at a corner near the twisted tape insert and the walls of the pipe. Unfortunately, a larger data set is required to better capture this turbulence phenomenon.

Chapter 5

CONCLUSION AND DISCUSSION

In this work, a passive heat transfer enhancement technique was studied that is currently considered for high heat flux applications, i.e. twisted tape inserts, in molten salt heat transfer systems. Molten salts are currently sought in innovative energy applications due to their efficient heat transfer properties and high operating temperatures. Unfortunately, these high operating temperatures, and the corrosive nature of the molten salt, make it challenging to study the heat transfer systems of these molten salts in laboratory settings. Additionally, the cost alone of buying large quantities of the molten salt required for accurate heat transfer studies exceeds the budgetary constraints of an early-stage university laboratory setup. That is without considering the high price tag of components and instrumentation that can withstand the operating temperatures of the molten salts. Initial heat transfer experiments that used molten salts typically focused on a simple geometry, a circular pipe. Initial results of the heat transfer characteristics of the molten salts led engineers to believe that molten salts had a unique heat transfer behavior, as Nusselt number predictions did not match conventional correlations. This was later dismissed as the lack of accurate thermophysical properties of the molten salts and the formation of the resistive layer were the cause of the inaccurate Nusselt number calculations. Due to this, surrogate fluids were sought that mimic heat transfer characteristics of molten salts at lower temperatures to explore more complex geometries.

Water was found to be a surrogate fluid for five molten salts, LiF - NaF - KF (FLiNaK), $NaNO_3$ - KNO_3, $NaNO_3$ - $NaNO_2$ - KNO_3, LiCl - KCl, and NaF - $NaBF_4$, for heat transfer experiments. Water matched the Prandtl number, a nondimensional number that quantifies the thermophysical properties of a fluid, of these molten salts at lower operating temperatures. The distortions that arise when using a surrogate fluid were studied, with the conclusion that the distortions were heavily dependent on the uncertainty of the thermophysical properties of the molten salt. For the largest distortion, water as a surrogate for $NaNO_3$ - KNO_3, the uncertainty in the thermophysical properties of the molten salt trumped or matched the distortion itself. Therefore, with improved quantification of the uncertainty in the thermophysical properties, the distortion might decrease. Further studies on the effects of improved uncertainty should be done to better quantify the overall distortion.

Additionally, a methodology for the propagation of the Prandtl number distortions to Nusselt number experimental data was done. The distortion in the Prandtl number was propagated to Nusselt number experimental data in a one-to-one relationship for a nonconservative analysis. The resulting Nusselt number probabilities showed smaller bandwidths than the experimental uncertainty for $NaNO_3$ - $NaNO_2$ - KNO_3 and NaF - $NaBF_4$, while for $NaNO_3$ - KNO_3 it skewed to lower Nusselt numbers. This methodology proved the further feasibility of water as a surrogate fluid for these molten salts and showed a method of nonconservative interpretation of the Prandtl number distortions propagated to the Nusselt number experimental data. In reality, the distortion probabilities depicted in Figures 2.17 to 2.19 are expected to decrease when propagated accordingly with Prandtl number and Nusselt number relationships.

The thermal performance and fluid flow of twisted tape inserts were studied using water as a surrogate fluid. Friction factor data was collected for eight different twisted tape geometries of varying pitch, y, and width, w/D, at Reynolds numbers ranging from $\approx$ 3,000 to 40,000. Relevant friction factor correlations failed to accurately predict the current experimental data, with the correlation for Manglik and Bergles [86, 87] accurately predicting the friction factor of a tight-fitting twisted tape insert $w/D = 1.0$. This led to the derivation of a factor to be added to the Manglik and Bergles correlations to account for loose-fitting twisted tape inserts. Initial work was done to develop correlations based on the hydraulic diameter of the twisted tape insert, to better account for the loose-fitting geometry, but matching exponents in the correlation would simply create another correlation in the countless out there which are only applicable to specific operating conditions. Thus, the addition of the factor to Manglik and Bergles correlation was chosen to better account for the wide range in their correlation with the addition of the current one and further account for loose-fitting twisted tape insert data. Friction factor predictions with the adjusted correlations matched with the experimental data across the seven loose-fitting twisted tapes, within experimental uncertainty.

Nusselt number data was obtained for three twisted tape inserts for pitches $y = 1.9$, 2.86, and 3.81 and width $w/D = 0.95$, at Reynolds numbers ranging from $\approx$ 3,000 to 24,000. Correlations found in the literature varied in the overall prediction of the experimental data. The most widely used correlations for heat transfer in twisted tape inserts describe a big jump in the transition between the laminar regime to the turbulent regime, with larger discontinuity for tighter pitches. This was not observed in the current experimental data, and the same shape of the data was observed for analytically derived correlations. The majority of the correlations isolate the fin effects created by the conduction between the walls of the pipe and the twisted tape insert. The current methodology is not sensitive enough to account for the fin effects observed in the data.

A channel flow methodology was explored as a method to predict friction factor and Nusselt number in the twisted tape inserts. The friction factor collapsed to a common form for all loose-fitting twisted tape inserts, while for the tight-fitting twisted tape insert ($w/D = 1.0$), it failed to transform the friction factor to the same common form. The Nusselt number data also collapsed to a common form, regardless of the twisted tape pitch. The channel flow methodology can provide further insights into the overall physics that is occurring inside these twisted tape inserts. The theorized jump in the Nusselt number data was observed for the channel flow transformation, though not as dependent on twisted tape pitch as all the data collapsed together to a common form. The treatment of channel flow for twisted tape inserts can lead to further applications of fouling and roughness in channel flow to be suitable for twisted tape inserts, as these behaviors are not fully understood in twisted tape insert geometries.

In addition, thermal performance was calculated for the three twisted tape inserts of width w/D = 0.95. Unfortunately, the uncertainty between both the friction factor and Nusselt number further propagated to the thermal performance for which no clear difference was observed between the three pitches. Literature has reported an increase in thermal performance with tighter twisted tape pitches, but this was not concluded in the current work. An increase in thermal performance was observed at lower Reynolds numbers for the three twisted tape inserts. Additionally, the thermal performance was observed to be dependent on the fluid used. Lower Prandtl number fluids showed lower thermal performance across all Reynolds numbers, with the exception of one study found in the literature. Further reinforcing the benefits of twisted tape inserts for high Prandtl number fluids, such as molten salts.

Fluid flow studies done using positron emission particle tracking on twisted tape inserts revealed interesting phenomena in the underlying flow structures. Three twisted tape inserts were studied with similar twisted tape pitch of $y \approx 2.8$, at Reynolds numbers of 17,700, 8,000, and 4,000. These Reynolds numbers encompassed the laminar, transitional, and turbulent regime in the twisted tape inserts. The fluid flow contours for the twisted tape insert of a width of w/D = 1.0 agreed with those previously reported in literature [68, 93, 131, 164]. High-velocity islands were reported near the twisted tape insert created by the rotation of the flow with the addition of an inflow region found at the center of the twisted tape insert. These two flow structures were heavily dependent on the width of the twisted tape insert, as they completely disappeared for the smallest width, w/D = 0.85. This behavior impacted the velocity profiles obtained across the different twisted inserts. The twisted tape inserts of width w/D = 1.0 and 0.95 reported higher velocities occurring near the 45^o angle, while the twisted tape width of w/D = 0.85 had a better mix in the fluid flow as the velocity profiles had a similar behavior across the three different angles studied. The transaxial velocity, V_θ, of the twisted tape insert was governed by the twisting motion of the twisted tape insert, as all azimuthally averaged $\theta-$velocities collapsed together when normalized by the mean flow of the empty pipe prior to the twisted tape insert.

The two locations of the vortices observed in the free stream flow after the twisted tape insert by Cazan and Aidun [130] were found in the twisted tape flow. The regions of high vorticity in the twisted tape insert were located near the twisted tape insert creating instabilities in the location of the twisted tape insert further noted in the loose-fitting twisted tape inserts. Additionally, the vortices observed for the loose-fitting twisted tape insert of w/D = 0.85 showed the stream-like vortices emerging at the gap of the twisted tape insert with the walls. These vortices propagated through the rest of the geometry influencing the overall flow structures at the higher Reynolds numbers.

5.1 Summary of findings

In short, the following summarizes the key findings of this work:

- Water showed to be a proper surrogate fluid for heat transfer experiments for five different molten salts.
- A methodology to quantify the distortions that occur between the surrogate fluid and molten salt was developed and further applied to experimental data.
- The distortions observed between water and the five molten salts can be mitigated with more accurate thermophysical properties of the molten salts.
- A channel flow transformation of the twisted tape insert geometry can provide further insight into the underlying fluid flow phenomena occurring to further understand fouling and roughness in twisted tape inserts.
- A factor that accounts for loose-fitting twisted tape inserts was added to the most widely used friction factor correlations with good agreement with current experimental data.
- The Nusselt number channel flow correlation requires a C coefficient for the centrifugal component of the overall Nusselt number. Current experimental data showed an underprediction at lower Reynolds for the original correlation, and the C coefficient was adjusted to better match current experimental data.
- A critical Reynolds number of the turbulent region was defined based on the hydraulic diameter and the channel flow velocity, $Re_{cr} = Re^* = 10{,}000$.
- Twisted tape inserts improve the thermal performance of heat exchangers, especially at low Reynolds numbers.
- Twisted tape width showed to be a crucial geometric parameter in the overall friction factor and fluid flow characteristics of twisted tape inserts. Something that only a handful of papers in the literature have explored thus far.

- The gap between the twisted tape insert and the circular pipe can create vortices that affect the overall flow structures.

In general, it is recommended that if a twisted tape insert is to be used in a heat exchanger, the overall twisted tape width should closely match the inner diameter of the pipe for better tight-fitting geometry. This will avoid unwanted flow structures that arise from the flow crossing between the two semi-circles and the fin effects created by the contact between the twisted tape and the walls at high heat flux environments will further improve the heat transfer.

5.2 Future Work

Future work is suggested herein as a path forward in the three main topics covered in this work. Based on the current findings and conclusions, future work is presented as a way to keep curiosity going for future researchers.

For the surrogate fluids work, the distortion propagation that was used in this work between the Prandtl number and Nusselt number should be studied further. This type of effort could only be done through molten salt heat transfer experiments and through the comparison of the predicted Nusselt number from the surrogate fluid and the actual molten salt result. On a trip to the Molten Salt Workshop hosted by Oak Ridge National Laboratory in the Fall of 2022, the author found out that is exactly what the molten salt reactor start-up company TerraPower is working on. TerraPower has studied different chloride salt heat transfer phenomena using surrogate fluids and is currently working on large integral effects testing facility to further study the predictions done by the surrogate fluids [165]. In addition, understanding the chemical effects of the molten salts are important to accurately implement the heat transfer results using surrogate fluids, but this is left for future work. Further work should be done in the collection of thermophysical properties with similar molar compositions and temperature ranges.

The additively manufactured test sections require further testing for accurate heat transfer results. The methodology described in this work, of the surface thermocouples for wall temperatures, was devised with the additively manufactured test sections in mind. Further work in the quantification of the thermal conductivity of the resin is required for accurate heat transfer measurements. The majority of heat transfer results reported in the literature with additive manufacturing components concluded that the lack of knowledge of the thermophysical properties of the resin was the leading factor to the lack of agreement with traditional correlations. With the proper groundwork, the FAST Research Group can possibly create and design heat transfer test sections that have never been developed before, with the ability to test the friction factor, heat transfer, and even fluid flow (through PEPT) of these novel geometries.

5.3 Final remarks

The work summarized in this dissertation comprised four years of work at Virginia Commonwealth University (VCU) for the FAST Research Group with the help of various bright-minded individuals at different stages of the four years. The author can't express enough gratitude towards his colleagues who kept pushing in different stages of this work. To my advisor, Dr. Carasik, thank you for helping me push through some crazy ideas and for guiding me with topics to cover. To Dr. Cody S. Wiggins, my time as a fellow PEPTer was short, but I hope I made you proud with some of my work and findings. PEPT was far more complex and complicated than I ever imagined. I will always cherish the long days working in the development, construction, and testing of MSETF-1 and you sparking an interest in baseball in me. To the entire FAST-Research group, teaching and learning with you all has been a pleasure. Thank you for making work interesting and challenging.

To whomever reads this thesis, thank you for your time and attention. Muchas gracias a todos.

BIBLIOGRAPHY

[1] Tanveer Ahmad and Dongdong Zhang. "A critical review of comparative global historical energy consumption and future demand: The story told so far". In: *Energy Reports* 6 (2020), pp. 1973–1991. ISSN: 2352-4847. DOI: https://doi.org/10.1016/j.egyr.2020.07.020. URL: https://www.sciencedirect.com/science/article/pii/S2352484720312385.

[2] Michael Jefferson. "Sustainable energy development: performance and prospects". In: *Renewable Energy* 31.5 (2006). SOUTH/SOUTH, pp. 571–582. ISSN: 0960-1481. DOI: https://doi.org/10.1016/j.renene.2005.09.002. URL: https://www.sciencedirect.com/science/article/pii/S0960148105002466.

[3] M. Siddique et al. "Recent Advances in Heat Transfer Enhancements: A Review Report". In: *International Journal of Chemical Engineering* 2010 (Sept. 2010). Ed. by Alfons Baiker. Publisher: Hindawi Publishing Corporation, p. 106461. ISSN: 1687-806X. DOI: 10.1155/2010/106461. URL: https://doi.org/10.1155/2010/106461.

[4] Jérôme Serp et al. "The molten salt reactor (MSR) in generation IV: Overview and perspectives". In: *Progress in Nuclear Energy* 77 (2014), pp. 308–319. ISSN: 0149-1970. DOI: https://doi.org/10.1016/j.pnucene.2014.02.014. URL: https://www.sciencedirect.com/science/article/pii/S0149197014000456.

[5] H Moriyama et al. "Molten salts in fusion nuclear technology". In: *Fusion Engineering and Design* 39-40 (1998), pp. 627–637. ISSN: 0920-3796. DOI: https://doi.org/10.1016/S0920-3796(98)00202-6. URL: https://www.sciencedirect.com/science/article/pii/S0920379698002026.

[6] K. Vignarooban et al. "Heat transfer fluids for concentrating solar power systems – A review". In: *Applied Energy* 146 (2015), pp. 383–396. ISSN: 0306-2619. DOI: https://

doi.org/10.1016/j.apenergy.2015.01.125. URL: https://www.sciencedirect.com/science/article/pii/S0306261915001634.

[7] NEA. *A State-of-the-Art Report on Scaling in System Thermal-hydraulics Applications to Nuclear Reactor Safety and Design*. Tech. rep. Paris: OECD Publishing, 2017.

[8] Arturo Cabral et al. “Identification of surrogate fluids for molten salt coolants used in energy systems applications including concentrated solar and nuclear power plants”. In: *International Journal of Energy Research* 46.3 (2022), pp. 3554–3571. DOI: https://doi.org/10.1002/er.7405. eprint: https://onlinelibrary.wiley.com/doi/pdf/10.1002/er.7405. URL: https://onlinelibrary.wiley.com/doi/abs/10.1002/er.7405.

[9] H. G. MacPherson. “The Molten Salt Reactor Adventure”. In: *Nuclear Science and Engineering* 90.4 (1985), pp. 374–380. DOI: 10.13182/NSE90-374. eprint: https://doi.org/10.13182/NSE90-374. URL: https://doi.org/10.13182/NSE90-374.

[10] W. Cottrell et al. *Operation of the Aircraft Reactor Experiment*. Tech. rep. ORNL-1845. Oak Ridge, Tenn.: Oak Ridge National Laboratory, 1955.

[11] “Development Status of molten-salt breeder reactors.” In: (Jan. 1972). DOI: 10.2172/4622532. URL: https://www.osti.gov/biblio/4622532.

[12] National Renewable Energy Laboratory. *Final Technical Report: Multijunction Concentrator Solar Cells*. NREL. 1997. URL: https://www.nrel.gov/docs/legosti/fy97/22835.pdf.

[13] ROBERT W BRADSHAW et al. “Final Test and Evaluation Results from the Solar Two Project”. In: (Jan. 2002). DOI: 10.2172/793226. URL: https://www.osti.gov/biblio/793226.

[14] World Nuclear Association. *Molten Salt Reactors*. World Nuclear Association. 2021. URL: https://world-nuclear.org/information-library/current-and-future-generation/molten-salt-reactors.aspx.

[15] U.S. Department of Energy. *Southern Company and TerraPower Prep Testing Molten Salt Reactor*. Energy.gov. 2023. URL: https://www.energy.gov/ne/articles/southern-company-and-terrapower-prep-testing-molten-salt-reactor.

[16] Bruno Merk et al. "On the Dimensions Required for a Molten Salt Zero Power Reactor Operating on Chloride Salts". In: *Applied Sciences* 11.15 (2021). ISSN: 2076-3417. DOI: 10.3390/app11156673. URL: https://www.mdpi.com/2076-3417/11/15/6673.

[17] W. R. Grimes and Stanley Cantor. "Molten salts as Blanket Fluids in Controlled Fusion Reactors". In: *The Chemistry of Fusion Technology*. Ed. by Dieter M. Gruen. Boston, MA: Springer US, 1972, pp. 161–190. ISBN: 978-1-4613-4595-4.

[18] Charles Forsberg et al. "Fusion Blankets and Fluoride-Salt-Cooled High-Temperature Reactors with Flibe Salt Coolant: Common Challenges, Tritium Control, and Opportunities for Synergistic Development Strategies Between Fission, Fusion, and Solar Salt Technologies". In: *Nuclear Technology* 206.11 (2020), pp. 1778–1801. DOI: 10.1080/00295450.2019.1691400. eprint: https://doi.org/10.1080/00295450.2019.1691400. URL: https://doi.org/10.1080/00295450.2019.1691400.

[19] Milton D Grele and Louis Gedeon. "Forced-convection heat-transfer characteristics of molten Flinak flowing in an Inconel X system". In: National Advisory Committee for Aeronautics, 1954.

[20] H W Hoffman and J Lones. "FUSED SALT HEAT TRANSFER. PART II. FORCED CONVECTION HEAT TRANSFER IN CIRCULAR TUBES CONTAINING NaF-Kf-LiF EUTECTIC". In: (Feb. 1955). DOI: 10.2172/4016896. URL: https://www.osti.gov/biblio/4016896.

[21] H. W. Hoffman and S. I. Cohen. “FUSED SALT HEAT TRANSFER–PART III: FORCED-CONVECTION HEAT TRANSFER IN CIRCULAR TUBES CONTAINING THE SALT MIXTURE NaNOsub2-NANOsub3-KNOsub3”. In: (Mar. 1960). DOI: 10.2172/4181833. URL: https://www.osti.gov/biblio/4181833.

[22] W. R. Huntley and P. A. Gnadt. “DESIGN AND OPERATION OF A FORCED-CIRCULATION CORROSION TEST FACILITY (MSR- FCL-1) EMPLOYING HASTELLOY N ALLOY AND SODIUM FLUOROBORATE SALT.” In: (Jan. 1973). DOI: 10.2172/4600150. URL: https://www.osti.gov/biblio/4600150.

[23] V.V. Ignat’ev et al. “Heat exchange during the flow of a melt of LiFNaFKF fluoride salts in a circular tube”. In: *Atomic Energy* 57.6 (1984), pp. 560–562. DOI: 10.1007/BF01123760. URL: https://doi.org/10.1007/BF01123760.

[24] Wu Yu-ting et al. “Convective heat transfer in the laminar–turbulent transition region with molten salt in a circular tube”. In: *Experimental Thermal and Fluid Science* 33.7 (2009), pp. 1128–1132. ISSN: 0894-1777. DOI: https://doi.org/10.1016/j.expthermflusci.2009.07.001. URL: https://www.sciencedirect.com/science/article/pii/S0894177709001010.

[25] Yu-Ting Wu et al. “Investigation on forced convective heat transfer of molten salts in circular tubes”. In: *International Communications in Heat and Mass Transfer* 39.10 (2012), pp. 1550–1555. ISSN: 0735-1933. DOI: https://doi.org/10.1016/j.icheatmasstransfer.2012.09.002. URL: https://www.sciencedirect.com/science/article/pii/S073519331200214X.

[26] D F Salmon. “TURBULENT HEAT TRANSFER FROM A MOLTEN FLUORIDE SALT MIXTURE TO SODIUM- POTASSIUM ALLOY IN A DOUBLE-TUBE HEAT EXCHANGER”. In: (Nov. 1954). DOI: 10.2172/4224867. URL: https://www.osti.gov/biblio/4224867.

[27] J C Amos, R E MacPherson, and R L Senn. “PRELIMINARY REPORT OF FUSED SALT MIXTURE NO. 130 HEAT TRANSFER COEFFICIENT TEST”. In: (Apr. 1958). DOI: 10.2172/4336046. URL: https://www.osti.gov/biblio/4336046.

[28] J. W. Cooke and B. Cox. “Forced-convection heat-transfer measurements with a molten fluoride salt mixture flowing in a smooth tube”. In: (Mar. 1973). DOI: 10.2172/4486196. URL: https://www.osti.gov/biblio/4486196.

[29] M. D. Silverman, W. R. Huntley, and H. E. Robertson. *Heat Transfer Measurements in a Forced Convection Loop with Two Molten-fluoride Salts: LiF–BeF2–ThF2–UF4 and Eutectic NaBF4–NaF.* Oak Ridge National Laboratory., 1976. URL: https://books.google.com/books?id=cGzewQEACAAJ.

[30] Karl Britsch and Mark Anderson. “A Critical Review of Fluoride Salt Heat Transfer”. In: *Nuclear Technology* 206.11 (2020), pp. 1625–1641. DOI: 10.1080/00295450.2019.1682418. eprint: https://doi.org/10.1080/00295450.2019.1682418. URL: https://doi.org/10.1080/00295450.2019.1682418.

[31] Philippe M. Bardet and Per F. Peterson. “Options for Scaled Experiments for High Temperature Liquid Salt and Helium Fluid Mechanics and Convective Heat Transfer”. In: *Nuclear Technology* 163.3 (2008), pp. 344–357. DOI: 10.13182/NT163-344. eprint: https://doi.org/10.13182/NT163-344. URL: https://doi.org/10.13182/NT163-344.

[32] N. Zweibaum et al. “Design of the Compact Integral Effects Test Facility and Validation of Best-Estimate Models for Fluoride Salt–Cooled High-Temperature Reactors”. In: *Nuclear Technology* 196.3 (2016), pp. 641–660. DOI: 10.13182/NT16-15. eprint: https://doi.org/10.13182/NT16-15. URL: https://doi.org/10.13182/NT16-15.

[33] Joel T. Hughes. “Experimental and Computational Investigations of Heat Transfer Systems in Fluoride Salt-cooled High-temperature Reactors”. PhD thesis. University of New Mexico, 2017. URL: https://digitalrepository.unm.edu/ne_etds/60.

[34] Lakshana Huddar et al. “Application of frequency response methods in separate and integral effects tests for molten salt cooled and fueled reactors”. In: *Nuclear Engineering and Design* 329 (2018). The Best of HTR 2016: International Topical Meeting on High Temperature Reactor Technology, pp. 3–11. ISSN: 0029-5493. DOI: https://doi.org/10.1016/j.nucengdes.2017.11.045. URL: https://www.sciencedirect.com/science/article/pii/S0029549317305678.

[35] Limin Liu et al. “Scaling and distortion analysis using a simple natural circulation loop for FHR development”. In: *Applied Thermal Engineering* 168 (2020), p. 114849. ISSN: 1359-4311. DOI: https://doi.org/10.1016/j.applthermaleng.2019.114849. URL: https://www.sciencedirect.com/science/article/pii/S1359431119348677.

[36] “Fluid-to-fluid scaling for a gravity- and flashing-driven natural circulation loop”. In: *Nuclear Engineering and Design* 151.1 (1994), pp. 49–64. ISSN: 0029-5493. DOI: https://doi.org/10.1016/0029-5493(94)90033-7. URL: https://www.sciencedirect.com/science/article/pii/0029549394900337.

[37] “Molten salts database for energy applications”. In: *Chemical Engineering and Processing: Process Intensification* 73 (2013), pp. 87–102. ISSN: 0255-2701. DOI: https://doi.org/10.1016/j.cep.2013.07.008. URL: https://www.sciencedirect.com/science/article/pii/S0255270113001827.

[38] R.R. Romatoski and L.W. Hu. “Fluoride salt coolant properties for nuclear reactor applications: A review”. In: *Annals of Nuclear Energy* 109 (2017), pp. 635–647. ISSN: 0306-4549. DOI: https://doi.org/10.1016/j.anucene.2017.05.036. URL: https://www.sciencedirect.com/science/article/pii/S0306454917301391.

[39] Jared Magnusson, Matthew Memmott, and Troy Munro. “Review of thermophysical property methods applied to fueled and un-fueled molten salts”. In: *Annals of Nuclear Energy* 146 (2020), p. 107608. ISSN: 0306-4549. DOI: https://doi.org/10.1016/j.anucene.

2020.107608. URL: https://www.sciencedirect.com/science/article/pii/S0306454920303066.

[40] M. Chrenková et al. “Density and viscosity of the (LiF-NaF-KF)eut-KBF4-B2O3 melts”. In: *Journal of Molecular Liquids* 102.1 (2003), pp. 213–226. ISSN: 0167-7322. DOI: https://doi.org/10.1016/S0167-7322(02)00063-6. URL: https://www.sciencedirect.com/science/article/pii/S0167732202000636.

[41] S. I. Cohen and T. N. Jones. “VISCOSITY MEASUREMENTS ON MOLTEN FLUORIDE MIXTURES”. In: (July 1957). DOI: 10.2172/4803933. URL: https://www.osti.gov/biblio/4803933.

[42] D. F. Williams. “Assessment of Candidate Molten Salt Coolants for the NGNP/NHI Heat-Transfer Loop”. In: (June 2006). DOI: 10.2172/1360677. URL: https://www.osti.gov/biblio/1360677.

[43] Donald A. Nissen. “Thermophysical properties of the equimolar mixture sodium nitrate-potassium nitrate from 300 to 600.degree.C”. In: *Journal of Chemical & Engineering Data* 27.3 (1982), pp. 269–273. DOI: 10.1021/je00029a012. eprint: https://doi.org/10.1021/je00029a012. URL: https://doi.org/10.1021/je00029a012.

[44] ALEXIS B ZAVOICO. “Solar Power Tower Design Basis Document, Revision 0”. In: (July 2001). DOI: 10.2172/786629. URL: https://www.osti.gov/biblio/786629.

[45] National Renewable Energy Laboratory. *System Advisor Model (SAM)*. NREL. 2012. URL: https://sam.nrel.gov/download/version-2012-5-11.html.

[46] Zhen Yang and Suresh V. Garimella. “Thermal analysis of solar thermal energy storage in a molten-salt thermocline”. In: *Solar Energy* 84.6 (2010), pp. 974–985. ISSN: 0038-092X. DOI: https://doi.org/10.1016/j.solener.2010.03.007. URL: https://www.sciencedirect.com/science/article/pii/S0038092X10001118.

[47] R.M. DiGuilio and A.S. Teja. "A rough hard-sphere model for the thermal conductivity of molten salts". In: *International Journal of Thermophysics* 13.5 (1992), pp. 855–871. DOI: 10.1007/BF00503912. URL: https://doi.org/10.1007/BF00503912.

[48] J. W. Koger. "CORROSION AND MASS TRANSFER CHARACTERISTICS OF NaBF*sub*4–NaF (92-8 mole PERCENT) IN HASTELLOY N." In: (Jan. 1972). DOI: 10.2172/4602933. URL: https://www.osti.gov/biblio/4602933.

[49] S. E. Haaland. "Simple and Explicit Formulas for the Friction Factor in Turbulent Pipe Flow". In: *Journal of Fluids Engineering* 105.1 (Mar. 1983), pp. 89–90. ISSN: 0098-2202. DOI: 10.1115/1.3240948. eprint: https://asmedigitalcollection.asme.org/fluidsengineering/article-pdf/105/1/89/5711465/89_1.pdf. URL: https://doi.org/10.1115/1.3240948.

[50] F.W. Dittus and L.M.K. Boelter. "Heat transfer in automobile radiators of the tubular type". In: *International Communications in Heat and Mass Transfer* 12.1 (1985), pp. 3–22. ISSN: 0735-1933. DOI: https://doi.org/10.1016/0735-1933(85)90003-X. URL: https://www.sciencedirect.com/science/article/pii/073519338590003X.

[51] Edward Blandford et al. "Kairos power thermal hydraulics research and development". In: *Nuclear Engineering and Design* 364 (2020), p. 110636. ISSN: 0029-5493. DOI: https://doi.org/10.1016/j.nucengdes.2020.110636. URL: https://www.sciencedirect.com/science/article/pii/S0029549320301308.

[52] Joel Tellinghuisen. "Least Squares Methods for Treating Problems with Uncertainty in x and y". In: *Analytical Chemistry* 92.16 (2020). PMID: 32678579, pp. 10863–10871. DOI: 10.1021/acs.analchem.0c02178. eprint: https://doi.org/10.1021/acs.analchem.0c02178. URL: https://doi.org/10.1021/acs.analchem.0c02178.

[53] C J Roy and Balch M S. "A Holistic Approach to Uncertainty Quantification with Application to Supersonic Nozzle Thrust". In: *International Journal for Uncertainty Quantification* 2 (2012).

[54] V. Gnielinski. "New equations for heat and mass transfer in turbulent pipe and channel flow". In: *Int. Chem. Eng* 16.2 (1976), pp. 359–368.

[55] A. E. Bergles et al. "Bibliography on augmentation of convective heat and mass transfer-II". In: (Dec. 1983). DOI: 10.2172/5028987. URL: https://www.osti.gov/biblio/5028987.

[56] Mohamed H. Mousa, Nenad Miljkovic, and Kashif Nawaz. "Review of heat transfer enhancement techniques for single phase flows". In: *Renewable and Sustainable Energy Reviews* 137 (2021), p. 110566. ISSN: 1364-0321. DOI: https://doi.org/10.1016/j.rser.2020.110566. URL: https://www.sciencedirect.com/science/article/pii/S1364032120308509.

[57] A Dewan et al. "Review of passive heat transfer augmentation techniques". In: *Proceedings of the Institution of Mechanical Engineers, Part A: Journal of Power and Energy* 218.7 (2004), pp. 509–527. DOI: 10.1243/0957650042456953. eprint: https://doi.org/10.1243/0957650042456953. URL: https://doi.org/10.1243/0957650042456953.

[58] Sashank Thapa et al. "A review study on the active methods of heat transfer enhancement in heat exchangers using electroactive and magnetic materials". In: *Materials Today: Proceedings* 45 (2021). Second International Conference on Aspects of Materials Science and Engineering (ICAMSE 2021), pp. 4942–4947. ISSN: 2214-7853. DOI: https://doi.org/10.1016/j.matpr.2021.01.382. URL: https://www.sciencedirect.com/science/article/pii/S2214785321004739.

[59] Tabish Alam and Man-Hoe Kim. "A comprehensive review on single phase heat transfer enhancement techniques in heat exchanger applications". In: *Renewable and Sustainable Energy Reviews* 81 (2018), pp. 813–839. ISSN: 1364-0321. DOI: https://doi.org/10.1016/j.rser.2017.08.060. URL: https://www.sciencedirect.com/science/article/pii/S1364032117312030.

[60] Zhi Tao, Lu Qiu, and Hongwu Deng. "Heat transfer in a rotating smooth wedge-shaped channel with lateral fluid extraction". In: *Applied Thermal Engineering* 87 (2015), pp. 47–55. ISSN: 1359-4311. DOI: https://doi.org/10.1016/j.applthermaleng.2015.04.073. URL: https://www.sciencedirect.com/science/article/pii/S1359431115004330.

[61] Lu Qiu et al. "Pressure drop and heat transfer in rotating smooth square U-duct under high rotation numbers". In: *International Journal of Heat and Mass Transfer* 66 (2013), pp. 543–552. ISSN: 0017-9310. DOI: https://doi.org/10.1016/j.ijheatmasstransfer.2013.07.055. URL: https://www.sciencedirect.com/science/article/pii/S0017931013006091.

[62] José L. Fernández and Robert Poulter. "Radial mass flow in electrohydrodynamically-enhanced forced heat transfer in tubes". In: *International Journal of Heat and Mass Transfer* 30.10 (1987), pp. 2125–2136. ISSN: 0017-9310. DOI: https://doi.org/10.1016/0017-9310(87)90091-3. URL: https://www.sciencedirect.com/science/article/pii/0017931087900913.

[63] Yukio Tada et al. "Heat transfer enhancement in a gas–solid suspension flow by applying electric field". In: *International Journal of Heat and Mass Transfer* 93 (2016), pp. 778–787. ISSN: 0017-9310. DOI: https://doi.org/10.1016/j.ijheatmasstransfer.2015.09.063. URL: https://www.sciencedirect.com/science/article/pii/S0017931015300703.

[64] Raj M. Manglik and Arthur E. Bergles. "Swirl flow heat transfer and pressure drop with twisted-tape inserts". In: ed. by James P. Hartnett et al. Vol. 36. Advances in Heat Transfer. Elsevier, 2003, pp. 183–266. DOI: https://doi.org/10.1016/S0065-2717(02)80007-7. URL: https://www.sciencedirect.com/science/article/pii/S0065271702800077.

[65] S. Bhattacharyya et al. "Thermal performance enhancement in heat exchangers using active and passive techniques: a detailed review". In: *J Therm Anal Calorim* 147 (2022), pp. 9229–9281. DOI: 10.1007/s10973-021-11168-5. URL: https://doi.org/10.1007/s10973-021-11168-5.

[66] "THE EFFECTS OF RETARDERS IN FIRE TUBES OF STEAM BOILERS". In: *Journal of the American Society for Naval Engineers* 8.4 (1896), pp. 779–781. DOI: https://doi.org/10.1111/j.1559-3584.1896.tb00751.x. eprint: https://onlinelibrary.wiley.com/doi/pdf/10.1111/j.1559-3584.1896.tb00751.x. URL: https://onlinelibrary.wiley.com/doi/abs/10.1111/j.1559-3584.1896.tb00751.x.

[67] Zimu Yang et al. "Numerical Analysis of FLiBe Laminar Convective Heat Transfer Characteristics in Tubes Fitted With Coaxial Cross Twisted Tape Inserts". In: *Frontiers in Energy Research* 8 (2020). ISSN: 2296-598X. DOI: 10.3389/fenrg.2020.00178. URL: https://www.frontiersin.org/articles/10.3389/fenrg.2020.00178.

[68] E. Clark et al. "Experiment attributes to establish tube with twisted tape insert performance cooling plasma facing components". In: *Fusion Engineering and Design* 100 (2015), pp. 541–549. ISSN: 0920-3796. DOI: https://doi.org/10.1016/j.fusengdes.2015.08.004. URL: https://www.sciencedirect.com/science/article/pii/S0920379615302593.

[69] A Kumar and B.N Prasad. "Investigation of twisted tape inserted solar water heaters—heat transfer, friction factor and thermal performance results". In: *Renewable Energy* 19.3 (2000), pp. 379–398. ISSN: 0960-1481. DOI: https://doi.org/10.1016/S0960-1481(99)00061-0. URL: https://www.sciencedirect.com/science/article/pii/S0960148199000610.

[70] A. Veera Kumar et al. "Influence of twisted tape inserts on energy and exergy performance of an evacuated Tube-based solar air collector". In: *Solar Energy* 225 (2021), pp. 892–904.

ISSN: 0038-092X. DOI: https://doi.org/10.1016/j.solener.2021.07.074. URL: https://www.sciencedirect.com/science/article/pii/S0038092X21006551.

[71] P Bradshaw. "Turbulent Secondary Flows". In: *Annual Review of Fluid Mechanics* 19.1 (1987), pp. 53–74. DOI: 10.1146/annurev.fl.19.010187.000413. eprint: https://doi.org/10.1146/annurev.fl.19.010187.000413. URL: https://doi.org/10.1146/annurev.fl.19.010187.000413.

[72] G. L. Converse, M. U. Gutstein, and J. R. Peterson. *Theoretical analysis and measurement of single-phase pressure losses and heat transfer for helical flow in a tube*. NASA Technical Note (TN) E-5743. NASA-TN-D-6097. Cleveland, OH, United States: NASA Lewis Research Center, 1970. URL: https://ntrs.nasa.gov/archive/nasa/casi.ntrs.nasa.gov/19710002738.pdf.

[73] Raj Mitra Manglik. "Heat transfer enhancement of in-tube flows in process heat exchangers by means of twisted-tape inserts". PhD thesis. Troy, NY: Rensselaer Polytechnic Institute, 1991. URL: https://hdl.handle.net/20.500.13015/3495.

[74] Emily Buckman Clark. "Computational Thermal-Hydraulics Modeling of Twisted Tape Enabled High Heat Flux Components". PhD thesis. University of Tennessee, 2017. URL: https://trace.tennessee.edu/utk_graddiss/4393.

[75] A. Hasanpour, M. Farhadi, and K. Sedighi. "A review study on twisted tape inserts on turbulent flow heat exchangers: The overall enhancement ratio criteria". In: *International Communications in Heat and Mass Transfer* 55 (2014), pp. 53–62. ISSN: 0735-1933. DOI: https://doi.org/10.1016/j.icheatmasstransfer.2014.04.008. URL: https://www.sciencedirect.com/science/article/pii/S0735193314001122.

[76] Varun et al. "Heat transfer augmentation using twisted tape inserts: A review". In: *Renewable and Sustainable Energy Reviews* 63 (2016), pp. 193–225. ISSN: 1364-0321. DOI: https://doi.org/10.1016/j.rser.2016.04.051. URL: https://www.sciencedirect.com/science/article/pii/S1364032116300843.

[77] Chirag Maradiya, Jeetendra Vadher, and Ramesh Agarwal. “The heat transfer enhancement techniques and their Thermal Performance Factor”. In: *Beni-Suef University Journal of Basic and Applied Sciences* 7.1 (2018), pp. 1–21. ISSN: 2314-8535. DOI: https://doi.org/10.1016/j.bjbas.2017.10.001. URL: https://www.sciencedirect.com/science/article/pii/S2314853517300070.

[78] Smith Eiamsa-ard, Chayut Nuntadusit, and Pongjet Promvonge. “Effect of Twin Delta-Winged Twisted-Tape on Thermal Performance of Heat Exchanger Tube”. In: *Heat Transfer Engineering* 34.15 (2013), pp. 1278–1288. DOI: 10.1080/01457632.2013.793112. eprint: https://doi.org/10.1080/01457632.2013.793112. URL: https://doi.org/10.1080/01457632.2013.793112.

[79] Sibel Gunes and Ersin Karakaya. “Thermal Characteristics in a Tube With Loose-Fit Perforated Twisted Tapes”. In: *Heat Transfer Engineering* 36.18 (2015), pp. 1504–1517. DOI: 10.1080/01457632.2015.1024985. eprint: https://doi.org/10.1080/01457632.2015.1024985. URL: https://doi.org/10.1080/01457632.2015.1024985.

[80] C. Thianpong et al. “Effect of perforated twisted-tapes with parallel wings on heat tansfer enhancement in a heat exchanger tube”. In: *Energy Procedia* 14 (2012). 2011 2nd International Conference on Advances in Energy Engineering (ICAEE), pp. 1117–1123. ISSN: 1876-6102. DOI: https://doi.org/10.1016/j.egypro.2011.12.1064. URL: https://www.sciencedirect.com/science/article/pii/S1876610211044845.

[81] S. Eiamsa-ard, C. Thianpong, and P. Eiamsa-ard. “Turbulent heat transfer enhancement by counter/co-swirling flow in a tube fitted with twin twisted tapes”. In: *Experimental Thermal and Fluid Science* 34.1 (2010), pp. 53–62. ISSN: 0894-1777. DOI: https://doi.org/10.1016/j.expthermflusci.2009.09.002. URL: https://www.sciencedirect.com/science/article/pii/S0894177709001393.

[82] Yuxiang Hong, Juan Du, and Shuangfeng Wang. “Turbulent thermal, fluid flow and thermodynamic characteristics in a plain tube fitted with overlapped multiple twisted tapes”.

In: *International Journal of Heat and Mass Transfer* 115 (2017), pp. 551–565. ISSN: 0017-9310. DOI: https://doi.org/10.1016/j.ijheatmasstransfer.2017.08.017. URL: https://www.sciencedirect.com/science/article/pii/S0017931017319713.

[83] R. Hosseinnezhad et al. "Numerical study of turbulent nanofluid heat transfer in a tubular heat exchanger with twin twisted-tape inserts". In: *J Therm Anal Calorim* 132 (2018), pp. 741–759. DOI: 10.1007/s10973-017-6900-5. URL: https://doi.org/10.1007/s10973-017-6900-5.

[84] Sungjin Kwon, Kihak Im, and Jong Sung Park. "Thermohydraulic Assessment for the Modified Concept of the K-DEMO Divertor Target". In: *Fusion Science and Technology* 72.4 (2017), pp. 737–746. DOI: 10.1080/15361055.2017.1350479. eprint: https://doi.org/10.1080/15361055.2017.1350479. URL: https://doi.org/10.1080/15361055.2017.1350479.

[85] E. Clark et al. "Computational Investigation of the Thermal-Hydraulic Performance for Twisted Tape Enabled High Heat Flux Components". In: *Fusion Science and Technology* 72.3 (2017), pp. 278–284. DOI: 10.1080/15361055.2017.1333823. eprint: https://doi.org/10.1080/15361055.2017.1333823. URL: https://doi.org/10.1080/15361055.2017.1333823.

[86] R. M. Manglik and A. E. Bergles. "Heat Transfer and Pressure Drop Correlations for Twisted-Tape Inserts in Isothermal Tubes: Part II—Transition and Turbulent Flows". In: *Journal of Heat Transfer* 115.4 (Nov. 1993), pp. 890–896. ISSN: 0022-1481. DOI: 10.1115/1.2911384. eprint: https://asmedigitalcollection.asme.org/heattransfer/article-pdf/115/4/890/5698659/890_1.pdf. URL: https://doi.org/10.1115/1.2911384.

[87] R. M. Manglik and A. E. Bergles. "Heat Transfer and Pressure Drop Correlations for Twisted-Tape Inserts in Isothermal Tubes: Part I—Laminar Flows". In: *Journal of Heat Transfer* 115.4 (Nov. 1993), pp. 881–889. ISSN: 0022-1481. DOI: 10.1115/1.2911383.

eprint: https://asmedigitalcollection.asme.org/heattransfer/article-pdf/115/4/881/5698486/881_1.pdf. URL: https://doi.org/10.1115/1.2911383.

[88] W.J. Marner and A.E. Bergles. "Augmentation of highly viscous laminar heat transfer inside tubes with constant wall temperature". In: *Experimental Thermal and Fluid Science* 2.3 (1989), pp. 252–267. ISSN: 0894-1777. DOI: https://doi.org/10.1016/0894-1777(89)90015-0. URL: https://www.sciencedirect.com/science/article/pii/0894177789900150.

[89] Z.H. Ayub and S.F. Al-Fahed. "The effect of gap width between horizontal tube and twisted tape on the pressure drop in turbulent water flow". In: *International Journal of Heat and Fluid Flow* 14.1 (1993), pp. 64–67. ISSN: 0142-727X. DOI: https://doi.org/10.1016/0142-727X(93)90041-K. URL: https://www.sciencedirect.com/science/article/pii/0142727X9390041K.

[90] Sami Al-Fahed and Walid Chakroun. "Effect of tube-tape clearance on heat transfer for fully developed turbulent flow in a horizontal isothermal tube". In: *International Journal of Heat and Fluid Flow* 17.2 (1996), pp. 173–178. ISSN: 0142-727X. DOI: https://doi.org/10.1016/0142-727X(95)00096-9. URL: https://www.sciencedirect.com/science/article/pii/0142727X95000969.

[91] Halit Bas and Veysel Ozceyhan. "Heat transfer enhancement in a tube with twisted tape inserts placed separately from the tube wall". In: *Experimental Thermal and Fluid Science* 41 (2012), pp. 51–58. ISSN: 0894-1777. DOI: https://doi.org/10.1016/j.expthermflusci.2012.03.008. URL: https://www.sciencedirect.com/science/article/pii/S0894177712000751.

[92] Cody S. Wiggins, Arturo Cabral, and Lane B. Carasik. "Investigation of Pressure Drop Calculation for Twisted Tape Swirl Tubes by Conventional Channel Flow Correlations with Fusion Applications". In: *Fusion Science and Technology* 77.3 (2021), pp. 206–219. DOI:

10.1080/15361055.2021.1872273. eprint: https://doi.org/10.1080/15361055.2021.1872273. URL: https://doi.org/10.1080/15361055.2021.1872273.

[93] E. Smithberg and F. Landis. "Friction and Forced Convection Heat-Transfer Characteristics in Tubes With Twisted Tape Swirl Generators". In: *Journal of Heat Transfer* 86.1 (Feb. 1964), pp. 39–48. ISSN: 0022-1481. DOI: 10.1115/1.3687060. eprint: https://asmedigitalcollection.asme.org/heattransfer/article-pdf/86/1/39/5743493/39_1.pdf. URL: https://doi.org/10.1115/1.3687060.

[94] R. Thorsen and F. Landis. "Integral methods in transient heat conduction problems with non-uniform initial conditions". In: *International Journal of Heat and Mass Transfer* 8.1 (1965), pp. 189–192. ISSN: 0017-9310. DOI: https://doi.org/10.1016/0017-9310(65)90108-0. URL: https://www.sciencedirect.com/science/article/pii/0017931065901080.

[95] P.K. Sarma et al. "A new method to predict convective heat transfer in a tube with twisted tape inserts for turbulent flow". In: *International Journal of Thermal Sciences* 41.10 (2002), pp. 955–960. ISSN: 1290-0729. DOI: https://doi.org/10.1016/S1290-0729(02)01388-1. URL: https://www.sciencedirect.com/science/article/pii/S1290072902013881.

[96] P.K. Sarma et al. "Laminar convective heat transfer with twisted tape inserts in a tube". In: *International Journal of Thermal Sciences* 42.9 (2003), pp. 821–828. ISSN: 1290-0729. DOI: https://doi.org/10.1016/S1290-0729(03)00055-3. URL: https://www.sciencedirect.com/science/article/pii/S1290072903000553.

[97] P.K. Sarma et al. "A combined approach to predict friction coefficients and convective heat transfer characteristics in A tube with twisted tape inserts for a wide range of Re and Pr". In: *International Journal of Thermal Sciences* 44.4 (2005), pp. 393–398. ISSN: 1290-0729. DOI: https://doi.org/10.1016/j.ijthermalsci.2004.12.001. URL: https://www.sciencedirect.com/science/article/pii/S1290072905000037.

[98] S.W. Churchill. “The development of theoretically based correlations for heat and mass transfer”. In: *Latin Amer. J. Heat Mass Transfer* 7 (1983), pp. 207–229.

[99] Aleksey V. Dedov et al. “Hydrodynamics and heat transfer in swirl flow under conditions of one-side heating. Part 2: Boiling heat transfer. Critical heat fluxes”. In: *International Journal of Heat and Mass Transfer* 53.21 (2010), pp. 4966–4975. ISSN: 0017-9310. DOI: https://doi.org/10.1016/j.ijheatmasstransfer.2010.05.035. URL: https://www.sciencedirect.com/science/article/pii/S0017931010002772.

[100] A.N. Varava et al. “Investigation of hydraulic drag and heat transfer in a single-phase swirl flow under one-sided heating”. In: *High Temp* 44 (2006), pp. 693–702. DOI: 10.1007/s10740-006-0084-1. URL: https://doi.org/10.1007/s10740-006-0084-1.

[101] A.N. Varava et al. “Study of pressure drop and heat transfer in a swirl flow with one-sided heating in a range of heat flowrates below boiling crisis”. In: *Therm. Eng.* 56 (2009), pp. 953–962. DOI: 10.1134/S004060150911010X. URL: https://doi.org/10.1134/S004060150911010X.

[102] R. F. Lopina and A. E. Bergles. “Heat Transfer and Pressure Drop in Tape-Generated Swirl Flow of Single-Phase Water”. In: *Journal of Heat Transfer* 91.3 (Aug. 1969), pp. 434–441. ISSN: 0022-1481. DOI: 10.1115/1.3580212. eprint: https://asmedigitalcollection.asme.org/heattransfer/article-pdf/91/3/434/5744551/434_1.pdf. URL: https://doi.org/10.1115/1.3580212.

[103] S. W. Hong and A. E. Bergles. “Augmentation of Laminar Flow Heat Transfer in Tubes by Means of Twisted-Tape Inserts”. In: *Journal of Heat Transfer* 98.2 (May 1976), pp. 251–256. ISSN: 0022-1481. DOI: 10.1115/1.3450527. eprint: https://asmedigitalcollection.asme.org/heattransfer/article-pdf/98/2/251/5556196/251_1.pdf. URL: https://doi.org/10.1115/1.3450527.

[104] B. Petukhov, L. Genin, and S. Kovalev. “Heat Transfer in Nuclear Power Plants”. In: *Teploobmen v Yadernykh Energeticheskikh Ustanovkakh*. Moscow, 1986.

[105] G.K. Filonenko. “Hydraulic Resistance in Pipes”. In: *Teploenergetika* 1.- (1954), pp. 40–44.

[106] Pongjet Promvonge. “Thermal augmentation in circular tube with twisted tape and wire coil turbulators”. In: *Energy Conversion and Management* 49.11 (2008). Special Issue 3rd International Conference on Thermal Engineering: Theory and Applications, pp. 2949–2955. ISSN: 0196-8904. DOI: https://doi.org/10.1016/j.enconman.2008.06.022. URL: https://www.sciencedirect.com/science/article/pii/S0196890408002483.

[107] P. Eiamsa-ard et al. “A case study on thermal performance assessment of a heat exchanger tube equipped with regularly-spaced twisted tapes as swirl generators”. In: *Case Studies in Thermal Engineering* 3 (2014), pp. 86–102. ISSN: 2214-157X. DOI: https://doi.org/10.1016/j.csite.2014.04.002. URL: https://www.sciencedirect.com/science/article/pii/S2214157X14000136.

[108] P. Murugesan et al. “Heat transfer and pressure drop characteristics in a circular tube fitted with and without V-cut twisted tape insert”. In: *International Communications in Heat and Mass Transfer* 38.3 (2011), pp. 329–334. ISSN: 0735-1933. DOI: https://doi.org/10.1016/j.icheatmasstransfer.2010.11.010. URL: https://www.sciencedirect.com/science/article/pii/S073519331000271X.

[109] Suriya Chokphoemphun et al. “Thermal performance of tubular heat exchanger with multiple twisted-tape inserts”. In: *Chinese Journal of Chemical Engineering* 23.5 (2015), pp. 755–762. ISSN: 1004-9541. DOI: https://doi.org/10.1016/j.cjche.2015.01.003. URL: https://www.sciencedirect.com/science/article/pii/S1004954115000324.

[110] N. Piriyarungrod et al. “Heat transfer enhancement by tapered twisted tape inserts”. In: *Chemical Engineering and Processing: Process Intensification* 96 (2015), pp. 62–71. ISSN: 0255-2701. DOI: https://doi.org/10.1016/j.cep.2015.08.002. URL: https://www.sciencedirect.com/science/article/pii/S0255270115300817.

[111] S. Naga Sarada et al. "Enhancement of heat transfer using varying width twisted tape inserts". In: *International Journal of Engineering, Science and Technology* 2.6 (2010), pp. 107–118. DOI: 10.4314/ijest.v2i6.63702.

[112] *WebPlotDigitizer*. https://automeris.io/WebPlotDigitizer/.

[113] N. Aksan. *Critical Review of Separate Effects Test Facilities (SETF) Data Used for Assessment of the Best-Estimate Thermal-Hydraulic System Codes*. 2008.

[114] Todd Allen et al. *Fluoride-Salt-Cooled High Temperature Reactor (FHR) Materials, Fuels and Components White Paper*. White paper. Report No. UCBTH-12-003. 2013. URL: http://fhr.nuc.berkeley.edu/wp-content/uploads/2013/08/12-003-FHR-Workshop-3-Report-Final.pdf.

[115] L. F. Moody. "An Approximate Formula for Pipe Friction Factor". In: *Trans. ASME* 69 (1947), pp. 1005–1011.

[116] Heinrich Blasius. *Das Aehnlichkeitsgesetz bei Reibungsvorgängen in Flüssigkeiten*. Vol. 131. Mitteilungen über Forschungsarbeiten auf dem Gebiete des Ingenieurwesens, insbesondere der Technischen Hochschulen. Springer, 1913, p. 70.

[117] C.G. Klingaa et al. "X-ray CT and image analysis methodology for local roughness characterization in cooling channels made by metal additive manufacturing". In: *Additive Manufacturing* 32 (2020), p. 101032. ISSN: 2214-8604. DOI: 10.1016/j.addma.2019.101032.

[118] E. N. Sieder and G. E. Tate. "Heat Transfer and Pressure Drop of Liquids in Tubes". In: *Industrial & Engineering Chemistry* 28.12 (1936), pp. 1429–1435. DOI: 10.1021/ie50324a027. eprint: https://doi.org/10.1021/ie50324a027. URL: https://doi.org/10.1021/ie50324a027.

[119] Ivel L. Collins et al. "A permeable-membrane microchannel heat sink made by additive manufacturing". In: *International Journal of Heat and Mass Transfer* 131 (2019), pp. 1174–1183. ISSN: 0017-9310. DOI: https://doi.org/10.1016/j.ijheatmasstransfer.

2018.11.126. URL: https://www.sciencedirect.com/science/article/pii/S0017931018341656.

[120] M. Ibragimov, E. Nomsfelov, and V. Subbotin. "Heat transfer and hydraulic resistance with swirl-type motion of liquid in pipes". In: *Teploenergetika* 8 (1961), pp. 57–60.

[121] H. H. Bruun. "Hot-wire anemometry : principles and signal analysis". In: 1996.

[122] I Grant. "Particle image velocimetry: A review". In: *Proceedings of the Institution of Mechanical Engineers, Part C: Journal of Mechanical Engineering Science* 211.1 (1997), pp. 55–76. DOI: 10.1243/0954406971521665. eprint: https://doi.org/10.1243/0954406971521665. URL: https://doi.org/10.1243/0954406971521665.

[123] Reinhardt Kotzé, Johan Wiklund, and Rainer Haldenwang. "Optimisation of Pulsed Ultrasonic Velocimetry system and transducer technology for industrial applications". In: *Ultrasonics* 53.2 (2013), pp. 459–469. ISSN: 0041-624X. DOI: https://doi.org/10.1016/j.ultras.2012.08.014. URL: https://www.sciencedirect.com/science/article/pii/S0041624X12001679.

[124] Nicholas P. Ramskill et al. "Magnetic resonance velocity imaging of gas flow in a diesel particulate filter". In: *Chemical Engineering Science* 158 (2017), pp. 490–499. ISSN: 0009-2509. DOI: https://doi.org/10.1016/j.ces.2016.10.017. URL: https://www.sciencedirect.com/science/article/pii/S0009250916305498.

[125] U. Hampel et al. "High resolution gamma ray tomography scanner for flow measurement and non-destructive testing applications". In: *Review of Scientific Instruments* 78.10 (Oct. 2007). 103704. ISSN: 0034-6748. DOI: 10.1063/1.2795648. eprint: https://pubs.aip.org/aip/rsi/article-pdf/doi/10.1063/1.2795648/15974319/103704_1_online.pdf. URL: https://doi.org/10.1063/1.2795648.

[126] Hamed Bashiri et al. "Investigation of turbulent fluid flows in stirred tanks using a non-intrusive particle tracking technique". In: *Chemical Engineering Science* 140 (2016),

pp. 233–251. ISSN: 0009-2509. DOI: https://doi.org/10.1016/j.ces.2015.10.005. URL: https://www.sciencedirect.com/science/article/pii/S0009250915006715.

[127] D.J. Parker et al. “Positron emission particle tracking - a technique for studying flow within engineering equipment”. In: *Nuclear Instruments and Methods in Physics Research Section A: Accelerators, Spectrometers, Detectors and Associated Equipment* 326.3 (1993), pp. 592–607. ISSN: 0168-9002. DOI: https://doi.org/10.1016/0168-9002(93)90864-E. URL: https://www.sciencedirect.com/science/article/pii/016890029390864E.

[128] E. V. Seymour. “Fluid flow through tubes containing twisted tapes”. In: *The Engineer* 222 (1966), p. 634.

[129] R. G. Backshall and Fred Landis. “The Boundary-Layer Velocity Distribution in Turbulent Swirling Pipe Flow”. In: *Journal of Basic Engineering* 91.4 (Dec. 1969), pp. 728–733.

[130] Radu Cazan and Cyrus K. Aidun. “Experimental investigation of the swirling flow and the helical vortices induced by a twisted tape inside a circular pipe”. In: *Physics of Fluids* 21.3 (Mar. 2009). 037102. ISSN: 1070-6631. DOI: 10.1063/1.3085699. eprint: https://pubs.aip.org/aip/pof/article-pdf/doi/10.1063/1.3085699/14055906/037102_1_online.pdf. URL: https://doi.org/10.1063/1.3085699.

[131] Cody S. Wiggins, Lane B. Carasik, and Arthur E. Ruggles. “Noninvasive interrogation of local flow phenomena in twisted tape swirled flow via positron emission particle tracking (PEPT)”. In: *Nuclear Engineering and Design* 387 (2022), p. 111601. ISSN: 0029-5493. DOI: https://doi.org/10.1016/j.nucengdes.2021.111601. URL: https://www.sciencedirect.com/science/article/pii/S0029549321005537.

[132] Cody Wiggins. “Multiple Particle Positron Emission Particle Tracking and its Application to Flows in Porous Media”. PhD thesis. University of Tennessee, 2019. URL: https://trace.tennessee.edu/utk_graddiss/5610.

[133] R. F. Shaw. “Signalling Particles for Introduction into Blood Flowing Through a Vessel of Interest”. US Patent No. 4,224,303. 1980.

[134] M. Bickell et al. “A new line density tracking algorithm for PEPT and its application to multiple tracers”. In: *Nuclear Instruments and Methods in Physics Research Section A: Accelerators, Spectrometers, Detectors and Associated Equipment* 682 (2012), pp. 36–41. ISSN: 0168-9002. DOI: https://doi.org/10.1016/j.nima.2012.04.037. URL: https://www.sciencedirect.com/science/article/pii/S0168900212003920.

[135] Yu-Fen Chang, Tom C.H. Adamsen, and Alex C. Hoffmann. “Using a PET camera to track individual phases in process equipment with high temporal and spatial resolutions: Algorithm development”. In: *2012 IEEE International Instrumentation and Measurement Technology Conference Proceedings*. 2012, pp. 2326–2330. DOI: 10.1109/I2MTC.2012.6229306.

[136] Cody Wiggins, Roque Santos, and Arthur Ruggles. “A novel clustering approach to positron emission particle tracking”. In: *Nuclear Instruments and Methods in Physics Research Section A: Accelerators, Spectrometers, Detectors and Associated Equipment* 811 (2016), pp. 18–24. ISSN: 0168-9002. DOI: https://doi.org/10.1016/j.nima.2015.11.136. URL: https://www.sciencedirect.com/science/article/pii/S0168900215015533.

[137] Kyung Sang Lee, Tae-Jong Kim, and Guillem Pratx. “Single-cell tracking with PET using a novel trajectory reconstruction algorithm”. In: *IEEE Transactions on Medical Imaging* 34.4, 25423651 (2015), pp. 994–1003. DOI: 10.1109/TMI.2014.2373351.

[138] Cody Wiggins, Roque Santos, and Arthur Ruggles. “A feature point identification method for positron emission particle tracking with multiple tracers”. In: *Nuclear Instruments and Methods in Physics Research Section A: Accelerators, Spectrometers, Detectors and Associated Equipment* 843 (2017), pp. 22–28. ISSN: 0168-9002. DOI: https://doi.

org/10.1016/j.nima.2016.10.057. URL: https://www.sciencedirect.com/science/article/pii/S0168900216311184.

[139] A. L. Nicuşan and C. R. K. Windows-Yule. "Positron emission particle tracking using machine learning". In: *Review of Scientific Instruments* 91.1 (Jan. 2020), p. 013329. ISSN: 0034-6748. DOI: 10.1063/1.5129251. eprint: https://pubs.aip.org/aip/rsi/article-pdf/doi/10.1063/1.5129251/13994176/013329_1_online.pdf. URL: https://doi.org/10.1063/1.5129251.

[140] CRK Windows-Yule et al. "Recent advances in positron emission particle tracking: a comparative review". In: *Reports on Progress in Physics* 85.1 (2022). DOI: 10.1088/1361-6633/ac3c4c.

[141] Cody S. Wiggins, Arturo Cabral, and Lane B. Carasik. "Coregistered positron emission particle tracking (PEPT) and X-ray computed tomography (CT) for engineering flow measurements". In: *Nuclear Engineering and Design* 403 (2023), p. 112125. ISSN: 0029-5493. DOI: https://doi.org/10.1016/j.nucengdes.2022.112125. URL: https://www.sciencedirect.com/science/article/pii/S0029549322004769.

[142] R. Pérez-Mohedano et al. "Positron Emission Particle Tracking (PEPT) for the analysis of water motion in a domestic dishwasher". In: *Chemical Engineering Journal* 259 (2015), pp. 724–736. ISSN: 1385-8947. DOI: https://doi.org/10.1016/j.cej.2014.08.033. URL: https://www.sciencedirect.com/science/article/pii/S1385894714010870.

[143] Cody Wiggins et al. "Qualification of multiple-particle positron emission particle tracking (M-PEPT) technique for measurements in turbulent wall-bounded flow". In: *Chemical Engineering Science* 204 (2019), pp. 246–256. ISSN: 0009-2509. DOI: https://doi.org/10.1016/j.ces.2019.04.030. URL: https://www.sciencedirect.com/science/article/pii/S0009250919303951.

[144] Jerel Houston et al. "Flow Visualization in a Flow Conditioner to Support PEPT Experiments of Advanced Reactor Components". In: *Proceedings of the American Nuclear Society Winter Meeting 2022*. Phoenix, Arizona, 2022.

[145] Fabio Chiti et al. "Using positron emission particle tracking (PEPT) to study the turbulent flow in a baffled vessel agitated by a Rushton turbine: Improving data treatment and validation". In: *Chemical Engineering Research and Design* 89.10 (2011), pp. 1947–1960. ISSN: 0263-8762. DOI: https://doi.org/10.1016/j.cherd.2011.01.015. URL: https://www.sciencedirect.com/science/article/pii/S0263876211000414.

[146] P. Pianko-Oprych, A.W. Nienow, and M. Barigou. "Positron emission particle tracking (PEPT) compared to particle image velocimetry (PIV) for studying the flow generated by a pitched-blade turbine in single phase and multi-phase systems". In: *Chemical Engineering Science* 64.23 (2009), pp. 4955–4968. ISSN: 0009-2509. DOI: https://doi.org/10.1016/j.ces.2009.08.003. URL: https://www.sciencedirect.com/science/article/pii/S0009250909005417.

[147] Chiya Savari, Kun Li, and Mostafa Barigou. "Multiscale wavelet analysis of 3D Lagrangian trajectories in a mechanically agitated vessel". In: *Chemical Engineering Science* 260 (2022), p. 117844. ISSN: 0009-2509. DOI: https://doi.org/10.1016/j.ces.2022.117844. URL: https://www.sciencedirect.com/science/article/pii/S0009250922004286.

[148] Robert P. Fishwick et al. "Hydrodynamic Measurements of Up- and Down-Pumping Pitched-Blade Turbines in Gassed, Agitated Vessels, Using Positron Emission Particle Tracking". In: *Industrial & Engineering Chemistry Research* 44.16 (2005), pp. 6371–6380. DOI: 10.1021/ie049191v. eprint: https://doi.org/10.1021/ie049191v. URL: https://doi.org/10.1021/ie049191v.

[149] A.-E. Sommer et al. "Application of Positron Emission Particle Tracking (PEPT) to measure the bubble-particle interaction in a turbulent and dense flow". In: *Minerals Engineering*

156 (2020), p. 106410. ISSN: 0892-6875. DOI: https://doi.org/10.1016/j.mineng.2020.106410. URL: https://www.sciencedirect.com/science/article/pii/S0892687520302302.

[150] K.E. Waters et al. “Positron emission particle tracking as a method to map the movement of particles in the pulp and froth phases”. In: *Minerals Engineering* 21.12 (2008). xxxx, pp. 877–882. ISSN: 0892-6875. DOI: https://doi.org/10.1016/j.mineng.2008.02.007. URL: https://www.sciencedirect.com/science/article/pii/S0892687508000320.

[151] M. Eesa and M. Barigou. “Horizontal laminar flow of coarse nearly-neutrally buoyant particles in non-Newtonian conveying fluids: CFD and PEPT experiments compared”. In: *International Journal of Multiphase Flow* 34.11 (2008), pp. 997–1007. ISSN: 0301-9322. DOI: https://doi.org/10.1016/j.ijmultiphaseflow.2008.06.003. URL: https://www.sciencedirect.com/science/article/pii/S0301932208000992.

[152] Rayhaan Perin et al. “On the Ability of Positron Emission Particle Tracking (PEPT) to Track Turbulent Flow Paths with Monte Carlo Simulations in GATE”. In: *Applied Sciences* 13.11 (2023). ISSN: 2076-3417. URL: https://www.mdpi.com/2076-3417/13/11/6690.

[153] Zsolt Sarnyai et al. “Performance Evaluation of a High-Resolution Nonhuman Primate PET/CT System”. In: *Journal of Nuclear Medicine* 60.12 (2019), pp. 1818–1824. DOI: 10.2967/jnumed.117.206243.

[154] Jacob Berg et al. “Experimental investigation of Lagrangian structure functions in turbulence”. In: *Phys. Rev. E* 80 (2 2009), p. 026316. DOI: 10.1103/PhysRevE.80.026316. URL: https://link.aps.org/doi/10.1103/PhysRevE.80.026316.

[155] M. Krstić. “Chapter 9 - MIXING CONTROL FOR JET FLOWS”. In: *Combustion Processes in Propulsion*. Ed. by Gabriel D. Roy. Burlington: Butterworth-Heinemann, 2006, pp. 87–96. ISBN: 978-0-12-369394-5. DOI: https://doi.org/10.1016/B978-012369394-

5/50013-5. URL: https://www.sciencedirect.com/science/article/pii/B9780123693945500135.

[156] L Jødal, C Le Loirec, and C Champion. "Positron range in PET imaging: an alternative approach for assessing and correcting the blurring". In: *Physics in Medicine Biology* 57.12 (2012), p. 3931. DOI: 10.1088/0031-9155/57/12/3931. URL: https://dx.doi.org/10.1088/0031-9155/57/12/3931.

[157] Cody S. Wiggins and Lane B. Carasik. "Design of Experimental Facility for Noninvasive Measurement of Flow in HTGR Primary Components". In: *American Nuclear Society 2021 Annual Meeting*. Online, 2021.

[158] E.M. Laws. "Flow conditioning—A new development". In: *Flow Measurement and Instrumentation* 1.3 (1990), pp. 165–170. ISSN: 0955-5986. DOI: https://doi.org/10.1016/0955-5986(90)90006-S. URL: https://www.sciencedirect.com/science/article/pii/095559869090006S.

[159] Eric Michael Moore. "Positron Emission Particle Tracking Software Maturation Project". MA thesis. University of Tennessee, 2017. URL: https://trace.tennessee.edu/utk_gradthes/4957.

[160] H. W. Kuhn. "Variants of the hungarian method for assignment problems". In: *Naval Research Logistics Quarterly* 3.4 (1956), pp. 253–258. DOI: https://doi.org/10.1002/nav.3800030404. eprint: https://onlinelibrary.wiley.com/doi/pdf/10.1002/nav.3800030404. URL: https://onlinelibrary.wiley.com/doi/abs/10.1002/nav.3800030404.

[161] James Munkres. "Algorithms for the Assignment and Transportation Problems". In: *Journal of the Society for Industrial and Applied Mathematics* 5.1 (1957), pp. 32–38. URL: http://www.jstor.org/stable/2098689 (visited on 06/23/2023).

[162] William W. Moses. “Fundamental Limits of Spatial Resolution in PET”. In: *Nuclear Instruments and Methods in Physics Research Section A* 648.Supplement 1 (2011), S236–S240. DOI: 10.1016/j.nima.2010.11.092.

[163] N. Mordant, A.M. Crawford, and E. Bodenschatz. “Experimental Lagrangian acceleration probability density function measurement”. In: *Physica D: Nonlinear Phenomena* 193.1 (2004). Anomalous distributions, nonlinear dynamics, and nonextensivity, pp. 245–251. ISSN: 0167-2789. DOI: https://doi.org/10.1016/j.physd.2004.01.041. URL: https://www.sciencedirect.com/science/article/pii/S0167278904000417.

[164] A.W. Date. “Prediction of fully-developed flow in a tube containing a twisted-tape”. In: *International Journal of Heat and Mass Transfer* 17.8 (1974), pp. 845–859. ISSN: 0017-9310. DOI: https://doi.org/10.1016/0017-9310(74)90152-5. URL: https://www.sciencedirect.com/science/article/pii/0017931074901525.

[165] U.S. Department of Energy. *Southern Company Services and TerraPower Build World’s Largest Chloride Salt System*. https://www.energy.gov/ne/articles/southern-company-services-and-terrapower-build-worlds-largest-chloride-salt-system. 2023.

[166] Novak Zuber. “The effects of complexity, of simplicity and of scaling in thermal-hydraulics”. In: *Nuclear Engineering and Design* 204.1 (2001), pp. 1–27. ISSN: 0029-5493. DOI: https://doi.org/10.1016/S0029-5493(00)00324-1. URL: https://www.sciencedirect.com/science/article/pii/S0029549300003241.

[167] M. Ishii and I. Kataoka. “Similarity analysis and scaling criteria for LWRs under single-phase and two-phase natural circulation”. In: (Mar. 1983). DOI: 10.2172/6312011. URL: https://www.osti.gov/biblio/6312011.

[168] Novak Zuber et al. “Application of fractional scaling analysis (FSA) to loss of coolant accidents (LOCA): Methodology development”. In: *Nuclear Engineering and Design* 237.15 (2007). NURETH-11, pp. 1593–1607. ISSN: 0029-5493. DOI: https://doi.org/10.

1016/j.nucengdes.2007.01.017. URL: https://www.sciencedirect.com/science/article/pii/S0029549307002270.

[169] J. N. Reyes. "The Dynamical System Scaling Methodology". In: *Proceedings of the 16th International Topical Meeting on Nuclear Reactor Thermal-Hydraulics (NURETH-16)*. Chicago, Illinois, 2015.

[170] *NIST Chemistry WebBook - Fluid Thermodynamic and Transport Properties*. Online. National Institute of Standards and Technology. URL: https://webbook.nist.gov/chemistry/fluid/.

[171] David E Cooper et al. "Additive Manufacturing for product improvement at Red Bull Technology". In: *Materials and Design* 41 (2012). DOI: https://doi.org/10.1016/j.matdes.2012.05.017.

[172] Ian Gibson et al. *Additive Manufacturing Technologies*. Nov. 2020. ISBN: 978-3-030-56127-7. DOI: 10.1007/978-3-030-56127-7.

[173] R. Hague *, S. Mansour, and N. Saleh. "Material and design considerations for rapid manufacturing". In: *International Journal of Production Research* 42.22 (2004), pp. 4691–4708. DOI: 10.1080/00207840410001733940. eprint: https://doi.org/10.1080/00207840410001733940. URL: https://doi.org/10.1080/00207840410001733940.

[174] Arturo Cabral et al. "Experimental Investigation of Twisted Tape Heat Transfer Enhancements Using Additive Manufacturing". In: *Advances in Thermal Hydraulics (2022)*. Anaheim, California: American Nuclear Society, 2022. DOI: 10.13182/T126-38346.

[175] Fredrick M. Mwema and Esther T. Akinlabi. *Fused Deposition Modeling*. Cham: Springer, 2020. DOI: 10.1007/978-3-030-48259-6.

[176] Jigang Huang, Qin Qin, and Jie Wang. "A Review of Stereolithography: Processes and Systems". In: *Processes* 8.9 (2020). ISSN: 2227-9717. URL: https://www.mdpi.com/2227-9717/8/9/1138.

[177] Rance Tino et al. “Additive manufacturing in radiation oncology: a review of clinical practice, emerging trends and research opportunities”. In: *International Journal of Extreme Manufacturing* 2.1 (2020), p. 012003. DOI: 10.1088/2631-7990/ab70af. URL: https://dx.doi.org/10.1088/2631-7990/ab70af.

[178] Behzad Rankouhi. “Characterization of Mechanical Properties of Gamma Irradiated Additively Manufactured Articles for In-Space Manufacturing”. Electronic Theses and Dissertations. South Dakota State University, 2016. URL: https://openprairie.sdstate.edu/etd/1062.

[179] *An Experimental Investigation of the Effects of Gamma Radiation on 3D Printed ABS for In-Space Manufacturing Purposes*. Vol. Volume 1: Advances in Aerospace Technology. ASME International Mechanical Engineering Congress and Exposition. V001T03A042. Nov. 2016. DOI: 10.1115/IMECE2016-67745. eprint: https://asmedigitalcollection.asme.org/IMECE/proceedings-pdf/IMECE2016/50510/V001T03A042/2495428/v001t03a042-imece2016-67745.pdf. URL: https://doi.org/10.1115/IMECE2016-67745.

[180] Samantha J. Talley et al. “Flexible 3D printed silicones for gamma and neutron radiation shielding”. In: *Radiation Physics and Chemistry* 188 (2021), p. 109616. ISSN: 0969-806X. DOI: 10.1016/j.radphyschem.2021.109616. URL: https://www.sciencedirect.com/science/article/pii/S0969806X21002668.

Appendix A

NONDIMENSIONALIZING, SCALING, AND OTHER SURROGATE FLUIDS

To show the viability of surrogate fluids, this Appendix focuses on nondimensionalizing the conservation equations and discussing the effects of using surrogate fluids for molten salt heat transfer experiments, distortions. This appendix consists of work published under Cabral et al [8].

A.1 Nondimensionalizing the Conservation Equations

This section describes the methodology used to nondimensionalize the conservation equations to obtain parameters of interest, such as the Reynolds and Prandtl numbers.

The first equation to be nondimensionalized consists of the momentum equation of the Navier-Stokes equations:

$$\rho \cdot (\frac{\partial \overrightarrow{V}}{\partial t} + \overrightarrow{V} \nabla \overrightarrow{V}) = -\nabla P + \mu \cdot \nabla \overrightarrow{V}^2 + \rho \cdot g. \tag{A.1}$$

To nondimensionalize it, a set of nondimensional quantities are introduced, defined by an asterisk (*):

$$V^* = \frac{\overrightarrow{V}}{U_0}; \quad P^* = \frac{P}{\rho \cdot U_0^2}; \quad \nabla^* = \nabla \cdot L_C; \quad t^* = \frac{t \cdot U_0}{L_C}; \quad g^* = \frac{g}{g_C}, \tag{A.2}$$

where U_0 is the free stream velocity, L_C is a characteristic length and g_C is a gravitational constant. Substituting Equation A.2 into Equation A.1 yields:

$$\rho \cdot (\frac{\partial V^*}{\partial t^*} \frac{U_0^2}{L_C} + \frac{U_0^2}{L_C} V^* \nabla^* V^*) = -\frac{\nabla^*}{L_c} P^* \rho U_0^2 + \frac{\mu \nabla^{*2}}{L_c^2} V^* U_0 + \rho g^* g_C. \tag{A.3}$$

Multiplying both sides by the factor of $L_C / \rho U_0^2$:

$$\frac{\partial V^*}{\partial t^*} + V^* \nabla^* V^* = -\nabla^* P^* + \frac{\mu \nabla^{*2}}{L_c \rho U_0} V^* + g^* \frac{g_C L_C}{U_0^2}. \tag{A.4}$$

From Equation A.4, nondimensional numbers: Euler, Eu, Reynolds, Re, and Froude, Fr, are introduced:

$$\frac{\partial V^*}{\partial t^*} + V^* \nabla^* V^* = -\nabla^* \cdot Eu + \frac{\nabla^{*2} V^*}{Re} + \frac{g^*}{Fr^2}. \tag{A.5}$$

Reynolds number is defined in Equation 2.2, while the Euler and Froude number are:

$$Eu = \frac{P}{\rho U_0^2} = P^*; \quad Fr = \frac{U_0}{\sqrt{g_C L_C}}. \tag{A.6}$$

The energy equation is defined as:

$$\rho \cdot c_P \cdot (\frac{\partial T}{\partial t} + \overrightarrow{V} \cdot \nabla T) = k \nabla^2 T, \tag{A.7}$$

where c_P and k are the specific heat and thermal conductivity of the fluid,and T is the temperature. Using similar nondimensional quantities as Equation A.2, and adding:

$$\theta^* = \frac{T - T_f}{T_i - T_f}, \tag{A.8}$$

where T_i and T_f are arbitrary initial and final temperatures. Substituting the variables yields:

$$\frac{\rho c_P U_0}{L_C}(\frac{\partial \theta^* (T_i - T_f)}{\partial t^*} + V^* \nabla^* \theta^* (T_i - T_f)) = \frac{k}{L_c^2} \nabla^{*2} \theta^* (T_i - T_f). \tag{A.9}$$

Multiplying by a factor of $L_C / \rho U_0 c_P (T_i - T_f)$ leads to a simplified version:

$$\frac{\partial \theta^*}{\partial t^*} + V^* \nabla^* \theta^* = \frac{k}{L_C U_0 \rho c_P} \nabla^{*2} \theta^*. \tag{A.10}$$

Substituting for the Reynolds and Prandtl number definitions yields:

$$\frac{\partial \theta^*}{\partial t^*} + V^* \nabla^* \theta^* = \frac{1}{Re \cdot Pr} \nabla^{*2} \theta^*. \tag{A.11}$$

Noting that Equations A.5 and A.11 simplify to the nondimensional numbers of interest, shows that by properly applying the nondimensional quantities, Equations A.2 and A.8, selecting fluids with similar thermophysical properties, Pr, and operating conditions, Re, a surrogate fluid can properly mimic behaviours of interest in molten salt systems.

A.2 Scaling Techniques

To study heat transfer systems in laboratory settings, the components are typically scaled down to reduce overall costs. The components are often too large for laboratory environments and operate and conditions that can be expensive to build, maintain and operate. This motivates the use of scaled components and surrogate fluids. Scaling down a prototypical heat transfer component can be complicated, and if not done properly, the experiment could yield results that are not applicable and useful to the intended design. On the other hand, the scaled down component can also be over-complicated to account for all the physical phenomena occurring. Zuber [166] highlights the current trend of over-complicated heat transfer research has become overly complex resulting in a loss in a deeper understanding of the physics involved.

To scale down heat transfer components, the desired physical phenomena to be investigated has to be identified in order to scale it down appropriately. Yadigaroglu and Zeller [36] and an OECD Nuclear Energy Agency report [7] describe four main scaling techniques for heat transfer experiments. More recently, two additional scaling techniques have also been found in literature, with a total of six scaling techniques:

- Linear scaling - This is the simplest scaling technique and is done by nondimensionalizing the mass, momentum, and energy equations. It conserves all length ratios, but causes time distortions between the original component and the experimental facility.
- Volumetric scaling - Also known as time-perserving scaling, this takes into consideration the time distortions and focuses on perserving the flow lengths by reducing the areas, volumes, flow rates, and power proportionally.
- Time distorted scaling - This technique was developed by Ishii and Kataoka [167] for a natural circulation loop under single- and two-phase flows. It couples the driving forces for natural and heat transfer processes.
- Hierarchical two-tiered scaling - This technique can simulate the interaction between components of a nuclear power plant or any thermal-fluid system.
- Fractional scaling analysis - This technique focuses on the temporal scaling of a system of an integral approach while including initial and boundary conditions of interest and can be applied to interacting components [168].
- Dynamical system scaling - This technique uses both Hierarchical two-tiered scaling and the fractional scaling analysis that accounts for the dynamic response of the system when performing scaling analyses [169].

A.3 Pumping and Heating Power Ratios

Pumping and heating power ratios were calculated between the surrogate fluid, water, and five different molten salts in Section 2.2. This section goes over the derivation to calculate the pumping and heating power ratios for the model example discussed in Section 2.2.

Pumping power is defined as:

$$Q_p = \dot{V} \cdot \Delta P = \dot{V} \cdot \rho \cdot g \cdot H, \tag{A.12}$$

where $\dot{V}$ is the volumetric flow rate and H is the pumping head. The volumetric flow rate was obtained by multiplying the velocity and the cross-sectional area, A_{xs}, of the geometry. The velocity was obtained based on the Reynolds number based on Equation 2.2:

$$V = \frac{Re \cdot \mu}{\rho \cdot D_h} \tag{A.13}$$

The friction factor and pressure drop are used to calculate the pumping head, H:

$$H = \frac{f \cdot L \cdot V^2}{2 \cdot D_h \cdot H} = \frac{f \cdot L \cdot Re^2 \cdot \mu^2}{2 \cdot D_h^3 \cdot g \cdot \rho^2}. \tag{A.14}$$

Equation A.14 simplifies the calculations for the pumping head as the nondimensional number, Re, can be used between the surrogate fluid and molten salt.

Plugging Equation A.14 into A.12 with the volumetric flow rate substituted with velocity and cross sectional area yields:

$$Q_p = \frac{f \cdot L \cdot Re^3 \cdot \mu^3 \cdot A_{xs}}{2 \cdot D_h^3 \rho^2}. \tag{A.15}$$

The pumping power ratio between surrogate fluids, sf, and molten, ms, was obtained by using Equation A.15. Based on the scaling technique, factors were cancelled between each other. The friction factor and Reynolds number were similar between the surrogate fluid and molten salt, and due to the linear scaling technique the cross sectional area was the same. This leads to a pumping power ratio only dependent on thermophysical properties:

$$Q_{p,r} = \frac{\mu_{sf}^3 \cdot \rho_{ms}^2}{\mu_{ms}^3 \cdot \rho_{sf}^2}. \tag{A.16}$$

A similar derivation can be done for the heating power ratio. It started with the heating power equation:

$$Q_h = \dot{m} \cdot c_P \cdot \Delta T, \tag{A.17}$$

where $\dot{m}$ is the mass flow rate:

$$\dot{m} = V \cdot A_{xs} \cdot \rho = \frac{Re \cdot \mu \cdot A_{xs}}{D_h}. \tag{A.18}$$

Equation A.18 was plugged in Equation A.17 to calculate the heating power ratio:

$$Q_{h,r} = \frac{\mu_{sf} \cdot c_{P,sf} \cdot \Delta T_{sf}}{\mu_{ms} \cdot c_{P,ms} \cdot \Delta T_{ms}}. \tag{A.19}$$

The only unknown factors in Equation A.19 are the ΔT for both surrogate fluid and molten salt. Bardet and Peterson [31] estimated this ratio based on scaling analysis for buoyancy driven flows. They equated the Grashof numbers and concluded that the temperature difference was equal to the ratio of thermal expansion, β, giving this relation:

$$\frac{\beta_{ms}}{\beta_{sf}} = \frac{\Delta T_{sf}}{\Delta T_{ms}} \approx \frac{T_{sf}}{T_{ms}}, \tag{A.20}$$

which allows for a simplification in Equation A.19:

$$Q_{h,r} = \frac{\mu_{sf} \cdot c_{P,sf} \cdot T_{sf}}{\mu_{ms} \cdot c_{P,ms} \cdot T_{ms}}. \tag{A.21}$$

Equations A.16 and A.21 were used to calculate the pumping and heating power ratio as a function of Prandtl number and are plotted in Figures A.1 and A.2. Figure A.1 shows that throughout the various Prandtl numbers that match between water and the different molten salts, the pumping power ratio remains lower than unity and relatively constant with small increases. Equation A.16 is only dependent on thermophysical properties of the fluids, while eliminating all geometric parameters as it was linearly scaled, thus the pumping power ratio curves in Figure A.1 are not universal but only applicable to the specific model example discussed in Section 2.2.

The heating power ratios calculated shown in Figure A.2 have a different behavior than the pumping power ratios. The heating power ratio between water and the other molten salts increases with decreasing Prandtl number. A trend is observed when comparing both the pumping and heating power ratios for water and the molten salts, in which at higher Prandtl numbers the ratios are

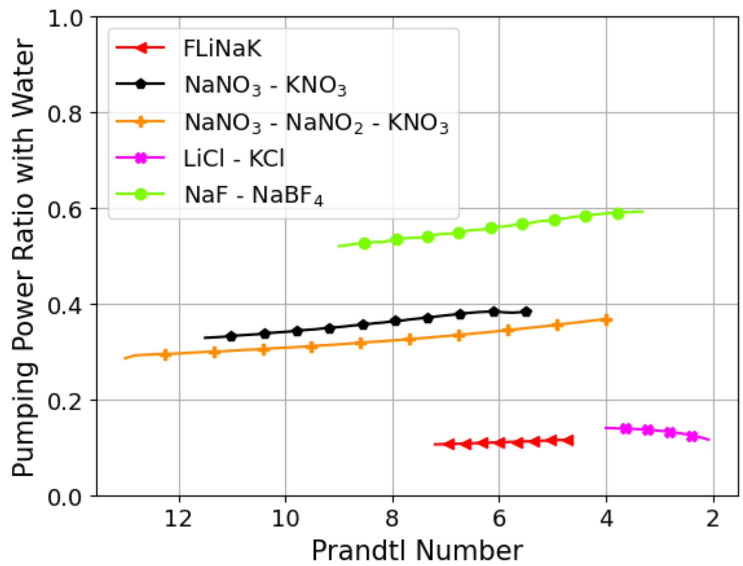

Figure A.1: Pumping power ratios of molten salts with water.

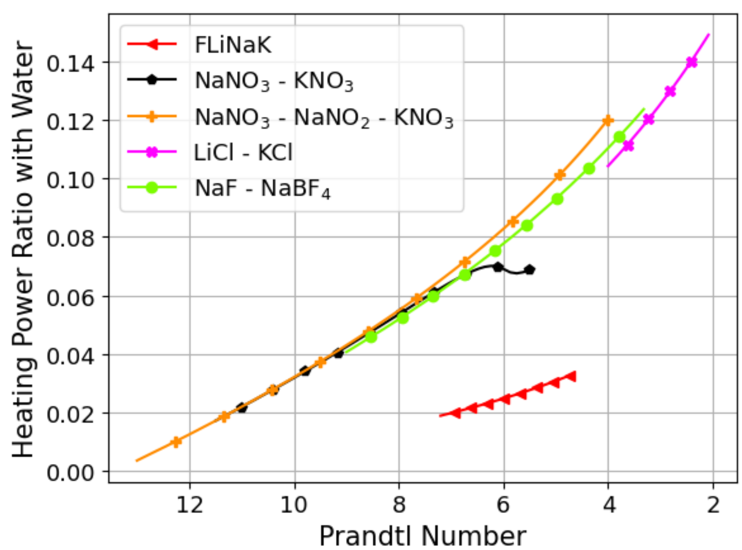

Figure A.2: Heating power ratios of molten salts with water.

smaller. Concluding that when using water to scale down heat transfer components for molten salt applications, water is more efficient at higher Prandtl numbers.

A.4 Other surrogate fluids

This work also focused on scaling other types of surrogate fluids to match Prandtl number ranges outside of water's Prandtl number range. These surrogate fluids consist of Dowtherm A, Freezium 60, and Zitrec S-25. Previous work [8] matched these surrogate fluids with the molten salts: LiF -

BeF_2 (FLiBe), NaF - BeF_2, LiF - NaF - BeF_2, Li_2CO_3 - Na_2CO_3 - K_2CO_3 (LiNaK), NaF - ZrF_4, and KF - ZrF_4. Figure A.3 plots the Prandtl numbers of the proposed surrogate fluids with the molten salts. Similarly to Figure 2.1, the temperatures of the molten salts are on the top x-axis and the surrogate fluids in the bottom x-axis.

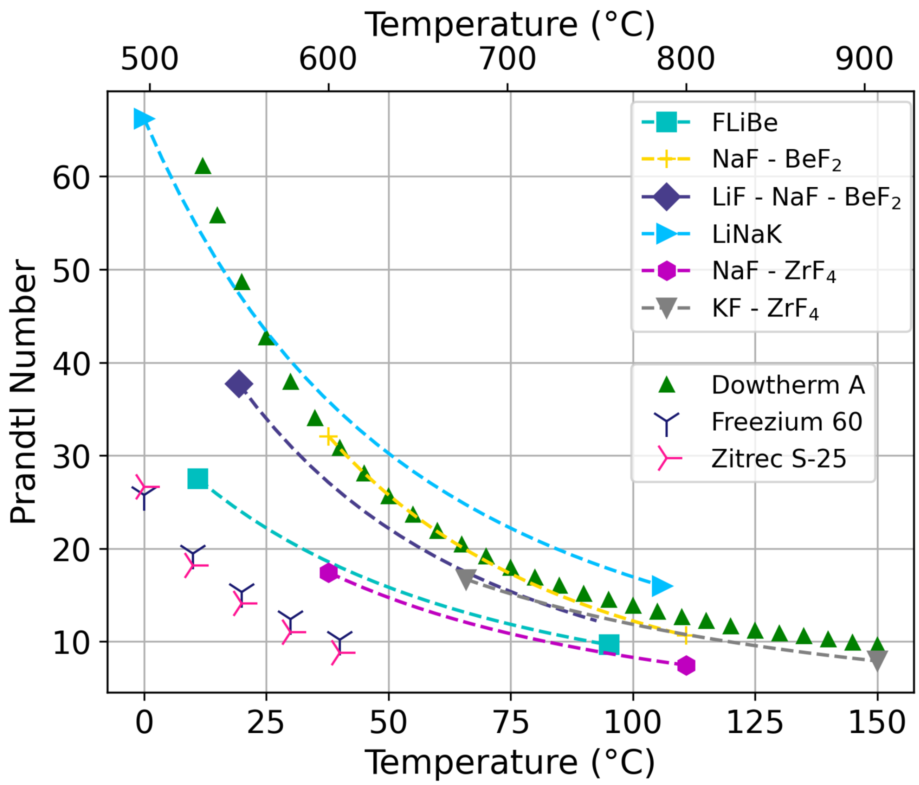

Figure A.3: Comparison of Prandtl numbers between molten salts (top horizontal axis) and surrogate fluids (bottom horizontal axis).

Dowtherm A was used to match the Prandtl numbers of FLiBe, NaF - BeF_2, LiF - NaF - BeF_2, and LiNaK as it has been explored previously in literature [32, 33, 35]. Freezium 60 and Zitrec S-25 were explored as surrogate fluids that can match the Prandtl number range in which water and Dowtherm A have a discontinuity between them. Freezium 60 and Zitrec S-25 were used to match the Prandtl numbers of NaF - ZrF_4, and KF - ZrF_4. Figures A.4 and A.5 plots the Prandtl numbers of the molten salts with their respective surrogate fluid.

Prandtl number distortions are plotted in Figure A.6 between the surrogate fluids, Dowtherm A, Freezium 60, and Zitrec S-25, with their respective molten salt paired. The distortions are similar to the ones shown in Figure 2.15, the distortions obtained from water, but with lower magnitudes. This shows the possibilities of using other types of heat transfer fluids to study scaled down molten salt components and can be done in an accurate manner.

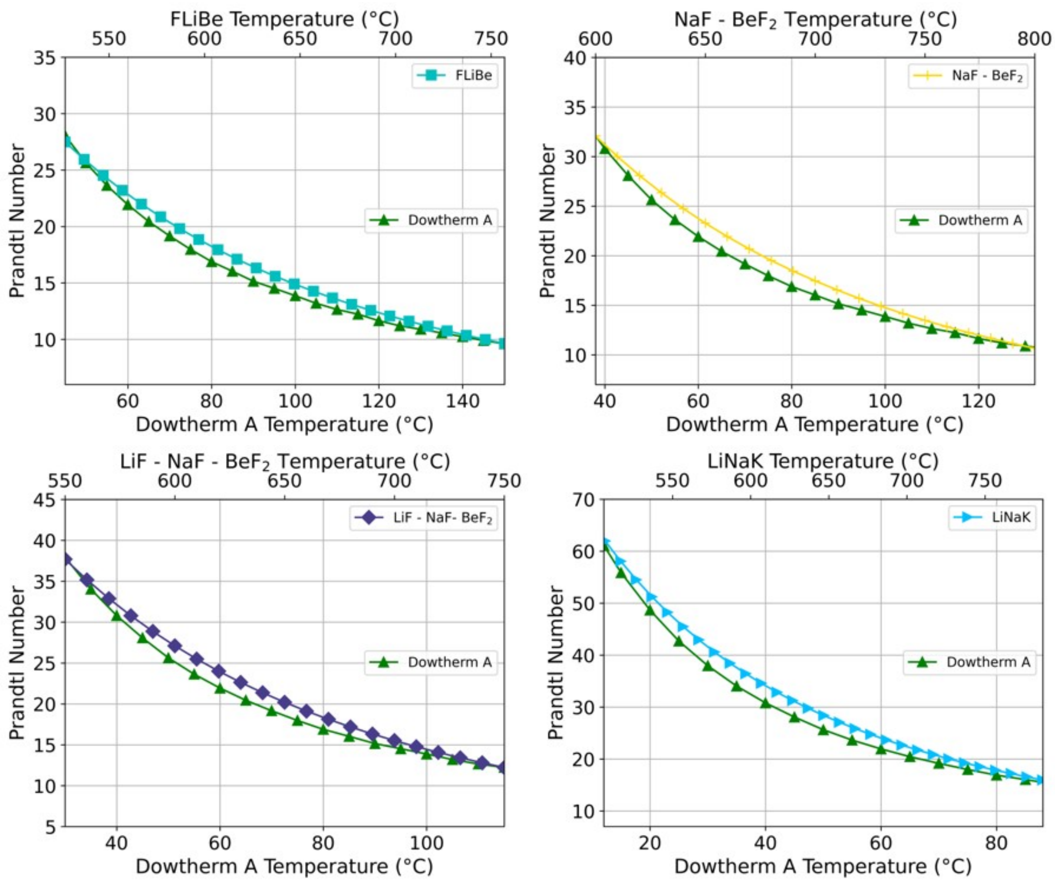

Figure A.4: Prandtl numbers for molten salts and Dowtherm A.

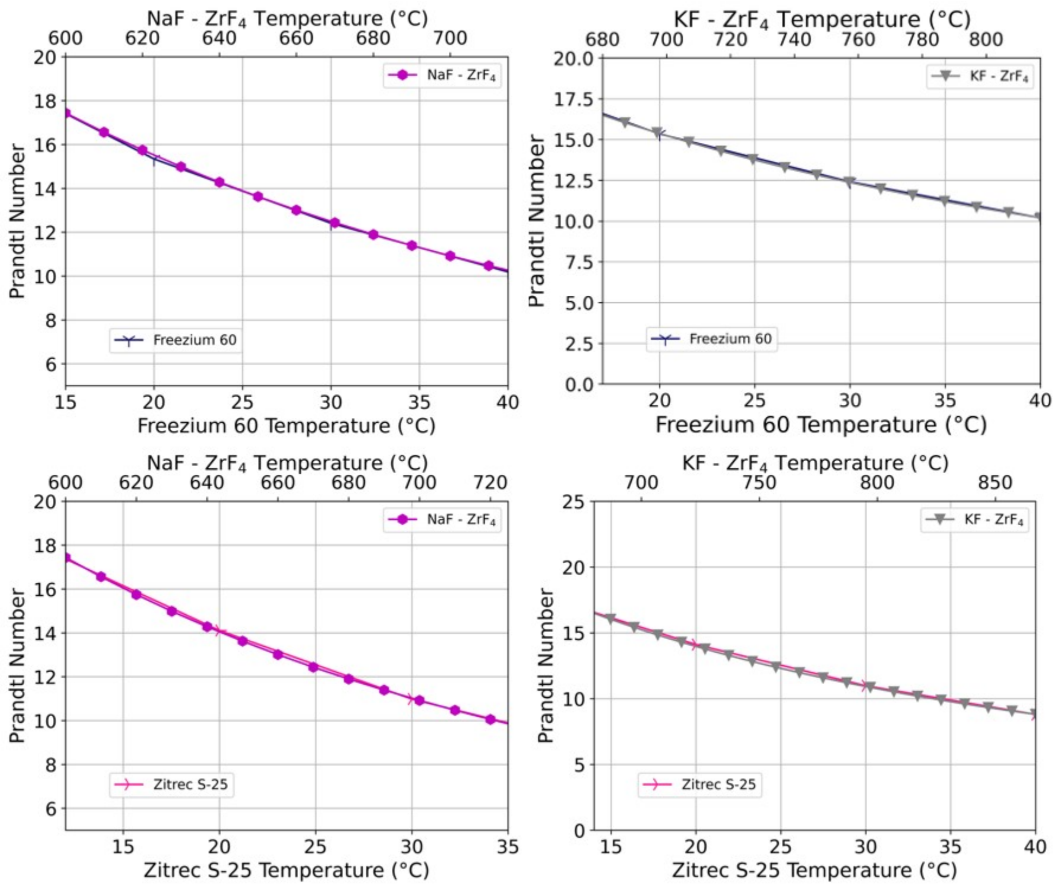

Figure A.5: Prandtl numbers for molten salts and Freezium 60 and Zitrec S-25.

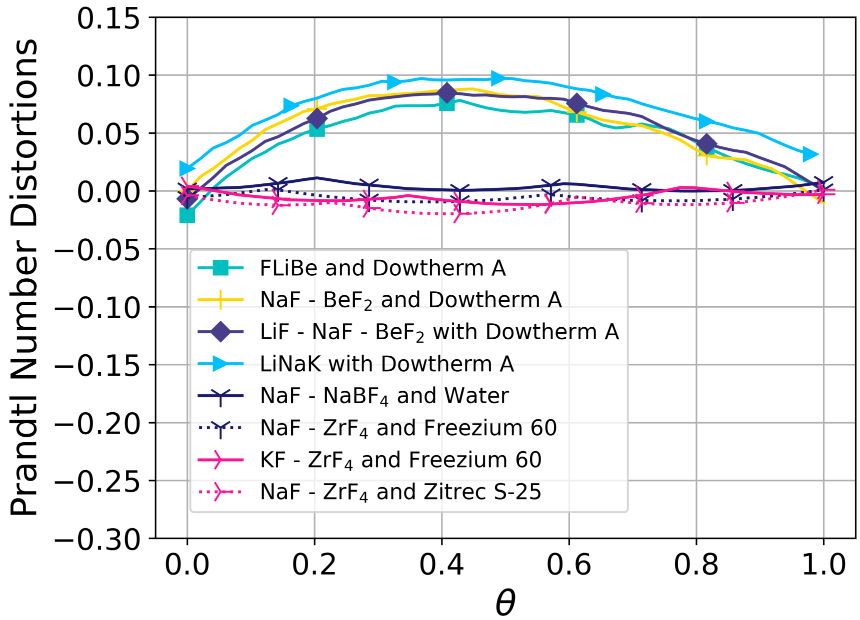

Figure A.6: Prandtl number distortions between the surrogate fluids and molten salts.

Appendix B

PROCEDURES FOR PRESSURE DROP AND HEAT TRANSFER EXPERIMENTS

This section consists of procedures done to run the pressure drop and heat transfer experiments using MSETF-1. These procedures consisted of fill up and drain the loop, and the experimental acquisition procedure. A schematic of MSETF-1 is shown in Figure 3.3 to properly guide through the procedures. Figure 3.3 shows the bulk of the experimental loop, though for pressure drop experiments the Mixing Section was removed to allow for proper pressure drop measurements of the Test Section.

To start the procedures, the common valve configuration consisted of:

- Throttle Valve: OPEN;
- Connecting Tank Valve: OPEN;
- Filling Valve: OPEN;
- Vent Valve: CLOSED;
- Drain Valve: CLOSED;
- Calibration Valve: CLOSED.

The valve configuration changes according to different procedures and scenarios, but this configuration was the normal operating configuration.

B.1 Filling Up and Degassing

MSETF-1 uses deionized water as its operating fluid. Water was chosen as a surrogate fluid for molten salt scaled down heat transfer experiment, for more information refer to Section 2.2. To start the filling up procedure, the following valve configuration was required:

- Throttle Valve: OPEN;
- Connecting Tank Valve: OPEN;
- Filling Valve: CLOSED;

- Vent Valve: OPEN;
- Drain Valve: CLOSED;
- Calibration Valve: CLOSED.

Figure B.1: Water filter system located in autoclave room of East Engineering Hall E1242 at VCU

In order to fill up MSETF-1, at the time of the pressure drop and heat transfer tests, buckets of deionized water were carried from the autoclave room in East Engineering Hall in room E1242. The buckets were filled using filter Getinge Group Series S100 shown in Figure B.1. Once the buckets were brought into MSETF-1's room, East Engineering room E1251, the water was introduced to MSETF-1 via the Outlet Tank-2. The water then filled up the Inlet Tank through the Connecting Valve. Once the Inlet Tank was filled, the Filling Valve was opened, to fill the pump with water. The Vent Valve was Open during this procedure to allow for air to escape MSETF-1. The pump was turned on to approximately 1000 RPM's once it had been filled. The Vent Valve was kept open until water started to exit the valve. MSETF-1 was considered full when Outlet Tank-1 was full and Inlet Tank had a capacity of at least 50 gallons.

To ensure MSETF-1 was water solid, or degassed, the pump was run at its highest frequency, 3450 RPM, with the Throttle Valve partially closed and opened to "shock" the system and to help any stuck bubbles get loose and flow out of the system. This was done with water flowing through the three tanks, which created a closed loop. As MSETF-1 was degassing, small bubbles accumulated in the Vent Valve, the user got rid of the excess bubbles by slightly opening the Vent Valve.

B.2 Pressure Drop

The MSETF-1 fill up and degassing procedure had to be done prior to starting the pressure drop procedure.

The following valve configuration was required to start the pressure drop experiments:

- Throttle Valve: OPEN;
- Connecting Tank Valve: OPEN;
- Filling Valve: OPEN;
- Vent Valve: CLOSED;
- Drain Valve: CLOSED;
- Calibration Valve: CLOSED.

The pressure water lines were bled while the pump was turned off. This procedure removed any air left inside the water lines. This was done by untightening the nuts near the pressure transducer and allowing water to flow until it became a steady stream and all the air was purged. This procedure was required for both pressure lines connecting to the differential pressure transducer.

Once the pressure lines had been bled, a zero test was run with the pump turned off. This was considered a zero-pressure reading and was intended to remove any small discrepancies and biases that occur by an uneven test section. The test sections were up to six feet long and small height discrepancies were captured by the pressure transducer when the friction factor was calculated. For further details on the data handling of this zero-pressure can be found in Appendix C.2. The zero-pressure drop test was run for 90 seconds at 1 kHz frequency.

After the zero-pressure test, the full range of experimental tests were performed while the users filled out a table similar to Table B.1 (just an example, not actual experimental data). The experiments were run for 30 seconds at a frequency of 1 kHz. Using this procedure, the users were able to repeat different experimental sets by matching the pump frequency and bulk temperature.

Once experiments were concluded, the pump was turned off and the data was analyzed and transferred to the FAST Research Group's Google Drive.

Table B.1: Example of test parameters written by experimentalists during a pressure drop test

Test Number	Bulk Temperature (^oC)	Flow Rate 1 (GPM)	Flow Rate 2 (GPM)	Pump Frequency (RPM)
1	21	1.11	1.13	800
2	21	1.42	1.41	900

B.3 Heat Transfer

Heat transfer procedures were divided into two sections: preparation and procedure. This was due to the sensitivity of performing these tests.

B.3.1 Heat Transfer - Preparation

The MSETF-1 fill up and degassing procedure had to be done prior to starting the heat transfer procedure and preparation.

To start the heat transfer preparation, the following configuration of valves was required:

- Throttle Valve: OPEN;
- Connecting Tank Valve: OPEN;
- Filling Valve: OPEN;
- Vent Valve: CLOSED;
- Drain Valve: CLOSED;
- Calibration Valve: CLOSED.

As shown in Figure 3.3, the in-house mixer was placed downstream of the test section and before the outlet temperatures. The configuration of thermocouples was crucial for successful heat transfer experiments. An incorrect configuration of thermocouples or bad thermal contact with the wall had an impact on the heat transfer coefficient calculations. MSETF-1 used a combination of surface and submerged T-Type thermocouples with the following configuration:

- Inlet thermocouples: 2
- Outlet thermocouples: 3
- Wall/Surface thermocouples: 10-11

A comparison between a surface and submerged thermocouple is shown in Figure 3.12. The submerged thermocouple had a metallic rod that interrogated the fluid temperature, while the surface thermocouple had an insulation layer and an adhesive side for easy installation into surfaces. The surface thermocouple had a flat junction making it ideal for surface temperature measurements.

The multiple inlet and outlet thermocouples were used to further reduce the uncertainty, further discussion can be found in Appendix C.4.2. The thermocouples were placed in different radial locations to better interrogate the fluid temperature. A plot of the inlet temperatures ($T_{in,A}$ and $T_{in,B}$) and outlet temperatures ($T_{out,A}$, $T_{out,B}$, and $T_{out,C}$) is shown in Figure B.2 with a radial configuration of the thermocouples in relationship with the pipe. The experimental results shown on the right of Figure B.2 show that the temperatures were independent of the radial location (fully mixed temperature profile) for both the inlet and outlet temperatures. While the inlet temperature was steady, the outlet temperature had oscillations. However, the amplitudes of the oscillation were less than 1 ^{o} C (the uncertainty of the thermocouple), therefore the oscillations were found to be acceptable. The thermocouple configuration shown in Figure B.2 was varied by radial location and submerged thermocouple, creating more statistically different tests. The thermocouple order was varied between: middle, low, high, low, high, middle, low, high, low, high, and middle (eleven thermocouples). Statistically different tests were obtained by varying the surface thermocouple location by changing the highs and the lows (while maintaining their number equivalent to each other).

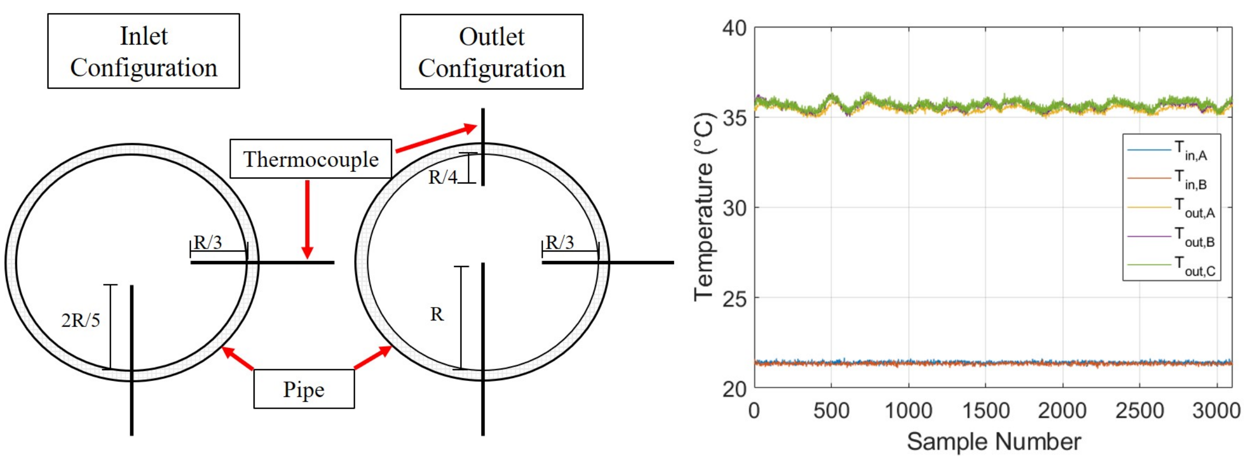

Figure B.2: Comparison between center and varied surface thermocouple configuration (Left) with a data set (Right)

The surface thermocouple locations were also varied. Initial tests done with the surface thermocouples consisted of the same angle location, in a horizontal manner at the center of the pipe, evenly spaced six inches from each other. Unfortunately, that configuration yielded low heat transfer coefficient calculations on the benchmark test, an empty pipe. The calculated heat transfer coefficient was consistently lower than the heat transfer coefficient obtained from an empty pipe Nusselt number correlations. A different approach was then taken, in which the angle where the surface thermocouple was placed varied. This allowed to better interrogate the real overall wall temperature. A comparison of the angle configuration change between the center and varied surface thermocouple locations is shown in Figure B.3.

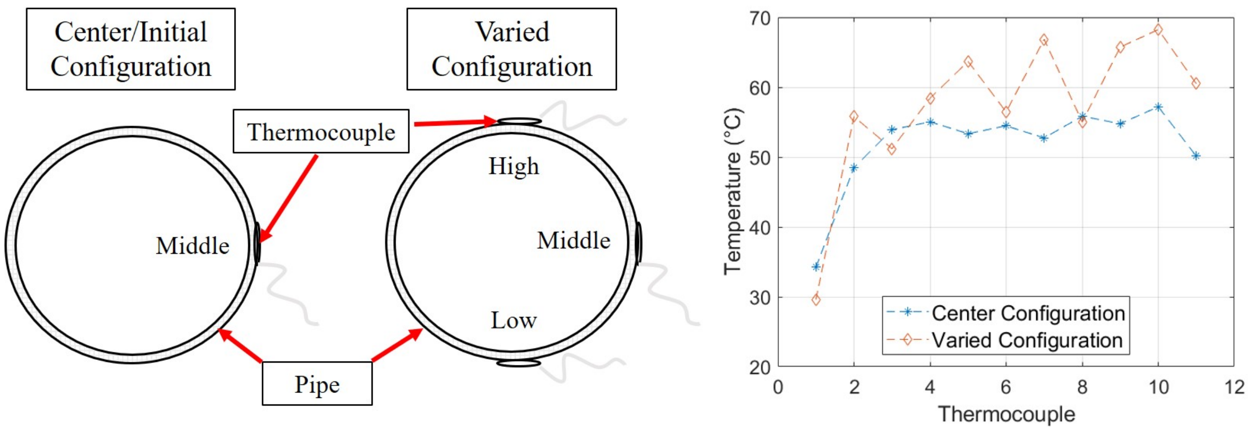

Figure B.3: Radial configuration of thermocouples (Left) with a data set (Right)

The surface thermocouples were designed with an adhesive side and an insulated side. The adhesive side was used to connect the surface thermocouple to the wall, but extra layers of insulation were required to further insulate and isolate the surface thermocouple from reading the temperature of the heaters and not the temperature of the wall. The insulation layers consisted of one layer of electrical tape and one layer of Saint-Gobain heat-resistant fiberglass tape. The size of the insulation layers varied, but their requirement consisted of fully covering the thermocouple junction. The thermocouple cover was also trimmed down from its original rectangular shape to an oval, decreasing the overall footprint of the thermocouple to only the essential sections of an adhesive side, an insulation side, the thermocouple wire, and the thermocouple junction. In addition, a small gap (5 mm) was left open from the heaters on top of the surface thermocouple junction. This was performed to ensure the temperature measured by the surface thermocouple was interrogating the wall's temperature and not the heaters' temperature. This was done as no amount of insulation tape between the thermocouple and the heaters prevented the reading of the heaters. A schematic of this configuration is shown in Figure B.4.

The test section was cleaned using isopropyl alcohol to remove any impurities and dirt from the surface of the test section before installing the heaters and thermocouples. Ten heaters were wrapped around the test section. The heaters were wrapped one by one, with tension of the heaters kept constant by wrapping it with the same Fiberglass Tape. The heaters were wrapped at both ends and installed simultaneously with the surface thermocouples.

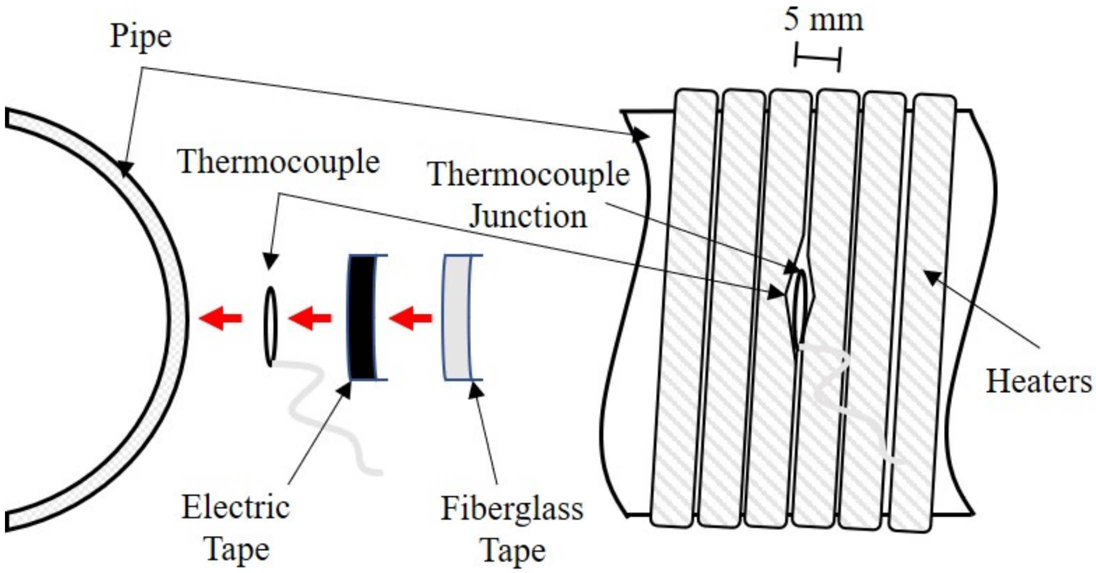

Figure B.4: Methodology to set up surface thermocouple on the side of the tube wall with different tapes and with the heaters.

A series of checks were done before collecting experimental data to ensure the spacing of the thermocouples was correct, there was good thermal contact between the wall and the thermocouples, and the heaters were locked in the correct place.

To check for adequate spacing between the thermocouple junction and the heaters as well as good thermal contact, the pump was turned on to a low flow rate (between 1 to 3 GPM), with the water allowed to circulate around MSETF-1 (the Connecting Valve Open). The heaters are turned ON with 70 Volts from the AC Power Suppliers. The temperature of the wall thermocouples was monitored and checked using the DAQ Assistant in LabVIEW. The temperature was monitored until a steady state was reached with the current flow rate. This was achieved due to the low heat supplied and the large amount of water in MSETF-1, causing a steady state to be achievable at low flow rate and power input. Once a steady state was achieved, the flow rate was increased to a range between 3 to 5 GPM (almost double the original), this caused the wall temperatures to decrease. Any temperature reading from the thermocouples that did not decrease either had incorrect thermal contact or was reading the temperature of the heaters. Adjustments were made accordingly. This consisted of re-taping the thermocouple or the heaters. Finally, the flow was increased to a range between 5 to 7 GPM to ensure all wall thermocouples were reading the wall temperature properly. Any adjustments were made accordingly.

The last check consisted of ensuring the heaters are locked in place. This was done by circulating water through MSETF-1 at a low flow rate (between 1 to 2 GPM) and turning on the heaters to supply 110 Volts. The low flow and high-voltage input caused the heaters to burn the fiberglass tapes and lock the fiberglass tapes in place. Smoking of the fiberglass tape occured on this stage. Once smoking was complete, the heaters had been locked in place.

Once heaters had been locked in place, thermocouples had been ensured to have good thermal contact and were reading the temperature of the walls, heat transfer experiments began. The water of the loop was also monitored until it reached room temperature, or if it was necessary, a small amount of ice was added to cool down.

Fiberglass insulation was used to insulate the mixing section to ensure no heat was lost from the last heater to the temperature measurement location. Initial heat transfer tests consisted of insulating the whole test section, but this caused issues with the current configuration of the thermocouples. Experiments were run between insulated and non-insulated test sections showed no difference in the wall temperatures due to the insulation in the wall thermocouples and the heaters.

B.3.2 Heat Transfer - Procedure

The heat transfer experimental procedure started by ensuring the water was at room temperature, and the Inlet Tank and Outlet Tank-1 were full. The following valve configuration were required:

- Throttle Valve: OPEN;
- Connecting Tank Valve: CLOSED;
- Filling Valve: OPEN;
- Vent Valve: CLOSED;
- Drain Valve: CLOSED;
- Calibration Valve: CLOSED.

Due to the time-sensitivity of the heat transfer tests, prior knowledge of the desired flow rates for the experiments was required before starting. To start the test, a zero test was obtained with MSETF-1 at a steady state and pump turned OFF with all AC voltage suppliers turned off too. The Connecting Tank Valve was also closed to create an open loop system to achieve temperature steady state. This also removed the feedback from the outlet temperature mixing with the inlet temperature. Further discussion of the data analysis of the zero-test can be found in Appendix C.3. The zero test consisted of 90 second at 100 Hz. The lower data collection frequency was due to the NI-9213 filtering and lowering data acquisition nature of the NI module.

The tests started by turning on the heaters to 110 Volts and allowing the wall temperatures to rise. Once the wall temperatures had reached approximately 60 ^{o}C (this occurred within seconds) the pump was turned ON to the desired flow rate. The overall temperatures were monitored using the DAQ Assistant until a steady state of all the wall, inlet and outlet temperatures were reached. Once a steady state was observed, the users waited for 30 seconds to ensure the system behaved accordingly (the thermocouples remained in place and it was a true steady state). After the waiting period, data was collected for 30 seconds at 100 Hz.

After the test, the water level of the Inlet Tank was checked to determine if enough water was left for another experimental run. If there was enough water to run another test, the pump was adjusted to achieve the new flow rate. The temperature of the system was monitored with the DAQ Assistant until a new steady state was obtained. The same procedure was performed, in which a 30 second waiting period was done to ensure a true steady state had been achieved and the system was behaving accordingly. Afterward, the data collection began.

Tests were run in a similar manner as long as the water level in the Inlet Tank was at operating height (higher than the tank fitting). This was done to ensure the pump was constantly filled with water and data acquisition could perform smoothly. If this was not the case, and the water level in Inlet Tank was not high enough, the Connecting Tank Valve was opened to let water fall from Outlet Tank-2. The AC power supplies were turned OFF and the pump was kept ON to remove all the heat from the walls. Afterwards, three to five gallons of water were drained by opening the Calibration Valve and stored in water buckets. The water was replaced with fresh deionized ice from the autoclave room.

The water was allowed to circulate through MSETF-1 to properly mix and reach room temperature. Water or ice were added to further decrease the water temperature accordingly. Once the water had reached a steady state and was at room temperature, the pump was turned OFF and the Connecting Tank Valve was closed. A new set of experiments at new flow rates were ran.

After all heat transfer experiments planned were completed, the pump was turned OFF, all the heaters unplugged, and data analysis began.

B.4 Draining MSETF-1

Draining MSETF-1 was an important component of MSETF-1's operation and maintenance. This was done to keep fresh deionized water in MSETF-1 to obtain accurate and repeatable measurements.

The valve configuration at the start of the draining procedure consisted of:

- Throttle Valve: OPEN;

- Connecting Tank Valve: OPEN;
- Filling Valve: OPEN;
- Vent Valve: CLOSED;
- Drain Valve: CLOSED;
- Calibration Valve: CLOSED.

The draining procedure started by draining water from the Outlet Tank-1 into buckets by opening the Calibration Valve. Once the Outlet Tank-1 was drained, the Throttle Valve was closed, a hose was connected to the end of the Calibration Valve section, and the pump was used to drain the Inlet Tank. The pump was used until the water level approached the outlet tank fitting of the Inlet Tank. Once it was low, the pump was turned OFF and the water was drained via the Drain Valve with buckets collecting the remaining water. Any amount of water left in the system was removed via water vacuums.

Appendix C

DATA HANDLING AND UNCERTAINTY QUANTIFICATION FOR PRESSURE DROP AND HEAT TRANSFER

The following sections discuss the processes for data handling, post-processing, and uncertainty quantification for the pressure drop and heat transfer experiments. Procedures on how to obtain the data and instrumentation required can be found in Appendix B. This appendix focuses on the steps done to obtain the desired friction factor and heat transfer data from the LabVIEW output files. A variety of codes have been created in both Matlab and Python by different FAST Researchers that use either '.xlsx' or '.lvm' files. This procedure only focuses on the '.xlsx' files.

C.1 Thermophysical Properties of Water

NIST water properties [170] were used to create a code that calculated the thermophysical properties of water based on temperature. The water properties were downloaded from the website in tabulated form and using the line-fitting feature in Excel, different correlations were used to estimate the thermophysical properties of water at different temperatures. The plots from the NIST values are shown in Figures C.1 to C.5. The polynomial best fit curves were coded into a Matlab code function, $WaterProperties.m$, which would output the different water properties at an input temperature in ^oC.

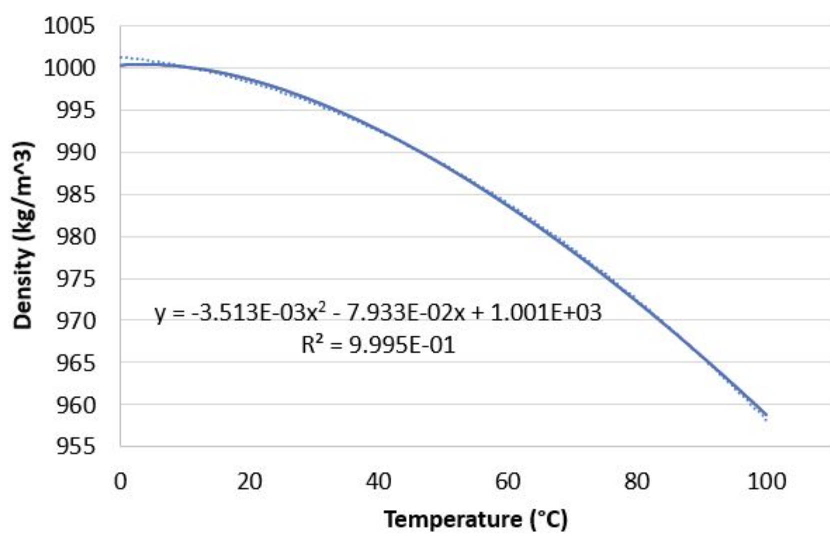

Figure C.1: Density of water obtained from NIST with polynomial fit from Excel

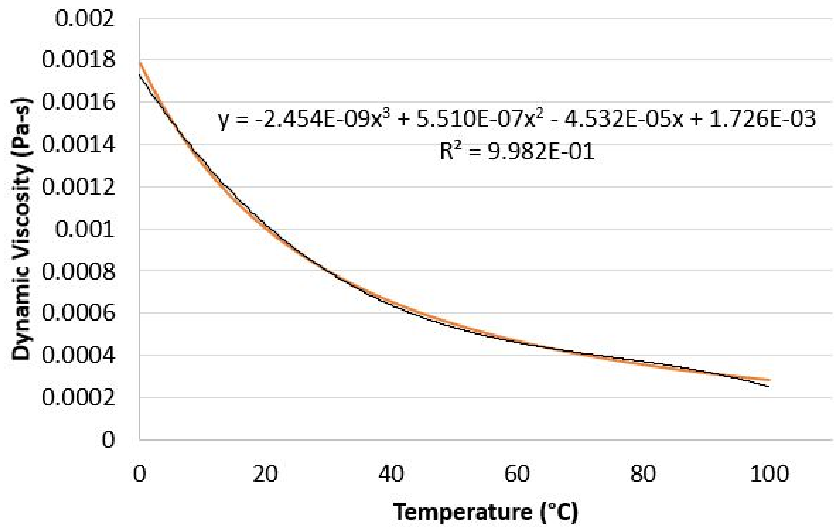

Figure C.2: Dynamic Viscosity of water obtained from NIST iwth polynomial fit from Excel

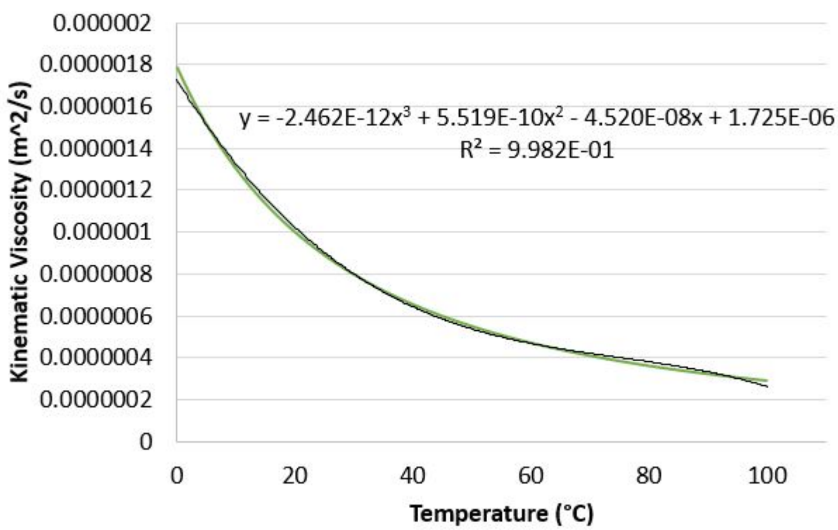

Figure C.3: Kinematic Viscosity of water obtained from NIST with polynomial fit from Excel

C.2 Isothermal Pressure Drop

A Matlab code was developed for the pressure drop post processing. The code consists of a main code, $PressureDrop\_main.m$, which read all files and averaged the important parameters to feed into Matlab function, $Friction\_Factor.m$, that does the overall friction factor calculations based on the bulk water temperature calculated from $WaterProperties.m$, described in the previous section.

$PressureDrop\_main.m$ asked the user for the folder in which the raw pressure drop files were located. The code then counted the number of files that have the correct file extension, '.xlsx,' and

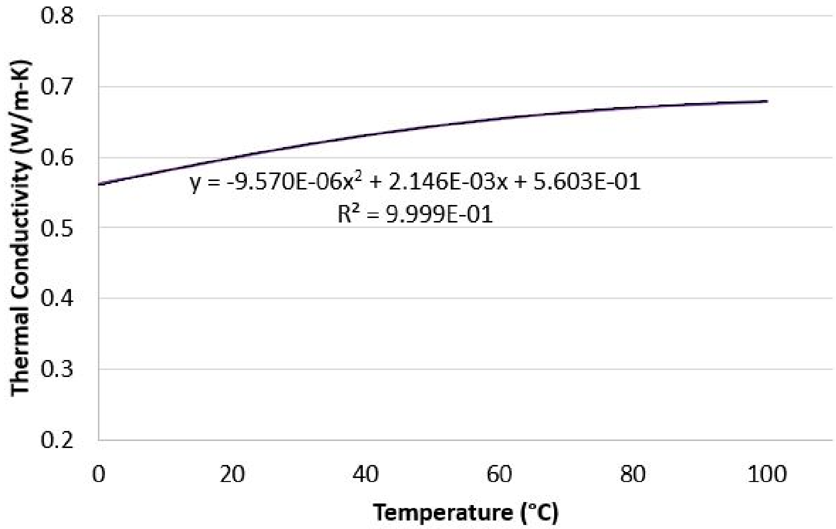

Figure C.4: Thermal conductivity obtained from NIST with polynomial fit from Excel

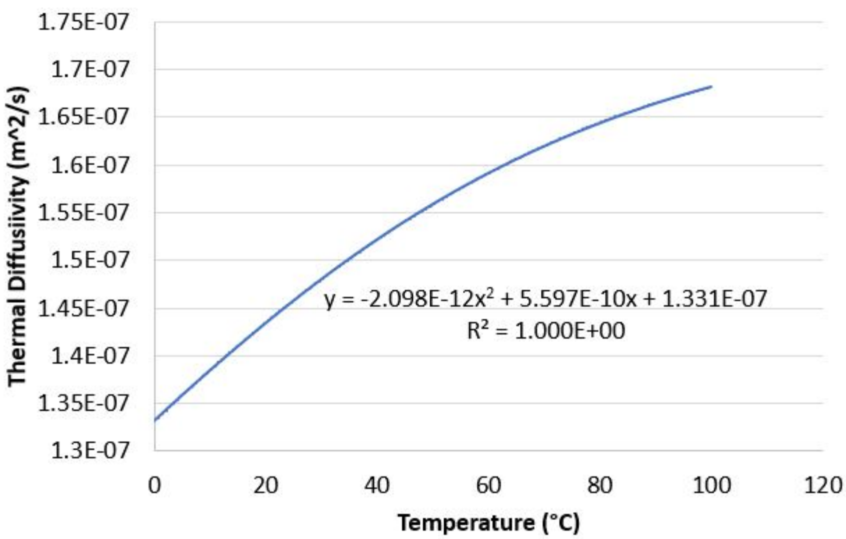

Figure C.5: Thermal diffusivity of water obtained from NIST with polynomial fit from Excel

reads the first file or the 'zero-test.' The zero-test was used to account for any height misalignment in the test section. The pressure drop at the laminar region was low enough that any height misalignment caused inconsistencies in the friction factor calculations. The averaged zero pressure was defined as *psid0*.

The code defined the various experimental inputs, such as inner diameter, D, test section length, L, extra length between pressure taps and test section, L_{extra}, and whether the test configuration had a twisted tape or a mixing section. Afterward, the user defined the volume flow rates collected manually from the flow meters.

The code looped through the various '.xlsx' files in order to individually average the values across the different files. It calculated a bulk temperature by averaging the inlet and outlet temperatures, T_{in} and T_{out}, through time. The bulk temperature was calculated by:

$$T_{bulk} = \frac{T_{out} + T_{in}}{2}. \tag{C.1}$$

The averaged pressure drop, defined as $psid$, the averaged zero pressure, $psid0$, and the volume flow rate, $\dot{V}$, and geometric configurations are sent to the friction factor function, $Friction\_Factor.m$.

$Friction\_Factor.m$ then calculated the thermophysical properties of water at bulk temperature using the *WaterProperties.m* code. The thermophysical properties calculated consisted of the kinematic viscosity, ν, the density, ρ, the thermal diffusivity, α, and the dynamic viscosity, μ. The velocity was then calculated based on the following equation:

$$u = \frac{\dot{V}}{15850 \cdot \pi \cdot (\frac{D}{2})^2}, \tag{C.2}$$

where 15850 is a conversion from gallons per minute to m^3/s. Using this velocity, the Reynolds number was calculated based on the empty pipe dimensions using Equation 2.2

The extra length between the test section and the pressure taps was accounted for using Moody's turbulent correlation [115] of friction factor based on the Reynolds number:

$$f_{extra} = \begin{cases} \frac{64}{Re}, & \text{if } Re_D \leq 3,000 \\ 0.0055 \cdot (1 + (\frac{20000 \cdot \epsilon}{D} + \frac{1e6}{Re_D})^{1/3}), & \text{if } Re_D > 3,000. \end{cases} \tag{C.3}$$

The pressure drop from the extra length was estimated by:

$$\Delta P_{extra} = \frac{\rho \cdot u^2 \cdot L_{extra} \cdot f_{extra}}{2 \cdot D \cdot Factor}, \tag{C.4}$$

where $Factor$ was used to change the pressure from Pascals to pounds per square inch. The actual pressure drop of the test section, $\Delta P_{t.s.}$ was then calculated by:

$$\Delta P_{t.s.} = (psid - psid0 - \Delta P_{extra}) \cdot Factor. \tag{C.5}$$

The friction factor was finally calculated by:

$$f = \frac{2 \cdot \Delta P_{t.s.} \cdot D}{L \cdot \rho \cdot u^2}. \tag{C.6}$$

The channel flow friction factor for the twisted tape was calculated by:

$$f^* = \frac{2 \cdot \Delta P_{t.s.} \cdot D_h}{L \cdot \rho \cdot u^{*2}}, \tag{C.7}$$

where D_h is the hydraulic diameter, and u^{*2} is the channel flow velocity derived in Section 3.2.5.

C.3 Heat Transfer

Similarly, to the pressure drop codes, a main code was written using Matlab, *HeatTransfer_ main.m*, that averages the individual test data and transfers it to a function, *Heat_Transfer.m*.

HeatTransfer_main.m asked the user for the folder where the '.xlsx' test files were located and counted the total number of files in the folder. The zero test is used to account for small temperature differences in the isothermal conditions. These values tended to be extremely small due to the calibration of the thermocouples. The code then calculated a zero bulk temperature, $T_{b,0}$, zero wall temperature to bulk difference, $T_{wb,0}$, and zero outlet vs inlet temperature, dT_0.

The code then defined the experimental inputs, as well as the user adjusted for different parameters. The main variables that were adjusted consisted of the heated length, L_{heated}, and the volumetric flow rate, $\dot{V}$. The heated length, L_{heated}, and the overall test section length, L, varied due to the heaters shrinking in size, causing changes in the overall length. The main code then calculated the average inlet and outlet temperatures from the five submerged thermocouples, $T_{in,A}$, $T_{in,B}$, $T_{out,A}$, $T_{out,B}$, and $T_{out,C}$, based on the following equations:

$$T_{in} = \frac{T_{in,A} + T_{in,B}}{2}, \tag{C.8}$$

$$T_{out} = \frac{T_{out,A} + T_{out,B} + T_{out,C}}{3}. \tag{C.9}$$

The average wall temperature was obtained from averaging the wall surface thermocouples:

$$T_w = \frac{1}{N_{surface}} \sum_{i=1}^{N_{surface}} T_{w,i}. \tag{C.10}$$

*HeatTransfer_ main.m*then provided the averaged and zero values to the function, *Heat_Transfer.m*. The function obtained the thermophysical properties of water using the bulk temperature from the

WaterProperties.m code. It then calculated the velocity from the flow based on Equation C.2 and Reynolds number from Equation 2.2. The mass flow rate was calculated by:

$$\dot{m} = \frac{\dot{V} \cdot \rho}{15850}. \tag{C.11}$$

The overall heat transfer, UA, from convection was calculated using Equation 3.26, simplifying it further and accounting for zero measured values yields:

$$UA = \frac{\dot{m} \cdot c_P \cdot (Tout - T_{in} - dT_0)}{(T_w - T_b - T_{wb,0})}. \tag{C.12}$$

Equation C.12 is similar to Equation 3.27 with the addition to the zero value measurement. The convective heat transfer coefficient, h is defined in Equation 3.28 and is further simplified using algebra to calculate it based on:

The heat transfer coefficient that accounts for the conduction through the wall is defined as:

$$h = (\frac{1}{UA} - \frac{ln(D_o/D)}{2 \cdot \pi \cdot k_{ss} \cdot L_{heated}})^{-1} \cdot \frac{1}{\pi \cdot D \cdot L_{heated}}. \tag{C.13}$$

C.4 Uncertainty Quantification

Uncertainty for pressure drop, heat transfer, and thermal performance factor was quantified using least squared method [52]. Initial studies of uncertainty showed that the largest sources of uncertainty were attributed to flow meters, pressure transducer, and in the case of heat transfer to the thermocouple uncertainty. For pressure drop tests, a single test was used for the plots presented in this document, but multiple tests were performed to ensure repeatability. In the case of heat transfer, the uncertainty grew up with Reynolds number, thus the higher Reynolds number Nusselt number data required more statistically independent tests.

This section goes over the uncertainty quantification for pressure drop, heat transfer and the thermal performance. The first set of uncertainty that was used for all calculations consisted of the uncertainty from the flow meters. The uncertainty of the flow meters was calculated based on two phenomena, the uncertainty provided by NIST (3% of the volumetric flow rate, $\sigma_{\dot{V},1}$) and the uncertainty shown in the flow meter's screen ($\pm 0.01 GPM$, $\sigma_{\dot{V},2}$). The uncertainties were combined to obtain an overall volumetric flow rate uncertainty. Since they were statistically different quantities, they can be combined via:

$$\sigma_{\dot{V}}^2 = \sigma_{\dot{V},1}^2 + \sigma_{\dot{V},2}^2 = (0.03 \cdot \dot{V})^2 + (0.02)^2. \tag{C.14}$$

The uncertainty of the volumetric flow rate can be used to calculate the uncertainty of the velocity:

$$\sigma_u^2 = (\sigma_{\dot{V}} \cdot \frac{\partial u}{\partial \dot{V}})^2 = (\sigma_{\dot{V}} \cdot \frac{1}{15850 \cdot \pi \cdot (D/2)^2})^2. \tag{C.15}$$

C.4.1 Pressure Drop

For pressure drop uncertainty, the uncertainty of the pressure transducer was obtained based on the number of samples, $N_{samples}$:

$$\sigma_{\Delta P}^2 = \frac{\sigma_{psid}^2}{N_{samples}}, \tag{C.16}$$

where σ_{psid}^2 was the standard deviation of the pressure transducer signal.

The overall uncertainty of the friction factor was obtained by combining the uncertainty of the flow meters and the pressure transducer:

$$\sigma_f^2 = (\sigma_{\Delta P} \cdot \frac{\partial f}{\partial \Delta P})^2 + (\sigma_u \cdot \frac{\partial f}{\partial u})^2 = (\sigma_{\Delta P} \cdot \frac{2 \cdot D}{L \cdot \rho \cdot u^2})^2 + (\sigma_u \cdot \frac{4\Delta P \cdot D}{L \cdot \rho \cdot u^3})^2. \tag{C.17}$$

C.4.2 Heat Transfer

The uncertainty quantification for the heat transfer coefficient was more complex than the pressure drop uncertainty. To start, the uncertainty for each thermocouple, $\sigma_{TC,X}$, was calculated based on the accuracy of the thermocouple, σ_{TC}, and the standard deviation divided by the number of samples. The uncertainty for each thermocouple was calculated based on the following equation:

$$\sigma_{TC,X}^2 = \sigma_{TC}^2 + \frac{\sigma_{temp,X}^2}{N_{samples}}, \tag{C.18}$$

where X corresponds to any of the thermocouples used, submerged or surface. The inlet temperature overall uncertainty was quantified based:

$$\sigma_{T_{in}}^2 = (\sigma_{T_{in,A}} \cdot \frac{\partial T_{in}}{\partial T_{in,A}})^2 + (\sigma_{T_{in,B}} \cdot \frac{\partial T_{in}}{\partial T_{in,B}})^2 = (\frac{\sigma_{T_{in,A}}}{2})^2 + (\frac{\sigma_{T_{in,B}}}{2})^2. \tag{C.19}$$

The overall outlet temperature uncertainty was calculated by:

$$\begin{aligned} \sigma_{T_{out}}^2 &= (\sigma_{T_{out,A}} \cdot \frac{\partial T_{out}}{\partial T_{out,A}})^2 + (\sigma_{T_{out,B}} \cdot \frac{\partial T_{out}}{\partial T_{out,B}})^2 + (\sigma_{T_{out,C}} \cdot \frac{\partial T_{out}}{\partial T_{out,C}})^2 \\ &= (\frac{\sigma_{T_{out,A}}}{3})^2 + (\frac{\sigma_{T_{out,B}}}{3})^2 + (\frac{\sigma_{T_{out,C}}}{3})^2. \end{aligned} \tag{C.20}$$

The inlet and outlet uncertainty was quantified by the following relationship:

$$\sigma^2_{T_{in},T_{out}} = \sigma^2_{T_{in}} + \sigma^2_{T_{out}}. \tag{C.21}$$

The overall uncertainty in the wall was quantified by:

$$\sigma^2_{T_W} = \sum_{i=1}^{N_{surface}} (\frac{\sigma_{T_{W,i}}}{N_{surface}})^2. \tag{C.22}$$

The uncertainty in the bulk temperature was defined as:

$$\sigma^2_{T_b} = (\frac{\sigma_{T_{in}}}{2})^2 + (\frac{\sigma_{T_{out}}}{2})^2. \tag{C.23}$$

The final temperature related uncertainty was defined between the difference of the bulk to wall temperatures:

$$\sigma^2_{T_w,T_b} = \sigma^2_{T_W} + \sigma^2_{T_b}. \tag{C.24}$$

The uncertainty in the mass flow rate, $\sigma_{\dot{m}}$, was obtained from the volumetric flow rate uncertainty in Equation C.14:

$$\sigma^2_{\dot{m}} = (\sigma_{\dot{V}} \cdot \frac{\partial \dot{m}}{\partial \dot{V}})^2 = (\sigma_{\dot{V}} \cdot \frac{\rho}{15850})^2. \tag{C.25}$$

The uncertainty in UA from Equation C.12 was defined as:

$$\sigma^2_{UA} = (\sigma_{\dot{m}} \cdot \frac{\partial UA}{\partial \dot{m}})^2 + (\sigma_{T_{in},T_{out}} \cdot \frac{\partial UA}{\partial T_{in} T_{out}})^2 + (\sigma_{T_W,T_b} \cdot \frac{\partial UA}{\partial T_W T_b})^2, \tag{C.26}$$

where:

$$\frac{\partial UA}{\partial \dot{m}} = \frac{c_P \cdot (T_{out} - T_{in} - dT_0)}{(T_W - T_b - T_{wb,0})}, \tag{C.27}$$

$$\frac{\partial UA}{\partial T_{in} T_{out}} = \frac{\dot{m} \cdot c_P}{(T_W - T_b - T_{wb,0})}, \tag{C.28}$$

and

$$\frac{\partial UA}{\partial T_W T_b} = \frac{\dot{m} \cdot c_P \cdot (T_{out} - T_{in} - dT_0)}{(T_W - T_b - T_{wb,0})^2}. \tag{C.29}$$

For mathematical simplicity in the uncertainty calculations, a variable was defined as f_{val}:

$$f_{val} = \frac{1}{h \cdot A_i}. \tag{C.30}$$

The uncertainty in f_{val} was calculated by using the following equation:

$$\sigma_{f_{val}}^2 = (\sigma_{UA} \cdot \frac{\partial f_{val}}{\partial UA})^2 + (\sigma_{L_{heated}} \cdot \frac{\partial f_{val}}{\partial L_{heated}})^2, \tag{C.31}$$

where:

$$\frac{\partial f_{val}}{\partial UA} = -\frac{1}{UA^2}, \tag{C.32}$$

and

$$\frac{\partial f_{val}}{\partial L_{heated}} = -\frac{ln(D_0/D)}{2 \cdot \pi \cdot k_{ss} \cdot L_{heated}^2}. \tag{C.33}$$

Finally, the uncertainty in the heat transfer coefficient was estimated by:

$$\sigma_h^2 = (\sigma_{f_{val}} \cdot \frac{\partial h}{\partial f_{val}})^2 + (\sigma_{A_i}^2 \cdot \frac{\partial h}{\partial A_i})^2, \tag{C.34}$$

where:

$$\frac{\partial h}{\partial f_{val}} = -\frac{1}{A_i \cdot f_{val}^2}, \tag{C.35}$$

$$\frac{\partial h}{\partial A_i} = -\frac{1}{A_i^2 \cdot f_{val}}, \tag{C.36}$$

and

$$\sigma_{A_i}^2 = (\sigma_{L_{extra}} \cdot \frac{\partial A_i}{\partial L_{extra}})^2. \tag{C.37}$$

Where:

$$\frac{\partial A_i}{\partial L_{extra}} = \pi \cdot D. \tag{C.38}$$

Finally, the uncertainty from the heat transfer coefficient, σ_h, was used to calculate the uncertainty in the Nusselt number:

$$\sigma_{Nu}^2 = (\sigma_h \cdot \frac{\partial Nu}{\partial h})^2, \tag{C.39}$$

where:

$$\frac{\partial Nu}{\partial h} = \frac{D}{k_w}. \tag{C.40}$$

Equation C.39 was used to obtain the uncertainty in the Nusselt number for a single test. From this uncertainty, a series of statistically independent tests where run to decrease the overall uncertainty across different Reynolds numbers. The final uncertainty for each Nusselt number was calculated based on:

$$\sigma_{Nu,total}^2 = \sum_{i=1}^{N_{tests}} (\frac{\sigma_{Nu}}{N_{tests}})^2. \tag{C.41}$$

C.4.3 Thermal Performance

To calculate the uncertainty in the thermal performance, four sets of uncertainty and data were required, based on the equation of thermal performance in Equation C.42. Where the friction factor and Nusselt number of the non-modified geometry (f_0 and Nu_0) are compared with the heat transfer enhancement (f and Nu). In which, in order to be adequately quantified, the variables have to have similar Reynolds numbers.

$$\eta = \frac{Nu/Nu_0}{(f/f_0)^{1/3}}. \tag{C.42}$$

The first set of uncertainty quantified comes from the friction factor uncertainty, Equation C.17. To simplify the calculation, dummy variables were chosen. In this case the uncertainty in friction factor was calculated based on the following variable:

$$\frac{f}{f_0} = f_{val2}, \tag{C.43}$$

where the partial derivatives in terms of the variable, f_{val2}, were defined as:

$$\frac{\partial f_{val2}}{\partial f_0} = -\frac{f}{f_0^2}, \tag{C.44}$$

and

$$\frac{\partial f_{val2}}{\partial f} = -\frac{1}{f_0}. \tag{C.45}$$

For an overall uncertainty in the friction factor component:

$$\sigma_{f_{val2}}^2 = (\frac{\partial f_{val2}}{\partial f_0} \cdot \sigma_{f_0})^2 + (\frac{\partial f_{val2}}{\partial f} \cdot \sigma_f)^2. \tag{C.46}$$

Similarly, a dummy variable was chosen for the Nusselt number portion:

$$\frac{Nu}{Nu_0} = f_{val3}. \tag{C.47}$$

With partial derivatives of the Nusselt number defined as:

$$\frac{\partial f_{val3}}{\partial Nu} = \frac{1}{Nu_0}, \tag{C.48}$$

and

$$\frac{\partial f_{val3}}{\partial Nu_0} = -\frac{Nu}{Nu_0^2}. \tag{C.49}$$

With the total uncertainty of f_{val3} defined as:

$$\sigma_{f_{val3}}^2 = (\frac{\partial f_{val3}}{\partial Nu} \cdot \sigma_{Nu})^2 + (\frac{\partial f_{val3}}{\partial Nu_0} \cdot \sigma_{Nu_0})^2. \tag{C.50}$$

Equation C.46 and Equation C.50 are used to calculate the overall uncertainty in the Thermal Performance Factor:

$$\sigma_\eta^2 = (\sigma_{f_{val3}}^2 \cdot \frac{1}{(f/f_0)^{1/3}})^2 + (\sigma_{f_{val3}}^2 \cdot (\frac{-1}{3} \cdot \frac{Nu/Nu_0}{(f/f_0)^{4/3}}))^2. \tag{C.51}$$

Appendix D

ADDITIVE MANUFACTURING METHODOLOGY

Additive manufacturing was explored as a method to fabricate geometries otherwise complicated with traditional manufacturing techniques due to material limitations [171]. The additive manufactured test sections were designed to be easily installed and tested in MSETF-1. The test sections had to be water tight, as it was MSETF-1's working fluid, capable to withstand high flow rates without fractures, maintain structural integrity at high temperatures, and have enough length to be fully developed hydrodynamic flow.

A method of "print and test" was done to address the different issues independently, similar to a "guess and check" strategy. This method was chosen as manufacturing 3D parts in large numbers is different than traditional manufacturing [172, 173]. This section goes through the details of each test iteration and further details can be found in [174]. Plastic materials were chosen to create the 3D printed test sections to keep costs accessible in comparison with metallic 3D printing.

D.1 Past Trials

This section is intended to show past failures and iterations in order to guide future experimental efforts in this area. The author believes that failures from the efforts done to obtain working additively manufactured test sections can be informative.

The first section built consisted of a 15.2 cm long test section with a twisted tape insert with 25.4 mm inner diameter and flanges on each end for easy installation in MSETF-1. The test section was printed using Fused Deposition Modeling (FDM) as it is one of the most popular printing techniques [175]. FDM has two different printing materials, ABS and PLA, the test section was printed using ABS as it is more heat resistant than PLA. The first test section was installed in MSETF-1 as shown in Figure D.1, but it didn't perform as expected as water went through the material. A different printing technique was then chosen, Stereolithography (SLA).

SLA was chosen as it was water tight [176]. A similar test section was printed using SLA with Formlabs standard resin. The test section was checked for water tightness and afterwards it was subjected to a constant heat flux applied by wrapping heaters around it until the wall temperature reached 70 ^{o}C. As the material reached the high temperatures, smoke was observed coming from the inside of the test section. After it cooled down, the wall started to fracture. The smoke and fracture are shown in Figure D.2. While the temperature didn't reach Formlabs standard resin's melting point (73 ^{o}C), it didn't cause material problems. The printing material was then chosen to

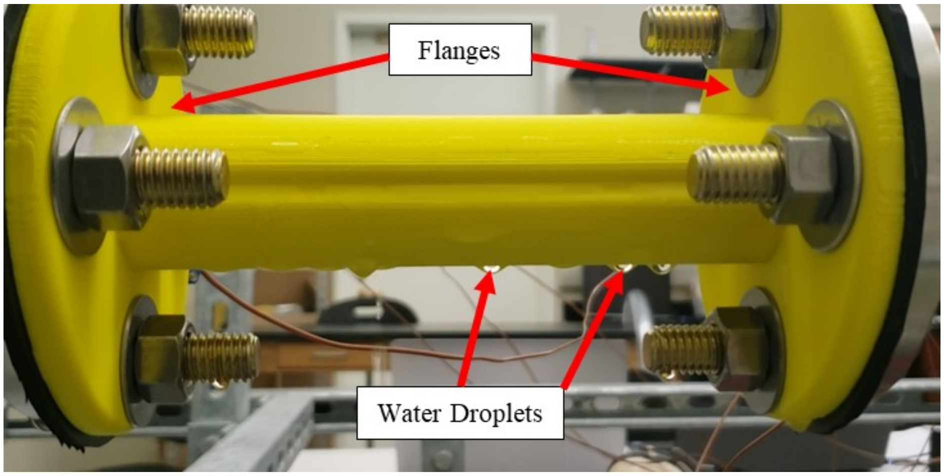

Figure D.1: FDM printed test section installed in MSETF-1 with water droplets.

Formlabs high temperature resin.

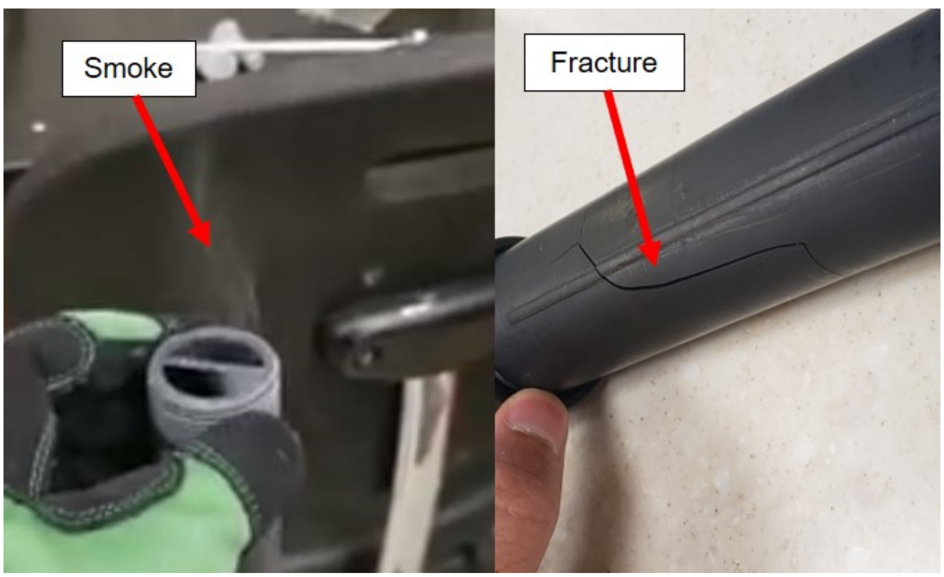

Figure D.2: SLA printed test section with smoke (Left) and fracture (Right).

With a printing material established, the next task consisted of creating a test section that was long enough to have fully developed flow. In order to create long test sections to achieve fully developed flow a methodology had to be developed as commercial 3D printers have a maximum printing volume. Test sections had to be printed in the same orientation to maintain constant surface roughness as previous work showed that printing orientation changes the surface roughness [117]. The first method to connect the test sections consisted of a coupling mechanism that had normal and inverted threaded threading so multiple test sections could be locked in together. This coupling mechanism allowed for a smooth transition between printed pieces, as can be shown in Figure D.3 obtained by a CT scan of the coupling mechanism.

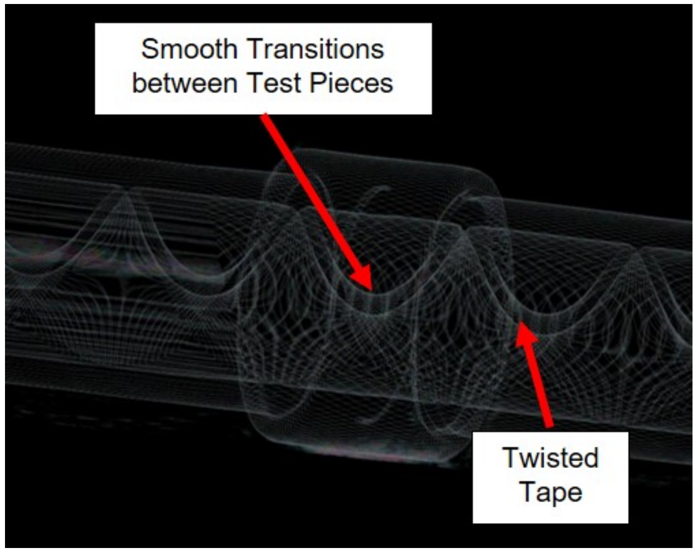

Figure D.3: CT scan showing coupling mechanism to create a smooth transition between printed pieces.

A set of empty pipe and twisted tape test sections were printed using this coupling mechanism and they were installed in MSETF-1, as shown in Figure D.4. Preliminary data were obtained using this locking mechanism with good agreement with established empty pipe correlations from Moody (using stainless-steel pipe's roughness) [115], Filonenko [105], and Blasius [116]. This data set was obtained with 12 individual test sections of 15.24 cm long with an inner diameter of 2.67 cm, with 11 connections.

The coupling mechanism proved to be effective, but it had long installation procedure, and the multiple connections meant the probability of leaking was very high. The experimentalists had to balance between tightening the coupling mechanism enough to make it water tight while not damaging the threads used to lock the test sections together. This proved to be more complex than initially thought out. Thus a final coupling mechanism consisting of gluing was designed and implemented.

D.2 Current Model

The current iteration consists of "gluing" the test sections together after they have been 3D printed individually and cured. Similar designs to the previous versions were used as starting points. The connection points consisted of male-female connections. Taking advantage of the SLA printing methodology, the male-female sides of two test sections were "glued" together by adding resin between the connection locations and then subjected to UV light for curing. This method was

Figure D.4: Individual coupling mechanism test sections (Left and Middle) and installed in MSETF-1 (Right).

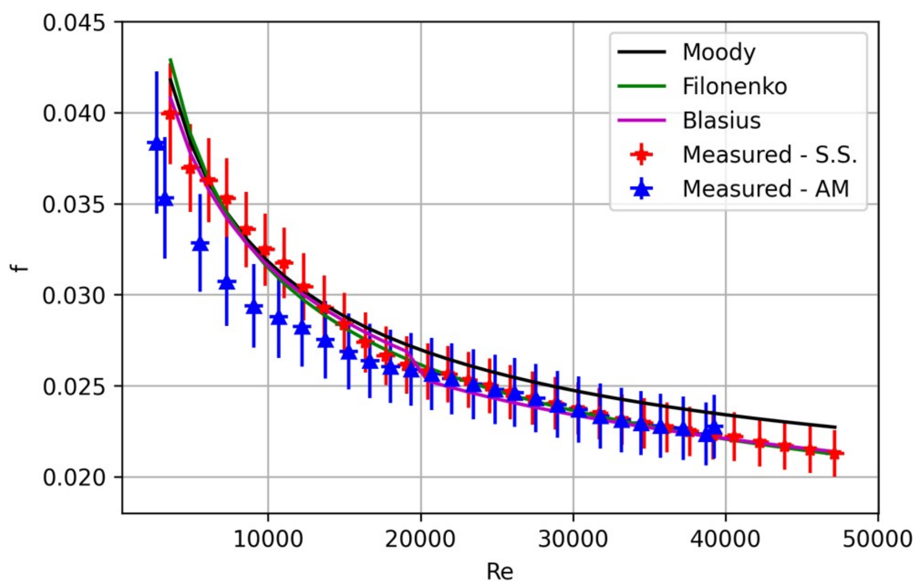

Figure D.5: Friction factor comparison between additively manufactured test section (AM), traditional stainless-steel pipe (S.S.) and correlations [105, 115, 116].

tested using a mock-up section that represented the connection in a smaller scale. The scaled parts are shown in Figure D.6 with a UV lamp to cure the resin and unite the parts.

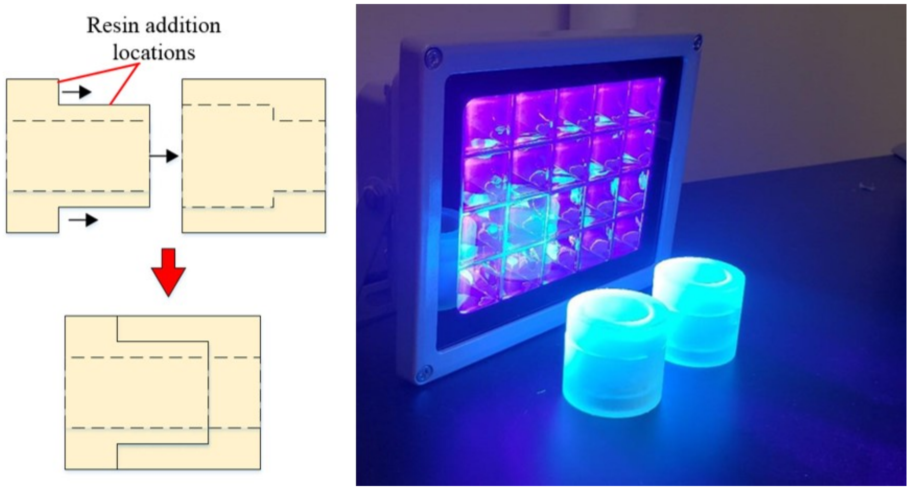

Figure D.6: Schematic showing the current design to build test sections with locations of where the additional resin was added (Left), and the curing of the parts togehter (Right).

Once the "gluing" mechanism was successful and was proven to be water proof, the design was incorporated to the actual test sections. A box was designed to glue multiple test section simultaneously by having two orifices at the top of the box where UV lamps rested. A set of mirrors were placed at the bottom to reflect UV light back to the "gluing" parts. While the mirrors aided for a more uniform curing of the test sections, the test sections were also rotated constantly to improve the overall curing. The curing box is shown in Figure D.7

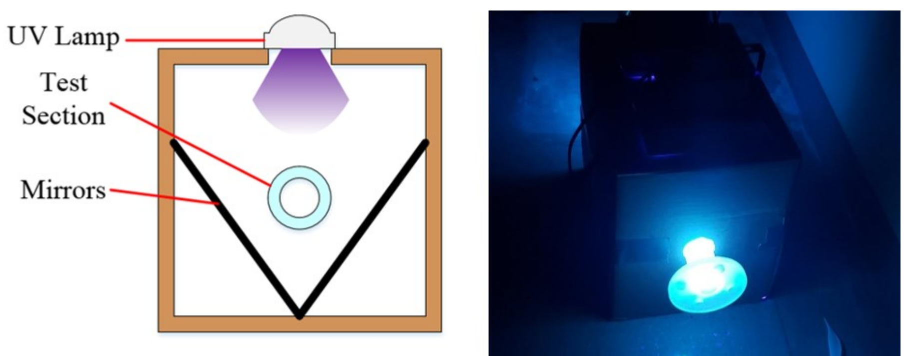

Figure D.7: Schematic of the curing box with location of mirrors, UV Lamp, and test section (Left) and the box curing together test sections (Right).

Longer test sections were then manufactured using this methodology. The curing technique proved to be extremely valuable as any leaks were fixed by adding more resin and further curing the section under UV light. The final design consisted of building the test section as one complete piece. Three different designs were created to build the overall test section. The first one consisted of the middle parts, the same repeating design glued together to build the middle of the test section. A schematic of the middle test section is shown in Figure D.8

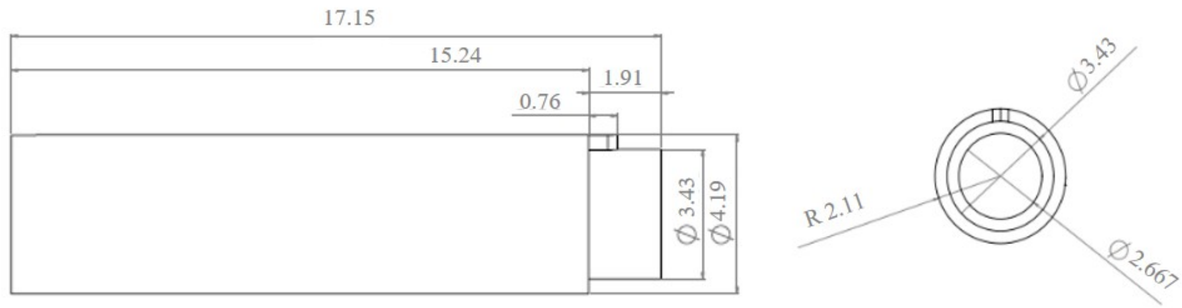

Figure D.8: Schematic of the middle parts with units in centimeters.

The second and third part of the test section consisted of the endings. The flanges were 3D printed with the overall test sections connected to one female or one male connection on the opposite side of the flange. The flange was designed to match commercial flanges bought for MSETF-1 for easy installation and removal. This overall method was used to create the test sections currently studied for friction factor and Positron Emission Particle Tracking.

D.3 Additive Manufacturing and PEPT

Flow distribution in additive manufactured parts was studied using Positron Emission Particle Tracking (PEPT), Section 4. The novelty of using additive manufacturing with a flow visualization tool such as PEPT required the validation that 3D printed parts would be capable to withstand the gamma radiation produced from the decay of the radiotracers Section 4.2. There is a limited amount of work previously done combining radiation and additive manufactured. The majority of the work found for additive manufactured parts subjected to radiation focused on the medical field for radiation oncology [177]. With other studies focused on space applications [178, 179] or shielding [180]. Unfortunately, the studies focused primarily on FDM printing or direct ink 3D printing, with a lack of studies using SLA.

While the overall radiation exposure to the material is low during PEPT experiments, a methodology to test the initial integrity of the 3D printing material and the "gluing" mechanism was designed. An SLA box with a puzzle-piece connection was 3D printed as shown in Figure D.10. The box was referred as the Tesseract as the image of the box under UV radiation to glue the puzzle piece together resembled that of the Tesseract of the Marvel Cinematic Universe, MCU. The box was designed with a hole on top to insert the aqueous radiation, while the bottom part was "glued" in a similar fashion as the test sections. This methodology was chosen to study both the effects of radiation in a fully cured section and in a "glued" section to mimic experimental conditions. A schematic of the radiation box is shown in Figure D.11.

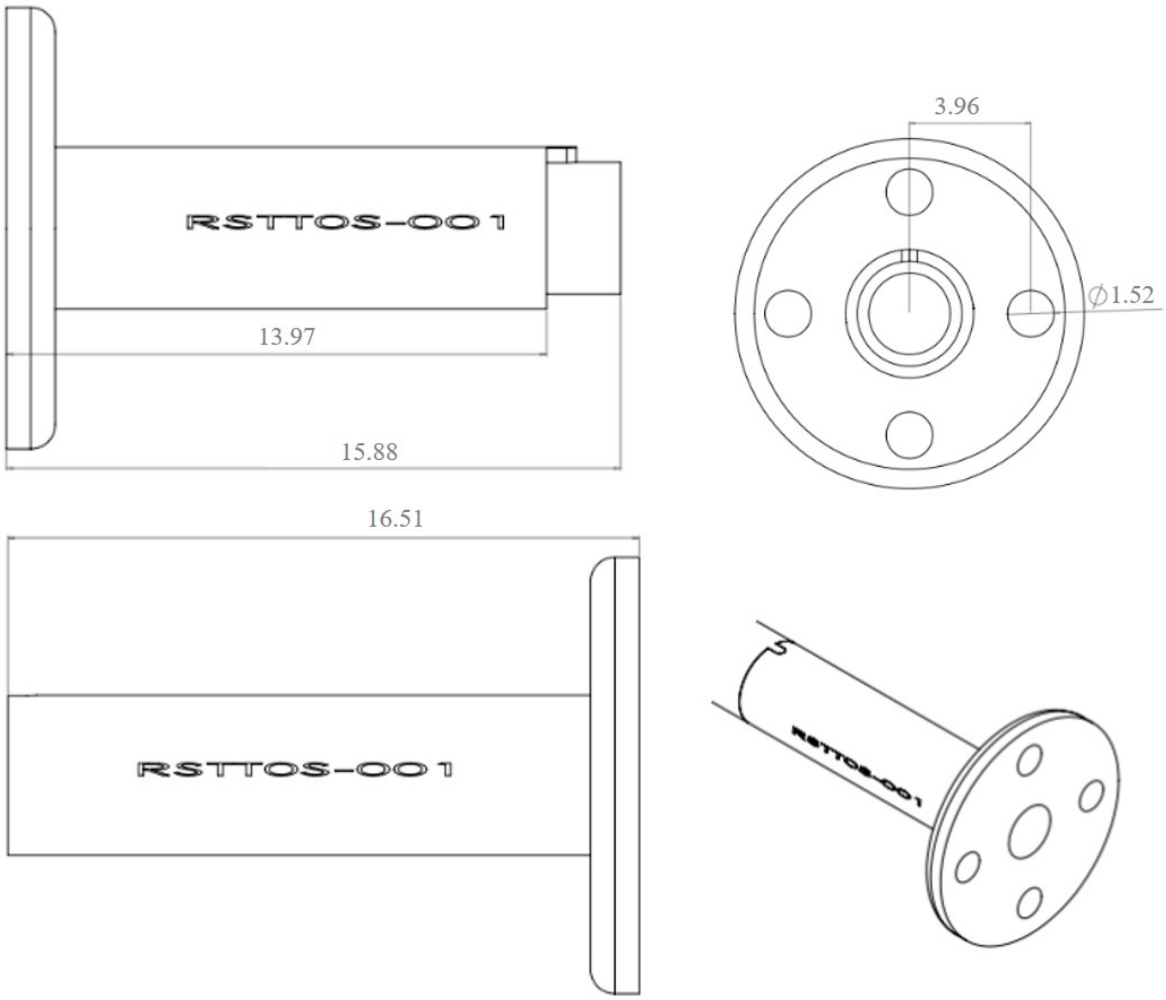

Figure D.9: Schematic of the endings of the test sections with flanges with units in centimeters.

The testing criteria consisted on whether the 3D printed box would leak after a long exposure to the radiation. While a lot of different mechanical tests could and should be done to fully understand the mechanical changes that occur due to the gamma radiation, but those kind of studies were left for future work. This study was to ensure the integrity of the parts was not compromised. This to guarantee that the test sections would not leak during tests and cause damage to the Mediso LFER scanner or cause undesired disturbances in the flow.

Figure D.12 shows the set up for the radiation test. The whole configuration, shield and syringe holder, was placed inside the scanner room (to limit radiation to the surrounding areas). The 3D printed box was placed inside a shield with paper towels in the bottom and filled with deionized water. The F-18 arrived in a syringe, and it was directly administered to the box through the hole on the top. Afterwards, the syringe was placed in the syringe holder.

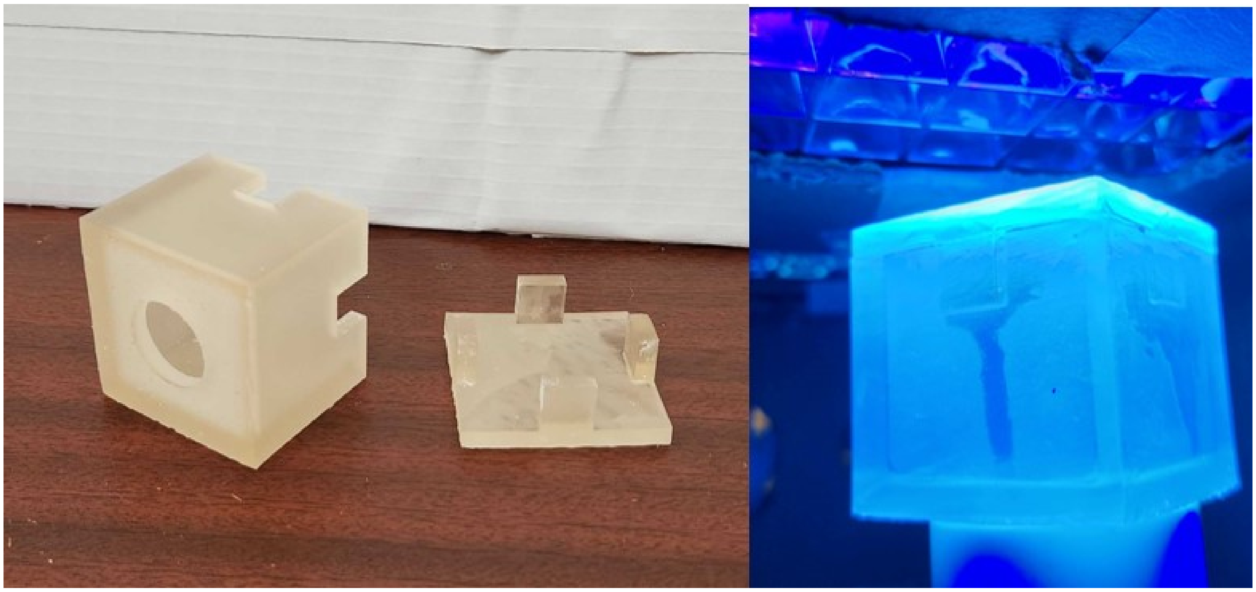

Figure D.10: Radiation box pre-gluing (Left) and while gluind (Right).

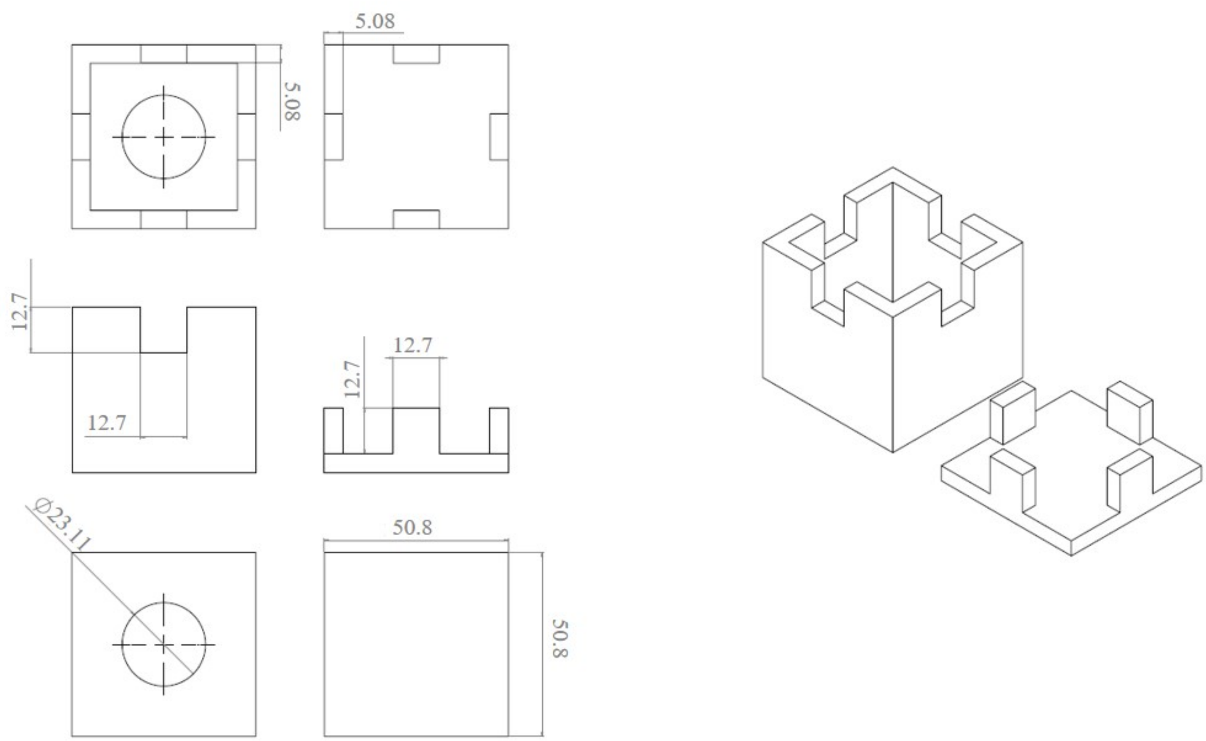

Figure D.11: Detailed schematic of radiation box with dimensions in millimeters.

The steps done for the radiation test were as follows:

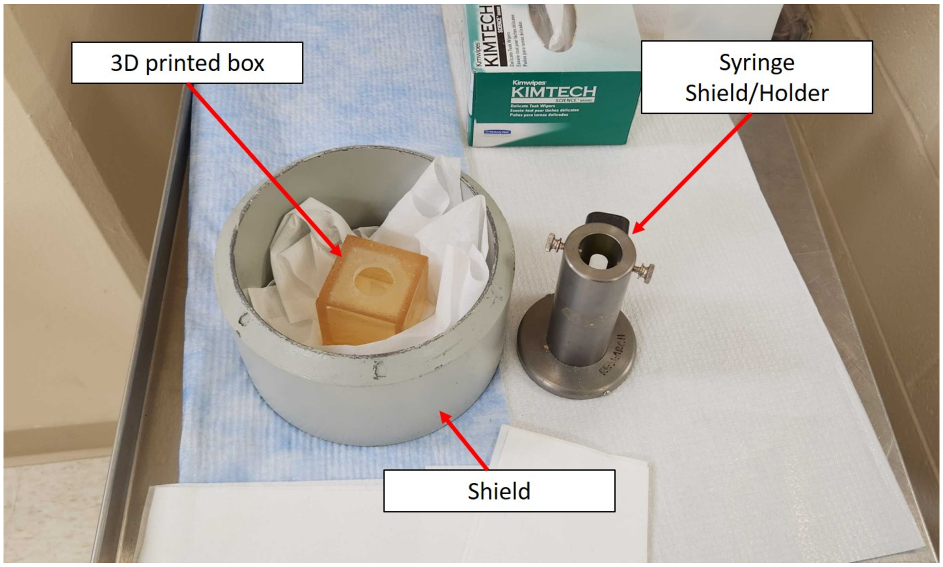

Figure D.12: Radiation test set up with 3D printed radiation box, shield, and syringe holder.

1. The F-18 was picked up in a shielded shipping cask, or lunch box;
2. The shield lunch box was brought inside the Mediso LFER room and placed as close to the set up as possible;
3. The shield lunch box was opened;
4. The F-18 was immediately administered into the radiation box;
5. The syringe was placed in the syringe holder;
6. The experimentalists ran from the room and the door was closed;
7. The experimentalists returned 3 days later to check on the status of the box and proceed with radiation safety paperwork and clean up.

In total, 30 mCi of aqueous F-18 were administered to the 3D printed box. This was more than expected in normal PEPT experiments as on average 10 mCi are actually administered to the entire loop. After the experiment, the integrity of the box remained the same and it was still water-tight, allowing for actual PEPT experiments to be performed in the additive manufactured parts.

Appendix E

PEPT AT VIRGINIA COMMONWEALTH UNIVERSITY

Positron Emission Particle Tracking (PEPT) is a fluid flow visualization technique that focuses on tracking a radiotracer through a field of view of a PET Scanner. PEPT was introduced and developed at Virginia Commonwealth University (VCU) through the efforts of Dr. Cody Wiggins. PEPT has been possible thanks to the partnership between the FAST Research Group led by Dr. Lane B. Carasik and the The Bioimaging and Applied Research Core (BARC) at VCU. This in the hopes of the continue usage of the Mediso LFER scanner and explore further capabilities within the University.

E.1 Mediso LFER - Software

This section describes the methodology and sequence of events to collect PET data from the Nucline Software. Figure E.1 shows the Nucline Software window to create a new protocol to collect PET Data. The option of "New" is selected which props open a window to input the name of the study, with a detailed description given to the name of the data set, and further select which Study Information was selected. In this case, a Study Information had already been created that accommodated the PEPT data acquisition set up of a vertical configuration.

E.2 Radiolabelling

Radiolabelling consisted of the methodology chosen to activate the OH anion resin particles with the ^{18}F aqueous solution bought from Sofie Biosciences, Inc. This section describes the radiolabelling practice at VCU initially developed by Dr. Cody Wiggins. A brief introduction to this technique is already discussed in Section 4.2.2, with one major change of the activity ordered from 30 mCi to 35 mCi to adjust for the varied time delivery from Sofie Biosciences.

Additionally, a couple of changes have been done to the procedure initially designed by Dr. Cody Wiggins. The first change consists of the order in which Glycerin is added to the particles to allow for more interaction between the Glycerin and the activated radiotracers before they are introduced to the PEPT flow loop. The second consists of the re-fill of the Transportation Vile in the case in which particles remained stuck in the vile after the injection.

The radiolabelling procedure started by preparing the particle solution. This was done by measuring 25 to 50 mg of the OH anion exchange solution described in Section 4.2.2 using a scale. This gave approximately 50,000 to 100,000 particles, as approximately 2,000 particles weighted one milligram. The particles were added to a conical Eppenderdof Tube labeled X with 200 μL already in it. The particles were kept in open air as little as possible, thus after being measured they were immediately submerged in the deionized water.

The desired concentrations were between 50 to 75 particles per μL. Depending on the amount of particles measured, as exactly 25 or 50 mg measured was not exact but an approximate, deionized water was added to tube A using a 20 - 200 μL Pipettor to obtain the desired concentration.

Tube A and the rest of the radiolabelling materials such as deionized water, sharps container, needle, filter tube labeled B, centrifuge, cylindrical tube labeled C (transportation vile), Eppendorf tubes, and a waste container were placed inside the castle.

Once the ^{18}F was delivered, in the form of a syringe, the detector was calibrated based on the current time, $T_{current}$, the calibrated time, $T_{calibrated}$, the decay time constant of the ^{18}F, λ, and the ordered activity, A_0:

$$A(t) = A_0 \cdot e^{-\lambda \cdot (T_{current} - T_{calibrated})}. \tag{E.1}$$

The usual calibration time consisted of 11:30 a.m. with an activity of 30 or 35 mCi.

After the detector was calibrated, the needle was connected to the syringe and the ^{18}F was added to the tube filter, tube B. Afterwards, the activity left in the syringe was measured as some activity was always left in the syringe. Finally, the syringe and needle were then placed under a shield intended for syringes.

The particles are introduced to the ^{18}F by inserting 20 μL of the concentration from tube A in to tube B the filter tube. At this point, the "marinating" of the particles occurred. This consisted of 21 minutes in which the particles and the ^{18}F were allowed to bond. Every 3 minutes the particles were agitated to increase the ionic bonding. The 21 minutes to activate, "marinate", the particle was chosen to allow the bonding between the ^{18}F and the OH anion resin while the time was minimal to reduce the decay of the ^{18}F.

After the marinating of the particles, the next step consisted of washing of the particles. This consisted of removing the extra ^{18}F that did not bond to the particles. To do this, an initial concentration activity was measured and then tube B was placed in the centrifuge. The centrifuge was set to 5080 RCF for 40 seconds. After the centrifuge stopped, 200 μL were added to the filter, the filter was then placed in a separate shield to measure the waste water.

This initial wash determined how well the radiolabelling procedure was executed. A good radio-labelling procedure consisted of a measured initial waste water lower than 1 mCi. In some cases, half of the activity was lost in the first wash. This was later determined to occur with ^{18}F aqueous solutions larger than 200 μL.

After the activity of the waste water was measured, the waste water was removed from tube B using the Eppendorf. The washing procedure was then repeated until the waste water activity was lower than 500 μCi. This meant the majority of the ^{18}F was now attached to the particles.

The next step consisted of transferring the particles to tube C, the transportation vial. Before the particles were transferred, a few drops of Glycerin were added to transportation vial. The particles were transferred using the Eppendorf. Afterwards, 200 μL were added to the filter to collect any particles left in the filter and tube B. This was then added to tube C. This procedure was repeated until tube C had 1000 μL.

The activity of tube C was measured before the particles were added to the flow loop. The particles were added to the flow loop by dropping the particles in tube C through the particle injection line. Afterwards, the activity of tube C was measured. If the activity was higher than 1 mCi, 200 μL of deionized water were added to tube C. The tube was then shacked and added to the flow loop through the particle injection line. The activity of tube C was then measured a final time.

Once the radiolabelling procedure was done, the PET and LabVIEW data were collected.

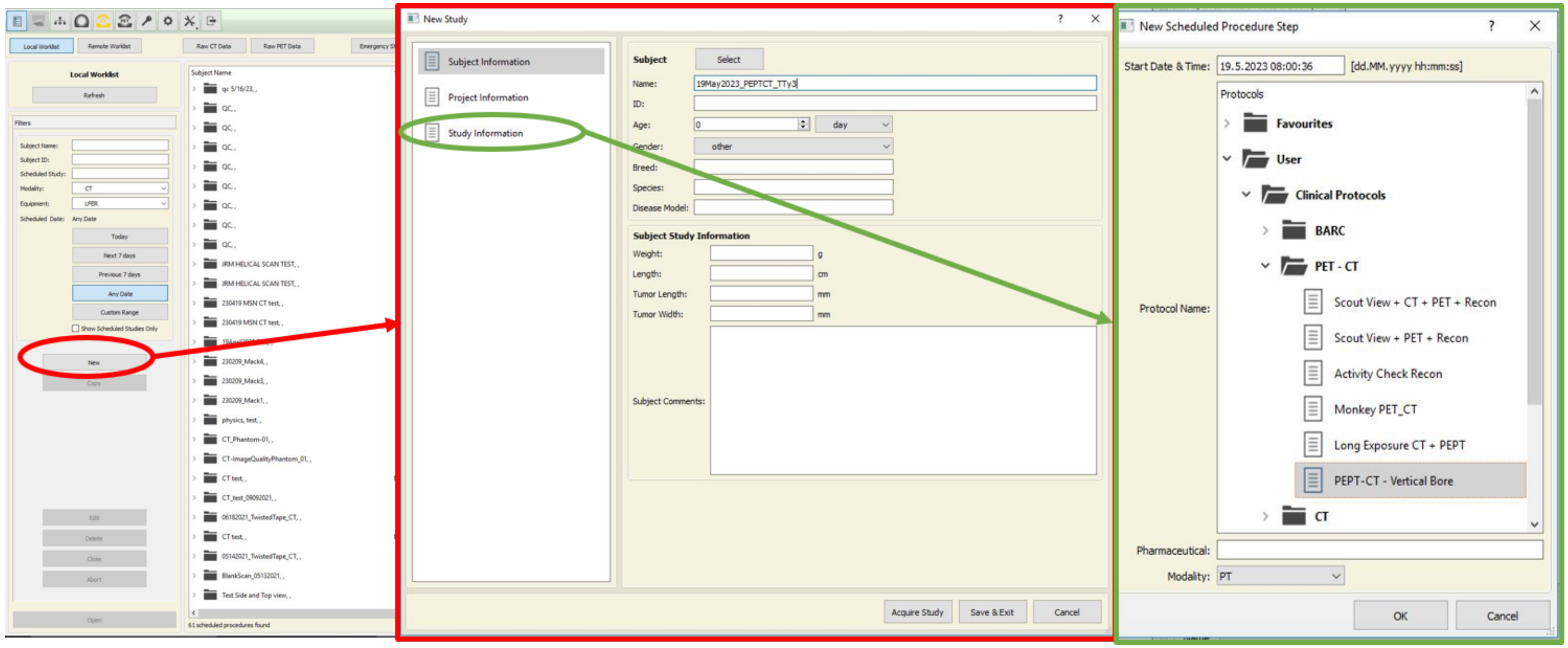

Figure E.1: Nucline Software window to start a new protocol with selections to name the new protocol and the study information.

VITA

Arturo Cabral was born in 1994 in Eagle Pass, Texas to Maria del Carmen and Gerardo Arturo Cabral. He was raised in Gomez Palacio, Durango, Mexico. He attended Colegio Ingles, in Torreon, Coahuila, Mexico for his elementary. The same school his mother taught and his sister, Marcela Cabral, attended. Arturo started playing tennis at the age of 10 years old in San Isidro Club, a country club in Torreon, where he fell in love with the sport. His mother, his sister, and Arturo moved to Eagle Pass, Texas, in the summer of 2008 in search of a better life, while his father stayed in Mexico to work. He attended Eagle Pass Junior High School and Eagle Pass High School, where he played for the tennis team.

In the Fall of 2013, Arturo enrolled at Texas A&M University, College Station in the Department of Nuclear Engineering. He began research with Dr. Yassin Hassan in June 2015, where he focused on thermal hydraulic experiments. He was able to attend multiple conferences in the U.S. and present his research to the American Nuclear Society. He graduated in December 2017 with a Bachelor of Science in Nuclear Engineering and a minor in Electrical Engineering.

In May 2018, Arturo interned for the International Atomic Energy Agency in Vienna, Austria. He worked on multiple projects, with a focus on publishing a Technical Document Number 1879. He was able to travel in Europe during his free time and visited multiple countries and cities. He finished his internship in May of 2019 and started an internship at Argonne National Laboratory (ANL) the following month. At ANL, Arturo worked on novel velocity instrumentation for advanced reactor concepts.

In the Fall of 2019, Arturo started his Doctor of Philosophy (Ph.D.) at Virginia Commonwealth University (VCU), in Richmond, Virginia under Dr. Lane B. Carasik to focus on heat transfer enhancement techniques for molten salt reactors. Arturo met Dr. Carasik at Texas A&M University while working under Dr. Yassin Hassan. During his Ph.D., Arturo interned for ANL in the summer of 2021 working on a velocity probe using a temperature sensor under Dr. Darius Lisowski. Arturo also interned at Kairos Power in the summer of 2022 under Dr. Giacomo Busco, working on computational fluid dynamic simulations for Kairos Power's reactor core. During his time at VCU, Arturo played tennis for VCU's club and soccer for different teams. Arturo will graduate from VCU with his Ph.D. in Mechanical and Nuclear Engineering in August 2023, and will start work at Northrop Grumman as a Hydrodynamics Engineer in September 2023.